THE UNIVERSITY OF CHICAGO

DARK MATTER HALOS AND THEIR ENVIRONMENTS

A DISSERTATION SUBMITTED TO
THE FACULTY OF THE DIVISION OF THE PHYSICAL SCIENCES
IN CANDIDACY FOR THE DEGREE OF
DOCTOR OF PHILOSOPHY

DEPARTMENT OF ASTRONOMY & ASTROPHYSICS

BY

PHILIP MANSFIELD

CHICAGO, ILLINOIS
AUGUST 2020

Dedicated to the 2016-2017 students of the KICP Space Explorers program:

the greatest scientists I have ever met.

"*To turn around that close to the summit...*," Hall mused with a shake of his head on May 6 as Kropp plodded past Camp Two on his way down the mountain. "*That showed incredibly good judgment on young Göran's part. I'm impressed - considerably more impressed than if he'd continued climbing and made the top.*"

— Jon Krakauer, Into Thin Air, pp. 190

TABLE OF CONTENTS

LIST OF FIGURES

LIST OF TABLES

ACKNOWLEDGMENTS

Completing a Ph.D is a difficult task: I spent (and continue to spend) perhaps 95% to 99% of my time being wrong about one issue or another, and the complexity, long time scales, and self-direction needed to complete a research project make it easy to burn out. I am eternally grateful that my advisor, Andrey Kravtsov, had very frank conversations with me about these hurdles during my first year of graduate school. It was this openness and willingness to discuss all parts of life as an academic that cemented my decision to stay as his student for these past six years.

We have weathered many storms together. Twice, we experienced the joy of losing seasons or years worth of work due to subtle technical mistakes. These are the moments which test your values as a scientist: it would be so easy to simply give up, or to be tempted by spurious rationalizations for why the problems aren't that big of a deal. Andrey guided me through these pivotal moments flawlessly, and in the end they helped form who I am as a scientist. Outside these big moments, Andrey has done a fantastic job transforming me into an independent researcher: he knew when to tell me what to do and when to let me make my own mistakes. I hope to do the same with my own students one day.

Having a good advisor is only part of the story. The writing of this thesis was only possible due to an army of formal and informal mentors who helped guide me through my journey. The other leader of UChicago's Computational Astrophysics group, Nick Gnedin, has been a constant source of advice since before I even matriculated to UChicago. He has an uncanny ability to condense weighty advice into concise packages. My collaborators – and frequent mentors – Benedikt Diemer and Camille Avestruz have helped me immensely on topics ranging from how to write job applications, to how to run simulations, to how to format the LaTeX in this thesis. Their recent faculty appointments will ensure that they continue to help students for years to come. Mike Gladders and Dan Fabrycky have also been very helpful throughout my time in graduate school (both informally and as members of my thesis committee), as has been my faculty mentor, Dan Hooper.

I would also like to thank Hy Trac and Bob Swendsen at Carnegie Mellon, who first introduced me to the world of physics research and taught me skills that I continue to use to this day. And I'd like to extend this thanks to Karen Wolfson, my high school AP Physics teacher. Her classes were what started me down the path to this thesis all those year ago. Looking back at the sheer number of people who were critical to the creation of this one Ph.D thesis has really emphasized to me how important it is to actively ensure that all students have a rich and robust support network.

Beyond research, one of my great passions in graduate school has been teaching and outreach. I realized how important this was to me as an undergraduate at Carnegie Mellon, thanks to the guidance and mentoring of David Kosbie when I was a TA in his introductory programming class, 15-110. At UChicago, many faculty and student helped me to become a better teacher, especially Randy Landsberg after I was hired as the KICP Space Explorers instructor. I would like to deeply thank him, Dovetta McKee, Terhonda Palacios, Phillip Wisecup, and Alex Lathan for the tireless work they put into this program during my time as the instructor, as well as Brian Nord and Rich Kron for helping to keep the program running in recent years. And I would like to once again thank Andrey for his endless patience with the amount of time I spent pursuing these efforts, and the many hours we have spent discussing the art of course design.

Lastly, I would like to thank my friends and family for the bottomless emotional support they offered me throughout graduate school, especially in the dark and turbulent times which accompanied the completion of this thesis. When this world becomes a better place, it will be your love and passion which took it there.

ABSTRACT

The structure and evolution of the universe at large scales is dominated by dark matter, particularly large clumps of dark matter called "dark matter halos." Soon after running the first large scale, high-resolution simulations, researchers realized that the growth of these dark matter halos was closely tied to their surrounding environment. This connection is called "assembly bias." Although this behavior is well-understood for the largest halos, the cause of assembly bias for smaller dark matter halos (such as the one which contains our galaxy, the Milky Way) has remained a mystery for the past fifteen years.

This thesis aims to resolve this mystery.

Accomplishing this goal requires constructing a substantial theoretical framework. One of the leading proposed causes for assembly bias stems from ambiguity of where halos end and where their surrounding environment begins. To this end, I develop SHELLFISH, the first code which is capable of measuring the boundary between the two, the "splashback surface."

Additionally, the study of assembly bias requires detailed analysis of large "cosmological" dark matter simulations. However, despite the long tenure of these simulations, there remain main unanswered questions about their accuracy. I perform extensive tests on the reliability of cosmological simulations, assessing the reliability of every major property of dark matter halos, and identifying previously unknown numerical biases which significantly impact a number of widely-used simulations.

Finally, using SHELLFISH to identity halo boundaries and these numerical tests to ensure reliability, I tackle the problem of galaxy-mass assembly bias. I identify the exact halos which are responsible for the assembly bias signal and use this identification to isolate the processes which lead to assembly bias. This analysis shows that galaxy-mass assembly bias is primarily caused by misidentified "splashback" subhalos, although a modest fraction of the effect comes from a small number of halos in massive filaments whose growth is slightly slowed by the tidal fields of their filaments and by gravitational heating.

CHAPTER 1

PROLOGUE

The story of this thesis begins on a paper-strewn table inside a Parisian palace in 1758. Three French mathematicians worked day and night over that table, desperately trying to beat a comet in a year-long race.

The comet in question was Halley's Comet. Decades earlier, England's Royal Astronomer, Edmund Halley, had predicted that the comet which would eventually bear his name would return in roughly 1758 [Cook, 1998].[1] Halley was an acolyte of the physicist Sir Isaac Newton and hoped that the comet would be the final proof that the rest of the world needed to accept Newton's theories of physics. While Newton had elegantly *explained* the previously measured motion of the planets through the solar system, the relatively static nature of the cosmos meant that there were few opportunities for him to *predict* new phenomena. Halley saw such an opportunity in this comet.

Halley had attempted to use Newton's theories to model the previous appearances of the comet, but this turned out to be a far more complicated task than he had anticipated and he was forced to make very crude approximations [Cook, 1998]. His estimates of the comet's path ended up being so inaccurate that the satirist Jonathan Swift devoted an entire chapter of Gulliver's Travels to relentlessly mocking Halley in specific and the Newtonian project of predicting celestial motion in general [Swift, 1726].

Halley's undoing was the existence of Jupiter and Saturn (as Newton had patiently explained to him several times; e.g., Newton, 1695). As his comet traveled through the solar system, it would be tugged slightly off its orbit by the gravity of the solar system's largest planets, speeding up or delaying its reappearance by up to two years. Predicting the behavior

1. Although the comet now bears his name, Halley certainly did not discover it. The first unambiguous written record of the comet comes from a Chinese astronomical journal in 239 BC [Kronk, 1999]. Halley did not discover the comet's periodic nature either: Raban Yehoshua offhandedly mentions the comet's approximate period in the Talmud [b. Hor. 10a]. This passage would have first been written down in $\approx 200 - 220$ CE, but could have entered Jewish oral tradition as early as 700 years prior to being written down.

of more than three objects interacting through gravity is a famously intractable task (called "the three-body problem"). This is not the type of calculation which can be worked out on a blackboard. Or a warehouse full of blackboards. However, these three French scientists had decided to attack the issue from a fundamentally new angle.

The leader of the group was Alexis Claude Clairaut. Clairaut's crowning achievement in life was mentoring Émilie du Châtelet, the woman who developed the concept of conservation of energy through a stunning combination of theoretical, empirical, and philosophical work [Zinsser, 2006]. du Châtelet was widely mocked in her time, so if you had asked his contemporaries, they would focus on other aspects of his work. They would tell you he was a titan of the French academy. They would laud his skilled but failed attempts to unseat Newton's theory of gravity, and his later defection to Newton's camp [Bodenmann, 2010]. They would tell you of his bitter (but victorious) rivalries with the terrifying and brilliant mathematician Leonhard Euler and the timid encyclopedia author Jean le Rond d'Alembert over long-standing mysteries related to the Moon's orbit [Bodenmann, 2010]. Clairaut hoped to leverage these earlier accomplishments to solve the mystery of Halley's comet and hoped that such a solution would cement him as the country's pre-eminent astronomer.

Helping Clairaut was the young astronomer Jérôme Lalande. While a capable theorist in his own right, Lalande's greatest gift was endurance and attention to detail. He made his name in the field through the creation of painstakingly detailed astronomical tables and by performing simple but laborious calculations which other astronomers could not bring themselves to finish [Grier, 2013]. Like Clairaut, Lalande was one of the few prominent physicists of the era who actively sought out and mentored female students in physics. One of these former students made the third member of the team, Nicole-Reine Lepaute.

Lepaute was a noblewoman who spent her spare time publishing mathematics and engineering treatises under her husband's name. Lalande realized her genius while working with her husband on a clock-making book and the two became lifelong friends and collaborators [Grier, 2013]. Lepaute was one of the only women during this time period to have an officially

recognized position within the French scientific community[2] and spent years as one of the chief contributors to the French Academy of Science's astronomical almanac. She had an inhuman endurance for number-crunching, a skill which even the resolute Lalande marveled at in his memoirs [Lalande, 1792].

Emboldened by the iron stomachs of his colleagues, Clairaut developed his plan of attack for predicting the return of Halley's comet. The three of them would sit at their table for almost a year. They would work through their meals, they would work late into the nights. Instead of developing an elegant theory for the path of the comet, Clairaut planned to brute force a solution.

In detail, Clairaut's plan was to estimate the lag and gain that Jupiter and Saturn imparted on the comet as it passed them, month by month and degree by degree [see Wilson, 1993, for a full technical summary]. Lalande and Lepaute would recalculate the locations of the major bodies in the solar system at each step and worked out those planets' respective gravitational influence on the comet. Clairaut, sitting at the opposite end of the table, would take the final step of working out how these forces would perturb the comet. Throughout the entire process, Clairaut would continually replot the latest data. He would study these points like a nervous ship captain might scan the horizon for the faintest sign of storm clouds, looking for faint changes in curvature that might indicate growing errors.

It was a miserable ordeal: the group had started their calculation well within the window of time in which Halley's comet could return, and they worked in constant fear that it would appear before they finished [Grier, 2013]. Clairaut had already used a host of mathematical tricks to reduce the calculation to its bare essentials, and he introduced increasingly radical simplifications as the team's desperation grew. The endless computation was enough to make the normally stalwart Lalande suffer a mental breakdown, and at times the project

2. There were, of course, many women contributing to the advancement of European astronomy during this time period. However, most would be forced to publish under the name of a male family member or were referred to as "assistants" despite performing work that was indistinguishable from that of their male peers.

was only pushed forward by Lepaute's utter unflappability in the face of endless arithmetic [Lalande, 1792].

At last, Clairaut presented their[3] results to the French academy of sciences on November 14^{th}. He predicted the comet would return in half a year, with its closest approach to the Sun occurring on April 15^{th} the following year. The group had gone through the calculation multiple times, which Clairaut used to tack on an expected error in this prediction: 30 days [Wilson, 1993].

The real impact of this presentation was somewhat lost on the audience: Clairaut was not simply outlining one of the first tests of Newton's theory of gravity, he was reporting the results of the world's first true physics simulation.

At the end of March that following year, astronomers saw Halley's comet appear from behind the Sun. Due to the geometry of the Sun, the comet, and the Earth, most of the astronomy community had missed the unfurling of the comet's dusty tail during its approach. However, that era's most prolific comet hunter – a young Charles Messier – had seen Halley's comet a few months after Clairaut's announcement and kept it secret to prevent the more senior astronomer from changing his answer [Wilson, 1993]. A flurry of calculations took place to determine when the comet had been closest to the Sun, and the verdict came in: the prediction was 33 days late.

By the standards of modern error analysis, this was completely consistent with the team's estimates. However, Clairaut's old nemesis, d'Alembert, immediately declared the calculation a humiliating failure, and many other scientists pointed to a myriad of flaws and errors in the analysis [Wilson, 1993]. Clairaut argued that not only was the prediction successful, but that this result was the greatest evidence for Newton's theory of gravity that the world had produced to that point. (I am inclined to agree with him.) He would, however, return to

3. Lalande would receive professorship not long afterwards. Lepaute did not get official recognition for her contributions to the project due to a last minute loss of nerve by Clairaut [Grier, 2013]. Lelande would use his newfound authority to ensure that she received official scientific positions for the rest of her life [Ogilvie and Harvey, 2000]

the calculations every few years as the public debate raged on and somehow always managed to find a way to reduce the error by a few more days.

Detailed reanalysis centuries later showed that the chief failing of Clairaut's strategy was perhaps an opportunity for discovery. If the same analysis had included the then-unknown planets Neptune and Uranus, it would have been wrong by only two weeks [Wilson, 1993]. But given how little attention Clairaut and his team paid to tracking down the sources of their errors, it is difficult to say if this was a coincidence.

Clairaut, Lalande, and Lepaute's work serves as a fitting prototype for simulations as a whole, whether they are performed by hand or on a computer. Their story demonstrates some of the core principles behind numerical work.

First, even the simplest physics theories lead to complicated and non-obvious results as soon as one starts to become interested in complicated systems, such as a comet navigating through the orbits of large planets. While the behavior of these systems can sometimes be brought into focus through the power of pure algebra, often times brute force is the only real path to a solution.

Second, these complicated systems are some of the best opportunities to test our theories of the universe. While there are no shortage of beautiful theories which can predict symmetric and simple phenomena, like nearly circular orbits around a star, the rubber really meets the road once you figure out how these theories behave when predictions and interactions get messy. This differentiating power is why simulations have been with us since the days of the first physicists and why they will continue to be performed until the days of the last physicist.

Third, all simulations are approximations and will fail at some level. The inescapable question which all simulators must confront is how deeply these failures have crept into their results. A robust error model is the difference between a career-defining achievement and an embarrassing public debate that never quite goes away. It is the difference between interpreting a number as the sum of a thousand arithmetic mistakes or interpreting it as the

first evidence for a new planet since the start of recorded history.

This thesis serves as an example what those same principles look like when gravity simulations are fast-forwarded by centuries: past ingenious mechanical models [Holmberg, 1941], past the first steps into the electronic world [von Hoerner, 1960, Aarseth, 1963], and past the maturation of cosmological simulations into their current form [e.g. Navarro et al., 1997, Klypin et al., 1999]. If simulations could prove Newton's law of gravity when tracing a single comet pushed human endurance to its limits, what can they do once tracking millions of galaxies becomes routine?

CHAPTER 2

AN INTERGALACTIC MURDER MYSTERY: WHY DO DARK MATTER HALOS DIE TOGETHER?

The central focus of this thesis is about how dark matter halos are connected to their environments. Although this thesis will touch on many aspects of this topic, its primary goal is to resolve a long-standing mystery: what causes galaxy-mass "assembly bias?" The goal of this chapter is to help a layperson understand the following:

- The basic astrophysical setting within which this mystery takes place. (section 2.1, "The Setting: Galaxies and Dark Matter Halos")
- What the mystery is and the context behind why it is important (section 2.2, "The Crime: Galaxy-Mass Assembly Bias")
- The different solutions that have been proposed to solve this mystery (section 2.3, "The Suspects: Tides, Heating, and Misadventure")
- The strategy behind this thesis and a qualitative overview of its results (section 2.4, "The Plan: The Structure of This Thesis").

I have bolded important scientific terms and jargon the first time they appear.

2.1 The Setting: Galaxies and Dark Matter Halos

2.1.1 Galaxies, Satellite Galaxies, and Distances

If you go out on a clear night in the suburbs, you will probably be able to see about a hundred stars over the course of the night.[1] On average, the light from the dimmest of these stars

1. I estimated these numbers through a combination of data-mining the Hipparcos stellar catalog [ESA, 1997] and the conventional wisdom of amateur astronomers on environmental visibility (e.g., http://www.icq.eps.harvard.edu/MagScale.html). The main factors that determine the number of stars you'll see are the weather, how close you are to a major city, and whether you can get above the local treeline.

takes about about 160 years to reach the earth, which means that their typical distances is roughly 50 **parsecs**. A parsec is the standard unit of distance in astrophysics and is geometrically defined through the impact that the earth's orbit has on the apparent location of nearby stars. It is such mind-bogglingly large distance that it is difficult to gain true intuition for what it means (1 parsec is about 31 trillion kilometers), but it is comparatively easy to use it as a ruler for understanding other distances in the universe: parsecs measure distances where it is still possible for the human eye to see individual stars.

If you go out to a dark place – a boat on the ocean, a rural farm field, a mountain top – you can see much further into the universe. The sky will be more full of stars (about ten times as many: you'll be able to see stars twice as far away as you could before), but the main attraction is a dim band of light across the sky: **the Milky Way**. Most stars in the universe, including every star we see in the night sky, are members of large clumps of stars called **galaxies**. Our own galaxy, the aforementioned Milky Way, is shaped like a dinner plate and the stars we see in the sky take up the same volume as a mustard seed near the edge of that dinner plate: our neighborhood of stars is a little more than eight thousand parsecs from the center of our galaxy [Gravity Collaboration et al., 2019]. As we look out through the Milky Way, most of its several tens of billions of stars are too dim to see individually, but collectively blend together into a fuzzy ring of light that encircles the night sky. This gives us the second rung on our intuitive distance ladder: **kiloparsecs** – a thousand parsecs – are used to measure the size of galaxies.[2]

If the dark place that you traveled to was in the southern hemisphere, you would be able to see two other dim objects to the south of the Milky Way's band. These objects are known as the **Magellanic Clouds** to modern astronomers.[3] They have featured prominently in the

2. Galaxies are quite diverse objects: one of the smallest that I know of is Kim 2, which is 0.024 kpc ($2 \times R_{1/2}$) across [Drlica-Wagner et al., 2019, and references therein]. It is only visible because it has ventured dangerously close to the Milky Way. One of the largest that I know of, Abell 2142, is 358 kpc across [Kravtsov et al., 2018] and is in the process of destroying multiple Milky Way-sized galaxies.

3. This is a regrettable convention, given that Magellan did not discover these objects and – more importantly – that his first actions upon encountering Pacific islanders on Guam was to kill and mutilate several of them and to burn down a village [Pigafetta, 1522]. I would prefer that they were officially referred

astronomy and mythology for tens of millennia [e.g. Adams, 1998, Johnson, 1998, Haynes, 1998, Snedegar, 1998, Orchiston, 1998]: by all accounts it would seem that the Magellanic clouds have been floating in basically the same location since the dawn of human civilization a hundred thousand years ago. But this apparent lack of movement is an illusion of humanity's embarrassingly short tenure relative to the 13.7 billion year lifetime of the universe.[4] In actuality, the Magellanic clouds are nearby **satellite galaxies** of the Milky Way [Leavitt, 1908, Leavitt and Pickering, 1912]. Along with a swarm of other small, dim satellite galaxies [e.g. Drlica-Wagner et al., 2019, and references therein], the Magellanic Clouds have been torn from nearby space by the Milky Way's gravity and now careen around it on a mess of interlocking orbits.

The term "satellite" invokes images of the serene, regular motion of a communications spacecraft around the Earth. This is not the case for satellite galaxies, which live erratic, violent, and (relatively) short lives. Satellite galaxies can form a variety of temporary alignments and structures as they whip around their hosts [Pawlowski, 2018] and can slosh from side to side in response to outside events [Conn et al., 2013]. The Milky Way has shredded many satellite galaxies which ventured too close to the massive disk of stars we see in the night sky [Garrison-Kimmel et al., 2017], and some large satellites have had the audacity to smash into the Milky Way itself [Belokurov et al., 2018, Helmi et al., 2018]. The drama of these satellites plays out repeatedly as destroyed objects are replaced by new small galaxies that the Milky Way's gravity drags from the local universe. This process ticks on as the Milky Way slowly creeps towards its own eventual fate.

The reminder of this fate can be seen for most of the year in the Northern Hemisphere. Just to the south of the Milky Way's disk is gray blob a few degrees across. It is faint: the blindspot in the center of your vision prevents you from seeing it if you look directly

either by one the many names given to them by cultures native to the Southern Hemisphere [e.g. Adams, 1998, Johnson, 1998, Haynes, 1998, Snedegar, 1998, Orchiston, 1998] or by the constellation-based naming convention used by modern satellite surveys.

4. Modern measurements indicate that over this time period, the Magellanic Clouds have moved less than a fiftieth of a degree across the sky [van der Marel and Sahlmann, 2016].

at it. This is the **Andromeda Galaxy**, the nearest major galaxy to the Milky Way. The two are very similar, although Andromeda is a more dominating presence. Like the Milky Way, Andromeda is a disk galaxy, only bigger [Sick et al., 2015]. Like the Milky Way, Andromeda is surrounded by a swarm of satellite galaxies, only the swarm is larger and deeper [McConnachie et al., 2009]. Recent measurements of Andromeda indicate that it will collide with the Milky Way in about six billion years, an event which will likely destroy both galaxies [van der Marel et al., 2012, 2019].

Despite its enormity, Andromeda appears tiny to us due to its distance. It is almost a hundred times further away from the Earth than the center of our own galaxy: 740 kpc or 0.74 **Megaparsecs** [Ribas et al., 2005, Vilardell et al., 2010]. This is the last rung on our qualitative distance ladder and the largest distance which the raw human senses have any connection to. A Megaparsec is the distance at which the entire expanse of the night sky – all the stars and constellations, the great disk of the Milky Way, its violent satellites, and its looming demise – are condensed to a faint smudge that you can block out with your thumb.

This is the realm ruled by dark matter.

2.1.2 Dark Matter

Most astronomers believe that the majority of matter in the universe is a completely clear, completely dark, and completely collisionless fluid called **dark matter**. In fact, most of the evidence for dark matter supports a far stricter model where all galaxies are nestled deep within the centers of large dark matter clumps. This would mean that the growth of galaxies and their motion through the universe is almost entirely dominated by dark matter: galaxies form when dark matter lets them form and move where dark matter tells them to move.

This section will focus on why astronomers believe that dark matter exists, while sections 2.1.3 and 2.1.4 will outline how a universe full of dark matter behaves.

The proposition that the universe is filled with dark matter is both breath-taking and extremely annoying. Astronomy is a measurement-based science whose practitioners were

brought up on horror stories of epicycles and spiral nebulae, and accepting a model where most of important dynamics are governed by a material which is so difficult to observe is a drastic step. Additionally, decoupling the visible matter from the gravitationally important matter severely complicates modeling and makes scientific analysis much more difficult. Both these facts push back strongly against the acceptance of such a model. How on Earth did the astronomy community end up accepting such a miserable state of affairs?

The question of where this story even starts is an interesting history of science problem. Many astronomers had caught on to hints of dark matter's existence since the early 1930's: Zwicky [1933] and Smith [1936] noticed that large clusters of galaxies should rip themselves apart without unseen matter, Babcock [1939] and Oort [1940] measured stars orbiting around the outskirts of galaxies faster than the visible matter in those galaxies should have allowed, and Kahn and Woltjer [1959] argued that the Milky Way and Andromeda's collision course was only sensible with some form of dark matter. The arguments these authors used were essentially correct. Perhaps some or all of these authors deserve credit for one of the greatest discoveries in modern astronomy?

All of these early works were brilliant, but the bar for credit is a bit higher than that. It is not enough to be right: you must make a strong case. The errors in these early studies were large and the modeling uncertainties were significant.[5] Because of this, scientists at the time found early arguments for dark matter uncompelling and either ignored them or published more thorough work contradicting the earlier results [e.g. Schwarzschild, 1954, de Vaucouleurs, 1959, Page, 1959, Peebles, 1970, Rubin, 2006]. The most famous of these early studies, Zwicky [1933], received only 12 peer-reviewed citations in its first 40 years – most of them from other papers written by Zwicky – but retroactively received thousands after the onrush of support for dark matter in the 70's.

This onrush was started by the astronomers Vera Rubin and Kent Ford. Ford had

5. For example, Babcock [1939]'s velocity measurements were off from more modern studies, like Carignan et al. [2006], by nearly a factor of two. Astronomers at the time realized that his errors were at least this large and were poorly characterized.

recently built a revolutionary new spectrograph and was hoping to find an appropriately grand target for it. Rubin was an analyst leading an effort to use this telescope to measure how fast Andromeda rotated [Rubin and Ford, 1970, Rubin, 2006].[6] Their plan centered on a physics principle called the **Doppler effect**. An observant fan of NASCAR or an attentive pedestrian listening for an ambulance to pass might notice that passing vehicles sound higher pitched during their approach and lower pitched as they drive away. This is a fundamental property of all waves, not just sound, and it causes light emitted by an object approaching an observer to become slightly bluer and light emitted by an object retreating from an observer to become redder. Astronomers had attempted to use the Doppler effect to measure Andromeda's rotation for decades [e.g. Babcock, 1939], but earlier instruments had required dozens of hours of exposure time to image the faint sources near Andromeda's edge, and jitters and telescope repositionings over that timescale seriously compromised the measurements [Sofue and Rubin, 2001, Rubin, 2006].

Rubin and Ford found that gas clouds at large distance from the bulk of Andromeda's visible matter orbited at roughly the same speed as those embedded within it [Rubin and Ford, 1970]. This is puzzling. The speed that objects orbit at is directly tied to how strongly they are pulled on by gravity. For example, in our solar system, Mercury travels at a much faster speed than the Pluto due to the latter's large separation from the Sun. Since the force of gravity decreases with distance, a constant speed meant that there was more mass contained within the orbits of more distant gas clouds, *even though there was no visible matter in those regions*. In other words, Andromeda was surrounded by an immense amount of invisible matter.

Rubin began to give talks about her preliminary results in 1970. She later recounted an encounter with another astronomer:

> After my talk, the esteemed Rudolph Minkowski asked when we would publish

6. Despite my view on who deserves discovery credit, Rubin attributed the discovery of dark matter to the astronomers Horace Babcock and Jan Oort in a review she coauthored, Sofue and Rubin [2001].

> the paper. I replied, "There are hundreds more regions that we could observe." He looked at me sternly and said, emphatically, "I think you should publish the paper now." We did. [Rubin, 2006]

This was fantastic advice. The 70's would bear witness to a torrent of new evidence for dark matter and if Rubin had waited to perform hundreds of additional measurements, she likely would have lost priority. Minkowski may have had some sense that the tide was about to shift, since he had been working on one of these new lines of evidence [Minkowski, 1962].

The line of evidence in question came from measurements of large clusters of galaxies. It is much easier to measure the Doppler shift of a bright galaxy that it is to measure the shift of the dim gas clouds targeted by Rubin and Ford, and astronomers had known that the galaxies in these clusters moved at high speeds – roughly 1000 km/s – since the 30's [Zwicky, 1933, Smith, 1936]. This would be not a problem if these clusters of galaxies were incredibly massive: if these clusters were several thousand times more massive than the Milky Way's stars, galaxies orbiting through them would naturally reach such high speeds. However, there were nowhere near enough galaxies in these clusters to account for so much mass through stars alone. Without enormous masses, these high velocities would mean that every cluster of galaxies in the universe was in the process of ripping itself apart.

This was not a slam dunk argument at first. One could avoid the inevitable conclusion of dark matter by questioning the assumed distances to the galaxy clusters,[7] questioning the models used to estimate the mass of the stars in a single galaxy, by introducing mostly dark – but still conventional – plasma in the cluster's center, or by thinking up any number of wild dynamical configurations. But by the 70's, these arguments were becoming almost impossible to make. By this point, the distances to galaxy clusters were known to about a factor of two [Tammann, 2006] and the conversion between luminosity and stellar mass had become reasonably robust (see the review in Faber and Gallagher, 1979). The last remaining

7. This was a rational thing to question in the 30's, since the prevailing method for measuring distances to galaxy clusters at the time was through combining mean recession velocities with Hubble [1929]'s wildly inaccurate $H_0 \approx 500$ km/s/Mpc.

piece of the puzzle was the weight of the plasma in the centers of these clusters.

While this plasma would emit essentially no visible light, the mass of these galaxy clusters meant that the plasma would shine brightly in high-energy X-rays. If it was possible to observe these X-rays, their energy would be an independent test of cluster masses, and their brightness would measure how much of that mass came from the plasma itself. Unfortunately for astronomers (and fortunately for the human race as a whole), the Earth's atmosphere blocks cosmic X-rays from reaching the ground, meaning that this measurement could only take place from a telescope orbiting the Earth. The first X-ray space telescope, UHURU, launched in 1970, allowing scientists to study cluster plasma for the first time [e.g., Gursky et al., 1971]. These measurements showed that these clusters were as massive as galaxy velocities had implied, but that the plasma was far too light to account for this extra mass. This substantial mismatch could only be interpreted as evidence for dark matter.

In addition to observational evidence for dark matter, the nascent field of computer simulations was also critical to establishing this paradigm. Ostriker and Peebles [1973] performed a set of simulations which showed that the beautiful disks of the Milky Way, Andromeda, and countless other galaxies would rapidly collapse into a spherical lump of stars unless embedded within an object at least as large (for example, a large ball of dark matter). This study, along with ever-improving measurements of the invisible mass around galaxies [Ostriker et al., 1974, Einasto et al., 1974, Roberts and Whitehurst, 1975] led to conversions en masse to the dark matter paradigm. By 1979, the popular sentiment in the astronomy community was well summarized by a famous review paper: "the case for invisible mass in the universe is very strong and becoming stronger" [Faber and Gallagher, 1979].

At the end of the 70's, astronomy was on the precipice of a great adventure. The next sections give a broad overview of our picture of this dark universe after 50 years of exploration.

2.1.3 Dark Matter Halos and Dark Matter Subhalos

Dark matter halos are at the soul of our current understanding of dark matter [e.g. White

and Rees, 1978]. Under our current understanding, every galaxy is embedded deep within a massive dark matter object called a halo. A halo is oblong lump of dark matter that gets progressively denser and more gravitationally intense as you approach its center.[8] Although the Andromeda galaxy appears to be only a few degrees across from the Earth, its dark matter halo is about the same size as a basketball held a foot from your nose.[9]

An image of a simulated dark matter halo is shown in Fig. 2.1. This image demonstrates the complexity of dark matter halos. The central object is composed of a tempest of interlocking streams and smaller halos, and is fed matter from its surroundings by a rich web of interlocking filaments and sheets (also composed of dark matter). How does such a structure come into existence?

The expansion and evolution of the universe is at the core of this story. Astronomers realized that the universe was expanding shortly after discovering that there *was* a universe outside the Milky Way [e.g. Friedmann, 1922, Lemaître, 1927, Hubble, 1929, Einstein and de Sitter, 1932]. Reversing this expansion backwards in time implies that billions of years in the past, the universe was a dense and hot mess filled with roiling particles which flitted in and out of existence due to quantum mechanics. All dark matter halos started as fluctuations within this turmoil. The early chaos eventually died away as the universe expanded and cooled, but these fluctuations remained as slight ripples in the density of the otherwise featureless and endless expanse of gas and dark matter. Ripples were enough.

While every inch of the universe was still filled with white-hot plasma, these ripples began their eternal battle with the expansion of the universe. Expansion frequently won out, pushing the ripples apart and flattening them. But gravity wins for many other ripples, pulling their outskirts tighter and tighter together until they collapse [Gunn and Gott, 1972a, Heath, 1977, Lahav et al., 1991]. These are the first dark matter halos. Their bat-

8. The image you should have in mind when you hear the word is less the ring-shaped halo over an angel's head and more the diffuse halo of light around the sun.

9. According to the galaxy luminosity-to-halo mass relation that my student, Maria Neuzil, developed as part of Neuzil et al. [2020].

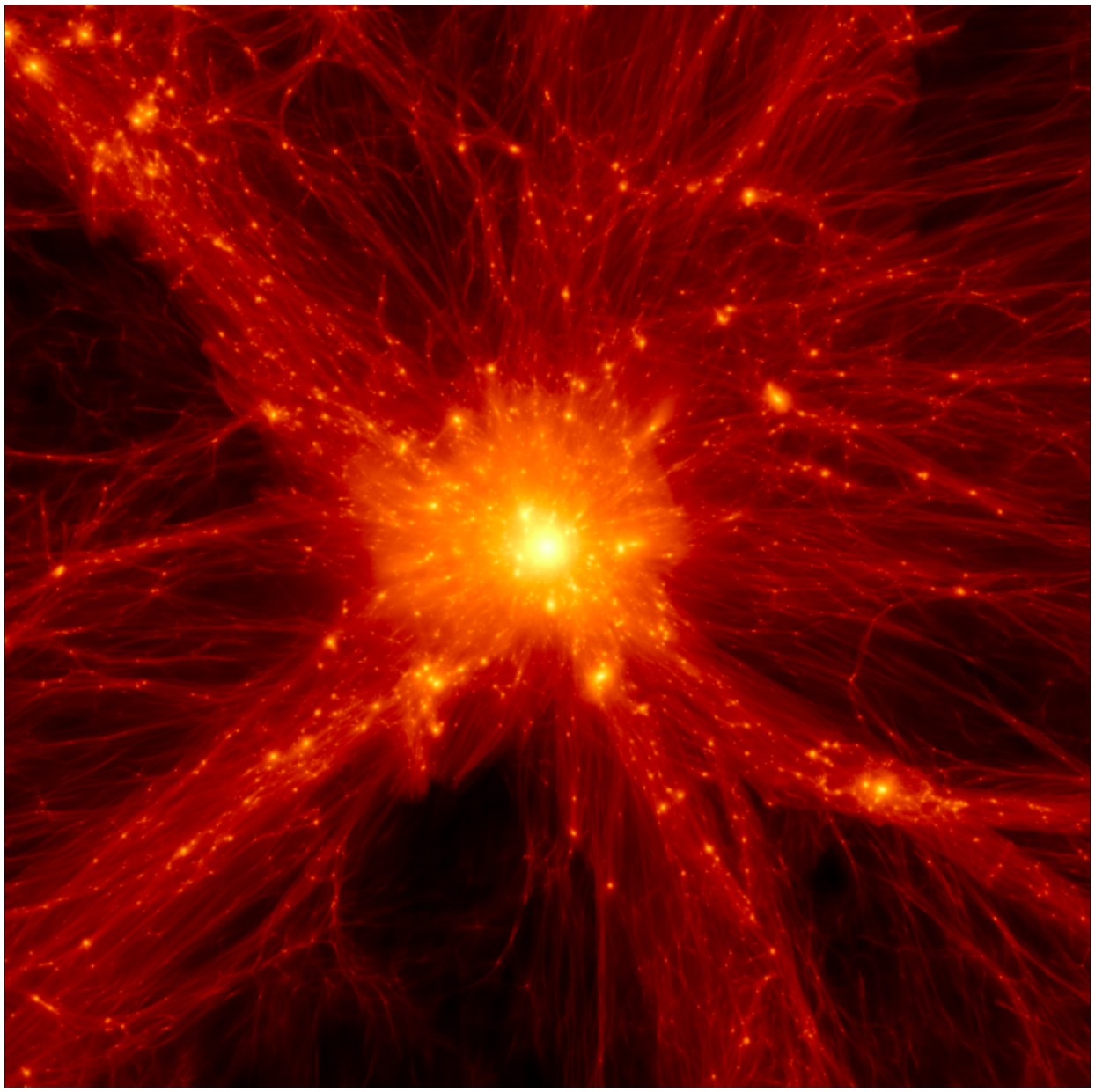

Figure 2.1: An image of a dark matter halo from one of the simulations run by Diemer and Kravtsov [2014]. The color in this image shows the density of dark matter, with brighter colors indicating higher density. The dark matter halo is the dense concentration of mass in the center of the image. This is a very large dark matter halo: this image is about twenty times wider than the separation between Milky way and Andromeda and in the real universe, such an object would contain many galaxies within it, like the Virgo or Coma clusters. It is fed matter and smaller dark matter halos from the surrounding universe through a series of capillary-like filaments. This image was generated by my imaging code called "gotetra" (`github.com/phil-mansfield/gotetra`) which is based on the algorithm developed by Abel et al. [2012b].

tle against expansion and eventual collapse form a preview for the formation of their much larger descendants.

To envision a dark matter halo collapsing, imagine a knot in the middle of a sheet. Imagine twisting that knot and pulling in more and more of the sheet into ever growing and ever complexifying folds. Imagine pulling in fabric from many sheets in all directions at once and imagine that this fabric was infused with smaller knots of all sizes. Lastly, imagine this process in motion, with folds constantly reweaving and oscillating around the knot and the smaller knots pulling in material as they themselves fall in [see, e.g., Vogelsberger and White, 2011, Abel et al., 2012b, for visualizations of this process].

What would a human have seen if they were transported back to such an early time?

With a few notable local exceptions, the universe has never been a hospitable place for humans, and the early universe least of all. For the first few hundred thousand years, quantum fluctuations and particle collisions would form a wall of instantly blinding light in all directions. This light would be strong enough to dissolve the human body quite rapidly: even 400 thousand years after the beginning of the universe, complete atomization would only take three days.[10] If you arrived during this time period, you would bear witness to a truly cosmic shift in the universe. All around you, the hot light-emitting plasma would be in the process of condensing into dark neutral hydrogen.

The switch would not be apparent to you immediately: the light from distant plasma takes time to reach your eyes. By the time the universe became almost entirely neutral[11], every direction you looked would still be the color and temperature of boiling lead. But as time progresses, this light must come from increasingly distant and ancient expanses of plasma, giving the expansion of the universe more time to redden and cool the light. After three million years, this visible plasma is farther away than Andromeda and has degraded to

10. This estimate takes the 3.6 eV carbon-carbon bond energy as a typical bond strength in the human body, assumes the human body has 7×10^{27} atoms [Freitas, 1999] and uses [Mosteller, 1987] to estimate a 1.9 m^2 surface area to the human body.

11. $z \approx 800$, $T_{\rm CMB} \approx 2100$ K, [Dodelson, 2003]

the muddy red of a horseshoe cooling after time in a blacksmith's forge [see the temperature tables in Chapman, 2019]. There is nothing but dark matter and formless gas between you and this wall of fire.

Soon, this light will slip into the infrared, invisible to human eyes, revealing the endless emptiness and perfect darkness of the universe you now find yourself in. This is not the darkness of our current universe, which is largely an illusion of our meager eyesight and can be solved with enough magnification [e.g. Beckwith et al., 2006]. This is a deeper existential darkness where there is truly nothing to see as far as you might look in every direction.

Ironically, the universe is saved from this dismal, lightless state by its ever-growing dark matter halos.

As dark matter halos continue to twist and grow, they pull in gas from their surroundings and much of this gas condenses until it is trapped in the halo's center. These clouds of gas are initially held up by their own internal pressure, but grow until their gravity overpowers their pressure and they collapse into the first stars [Haiman et al., 1996, Tegmark et al., 1997]. Single stars begin to form in the hearts of dark matter halos throughout the universe. These primeval stars are enormous and burn hot: their light breaks apart and ionizes the surrounding gas. As these dark matter halos continue to grow, the gas clouds trapped inside form larger groups of stars, and the first galaxies begin peek out from behind the receding neutral gas. These the stars and black holes in these galaxies accelerate the removal neutral gas even more. In less than a billion years, it is entirely vanquished.

Still, the dark matter halos continue to grow and their growth provides fuel for their inner galaxies. It takes a further 13 billion years to reach our current universe, and by this time galaxies have grown from from relatively paltry collections of stars to the massive configurations seen today. Invisibly, their dark matter halos have undergone a similar transformation, eventually reaching the incredible masses they enjoy today.

The complexity of halo collapse and formation is worthy adversary for modern computer simulations. Theorists created "simple" models of halo formation which could mostly be

worked through by hand [Gunn and Gott, 1972a, Fillmore and Goldreich, 1984, Bertschinger, 1985, Hoffman and Shaham, 1985], but these models did not capture the true mayhem that accompanies a dark matter halo's formation and were particularly ineffective at predicting what halos should look like in the inner regimes where most observations took place. In pursuit of this issue, many intrepid theorists took a page from Clairaut, Lelande, and Lepaute's book and immediately attempted to brute-force the solution with simulations [White, 1976].[12] Unlike their 18$^{\text{th}}$ century predecessors, these scientists were not constrained to simulating a single point: the recent proliferation of Cray-I supercomputers meant that an astronomer with generous grants and a knack for writing efficient Fortran could simulate a dark matter halo with several hundred particles. The early stages of this endeavor reached their conceptual zenith with the publication of Navarro et al. [1997], the first study which could reliably resolve the inner regions of dark matter halos in realistic environments. (This paper become one of the most cited theoretical papers in all of astrophysics, according to the NASA Astrophysics Data System). Since this point, dark matter simulations have continued to grow exponentially, with largest that I know of containing more than 2 trillion particles [The Uchuu simulation Ishiyama et al., 2020]. This growth has allowed simulations to study ever-increasing samples of dark matter halos and to probe the nature of the large scale structures that they form.

2.1.4 The Cosmic Web and Large Scale Structure

Dark matter halos do not grow in isolation, but as part of a large interconnected structure of matter which is woven into enormous sheets and filaments. This structure is called **the cosmic web** [Bond et al., 1996]. Fig. 2.2 shows a simulated image of a small part of the cosmic web.

The study of large scale structure is a dense topic, as one might expect from the complex-

12. Simulations of dark matter halos actually predate the dark matter model [Aarseth, 1963, Peebles, 1970]. These early works would simulate collections of "galaxies," but these galaxies were so simplistically modeled that the simulations were actually numerically equivalent to dark matter simulations.

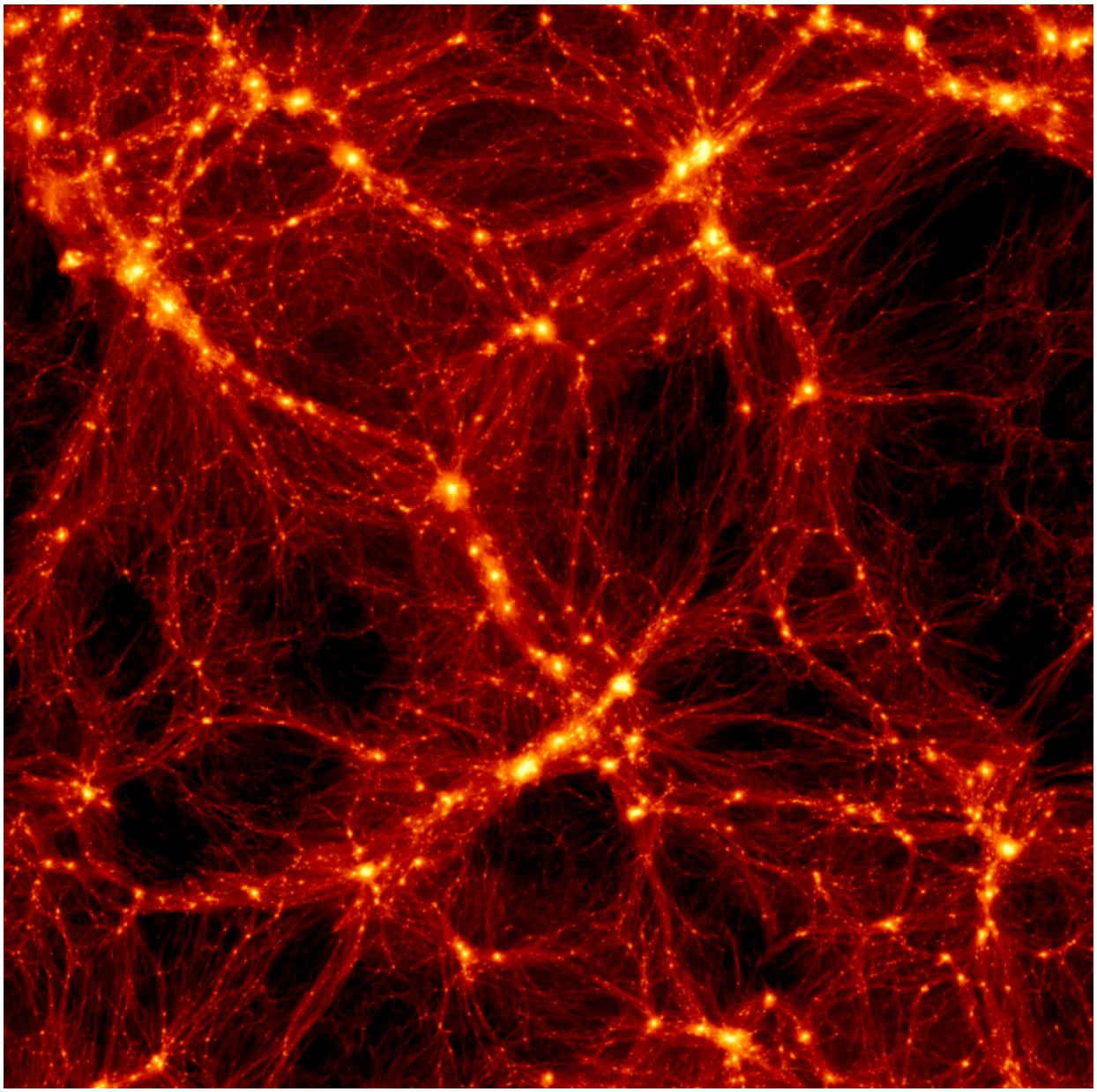

Figure 2.2: An image of of the cosmic web from one of the simulations run by Diemer and Kravtsov [2014]. This image is similar to Fig. 2.2 except that it shows a much larger scale: about a 120 times larger than the distance between the Milky Way and Andromeda. At large scales, the universe is filled with a vast network of filaments and sheets connecting dark matter halos of all sizes. Galaxy surveys show similar structures in the visible universe [famously, in Blanton et al., 2003]. The largest dark matter halos are clumped together in the densest parts of the cosmic web, a fact – called "mass bias" – which is important to studies of assembly bias.

ity of Fig. 2.2.[13] As such, rather than giving a complete overview, I would like the reader to take away three specific facts about the large scale structure of matter in the universe.

The first is that the formation of structure is divided into two stages: simple early growth and extremely complicated later growth. As primordial ripples of dark matter begin to collapse and become denser, their initial evolution is simple enough that lecturers routinely work through the equations which govern the behavior of these ripples over the course of a couple classes. This is called the **linear** regime. These simple equations become less accurate as the contracting perturbation becomes denser and break down altogether by the time the perturbations reach around twice the density of the surrounding universe. This later growth is called **non-linear**, and the only way to gain a theoretical understanding of what happens after this time period is to develop models which are empirically tested against simulations. On average, it takes longer for larger structures to reach the non-linear stage than it does for smaller structures.[14] This means that at large distance scales the universe is still evolving simply enough that detailed predictions can be worked out by hand, but that at small distances it is all-but impossible to predict what should happen without at least some use of simulations.

The second key fact is that there is a fairly definite limit to how large dark matter halos can get. In physics we often get comfortable with the idea that there is always "a bigger fish." A human is tiny compared to a planet, a planet is tiny compared to a star, a star is tiny compared to its solar system, a solar system is tiny compared to a galaxy, and so on. However, this process does eventually end: there is a class of dark matter halos which sit at the top of the size scale.[15]

13. For evidence of this claim, I direct the reader to the 259 page review paper, Desjacques et al. [2018], which concerns itself only with how common galaxies are in regions of the universe with different densities.

14. This is true in Λ-Cold Dark Matter, the current leading cosmological model, but different behavior can occur in other cosmological models.

15. There are collections of nearby dark matter halos which are more massive than the biggest individual halos – you can pick many of them out by eye in Fig. 2.2 – but these are not gravitationally "bound" objects yet. Some of these collections are especially large perturbations which are in the process of collapsing but haven't had time to complete the journey yet.

These rulers of the universe have a fairly boring name: **galaxy clusters**. But this name belies how intense these objects are. Galaxy clusters can reach sizes that are up to ≈ 3000 times larger than the Milky Way [16], they can contain hundreds or thousands of Milky Way-sized galaxies [e.g. Ge et al., 2019], and their strong gravity heats cluster gas to hundreds of millions of degrees, causing them to shine brightly in X-rays [e.g. Vikhlinin et al., 2006]. Galaxy clusters play a central role in many of the theoretical models that are discussed in later sections.

The last key fact about large scale structure is that galaxy clusters are significantly more common in dense regions of the universe, to the point that you're essentially guaranteed to find a few of them lurking in the distance if you travel to a dense region. This is not simply because there are more objects in these dense regions: halos become more **biased** relative to underlying density at higher masses [Bahcall and Soneira, 1983, Klypin and Kopylov, 1983, Kaiser, 1984]. Although there are a host of formal statistical tests which can demonstrate this fact, you can also see this by eye in Fig. 2.2: while smaller dark matter halos (smaller blobs) are spread throughout the web, cluster halos (the largest blobs) are mostly found in the very dense regions where multiple filaments join together.

2.2 The Crime: Assembly Bias

To summarize the previous sections, the story of the universe is one that we read through measurements of stars, galaxies, and gas, but that story is written by dark matter structures and their growth. And there is a mystery hidden in the growth of dark matter halos.

Specifically, Sheth and Tormen [2004] and Gao et al. [2005] found that dying galaxy-mass halos – halos which had gone billions of years without significant growth – were strongly clustered together. This interaction between clustering and halo growth is called **assembly bias**. Assembly bias is illustrated qualitatively in Fig. 2.3, and can measured quantitatively

16. The most massive galaxy cluster I know of is ACT-CL J0102-4915 [Jee et al., 2014]. Its nickname is El Gordo, "The Fat One."

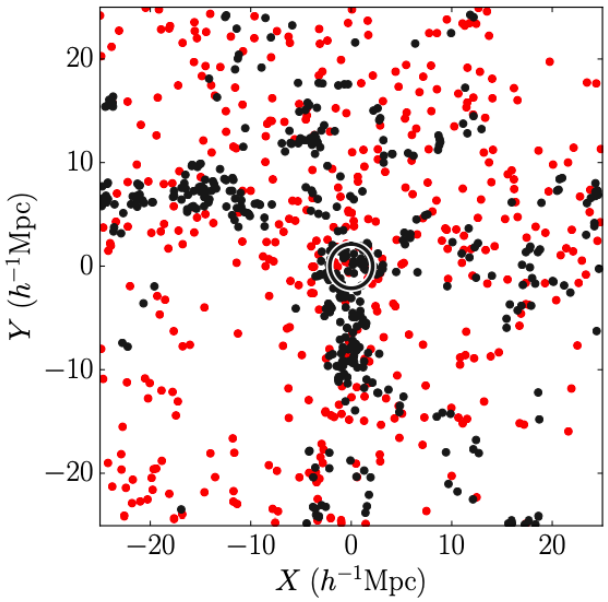

Figure 2.3: The locations of dark matter halos in a cosmological simulation. The dark matter halos shown here are roughly the same size as the halo surrounding the Milky Way and the width of the Figure is about a hundred times larger than the distance between the Milky Way and Andromeda. Halos are colored by age: the "oldest" 15% of halos (the ones growing the slowest) are shown in black and the "youngest" 15% are shown in red. The black circle shows the size of the largest halo in the simulation to give a sense of scale. Old halos are tightly clustered on large scales which exceed the size of even the largest halos. Readers interested in a technical discussion of this Figure and the associated definitions can find it in chapter 6.

through a host of statistical tests.

Halo growth is intertwined with nearly every halo property, meaning that this finding has wide-ranging implications. Consider a dying halo whose supply of matter from the surrounding universe has largely dried up over the past billion years. This dying halo continues to destroy and consume its subhalos which means that now that its supply is no longer replenished its substructure will slowly be depleted [$f_{\rm sub}$ decreases; Gao et al., 2004]. Matter and substructure stops becomes more centered and symmetric [$X_{\rm off}/R_{\rm vir}$ decreases; Macciò et al., 2007]. Orbital dynamics cause the halo's core to grow more slowly than the rest of the halo when it is starved of additional matter [$R_s/R_{\rm vir}$ decreases; Wechsler et al., 2002]. The outer edge of the halo expands [$R_{\rm sp}/R_{\rm 200m}$ increases; Diemer and Kravtsov, 2014] and bulk of the matter starts to relax into rounder shape [c/a approaches 1; Allgood et al., 2006].

The halo's spin – already slight – begins to slow down [λ decreases; Vitvitska et al., 2002].

The connection between the age of dark matter halos and the properties of their inner galaxies is a far more complex topic [e.g. Wechsler and Tinker, 2018], but there are a host of reasons to expect that galaxy properties are tightly connected to growth histories of their dark matter halos. Of particular note is the potential connection between halo growth and the rate the stars form in the halo's galaxy, since the star formation rate is closely connected to a host of galaxy properties, like appearance, color, and dust obscuration. Observational studies have demonstrated a close connection between halo mass and galaxy mass (see Wechsler and Tinker, 2018 for an overview and Huang et al., 2020 for a particularly breath-taking recent study), a correlation which requires that star formation and halo growth are strongly connected. Theoretical models which assume halo growth is the driving factor behind star formation can be calibrated to predict a wide range of complex observations [e.g. Behroozi et al., 2018]. Simulations which attempt to model both processes simultaneously explicitly show a strong connection between them [e.g. Matthee et al., 2017].[17]

Put more directly: *assembly bias means that dark matter halos and their galaxies look and behave differently in different parts of the universe, even at a fixed halo mass.*[18]

There are a large number of studies which are impacted by this fact. Perhaps no field of astronomy is more affected than the massive theoretical effort over the past twenty years to develop theoretical models which attempt to "paint" galaxies onto dark matter halos so that our observations of the universe can be compared against the unobservable theoretical predictions of a dark matter-dominated universe [e.g. Berlind and Weinberg, 2002, Yang et al., 2003]. However, the majority of these analyses have explicitly assumed that

17. There are some reasons for skepticism. Observationally, some recent studies which purport to measure halo growth rates in the local universe claim that galaxy and halo growth are uncorrelated [Behroozi et al., 2015, Tinker et al., 2017, O'Donnell et al., 2020]. The theoretical models which assume a connection between halo growth and galaxy growth make some incorrect predictions unless ad hoc components (orphan galaxies) are added to them [e.g. Campbell et al., 2018]. Lastly, simulations that track stars and gas do not resolve many critical processes, have many tunable parameters, and require complex verification regimens [e.g. Hopkins et al., 2018], which can make it complicated to interpret how strong a given prediction is. Suffice to say, there are many papers left to be written on this topic.

18. This statement has been confirmed by a wide array of studies, see the overview in Mao et al. [2018].

assembly bias never reaches its tendrils into the observable properties of galaxies, meaning that the existence of assembly bias and the uncertainty in the connection between galaxies and their halos has loomed over this field like the Sword of Damocles [Zentner et al., 2014]. Assembly bias impacts astronomy in less obvious ways, as well. For example, most of our understanding of dim satellite galaxies comes from observations of a handful of nearby galaxies [see Carlsten et al., 2020, for an overview]. But all these observations take place in the same local environment, and that environment is not a particularly common one [Neuzil et al., 2020]. Any connection between this environment and the structure and character of these satellite systems could strongly impact our ability to interpret these observations [e.g. Libeskind et al., 2015].

Efforts to resolve and model the effects of assembly bias have been stymied because it isn't clear why assembly bias happens at galaxy masses. Early measurements of assembly bias were a shot out of the blue: theories of halo growth at the time [most notably Press and Schechter, 1974] were built on the foundational assumption that large-scale structure had little-to-no effect on halo properties, and it was clear that radical adaptations were needed [Gao et al., 2005].

The problem of assembly bias is to theorists as a lantern is to moths, and soon there were no shortage of reasonable-sounding explanations. However, the proposed causes of assembly bias would affect halo growth in different ways and would impact different groups of halos, raising the question of which explanation is actually correct. The following section lists the most prominent models for this effect.

2.3 The Suspects: Tides, Heating, and Misadventure

The oldest attempted explanations for assembly bias (and those first suggested by Gao et al., 2005) tried to alter the models of how of primeval dark matter perturbations contract and collapse [e.g. Sandvik et al., 2007, Desjacques, 2008, Dalal et al., 2008, Chue et al., 2018]. This undertaking proved to be a fantastic success in understanding how assembly bias impacts

galaxy clusters [Dalal et al., 2008], but unfortunately, this success did not translate down to galaxy masses. There was a simple reason for this: galaxy clusters are massive and unlikely to be disturbed by larger objects while growing. This means that individual perturbations can largely be considered in isolation at high masses, but that this analysis will insufficient for many smaller mass halos.

Because of the failures of single-perturbation collapse models, theorists have ventured into the multi-object complexities of the non-linear regime. What happens to the growth of halos when they spend their lifetime navigating beneath the shadows of objects thousands of times their mass?

One of the most pressing concerns in the non-linear world comes from subhalos which have temporarily wandered far from their host halos. As discussed in section 2.1.1 and 2.1.3, the satellites of large dark matter halos have a tumultuous life. While some distinct halos may stop growing when they run out of material to accrete, virtually all subhalos stop growing as they are tossed about and ripped apart by their hosts [van den Bosch, 2017, gives an astonishingly complete overview of this topic]. This is a problem because researchers rarely actually check whether an object is a subhalo. Instead, the typical approach is to draw an ad hoc boundary around each halo or galaxy[19] and use this boundary to determine which objects are or are not subhalos [e.g. Gao et al., 2005, Wechsler et al., 2006, and many others].

However, subhalos can actually orbit far beyond the boundaries researchers often adopt [Balogh et al., 2000]. Because of this, when the most massive halos in the universe are analyzed with standard techniques, it appears as if they are surrounded by swarms of dying Milky Way-sized galaxies and halos. Because these massive galaxy clusters are only found in the densest regions of the universe, this misclassification means the oldest galaxy-mass halos are also found in these regions. Multiple researchers have attempted to quantify the impact of these errant subhalos on assembly bias, but came to different conclusions over

19. i.e. The so-called "virial radius."

how important they are [Wang et al., 2009, Li et al., 2013, Wetzel et al., 2014, Sunayama et al., 2016]. This confusion stems from a combination of different definitions, ambiguity over when a subhalo first enters its host, and disagreements over the difference between a subhalo which merely has a distant orbit and a subhalo which has been completely ejected from its host.

Other groups of researchers have proposed that these massive galaxy clusters play a second, even more important role: their intense gravitational field can stifle the growth of halos long before those halos fall into the cluster [Hahn et al., 2009, Behroozi et al., 2014, Hearin et al., 2016b, Salcedo et al., 2018]. Consider a satellite around the Earth. While this satellite is close to Earth, it has no trouble orbiting. But at large distances, the Sun's gravity will become more important and will eventually pull this satellite out of its orbit around the Earth and into an orbit around the Sun.[20] In this sense, the Sun's **tidal field** prevents objects from orbiting the Earth beyond a certain distance (it's "tidal radius"). This region where it is possible to orbit the Earth would decrease in size if the Earth moved closer to the Sun or if the Sun grew in more massive. Massive galaxy clusters have the same impact on Milky Way-sized dark matter halos which venture too close to them: the intense tidal fields limit how far away these smaller halos can attract fresh matter and therefore suppresses their growth. Because the massive halos hosting these galaxy clusters are clumped together in the densest regions of the universe, tidal fields can lead to dense portions of the cosmic web being filled with slowly-growing halos.

A related model proposes that the key factor isn't tidal fields from individual galaxy clusters, but instead the fields produced by the filaments and sheets of large scale structure itself [Hahn et al., 2009, Wang et al., 2011, Paranjape et al., 2018, Musso et al., 2018]. The

20. Where this occurs is a surprisingly subtle topic. The influence of the Sun on objects orbiting the Earth was the subject of several bitter academic fights during the early years of Newtonian astronomy [Bodenmann, 2010] and our friend Alexis Clairaut was a central character in this drama. Clairaut's lifelong enemy, Leonhard Euler, worked out the fundamentals during the year of Clairuat's death [Euler, 1765]. Put simply: at close distances, objects can orbit the Earth. At moderate distances, objects can appear to orbit the Earth while actually primarily orbiting the Sun (the Moon does this). At large distances neither is possible and objects can only orbit the Sun.

largest of these structures contain immense amounts of mass, meaning that their tidal fields can can have a strong impact on the objects floating inside of them. If true, this would mean that assembly bias stems from an effect that impacts *all* halos in these dense regions, rather than just the ones that happen to be next to galaxy clusters.

Lastly, some scientists have focused on another property of filaments: the velocity of objects inside them [Wang et al., 2007, Dalal et al., 2008]. As objects fall towards a massive filament, their velocity increases. This means that every object within these filaments is moving around at high speeds. This increased speed makes it more difficult for halos within these filaments to capture the matter around them and slows down their growth. Like large scale tidal fields, this effect impacts all halos within filaments, but leads to filaments of different sizes doing most of the heavy lifting.

To date there has been no attempt to compare or unify these explanations. There have been many papers arguing for one potential cause or the other, but these works rarely address competing papers and I am not aware of any which attempted an explicit comparison between the models. This has led to an unintentional Balkanization of the assembly bias literature, with authors citing work associated with one class of theories and largely ignoring other approaches. The goal of this thesis is to unify the theoretical assembly bias literature into a cohesive model.

2.4 The Plan: The Structure of This Thesis

This thesis compares these different explanations and argues for a synthesized model for galaxy-mass assembly bias: *most assembly bias at this mass scale is caused by misclassified subhalos. The remainder is caused by the impact of gravitational heating and large-scale tidal fields on a relatively small fraction of halos in large filaments.* I work through how I arrive at answer this in chapter 6. The journey requires building a substantial theoretical framework: it requires building tools to measure quantities which have never been measured before and requires putting simulations through tests which have never been performed before. I build

this framework up in chapters 4 and 5. Chapter 3 contains technical background information shared by all three chapters

At the start of my Ph.D, a number of collaborating research groups showed that simulated dark matter halos have distinct edges: the **splashback surface** [Diemer and Kravtsov, 2014, Adhikari et al., 2014, More et al., 2015].[21] The splashback surface is an edge in the density field around halos which is caused by particles and subhalos "piling up" far away from the halo halfway through their first orbits. These first studies could not reliably measure this edge in individual halos, but could find it by combining large groups of halos[22] or in simplified simulations. If it were possible to measure this boundary measure for individual halos, there would be an unambiguous way to identify subhalos: the splashback boundary splits infalling matter from all orbiting matter.

Chapter 4 develops the code SHELLFISH,[23] the first tool which could measure splashback surfaces around individual objects. Although the ultimate goal of this thesis primarily uses SHELLFISH to identify subhalos, chapter 4 covers other useful features of splashback surfaces, ranging from shapes and sizes, to their connection to the inner parts of halos, to their alignment with large scale structure. This chapter corresponds to the paper Mansfield et al. [2017]

Although dark matter simulations have existed for decades (see section 2.1.3), many questions about their reliability remain unanswered. In chapter 5, I perform wide-ranging tests on many of the highest-resolution dark matter simulations available today. I originally started writing this chapter to determine the reliability of the halos for assembly bias studies, but its conclusions are further ranging that this. Chapter 5 performs reliability tests on many dark matter halo properties (in some cases, these are the first tests that have ever

21. This had been predicted by some early models of halo growth [Fillmore and Goldreich, 1984, Bertschinger, 1985], but the significance of these predictions was not appreciated at the time.

22. This technique would soon be successfully used in observations [More et al., 2016, Chang et al., 2018]

23. The name is an acronym which stands for SHELL Finding In Spheroidal Halos. I came up with the name during the Physical Sciences Division's happy hour.

been performed on these properties), demonstrates that high-resolution simulations disagree to a larger extent than was previously believed, and shows that many aspects of simulations depend strongly on a subtle numerical parameter called the "force softening scale" (first introduced in Aarseth, 1963). Chapter 5 corresponds to the paper Mansfield and Avestruz [in prep].

With the field set, chapter 6 addresses the central question of this thesis: what causes galaxy-mass assembly bias? The approach I use in this chapter is to estimate how strongly the different effects listed in section 2.3 affect every halo in a simulation. Using these estimates, I determine how efficiently the different effects can create a universe with assembly bias, which allows me compare how closely connected these different processes are to assembly bias. I also synthesize the low-mass and high-mass treatments of assembly bias, and resolve some long-standing disputes over the nature of assembly bias by showing that they are the result of definitional differences. This chapter continues the tradition of chapters 4 and 5, with a heavy focus on understanding halo boundaries and an equally heavy focus on demonstrating the robustness and reliability of various measurements. Chapter 6 corresponds to the paper Mansfield and Kravtsov [2019].

CHAPTER 3

TECHNICAL BACKGROUND

This chapter covers the technical background shared by the later chapters in this thesis. While this chapter is more pedagogical than chapters 4, 5, and 6, it is more technical than the preceding chapters.

3.1 Simulations

This thesis uses eight simulation suites: Erebos_CBol [Diemer and Kravtsov, 2014, 2015], Erebos_CPla [Diemer and Kravtsov, 2015], Multidark-Planck [Klypin et al., 2016], Chinchilla [Lehmann et al., 2017], Bolshoi [Klypin et al., 2011], BolshoiP [Klypin et al., 2016], ν^2-gc [Ishiyama et al., 2015], and IllustrisTNG-Dark [Naiman et al., 2018, Pillepich et al., 2018, Nelson et al., 2018, Marinacci et al., 2018, Springel et al., 2018]. The properties of these simulations are summarized in Tables 3.1 and 3.1. Erebos_CBol is used in chapter 4, every simulation suite is used in chapter 5, and Bolshoi and BolshoiP are used in chapter 6.

Each simulation suite is the product of one of four simulation codes, each with varying gravity solvers and timestepping schemes. Bolshoi and BolshoiP were run using ART [Kravtsov et al., 1997, Kravtsov, 1999, Gottloeber and Klypin, 2008], the Multidark-Planck, Erebos_CBol, Erebos_CPla, and Chinchilla suites were run with Gadget-2 [Springel, 2005]. IllustrisTNG-Dark was run using Arepo [Springel, 2010, Weinberger et al., 2019] which performs gravitational calculations using an updated version of the Gadget-2 gravity-solving algorithm. ν^2-gc was run with GreeM^3 [Ishiyama et al., 2012, 2015].

An important aspect of these codes is the scheme they use for setting timestep sizes. Three of the four codes, Gadget-2, Arepo, and GreeM^3 use an adaptive timestepping scheme dependent on the local gravitational acceleration [Springel, 2005, Weinberger et al., 2019, Ishiyama, personal communication], and ART timesteps are density-dependent [Klypin et al.,

Code	Suite	$\Omega_{M,0}$	h_{100}	σ_8	η	Simulation
GreeM^3	ν^2-GC	0.31	0.68	0.83	0.045	ν^2-GC-L
						ν^2-GC-H1
						ν^2-GC-H2
ART	Bolshoi	0.27	0.7	0.82	–	Bolshoi
	BolshoiP	0.307	0.678	0.823	–	BolshoiP
Gadget-2	Chinchilla	0.286	0.7	0.82	0.025	L125
						L250
						L400
	Multidark	0.307	0.678	0.823	0.01	ESMDPL
						VSMDPL
						SMDPL
						MDPL2
						BMDPL
						HMDPL
	Erebos_CBol	0.27	0.7	0.82	0.025	CBol_L63
						CBol_L125
						CBol_L250
						CBol_L500
						CBol_L1000
						CBol_L2000
	Erebos_CPla	0.32	0.67	0.82	0.025	CPla_L125
						CPla_L250
						CPla_L500
Arepo	IllustrisTNG-Dark	0.3089	0.6774	0.8159	0.012	TNG100-1-Dark
						TNG100-2-Dark
						TNG100-3-Dark

Table 3.1: A list of simulations used in this work. The first six columns contain information common to all simulations in a given suite: the code used to run the suite, the suite name, the cosmological parameters Ω_M, $h_{100} = H_0/(100\,\mathrm{km/s/Mpc})$, σ_8, and the Gadget-like timestepping parameter, η. Note that ART does not use this timestepping scheme (see section 3.1 for details). This additional columns of this Table are given in Table 3.1.

Simulation	L (h^{-1}Mpc)	N^3	m_p ($h^{-1}M_\odot$)	ϵ/l
ν^2-GC-L	1120	8192^3	2.27×10^8	0.04
ν^2-GC-H1	140	2048^3	2.75×10^7	0.04
ν^2-GC-H2	70	2048^3	3.44×10^6	0.04
Bolshoi	250	2048^3	1.36×10^8	0.0082
BolshoiP	250	2048^3	1.55×10^8	0.0082
L125	125	2048^3	1.80×10^7	0.0082
L250	250	2048^3	1.44×10^8	0.0082
L400	400	2048^3	5.91×10^8	0.0082
ESMDPL	64	2048^3	2.60×10^6	0.032
VSMDPL	160	3840^3	6.16×10^6	0.024
SMDPL	400	3840^3	9.63×10^7	0.014
MDPL2	1000	3840^3	1.50×10^9	0.019
BMDPL	2500	3840^3	2.35×10^{10}	0.015
HMDPL	4000	4098^3	7.92×10^{10}	0.026
CBol_L63	62.5	1024^3	1.70×10^7	0.016
CBol_L125	125	1024^3	1.36×10^8	0.02
CBol_L250	250	1024^3	1.09×10^9	0.024
CBol_L500	500	1024^3	8.72×10^9	0.029
CBol_L1000	1000	1024^3	6.98×10^{10}	0.034
CBol_L2000	2000	1024^3	5.58×10^{11}	0.033
CPla_L125	125	1024^3	1.62×10^8	0.02
CPla_L250	250	1024^3	1.29×10^9	0.024
CPla_L500	500	1024^3	1.03×10^{10}	0.029
TNG100-1-Dark	75	1820^3	6.00×10^6	0.018
TNG100-2-Dark	75	910^3	4.80×10^7	0.018
TNG100-3-Dark	75	455^3	3.84×10^8	0.018

Table 3.2: A continuation of Table 3.1. The last four columns give information specific to each individual simulation: the simulation name, the box width, L, the number of particles, N^3, the particle mass, m_p, and the force softening scale at $z = 0$ in units of the mean interparticle spacing, ϵ/l. For the last column, we use Eq. 3.4 to convert from the formal resolution, h, to ϵ.

2011]. The former use adaptive time steps, with

$$\Delta t = \sqrt{2\eta\epsilon/|\vec{a}|}. \tag{3.1}$$

Here, $\vec{a}$ is the local gravitational acceleration, ϵ is the 'Plummer-equivalent' force softening scale which will be discussed below, and η is a user-defined parameter (also referred to as `ErrTolIntAcc`) that is typically set to $\gtrsim 0.01$. In practice, Δt is evaluated for each particle, the values are used to place particles into the coarsest logarithmic timestepping bin, $\Delta t_i = t_0 2^- i$, such that $\Delta t_i \leq \Delta t$. As such, the actual timestep size a particle experiences may be smaller than Eq. 3.1 by a factor of two. We note that while the initial GreeM^3 implementation used a different adaptive scheme [Ishiyama et al., 2009], GreeM^3 used the adaptive scheme described above to produce ν^2-gc (Ishiyama, personal communication).

ART timesteps vary at different depths of the refinement tree, meaning that they depend on density instead of acceleration. Both Bolshoi and BolshoiP use timesteps of $\Delta a \approx 2-3\times 10^{-3}$ at the 0^{th} (coarsest) refinement level with time steps decreasing by a factor of two for each successive level of spatial refinement, leading to timesteps of $\Delta a \approx 2-3\times 10^{-6}$ at the tenth level [Klypin et al., 2011]. The ART timestepping scheme leads to far finer timesteps than any of the other simulations considered in this paper.

3.1.1 Force Softening

Cosmological simulations do not model particles as point sources. Infinitesimal point sources will scatter off one another during close encounters, which leads to aphysical energy exchange between particles and can potentially thermalize the inner regions of dark matter haloes [see overview in Ludlow et al., 2019]. Additionally, these close encounters require much finer timesteps to resolve than typical orbits through a halo's potential, meaning that codes are forced to either spend large amounts of computation time resolving an aphysical process or risk conservation of energy errors (See section 5.6.1). To minimize these effect, codes

will 'soften' forces to be weaker than Gm_1m_2/r^2 below some resolution level, h. The exact meaning of h varies between codes.

The GreeM^3 code softens forces through a Plummer kernel [Ishiyama et al., 2012, 2015], the simplest force softening scheme. In this scheme, the gravitational potential of a particle is given by

$$\phi(r) = \frac{GM}{\sqrt{r^2 + h^2_{\rm Plummer}}}. \tag{3.2}$$

Here, ϕ is the gravitational potential a distance r away from a particle of mass M.

In Gadget-based simulations [Springel et al., 2001b, Springel, 2005, 2010], the density distribution function of particles, $\delta(r)$, changes from a Dirac delta function to the SPH kernel of Monaghan and Lattanzio [1985]:

$$\delta(x) = \frac{8M}{\pi h^3} \begin{cases} 1 - 6x^2 + 6x^3, & \text{if } x < \frac{1}{2}, \\ 2\,(1-x)^3, & \text{if } \frac{1}{2} < x < 1, \\ 0, & \text{if } x > 1, \end{cases} \tag{3.3}$$

for $x = r/h_{\rm Gadget}$. This leads to perfectly Newtonian force beyond $r > h_{\rm Gadget}$.

In ART [Kravtsov et al., 1997, Kravtsov, 1999, Gottloeber and Klypin, 2008], differentiation errors in the underlying grid naturally soften gravitational forces according to the local grid cell width, $h_{\rm ART}$. Because ART grids are adaptive, this means that the formal resolution is also adaptive. Typically, the highest resolution level used within a halo is cited as the formal resolution of that halo.

The analysis in this paper focuses on the impact of force softening at large scales. Throughout this thesis I adopt the following convention for converting between formal resolutions, which matches their impact on the halo rotation curves for $r \gg \epsilon$,

$$\epsilon = 1.284\, h_{\rm Plummer} = h_{\rm ART} = 0.357\, h_{\rm Gadget}. \tag{3.4}$$

The methodology behind this conversion is laid out in Appendix 5.8.1, along with the best-fitting impact of large-ϵ on rotation curves.

This conversion differs from those used in previous works. The most common convention is derived from Kravtsov et al. [1997], Springel et al. [2001b] which demonstrated that the force errors induced by these schemes are comparable for $r < \epsilon'$, where ϵ' is the 'Plummer equivalent force-softening scale' given by $\epsilon' = h_{\rm Plummer} = h_{\rm ART} = 0.357\, h_{\rm Gadget}$. Additionally, the depth of each particle's potential is the same at a constant value of ϵ' under this scale. Different authors have also adopted different conversions between $h_{\rm ART}$ and ϵ' (e.g. Diemer and Kravtsov, 2015, Klypin et al., 2016) due to the ambiguity of which scales force errors should be matched on. The parametrization in Eq. 3.4 does not depend on choosing such a scale.

3.2 Halo Finding and Halo Properties

After a simulation has finished running, the output is a large collection of particles with different positions and velocities. However, the analysis in this thesis (and in a great many papers) relies on knowing the location and properties of the simulation's halos. This data is produced by a tool known as a "halo finder." Many different halo finders have been developed over the years, but the analysis in this thesis focuses on the results of the ROCKSTAR halo finder [Behroozi et al., 2013c]. The ROCKSTAR halo finder is designed to robustly identify subhalos and is centered around an adaptive friends-of-friends algorithm performed in 6D phase space. ROCKSTAR stacks up well against other halo finders in specialized tests [Knebe et al., 2011] and chapter 5 performs an extensive battery of tests on the output of this code.

After halos are generated, a second piece of software is needed to connect younger and older versions of the same halo across time. This connection allows the research to study how halo properties and locations evolve with time and is referred to as a "merger tree." We use ROCKSTAR's sister program, CONSISTENT-TREES [Behroozi et al., 2013b] to generate merger trees.

Dark matter halos are complex objects with a number of scientifically useful properties. Many of these properties are used throughout the remaining chapters of this thesis. The rest of this section describes many of their most commonly used properties, as computed by the ROCKSTAR halo finder.

Bound vs. Unbound Particles: ROCKSTAR separates particles into 'bound' and 'unbound' groups and primarily analyses bound particles. This is done because if particles were classified with a simple geometric cut, subhalos would be contaminated with a large number of particles from their host halos. There is no unambiguous way to perform this procedure due to the importance of tidal fields in true boundedness calculations, but ROCKSTAR takes a reasonable approach and determines boundedness by performing pairwise potential calculations and comparing against the kinetic energy of particles in the rest frame of the halo center.

Halo mass: The most basic properties of a halo are its size and, equivalently, its mass. In most studies, the 'overdensity radius' definition of the halo boundary is used to define these properties. Under this definition, the halo is a sphere of radius R_Δ which encloses the bound mass $M_\Delta = M_{\rm bound}(< R_\Delta)$ such that

$$M_\Delta = \frac{4\pi}{3}\Delta\rho_{\rm ref}R_\Delta^3. \tag{3.5}$$

Here, Δ is some constant and $\rho_{\rm ref}$ is a cosmological reference density. The reference density is typically either the background matter density, $\rho_{\rm m}$, or the critical density, $\rho_{\rm c}$.

The choice of reference density is more of an art than a science. Chapter 4 reviews the scientific justification (or lack thereof) for different choice of the halo boundary, but to clarify notation, the primary radius definition in this thesis is $R_{\rm vir}$. $R_{\rm vir}$ corresponds to $\Delta\rho_{\rm ref}$ as given by the relation in Bryan and Norman [1998]. At various points throughout this thesis, I also consider the bound masses enclosed within $R_{\rm 200m}$ ($\Delta\rho_{\rm ref} = 200\rho_{\rm m}$), $R_{\rm 200c}$ ($\Delta\rho_{\rm c} = 200\rho_{\rm c}$), $R_{\rm 500c}$ ($\Delta\rho_{\rm ref} = 500\rho_{\rm c}$), and $R_{\rm 2500c}$ ($\Delta\rho_{\rm ref} = 2500\rho_{\rm c}$).

ROCKSTAR computes overdensity radii by constructing radial density profiles using only particles within the coarse-grained friends-of-friends (FOF) group that contains the halo center. The linking length parameter used to identify the FOF group has a substantial effect on the convergence properties of M_{200m} (see Appendix 6.6.1).

Virial Scaling: $M_{\rm vir}$ and $R_{\rm vir}$ are commonly used as characteristic scales to remove the dimensionality of other halo properties. Some unscaled halo properties have units of time in their dimensions, requiring the introduction of a third characteristic scale, the "virial velocity:"

$$V_{\rm vir} = \sqrt{\frac{GM_{\rm vir}}{R_{\rm vir}}}. \tag{3.6}$$

Maximum circular velocity: One of the most fundamental properties of a dark matter halo is $V_{\rm max}$. $V_{\rm max}$ is the maximum velocity reach by a halo's "rotation curve," $V_{\rm circ}(r) = \sqrt{GM/r}$. $V_{\rm max}$ enjoys widespread use because it is both closely connected both to the theoretical distribution of dark matter and to observational quantities like rotation curves [e.g. Rubin and Ford, 1970]. $V_{\rm max}$ is also a non-parametric halo property, meaning that in principle it can be measured without needing to assume a model for the distribution of mass throughout the halo[1]

$V_{\rm max}$ is a well-defined halo property in its own right, but when scaled by $V_{\rm vir}$, it becomes a measure of halo "concentration." Halos whose masses are highly concentrated in their centers will have higher values of $V_{\rm max}/V_{\rm vir}$ and halos with more diffuse mass distributions will have lower $V_{\rm max}/V_{\rm vir}$ values.

A related, but distinct, quantity is $V_{\rm rms}$,

$$V_{\rm rms} = \sqrt{\sum_i \vec{v}_i - \langle\vec{v}\rangle}. \tag{3.7}$$

Here, the sum and average are performed over the velocities of every particle in the halo.

1. In practice, observations of rotation curves generally do not reach radii large enough to resolve $V_{\rm max}$ [e.g. de Blok et al., 2008]. This means that inferring $V_{\rm max}$ from observations necessarily has a theoretical and parametric component.

Halo concentration: Although $V_{\rm max}/V_{\rm vir}$ is a useful measurement of concentration, the most widely used tracer of concentration is $c_{\rm vir} = R_{-2}/R_{\rm vir}$, where R_{-2} is the radius where the halo's logarithmic radially-averaged density slope equals -2. Although R_{-2} can be measured without adopting a halo model for profiles averaged over large halo populations, the noise in halo profiles requires fitting a particular functional form if individual measurements of $c_{\rm vir}$ are required.

This thesis performs fits against the Navarro-Frenk-White (NFW) profile [Navarro et al., 1997]. The NFW profile has the form

$$\rho(r) = \frac{\rho_0}{r/R_s(1+r/R_s)^2}, \tag{3.8}$$

where ρ_0 and R_s are free parameters of the fit. For this funcitonal form, $R_{-2} = R_s$, $c_{\rm vir} \equiv R_{\rm vir}/R_s$. This fit is delicate and different fitting strategies lead to different concentration statistics. ROCKSTAR performs a χ^2-minimization of Eq. 3.8 against binned density profiles, ignoring bins with fewer than 15 particles and heavily down-weighting bins with $r < 3\epsilon_\phi$.

Related is $R_{1/2}$, the radius which encloses half of the bound mass within $R_{\rm vir}$.

Halo shape: ROCKSTAR follows the recommendations of Zemp et al. [2011], and computes halo shapes using iterative, weighted mass distribution tensors. Specifically, ROCKSTAR first computes the mass distribution tensor

$$M_{ij} = \frac{\sum_k^N (\vec{r}_k)_i (\vec{r}_k)_j |\vec{r}_k|^{-2}}{N \sum_k^N |\vec{r}_k|^{-2}} \tag{3.9}$$

over all bound particles k within $R_{\rm vir}$ and computes the eigenvalues, λ_i, of M_{ij}. Then, ROCKSTAR estimates axis ratios as $\sqrt{\lambda_i/\lambda_j}$ for each pair of axes, i and j, repeating the process for all bound particles in an ellipsoid with the corresponding axis ratios and a minimum axis length of $R_{\rm vir}$. This process repeats until axis ratios converge to 1%. Note that the axis ratio measurement is sensitive to the central mass distribution.

Halo spin: To track halo spin, researchers typically use the dimensionless Peebles and

Bullock spin parameters. The classical Peebles spin parameter [Peebles, 1969] is given by,

$$\lambda_{\rm Peebles} = \frac{|\vec{J}|}{G|E_{\rm tot}|M_{\rm vir}^{5/2}} \tag{3.10}$$

where $\vec{J}$ is the angular momentum vector of the halo and $E_{\rm tot}$ is the total energy of the bound particles. However, the normalization by $E_{\rm tot}$ presents pragmatic difficulties (see the discussion of boundedness above) and makes $\lambda_{\rm Peebles}$ sensitive to recent merger history which is often undesirable. An alternate dimensionless parameter is the simpler Bullock spin parameter [Bullock et al., 2001] which normalizes by virial properties:

$$\lambda_{\rm Bullock} = \frac{|\vec{J}|}{\sqrt{2}M_{\rm vir}R_{\rm vir}V_{\rm vir}}. \tag{3.11}$$

Dynamical State Indicators: There are numerous halo properties which track the dynamical state of a dark matter halo. These include: $T/|U|$, the ratio of kinetic to potential energy, $x_{\rm off} = X_{\rm off}/R_{\rm vir}$, the normalized offset between the density peak of the halo and its center of mass, and $V_{\rm off}$, the offset between the velocity of the halo's density peak and the mean velocity of all its particles. The first two have been found to correlate with recent accretion activity [Power et al., 2012] and age indicators, such as concentration [Neto et al., 2007]. All three can be used to predict the accretion history prior to the epoch of measurement.

Mass Accretion History: Beyond the single-epoch halo properties measured by ROCKSTAR, the merger trees constructed by – for example – the CONSISTENT-TREES code allow direct measurements of halo growth. The most fundamental such property is the accretion rate,

$$\Gamma(\Delta t) = \frac{M_{\rm vir}(t_0) - M_{\rm vir}(t_0 - \Delta t)}{\Delta t}, \tag{3.12}$$

where t_0 is the current age of the universe. This thesis focuses on two different accretion

rates. Chapter 5 uses $\Gamma(t_{\rm dyn})$ measured over the halo's dynamical time,

$$t_{\rm dyn} = \frac{1}{\sqrt{\frac{4}{3}\pi G(\Delta\rho_{\rm m})_{\rm vir}}}. \tag{3.13}$$

Here, $(\Delta\rho_{\rm m})_{\rm vir}$ is the Bryan and Norman [1998] virial density contrast. This is a very commonly used accretion rate definition, but for consistency with previous literature [Diemer and Kravtsov, 2014, More et al., 2015], chapter 4 chiefly considers $\Gamma_{\rm DK14}$:

$$\Gamma_{\rm DK14} \equiv \frac{\ln M_{\rm 200m}(z_{i+1}) - \ln M_{\rm 200m}(z_i)}{\ln a(z_{i+1}) - \ln a(z_i)}, \tag{3.14}$$

here z_i come from a set of redshift intervals which are separated by roughly a dynamical time. The inverval used by chapter 4 is $z_i = \{0, 0.5, 1, 2, 4\}$.

Accretion rates are most sensitive to recent mass growth. A common measurement used to trace growth on longer timescales is $a_{0.5}$. This quantity corresponds to the earliest scale factor at which a mainline progenitor of the halo has half the mass of the present-day halo. Another measure that probes similarly long timescales is $a_{\rm MM}$, the most recent scale factor at which CONSISTENT-TREES detected a merger where the secondary-to-primary mass ratio was larger than 0.3.

Finally, merger trees allow one to compute $M_{\rm peak}$ and $V_{\rm peak}$, the largest values that $M_{\rm vir}$ and $V_{\rm max}$ have taken on throughout the lifetime of the halo, respectively. These values are frequently used when analyzing subhalos because the dark matter halo of a satellite galaxy is disrupted long before the central stellar component is. 'Peak' quantities allow modeling in which galaxies grow their stellar mass components in step with their dark matter halos and maintain it after being captured by a host halo. Such modeling has been shown to be effective at predicting a wide range of observables [e.g., Reddick et al., 2013].

Mass and Velocity Functions Using these halo properties, it is possible to define differential mass and velocity functions, $\phi(X)$. $\phi(X)$ is defined as the number of halos in logarithmic bins of a given mass or velocity definition, $\log_{10}(X)$, divided by the log-

arithmic width of that bin. This thesis considers the mass and velocity definitions of $X \in \left\{M_{\rm vir},\, M_{\rm 2500c},\, M_{\rm 500c},\, M_{\rm 200c},\, M_{\rm 200m},\, M_{\rm peak},\, V_{\rm max},\, V_{\rm rms},\, V_{\rm peak}\right\}$.

Isolated Halo vs. Subhalo Classification: The classification of halos into "isolated halos" and "subhalos" plays a critical role in halo analysis, because subhalos behave very differently from non-subhalos at the same mass. This is because subhalos tend to be rapidly losing mass and are within extreme tidal environments. Overwhelmingly, the most common approach is to classify objects within some overdensity radius, R_{Δ}, of a larger halo as subhalos and everything else as isolate halos. Chapter 6 critically evaluates this approach at length.

CHAPTER 4

SPLASHBACK SHELLS OF COLD DARK MATTER HALOS

This chapter is a modified version of my paper, Mansfield et al. [2017].

4.1 Introduction

In the Cold Dark Matter (CDM) paradigm of structure formation, dark matter halos form via the collapse of density peaks in the initial random Gaussian perturbation field. In the commonly used "tophat model" the peak density contrast profile is approximated as uniform within a given radius [e.g., Tolman, 1934]. The constant overdensity in such approximations results in a uniform collapse time for different radial shells and a single well-defined collapse time for the peak. This, along with the assumption that virial equilibrium is reached immediately following collapse, allows one to predict the density contrast within the boundary of the collapsed objects [Gunn and Gott, 1972b, Heath, 1977, Lahav et al., 1991].

Accordingly, the most commonly used boundary definition for CDM halos is a sphere of radius R_Δ (see Eq. 3.5) for various choices of Δ. However, the overdensity profile in real Gaussian peaks is not constant, but decreases with increasing radius [see, e.g., Figure 2 in Dalal et al., 2010]. Because the overdensity within a given radius controls the timing of the collapse, the collapse of different radial shells in such peaks is extended in time. Real halos also undergo mergers during their formation, which further redistribute mass within them. Real CDM halos thus do not have an edge at the density contrast predicted by simple uniform peak collapse models [see, e.g., Kravtsov and Borgani, 2012, More et al., 2015], meaning that R_Δ radii are a rather arbitrary definition of halo extent and do not correspond to any particular feature in the density profile or in the profiles of other physical properties [e.g., Diemer et al., 2013a]. This arbitrariness may be problematic when this radius is used to classify objects into groups which are meant to be qualitatively distinct from one another, such as subhalos and isolated halos. Indeed, multiple recent studies have suggested that a

significant fraction of the halo assembly bias effect may be due to the fact that some subhalos which have orbited larger hosts are misclassified as isolated halos when R_Δ is used as a halo boundary for classification [Wang et al., 2009, Wetzel et al., 2014, Sunayama et al., 2016, Zentner et al., 2016]. However, these so-called "backsplash" halos would still necessarily be contained within their hosts' splashback shells, meaning that switching to a splashback-based definition could help alleviate this issue.

Furthermore, regardless of the choice of Δ or $\rho_{\rm ref}$, contrast-based radius and mass definitions encounter several problems when the mass accretion histories of halos are estimated. First, as mentioned above, during major mergers there is mass redistribution within halos, with a non-trivial amount of mass moving to radii outside of R_Δ for typical values of Δ [Kazantzidis, Zentner, and Kravtsov, 2006]. This causes spherical overdensity masses to be non-additive during mergers in excess to the degree that would be expected purely from slingshot processes. Second, the evolution of both $\rho_{\rm m}$ and $\rho_{\rm crit}$ with time causes evolution in R_Δ and M_Δ, even for completely static density profiles. This "pseudo-evolution" of halo radius and mass typically results in the near doubling of mass of Milky Way-sized halos between $z = 1$ and $z = 0$, even when there is no accretion of new mass [Diemer et al., 2013b].

Given the problems with the standard R_Δ definition, one can ask whether there is a more physical way to define halo boundary, one which would separate the matter that has already collapsed (i.e., orbited within halo at least once) and matter that is still infalling onto halo for the first time. In collapse models of spherical and ellipsoidal peaks with power law density profiles, such a boundary exists and is associated with a sudden drop in the density profile of collapsed halos [Fillmore and Goldreich, 1984, Bertschinger, 1985, Adhikari et al., 2014, Shi, 2016]. The drop is due to the caustic formed by the "pile up" of mass elements that have just reached the apocenter of their first orbits and is thus the maximum radius of matter that has orbited through halo at least once.

Recently, such drops in the density profile have also been detected in both simulated and

real CDM halos [Diemer and Kravtsov, 2014, Adhikari et al., 2014, More et al., 2015, 2016, Adhikari et al., 2016]. The most distant apocenters of orbits in real halos form a surface that we will call the *splashback shell*. This shell can be viewed as the halo boundary. Due to the assumption of spherical symmetry, all previous studies have necessarily been restricted to analyzing the characteristic scale of this shell, the *splashback radius*, $R_{\rm sp}$.

The primary challenge in using the splashback shell as a physical boundary definition for halos is that it is technically challenging to detect and quantify in individual objects, both in cosmological simulations and in observations. The key problem is that splashback shells are generally located at low densities, where the presence of individual neighboring halos or filaments can complicate the interpretation of the density field.

Consequently, analyses of the splashback radius have so far been carried out using stacked radial density profiles of either mass or subhalo abundance [Diemer and Kravtsov, 2014, Adhikari et al., 2014, 2016, More et al., 2015, 2016]. After stacking, $R_{\rm sp}$ for the population is operationally defined as the radius of the steepest logarithmic slope, $\mathrm{d}\ln\rho/\mathrm{d}\ln r$ (or $\mathrm{d}\ln n_{\rm sub}/\mathrm{d}\ln r$). In principle, this procedure averages out the noise in the individual profiles, allowing for comparisons of the splashback radius between different halo populations. However, stacking of different halo profiles can also "wash out" the sharp density gradient associated with the splashback shells, if such shells exhibit scatter for individual halos.

Studies of the splashback radius based on stacked density profiles have shown that there is a strong relation between $R_{\rm sp}/R_{\rm 200m}$ and halo mass accretion rate, $\Gamma_{\rm DK14}$, [Diemer and Kravtsov, 2014, More et al., 2015]. $\Gamma_{\rm DK14}$ is defined in Eq. 3.14 (although future studies may benefit strongly from revisiting this choice in definition). Such a dependence is expected theoretically due to the contraction of particle orbits in a rapidly deepening potential of high-$\Gamma_{\rm DK14}$ halos [Diemer and Kravtsov, 2014, Adhikari et al., 2014].

Hints of density steepening due to the splashback radius in the mass and galaxy distribution around individual clusters have been reported in several recent studies [Rines et al., 2013, Tully, 2015, Patej and Loeb, 2016, Umetsu and Diemer, 2017]. Interestingly, the first

reliable observational estimates of the splashback radius from the radial number density profiles of satellite galaxies in clusters are in tension with the predictions of simulations [More et al., 2016].

The operational simplicity of the stacked-profile approach makes it very useful, particularly when comparing simulations to observations, but it is not without weaknesses. First, spherical averaging discards all information about the shapes of the splashback shells, even though the filamentary nature of the cosmic web causes accretion to be highly aspherical, which implies that splashback shells should also be highly aspherical. Second, the stacking procedure removes information about individual halos, making it impossible to study the evolution of a single halo's shell over time, the properties of subhalos contained within shells, or the scatter around mean relations. Third, the relationship between the splashback radius estimated from the stacked profiles and the underlying distribution of individual splashback radii is unknown and can be complicated. In particular, as we show in section 4.4.3, the contribution of massive subhalos in a minority of individual density profiles introduces significant bias in the estimate of the splashback radius derived from stacked profiles.

To address these issues and to explore the properties of splashback shells around individual halos, in this chapter we present an algorithm which identifies the splashback shells around individual halos using single particle snapshots from cosmological N-body simulations, and an implementation of the algorithm in the code Shellfish (SHELL Finding In Spheroidal Halos), which we use to generate halo catalogs with measured splashback shells and perform analyses of their basic properties, such as radius and shape, and quantify their relationships to other halo properties, such as mass accretion rate and peak height. A public version of Shellfish, along with tutorials and documentation can be found at `github.com/phil-mansfield/shellfish` with a Digital Object Identifier (DOI) given by Mansfield [2017].

This chapter is organized as follows. An overview of our method is shown in Figure 4.1 and our key result, the $\Gamma_{\rm DK14}$ - $R_{\rm sp}$ relation for individual halos, is shown in Figure 4.9. In

section 4.2 we describe our algorithm to identify the splashback shells from a halo's particle distribution, in section 4.3 we present extensive tests of the correctness and convergence properties of the shells identified by our implementation of the algorithm. In section 4.4 we discuss the shapes of the splashback shells and present the relation between shell size and mass accretion rate. We compare the latter relation to that derived from the stacked profiles, and show that the stacking introduces significant bias in the estimates of the splashback radius of rapidly growing halos. We summarize our results in section 4.5. Appendix 4.6.1 contains a description of a high performance ray-tracing algorithm that we developed as a component of SHELLFISH.

A reader not interested in the details of the algorithm itself, but only in the properties of identified shells can skip directly to section 4.4. We caution, however, that proper interpretation of the issues discussed in section 4.4 requires at least a basic understanding of our shell finding algorithm.

4.2 Methods

4.2.1 Simulations

The analysis in this chapter uses a subset of the suite of simulations first introduced in Diemer and Kravtsov [2014]. These simulations have box sizes between $62.5h^{-1}$ Mpc and $500h^{-1}$ Mpc, allowing us to study halos with a wide range of masses and accretion rates. The simulations, along with the mass ranges which we analyze, are shown in Table 4.2.1. The numerical details of these simulations are summarized in Tables 3.1 and 3.1 and section 3.1.

Halo catalogs were generated using the ROCKSTAR halo finder [Behroozi et al., 2013d] and main progenitor lines were found through the merger tree code CONSISTENT-TREES [Behroozi et al., 2013e].

Name	$M_{200\mathrm{m,min}}$ $(h^{-1}\,M_\odot)$	$M_{200\mathrm{m,max}}$ $(h^{-1}\,M_\odot)$
L0500	4×10^{14}	-
L0250	5×10^{13}	2×10^{14}
L0125	7×10^{12}	5×10^{13}
L0063	9×10^{11}	7×10^{12}

Table 4.1: The mass ranges used for each simulation in this chapter.

4.2.2 Algorithm Description

Our aim is to develop an algorithm which can identify splashback shells around halos using only their density distribution at a single point in time. In other words, this will be an algorithm which uses no dynamical information about the halo's particles and will rely solely on identifying the density caustic generated by the splashback shell. This restriction would allow such an algorithm to work on simulations that are only sparsely sampled in time.

Relaxing this restriction allows for alternative measurements of R_{sp} which can leverage the full dynamical information of the simulation. For example, Diemer [2017b] develops an algorithm, SPARTA, for finding splashback radii by locating the apocenters of orbiting particles which requires access to approximately 100 snapshots over the lifetime of the target halos. An extended comparison between SPARTA and SHELLFISH can be found in Diemer et al. [2017].

Below we describe such an algorithm which does not require any dynamical information and demonstrate that it identifies correct splashback shells, provided that target halos are resolved with a sufficient number of particles (see section 4.3) and provided that target halos are not embedded in very dense environments (see section 4.4.3).

Specifically, our algorithm consists of four steps:

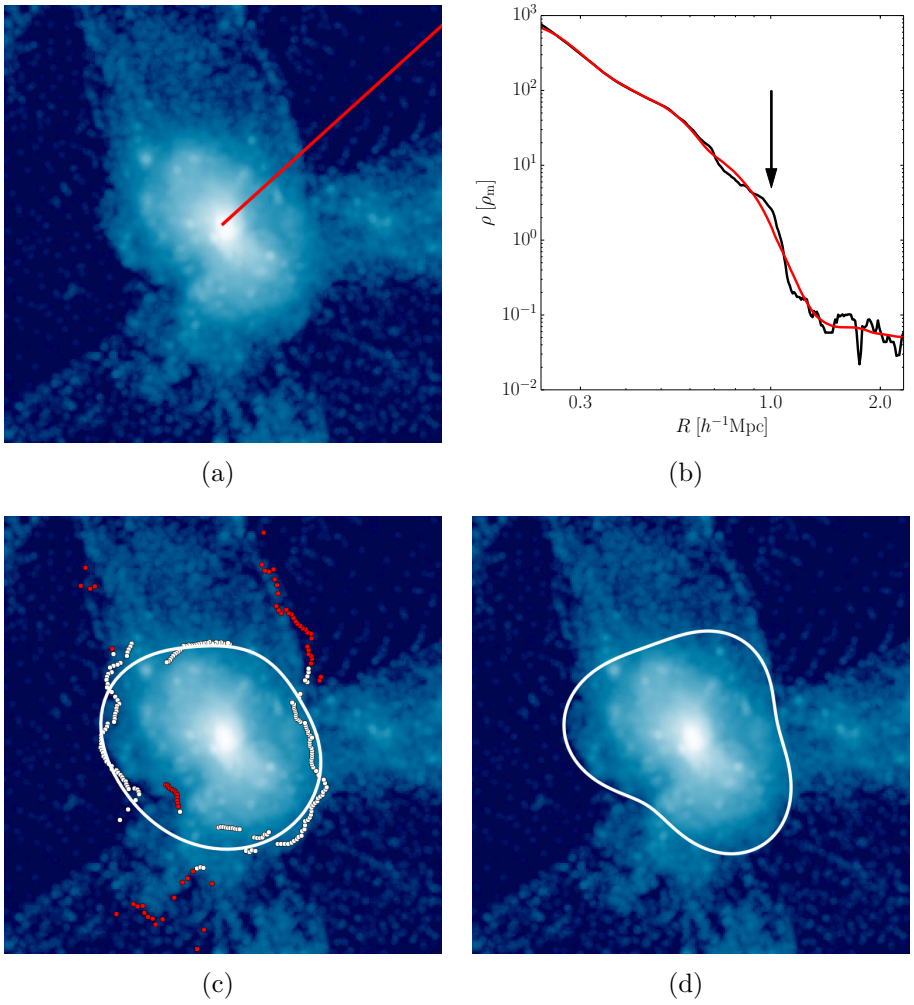

Figure 4.1: An overview of the steps in our shell-finding algorithm for a cluster-sized halo (This halo is also shown in Figure 4.2(d) below). Figure 4.1(a) shows a random line of sight traced through this halo's density field (see §4.2.2 and Appendix 4.6.1). Figures 4.1(b) shows a density profile measured along along this line of sight before smoothing (black line) and after smoothing with a Savitzky-Golay filter (red line). The arrow indicates the point of steepest slope in the smoothed profile (see §4.2.2). Figure 4.1(c) shows the points of steepest slope for the 256 lines of sight in the viewing plane and shows the point classification that the algorithm generates for these points (see Appendix 4.6.2). The white curve shows the filtering spline created during the point selection process. Points which are close enough to this curve to pass the filter are shown in white and those which are too far away are shown in red. Figure 4.1(d) shows the cross-section of the best fit Penna-Dines surface from the overall distribution of splashback points from 100 randomly oriented planes in which such a procedure was carried out (see §4.2.2). See the text in the corresponding sections for details. All analysis is done with the parameter values listed in Table 4.2.4, but the underlying images are rendered using spherical kernels of radius $0.05R_{\rm 200m}$ to make the structures around halos more clear.

1. The density field is sampled along tens of thousands 1-d lines of sight anchored at the center of a halo. The specific design decisions governing how the lines of sight are oriented and how densities along them are estimated are described in section 4.2.2 and Appendix 4.6.1, respectively, and are depicted in Figure 4.1(a).

2. The locations of the steepest slope in the density profiles of each line of sight are estimated using a smoothing filter. This part of the algorithm is described in section 4.2.2 and is depicted in Figure 4.1(c).

3. The set of profiles is pruned to remove the profiles where the point of steepest slope corresponds to the splashback associated with a nearby halo or filament. The pruning procedure is described in section 4.2.2 and Appendix 4.6.2 and is depicted in Figure 4.1(c).

4. We fit the 3-d shape of the shell with a smooth, flexible, functional form using the locations of the steepest slope in the profiles that remain after the pruning step. This is described in section 4.2.2 and is depicted in Figure 4.1(d).

The design choices made in step 1 are the most important for ensuring good performance of the algorithm and the design choices made in step 3 are the most important for ensuring that the identified shells are correct.

The free parameters of the algorithm that will be introduced and discussed in the subsequent sections are summarized in Table 4.2.4. The logic and procedures of specific parameter choices are discussed in Appendix 4.6.3.

Density Estimation Along Lines of Sight

To construct a density profile along a given line of sight we must choose a way to interpolate particle positions and masses onto that line. For simplicity, we choose to approximate particles as tophat spheres of radius $R_{\rm kernel}$ uniform density. Other choices, such as tetrahedral,

trilinear, or tricubic tessellations of phase space [e.g., Abel et al., 2012a, Hahn and Angulo, 2016], are also implemented in SHELLFISH and could in principle be used in this work. However, we find that these estimators converge slowly and do not allow splashback shells for halos with $N_{200\mathrm{m}} \lesssim 10^7$ to be identified reliably and thus do not use them in practice. A detailed convergence study of phase space density estimators will be the subject of future work.

The algorithm represents every line of sight as an array of N_{bins} bins logarithmically distributed between the radii R_{min} and R_{max}. The density along a line of sight, l, which passes through a set of constant-density spheres is given by

$$\rho_l(r) = \sum_{i=0}^{i<N} \mathbb{I}_{\mathrm{intr},il} \rho_i H(r - r_{\mathrm{in}}) H(r_{\mathrm{out}} - r). \tag{4.1}$$

Here, i indexes over all particles, $\mathbb{I}_{\mathrm{intr},il}$ is an indicator function which is 1 if l intersects with the sphere of particle i and is 0 otherwise, ρ_i is the density of sphere i, H is the Heaviside step function, and r_{in} and r_{out} are the distances to entrance and exit intersection points of l for a given sphere, respectively.

Evaluating Equation 4.1 is easy if a conventional estimator (such as cloud-in-cell or SPH) is used to write densities to an intermediate grid before they are translated onto the lines of sight, since the grid cell that corresponds to a point at radius r of given ray can be calculated in $O(1)$ operations. However, using an intermediate grid has a number of disadvantages. First, maintaining the high-resolution grid required to accurately measure the contours of the splashback shell consumes a large amount of memory. This restricts the number of halos which can be maintained in memory at once; when generating large catalogs of shells, this can force particle catalogs to be read many times, leading to a significant performance cost. Second, writing the density estimate to a grid is expensive as it involves either an exact rasterization scheme (see, for example, Powell and Abel 2014) of the objects, or Monte Carlo sampling of each solid with sufficiently many points to eliminate shot noise in each cell.

Both approaches also require that density estimates are calculated for grid cells which are not intersected by any line of sight. Third, introducing an intermediate grid reduces the fidelity of the line of sight density estimates due to pixelation. This is most apparent as small radii.

We find that in practice these three disadvantages, particularly the second, are significant and make the use of grids for density estimation undesirable. For this reason we evaluate Equation 4.1 by *directly* computing the intersection radii between every line of sight and every sphere with no intermediary grid. Attempting this evaluation naively would be computationally intensive, so we use a specialty ray-tracing algorithm, described in the Appendix 4.6.1, which takes advantage of the fact that the vast majority of the terms in Equation 4.1 are zero. This algorithm speeds up density assignment by several orders of magnitude compared to both the brute-force geometric approach and the grid-based approach, while still maintaining a comparatively light memory footprint.

The nature of the ray-tracing algorithm requires that the lines of sight are confined in N_{planes} planes and are uniformly spaced in polar angle within these planes. Each plane then contains N_{los} lines of sight within it. This means that the line shown in in Figure 4.1(a) could not be evaluated alone and would need to be evaluated simultaneously along with several hundred other other profiles within the viewing plane. This turns out to be a convenient configuration for later steps in the shell finding algorithm.

Measuring the Point of Steepest Slope for Line of Sight Profiles

After the density estimation step, we smooth the density profiles of each line of sight using a fourth order Savitzky-Golay filter [Savitzky and Golay, 1964] with a window length of N_{SG} bins in $\log r$ - $\log \rho$ space. A filter is necessary because a high precision determination of r_{steep} requires that N_{bin} be large, but using a large number of bins allows for noise in low-density regions. For bins in which $\rho(r) = 0$, the density is set equal to a small background density value, ρ_{bg}. Once the density profile of a line of sight is smoothed, we find the radius

of the steepest logarithmic slope, $r_{\rm steep}$.

We choose to use a Savitzky-Golay filter because it is effective at removing small scale noise and because it generally doesn't move the location of the point of steepest slope, even for large window sizes.

We find that the best results are obtained for $N_{\rm SG} \approx N_{\rm bin}/4$ to $N_{\rm bin}/2$, as this allows the filter to remove even moderately large features, such as subhalos. The exact value chosen is given in Table 4.2.4. For most lines of sight, the density drop associated with crossing the splashback shell is the most prominent feature in the profile, and thus such an aggressive filter window does not remove it. The smoothing process will flatten the slope at $r_{\rm steep}$, but the actual value of the slope is not used by our algorithm.

This process is illustrated in Figure 4.1(b), which shows the line of sight highlighted in Figure 4.1(a). The black curve shows the raw profile after the density estimation step, the red curve shows the profile after applying a Savitzky-Golay filter with a window size of $N_{\rm SG} = N_{\rm bin}/2$. The vertical arrow shows $r_{\rm steep}$ for the smoothed profile. This figure demonstrates several key points. First, the discontinuity due the splashback shell is very strong. Second, the unsmoothed profile contains several points with slopes steeper than the splashback discontinuity due to particle noise. Lastly, the location of $r_{\rm steep}$ has not moved significantly between the smoothed and unsmoothed profiles.

As mentioned in section 4.2.2 (see also Appendix 4.6.1), the density estimation step of our algorithm requires that lines of sight are confined to a set of planes. The locations of $r_{\rm steep}$ for 256 such lines of sight are shown in Figure 4.1(c). This illustrates that, generally, the values of $r_{\rm steep}$ found by this step are in good agreement with the visual appearance of density discontinuities. However, some of the density discontinuities are clearly not associated with the halo itself but are due to nearby filaments or nearby halos. Although this happens in the minority of lines of sight, these can bias the shape of the inferred splashback shell significantly. Therefore, the algorithm makes an additional step in which lines of sight for which the steepest slope points are likely associated with other halos and filaments are pruned

from the set.

Filtering Out Problematic Points of Steepest Slope

We remove lines of sight with points of steepest slope that are likely to be associated with other halos and filaments candidate points through an additional filtering step. Filaments have their own elongated splashback shells which are created by the apocenters of matter accreted onto filaments from surrounding void regions. The density jumps associated with these surfaces are comparable to those found around halos. Therefore, it is difficult to differentiate between steepest slope points caused by central halos splashbacks and points caused by filament splashbacks using only the information contained in a single line of sight profile. We experimented with a number of different heuristic approaches of this type and found that they generally require extensive fine-tuning and are, at best, modestly effective at removing filament points.

To classify the splashback points, we consider all of the splashback points within a given plane simultaneously and filter out points which deviate too sharply from the locations of their neighbors. We do this by heuristically constructing a *filtering loop*, a curve which smoothly passes close to most of the plane's candidate points but which is too stiff to accommodate sharp changes in radius. We then remove points which are too far away from the filtering loop.

Our filtering algorithm employs a spline curve to approximate the shape of the splashback in a given slice and is described in detail in Appendix 4.6.2. The algorithm introduces two new free parameters, η, which controls the strictness of the filter and the "stiffness" of the loop, and $N_{\rm rec}$, which affects the angular resolution of the filtering loop. Larger values of η will remove outliers more aggressively, but would also likely prune a larger number of points associated with halo. Qualitatively, points which come from features that deviate by more than $R_{\rm max}/\eta$ from neighboring regions on angular scales of $2\pi/2^{N_{\rm rec}}$ will be removed from the set of lines of sight.

Fitting the Shape of the Splashback Shell

After the filtering step, we fit the remaining points using a family of spheroidal functions introduced by Penna and Dines [2007, hereafter "Penna-Dines functions"]. A Penna-Dines function of order P is defined by $2P^2$ coefficients, c_{ijk}, where i and j range from 0 to $P-1$ and k ranges from 0 to 1. The shape of a shell with a particular set of coefficients is given by the function

$$r(\phi,\theta) = \sum_{i,j=0}^{P-1} \sum_{k=0}^{1} c_{ijk} \sin^{i+j}\theta \ \cos^{k}\theta \ \sin^{j}\phi \ \cos^{i}\phi, \tag{4.2}$$

where θ is the polar angle and ϕ is the azimuthal angle. Penna-Dines functions are similar to spherical harmonics in that adding higher order terms allows for the representation of increasingly aspherical shells. We choose to fit these functions because their low order forms are qualitatively similar to the shapes found in splashback shells (this class of functions is specifically designed to represent lobed shapes) and because an optimal fit can be found through the relatively simple and efficient pseudoinverse matrix operation.

Namely, for a set of N points with coordinates given by $r_n = \sqrt{x_n^2 + y_n^2 + z_n^2}$, the best fit coefficients can be computed by the operation

$$c_{ijk} = r_n^{2P-1} M^T (M M^T)^{-1}. \tag{4.3}$$

Here, r_n^{2P-1} is a height N vector containing the radii of every point and M is a $N \times 2P^2$ matrix with elements

$$M_{i+jP+kP^2,n} = r_n^{2P-1-i-j-k} x_n^i y_n^j z_n^k. \tag{4.4}$$

4.2.3 Definitions of Basic Splashback Shell Properties

While a full set of Penna-Dines coefficients is necessary for computing subhalo/particle membership and for visualizing shells, it is also useful to encapsulate key properties of the splashback shells in a few representative parameters. To this end, we use a set of properties which

parameterize the shape of the splashback shells: $R_{\rm sp}$, the volume-equivalent splashback radius; $\rho_{\rm sp}$, the net density of shell; $a_{\rm sp}$, $b_{\rm sp}$, and $c_{\rm sp}$, the inertia tensor equivalent major axes of the shell; $E_{\rm sp}$, the shell ellipticity; and $A_{\rm sp}$, the shell asphericity:

$$R_{\rm sp} \equiv \left(\frac{3V_{\rm sp}}{4\pi}\right)^{1/3} \tag{4.5}$$

$$\rho_{\rm sp} = M_{\rm sp}/V_{\rm sp} \tag{4.6}$$

$$a_{\rm sp},\ b_{\rm sp},\ c_{\rm sp} \equiv {\rm Axes}(I_x,\ I_y,\ I_z) \tag{4.7}$$

$$E_{\rm sp} \equiv \frac{a_{\rm sp}}{c_{\rm sp}} - 1 \tag{4.8}$$

$$A_{\rm sp} \equiv 1 - \frac{S_{\rm sp}}{(36\pi V_{\rm sp}^2)^{1/3}} \tag{4.9}$$

Here, $V_{\rm sp}$ is the volume enclosed by the shell, $M_{\rm sp}$ is the mass of all the particles contained within the shell, $S_{\rm sp}$ is the surface area of the shell, and Axes(I_x, I_y, I_z) is a function which computes the axes of a uniform density ellipsoidal shell which has the moments of inertia I_x, I_y, and I_z. The construction of this function is described in Appendix 4.6.6. In Equation 4.8, we take the standard convention that $a_{\rm sp}$ is the major axis and $c_{\rm sp}$ is the minor axis.

$E_{\rm sp}$ is defined such that it is zero for a sphere and increases for increasingly elliptical shells. $A_{\rm sp}$ is defined such that it is zero for a sphere and increases for increasingly aspherical shells. Our numerical experiments with randomly-shaped shells indicate that it is probable that prolate ellipsoids are the surfaces which minimize $A_{\rm sp}$ for a given value of $E_{\rm sp}$.

4.2.4 Summary of the Algorithm Parameters

The splashback shell finding algorithm described above has 11 free parameters. The parameters and their adopted fiducial values in in SHELLFISH are summarized in Table 4.2.4. Fortunately, there are three empirical properties of this parameter family, which allow for a fairly straightforward way of choosing their values. First, the shapes of the final splashback shells depend only weakly on most of these parameters. Second, the optimal set of

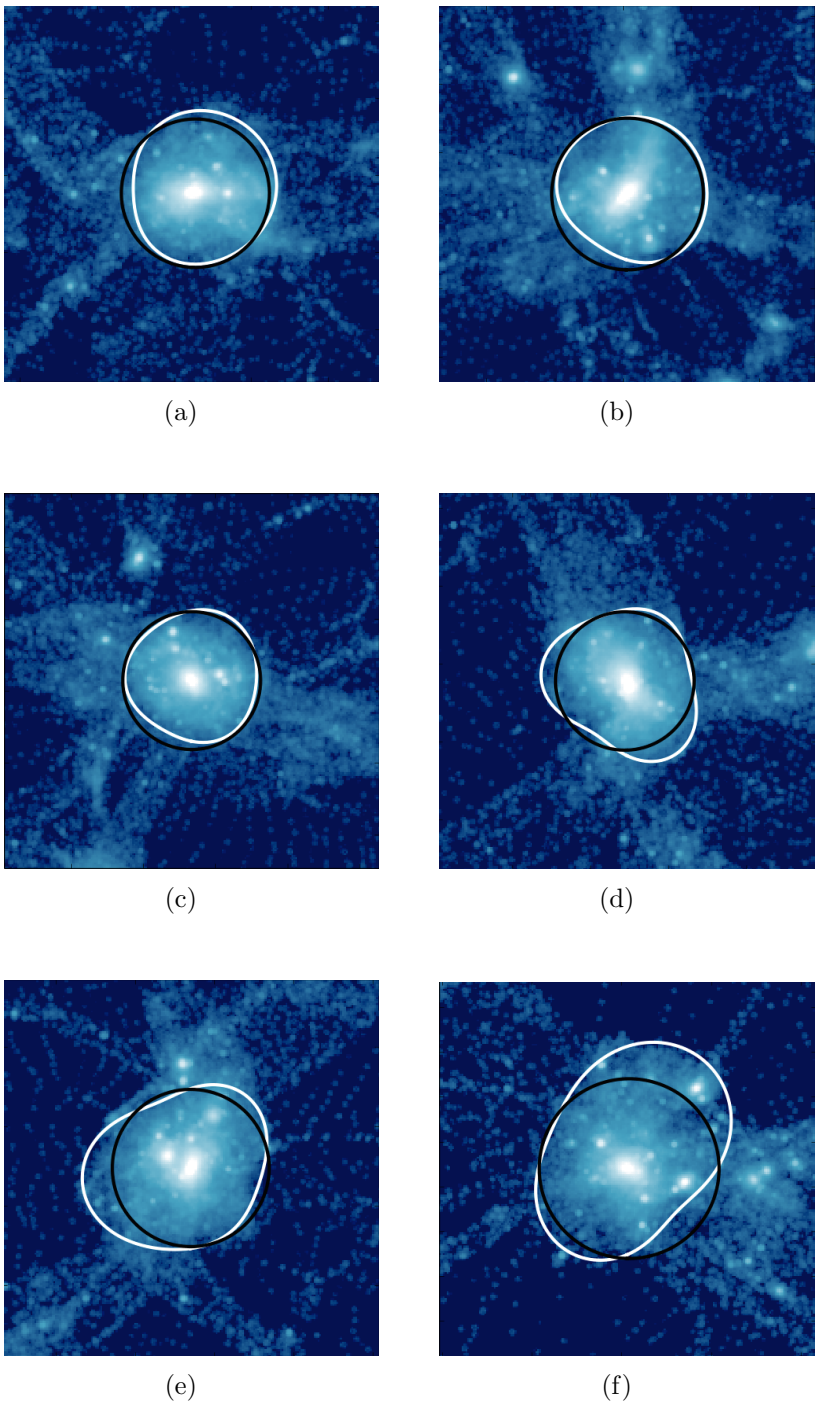

Figure 4.2: Density slices of six halos are shown within boxes of size $5R_{200\mathrm{m}}$ along with cross-sections of each halo's splashback shell identified by our algorithm (white lines) and cross-sections of spheres with the same volume as the splashback shell (black circles). The six halos were picked randomly by sampling halos uniformly from within in the $\log M_{200\mathrm{m}} - \Gamma_{\mathrm{DK14}}$ plane in our L0063 simulation box. Note that Figure 4.2(d) shows the halo used to illustrate our algorithm in Figure 4.1.

Parameter	Definition	Value	Optimization Method
$R_{\rm min}$	§4.2.2	0.3 $R_{\rm 200m}$	A
$R_{\rm max}$	§4.2.2	3 $R_{\rm 200m}$	A
$R_{\rm kernel}$	§4.2.2	0.2 $R_{\rm 200m}$	§4.6.4
$\rho_{\rm bg}$	§4.2.2	0.5 $\rho_{\rm m}$	B
$N_{\rm planes}$	§4.2.2	100	§4.6.5
$N_{\rm los}$	§4.2.2	256	A
$N_{\rm bins}$	§4.2.2	256	A
$N_{\rm SG}$	§4.2.2	121	B & §4.2.2
η	§4.6.2	10	C
$N_{\rm rec}$	§4.6.2	3	C
P	§4.2.2	3	C

Table 4.2: The first column gives the parameter name, the second column gives the section where we define this parameter, the third column is the adopted fiducial value of each parameter within SHELLFISH, and the fourth column indicates the method used to identify the fiducial value. Methods A, B, and C are described in Appendix 4.6.3.

parameters does not appear to change for different halo masses or different halo accretion rates. Third, the optimal value of a particular parameter generally does not change as other parameters are changed or can be easily rescaled to reflect such changes.

A discussion on the procedure we use for choosing specific parameter values can be found in the Appendix 4.6.3.

4.3 Tests

In this section we present several tests of the algorithm described in the previous section. The parameters of the algorithm have been set to the default values listed in Table 4.2.4.

The first basic test is a qualitative visual assessment of the correctness of the splashback shells identified by SHELLFISH.

We find that, in general, the identified shells trace the sharp discontinuities in the density field around halos. We illustrate this for six randomly-selected example halos in Figure 4.2,

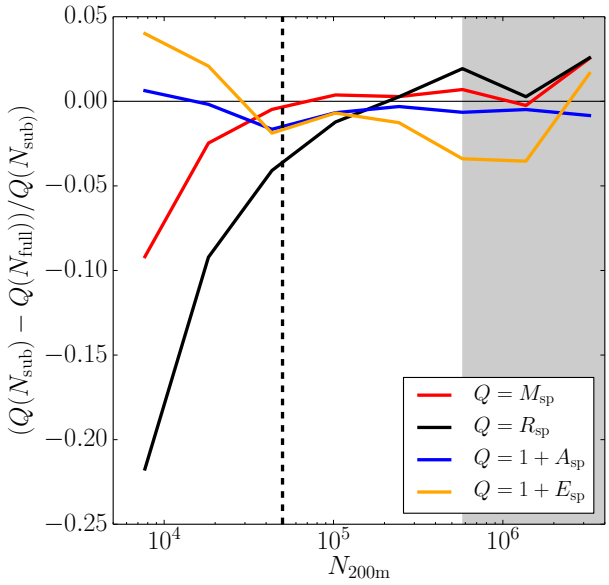

Figure 4.3: Convergence tests for the properties of splashback shells defined in Equation 4.5 - Equation 4.9 : enclosed mass, M_{sp}, radius of the sphere of equivalent radius, R_{sp}, ellipticity, E_{sp}, and asphericity, A_{sp} as a function of the number of dark matter particles within $R_{200\mathrm{m}}$, $N_{200\mathrm{m}}$. The vertical dashed line corresponds to $N_{200\mathrm{m}} = 50,000$, the lower limit used for the analysis in this chapter, and the shaded vertical region indicates bins which contain two or fewer halos and are therefore dominated by individual halo error. Within the converged particle count range there is typically a scatter of $\approx 2\%$ about the median relation, which has not been plotted here for visual clarity. See section 4.3 for details and discussion on this figure.

where the white curves show the cross-sections of the identified shells and the black circles show cross-sections of spheres with radii $R_{\rm sp}$ for those halos. Here $R_{\rm sp}$ corresponds to the volume-equivalent definition given in Equation 4.5. While we found that this type of simple visual inspection proved to be very effective in identifying ineffective filtering algorithms and parameter sets, it is necessarily a qualitative test and cannot provide a quantitative error estimate.

In our second test, we compare the values of $R_{\rm sp}$ measured by SHELLFISH to halos which have an unambiguous steepening in their profiles relative to the asymptotic high-R NFW slope due to the splashback shell. SHELLFISH is unambiguously incorrect for any halos where it measures $R_{\rm sp}$ outside of this steepening region. The difficulty with this test is that is that it is hard to programmatically detect the extent of this steepening region in a robust way. Additionally, large substructure and dense filaments can create steepening regions in the outskirts of host halos which appears similar to the steepening caused by the splashback shell, but occurs in the wrong locations. For these reasons, we resort to manual inspection of halos to perform this test.

We inspected the outer profiles of roughly 5,000 $z = 0$ halos with $N_{\rm 200m} > 50,000$ and identified 906 which had a clear steepening of the density profile in their outskirts and did not have a significant subhalo presence in that region. We then identified the starting and ending radii that bracketed the steepening region of each of these halos, $R_{\rm start}$ and $R_{\rm end}$, by eye. We then compared these radial ranges to $R_{\rm sp}$ calculated through Equation 4.5. We found that only four halos had $R_{\rm sp}$ measurements outside of the ranges measured from the profiles, corresponding to a *minimum* failure rate of $\approx 0.5\%$. $R_{\rm start}$ and $R_{\rm end}$ can span a wide range of radii (see, e.g., Figure 4.7(a) and Figure 4.16(a)), so this test is not effective at catching $\approx 20\%$ errors. This test is chiefly sensitive to catastrophic failures, which we found could be as common as 25% for poorly constructed filtering algorithms or improperly set parameters. Figure 4.4 shows an example of a typical catastrophic failure. In this case, there is no strong feature in the surrounding density field which forces SHELLFISH to generate an

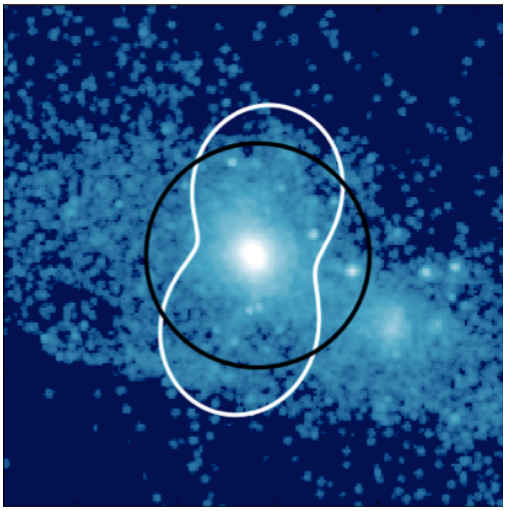

Figure 4.4: A density slice around one of the halos which fails the second test described in section 4.3 (i.e. a "catastrophic failure"). The image dimensions and the meanings of the white and black curves are identical to those in Figure 4.2. We found that these halos can be very common for improperly calibrated filtering algorithms, but when the parameters shown in Table 4.2.4 are used, these halos make up only $\approx 0.5\%$ of our total halo population.

unphysical shell. Achieving a low failure rate on this test is a necessary, but not sufficient, condition for any accurate splashback-measuring code.

As a third test, we also carried out a convergence study of the shell properties defined in Equations 4.5 - 4.9 with respect to the number of dark matter particles within a halo, $N_{200\mathrm{m}}$. These were performed by generating a representative sample of halos and fitting two Penna-Dines shells to each of them. The first shell is calculated using only one eighth of the halo's particles and the second is calculated using all the halo's particles. We use the notation that the number of particles in subsampled halos is $N_{200\mathrm{m}}/8 = N_{\mathrm{sub}}$, and that the number of particles in fully sampled halos is $N_{200\mathrm{m}} = N_{\mathrm{full}}$. The results of this test are shown in Figure 4.3.

Figure 4.3 shows that for $N_{200\mathrm{m}} > 50,000$, the systematic error due to particle count in M_{sp} is at the per cent to sub per cent level, and that the error in R_{sp}, $1 + E_{\mathrm{sp}}$, and $1 + A_{\mathrm{sp}}$ in the same range is at the few per cent level. The shaded region in Figure 4.3 indicates bins in which our simulation suite produced two or fewer halos. Figure 4.3 indicates that to identify splashback shells reliably, halos need to be resolved with at least 5×10^4 particles.

It is not clear to what extent there is a second order trend in radius after the first order convergence at $N_{200\mathrm{m}}$. It would not be unreasonable to see a trend of this type: as $N_{200\mathrm{m}}$ increases, SHELLFISH may be able to resolve and fit smaller scale features in halos which could result in small changes in volume. For this reason, we cannot yet rule out that there is a systematic $\lesssim 5\%$ trend with mass for R_{sp}.

4.3.1 Comparison to Particle Trajectories

As a fourth test of the algorithm, we inspect the trajectories of individual particles near the splashback shell. Particles near the correctly identified splashback shells can be expected to be either infalling for the first time or to be at the apocenter of their first orbit. Trajectories of the infalling particles should be roughly perpendicular to the shell locally and should not show any deflection when crossing the shell. The trajectories of the particles that have orbited through the halo should show a sharp turnaround at the shell location. The relative fractions of particles of these two types will depend on the mass accretion rate of each specific halo, but the apocenters of particles of the second type should coincide with the identified splashback shell. Given that our algorithm does not use any information about particles trajectory, this test is a useful independent check on whether our algorithm identifies shells corresponding to the actual outermost apocenters of particle orbits.

To perform this test on a target halo, we first use SHELLFISH to identify a splashback shell around the halo at some redshift $z_1 > 0$. We then find all particles within some small distance δ of this shell and track their trajectories through a redshift range $z_0 < z_1 < z_2$.

The results of such a test are shown for four representative clusters with $M_{200\mathrm{m}} \approx 10^{14} h^{-1}\ M_\odot$ from the L0250 simulation in Figure 4.5, where we used $\delta = R_{200\mathrm{m}}/50$, $z_0 = 0.32$, $z_1 = 0.13$, and $z_2 = 0$. The location of the particles at $z = z_1$ is shown by red points. The trajectories of particles from z_0 to z_1 are shown as red curves and the trajectories from z_1 to z_2 are shown as yellow curves. Infalling particles have red curves pointing outside of the halo and yellow curves pointing inside the halo. Particles moving outwards have reversed

colors: yellow curves pointing to the outside and red curves pointing to the inside. Particles at their apocenters will have both curves pointing to the inside.

Figure 4.5 shows that for the cluster-sized halos shown, most particles around the splashback shell are infalling, as can be expected for rapidly accreting halos. At the same time, there is a fraction of particles that exhibit a sharp turnaround near the identified splashback shell: i.e., the apocenters of their orbit coincide with the splashback shell identified from the density field.

Figure 4.5(c) does show several trajectories in the southern portion of the halo which travel outside the identified shell. It is not clear whether this is because Shellfish was unable to identify the correct splashback shell due to the high-density filament or whether those particles were perturbed from their orbits in later time steps by the nearby subhalo. Such trajectories, however, are a small fraction of the total.

We have carried out such visual inspection of trajectories for a large number of halos and found results qualitatively similar to those shown in Figure 4.5. This indicates that our algorithm is reliably picking out splashback shells that coincide with the most distant apocenters of particle orbits. This analysis has been confirmed by comparison with an alternative splashback-measuring code, Sparta, which showed that the radii measured by Shellfish correspond to high-percentile moments of a halo's apocenter distribution [Diemer et al., 2017].

4.4 Results

4.4.1 Sample Selection

To analyze the properties of splashback shells identified using our algorithm we construct a sample of halos drawn from the halo catalogs of all the simulations listed in Table 4.2.1. Based on the convergence test results reported in section 4.3 (see Figure 4.3), we select halos with $N_{200\mathrm{m}} > 50,000$, so that shell properties are converged to the level $\lesssim 5\%$. We

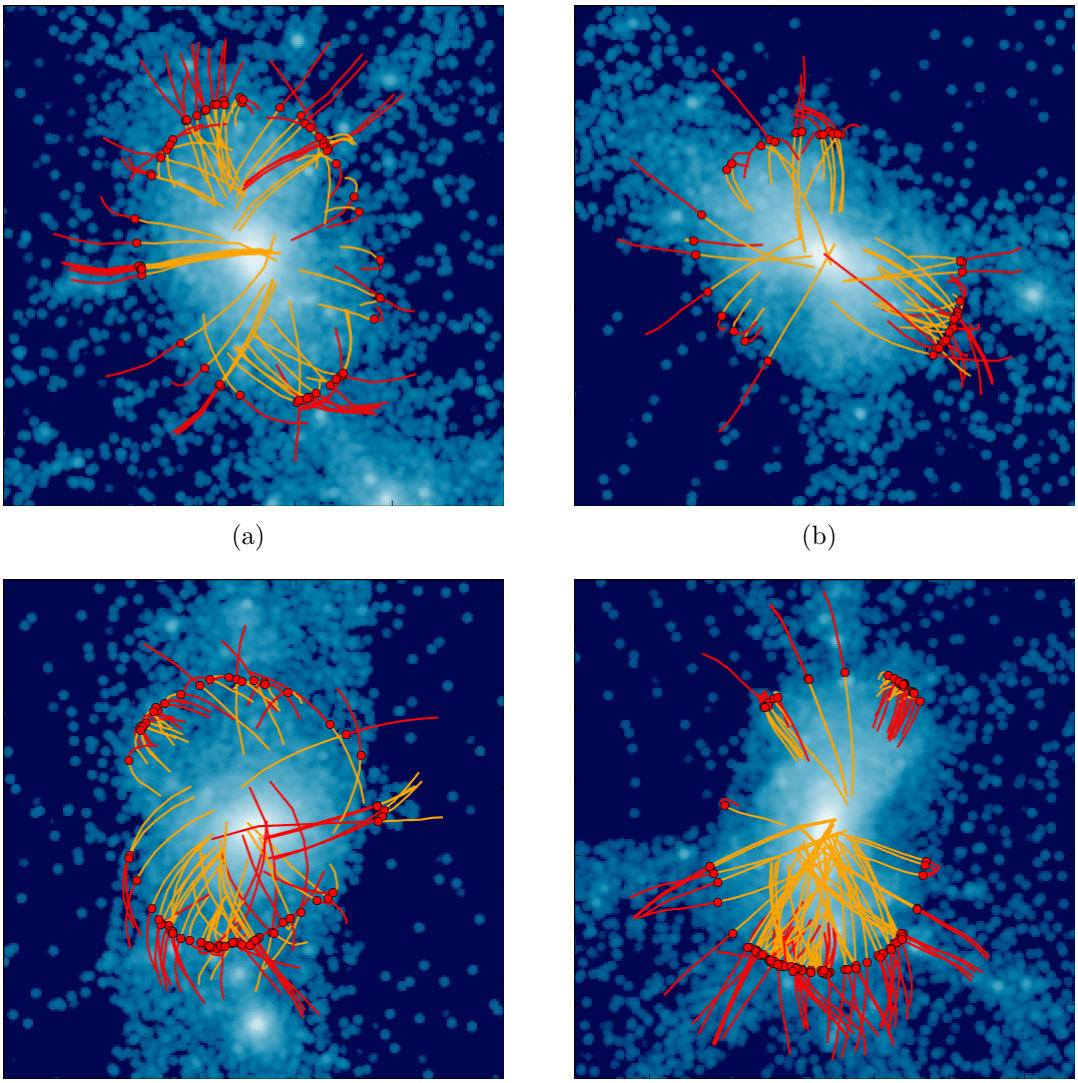

(a) (b) (c) (d)

Figure 4.5: Trajectories for particles during the redshift interval $z \in [0.32, 0]$ near the splashback shell of four clusters from the L0250 simulation with $M_{200\mathrm{m}} \approx 10^{14} h^{-1}\ M_\odot$ identified at $z_1 = 0.13$. Each figure shows a slice through the density field in a region centered on the halo with a width of $5R_{200\mathrm{m}}$ and a depth of $R_{200\mathrm{m}}/5$. Every particle in this slice located within $R_{200\mathrm{m}}/50$ of the splashback shell identified by SHELLFISH at $z_1 = 0.13$ is shown as a red point. The trajectory of each particle during the redshift interval $[0.31, 0.13]$ is shown by red line, while the trajectory during the redshift interval $[0.13, 0]$ is shown by yellow lines. See section 4.3.1 for details.

also restrict the maximum mass of halos drawn from the smaller box simulations so that the $\Gamma_{\rm DK14}$ distribution of the largest halos in those simulations is similar to that of halos of the same mass in the larger boxes. This limit is imposed because small box size may limit the mass accretion time of the largest halos, as evolution becomes nonlinear on scales comparable to the box size. The mass ranges sampled by each box are given in Table 4.2.1.

With these mass limits in place, we construct the halo sample for analysis by subsampling all host halos within the mass range of each box in such a way as to obtain a uniform distribution of halos in both $\log M_{\rm 200m}$ and $\Gamma_{\rm DK14}$. This procedure is repeated for $z = 0$, $z = 0.5$, $z = 1$, and $z = 2$, resulting in a total sample sizes of 1095, 1198, 846, and 467 halos, respectively.

4.4.2 Comparison With Stacked Radial Density Profiles

Figure 4.6 presents a comparison between the distribution of $R_{\rm sp}/R_{\rm 200m}$ values measured by SHELLFISH and the predictions of stacked profile analysis as a function of accretion rate. In particular, we choose to compare against the $\Gamma_{\rm DK14}$ vs. $R_{\rm sp}/R_{\rm 200m}$ fit reported in More et al. [2015]. We have chosen $z = 0.5$ for illustration in this figure, because the $z = 0.5$ halo sample contains a good mix of well-converged, high particle-count halos which become more abundant as redshift decreases, and halos with large accretion rates, which become more abundant as redshift increases.

The figure shows that at $\Gamma_{\rm DK14} \lesssim 1.5$ our algorithm estimates splashback radii similar to those from stacked profiles, while for $\Gamma_{\rm DK14} \gtrsim 1.5$, SHELLFISH estimates progressively larger $R_{\rm sp}$ values compared to the values from the stacked profiles. The discrepancy in $R_{\rm sp}/R_{\rm 200m}$ is $\approx 30\%$ for $\Gamma_{\rm DK14} \approx 4$. This discrepancy exists at all redshifts.

Given that the tests presented in section 4.3 indicate that our code identifies splashback shells reliably and estimates their properties to better than 5% accuracy at the resolution level shown in Figure 4.6, it is highly unlikely that the discrepancy is due to any issue of our algorithm. In particular, a systematic overestimation of $R_{\rm sp}$ by 30% would be immediately

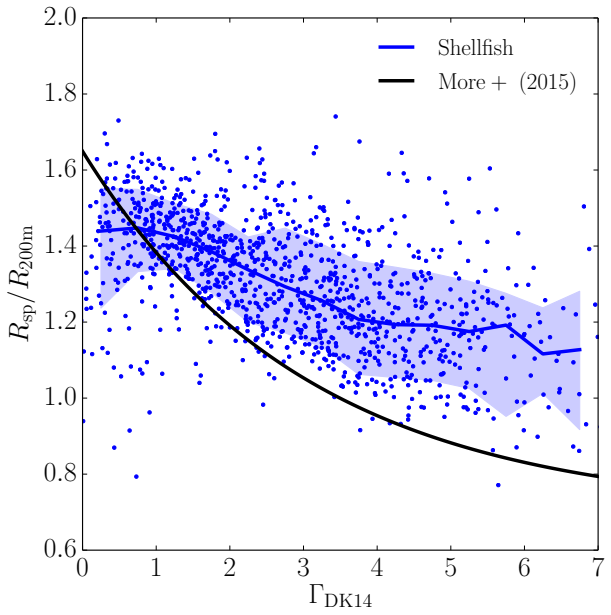

Figure 4.6: Comparison between the distribution of $R_{\rm sp}/R_{\rm 200m}$ values measured by SHELLFISH to the prediction of stacked density profile analysis at $z = 0.5$. The black curve shows the best fit to location of steepest slope in the stacked density profiles as a function of accretion rate, $\Gamma_{\rm DK14}$. We use the parameterization for this fit reported in More et al. [2015]. The blue points show SHELLFISH $R_{\rm sp}/R_{\rm 200m}$ measurements for individual halos, the blue curve shows the median measurement, and the blue contours show the 68% envelope. The SHELLFISH curve differs from stacked profiles in both amplitude and shape, becoming ≈30% larger for halos with $\Gamma_{\rm DK14} > 4$. A qualitatively similar difference can be seen at all redshifts. We argue that this difference is due to stacked profiles splashback measurements being artificially biased inwards by massive subhalos in section 4.4.2.

apparent in the visual comparison of the identified splashback shells and the underlying density field. Instead, we find a good agreement in such comparisons. Additionally, we were able to independently reproduce the results of More et al. [2015] using the halo sample described in section 4.4.1. Thus, the discrepancy shown in in Figure 4.6 is the real difference between the two methods.

To better understand the origin of this difference, we visually inspected the radial density profiles of all the halos in our sample and classified them into one of three qualitative classes. First, we flagged every halo as either containing a visually distinct steepening region in its outskirts or as containing no such region. Halos of the latter type we classify as "featureless"-type profiles. The red curve in Figure 4.7 is an example of such a halo.

The remaining halos contain distinct regions in the density profiles where the logarithmic slope steepens considerably over a limited range of radii. For these halos we visually identify the starting radii, $R_{\rm start}$, and ending radii, $R_{\rm end}$ of their respective steepening regions. We find that almost all such halos separate neatly into one of two classes: 1) halos which have relatively sharp and narrow steepening regions that closely correspond to the radial range of the splashback shell found by SHELLFISH for that halo; and 2) halos which have a relatively shallow and wide steepening region with an $R_{\rm start}$ value significantly smaller than the minimum radius of the shell found by SHELLFISH. We refer to halos of the first type as "short"-type profiles and halos of the second type as "long"-type profiles, respectively. The blue and yellow curves in Figure 4.7 are examples of these two types of profiles, respectively. The number of halos is roughly similar in the three classes of "featureless", "short", and "long" profile types, but the exact fractions of halos in each class changes with accretion rate and with mass.

We find that when we derive splashback radii from the stacked density profiles using only halos of the short and featureless types, the difference from the median $R_{\rm sp}$ measured by SHELLFISH decreases to $\lesssim 5\%$ at high $\Gamma_{\rm DK14}$. This is not surprising, given that we noted that the steepening range in the short-type profiles is consistent with the radial range of the

splashback shells derived by SHELLFISH, but demonstrates that the difference in $R_{\rm sp}$ is due almost entirely to the effect of the halos with the long-type profiles on the stacked density profile.

Our analysis shows that the steepening region in the density profiles of long-type halos is not caused by the splashback shell, but by the presence of massive subhalos. Specifically, visual inspection of the density fields of long-type halos generally reveals that no portion of the splashback shell can be found as far inwards as $R_{\rm start}$ for these halos. Instead, we almost always find that a massive subhalo is present at $R \approx R_{\rm start}$ for these halos. Thus, the steepening region is associated with the presence of subhalo, not the splashback. Given that subhalos in different halos with the same accretion rate will be located at different R, the combined effect of the massive subhalos on the stacked profile is to "wash out" the signature of the splashback shell and to bias the start of the steepening region to smaller radii.

Thus, halos with no massive subhalos in the outskirts have the short-type profiles, while those that do have such subhalos have long-type profiles. Halos that either have large neighboring halos outside their splashback shells or which exist in dense filaments have the steepening due to splashback shell erased completely and thus have featureless-type profiles. The expectation is then that if contribution of massive subhalos is removed from the density profiles the $R_{\rm sp}$ derived from the stacked density profiles should be consistent with the values estimated by SHELLFISH. We demonstrate that this is the case in the next subsection.

4.4.3 Angular Median Density Profiles of Halos

There are many possible ways of mitigating the contribution of subhalos to the density profiles of their host halos. We choose one of the simplest methods for doing this, one which does not rely on the availability of robust subhalo catalogs, and which could, in principle, be adapted for use on observed galaxy clusters. The idea is to construct density profiles using the median estimate of density in each radial shell instead of the mean density. A similar approach has been used in the analysis of the gas distribution in clusters [Zhuravleva et al.,

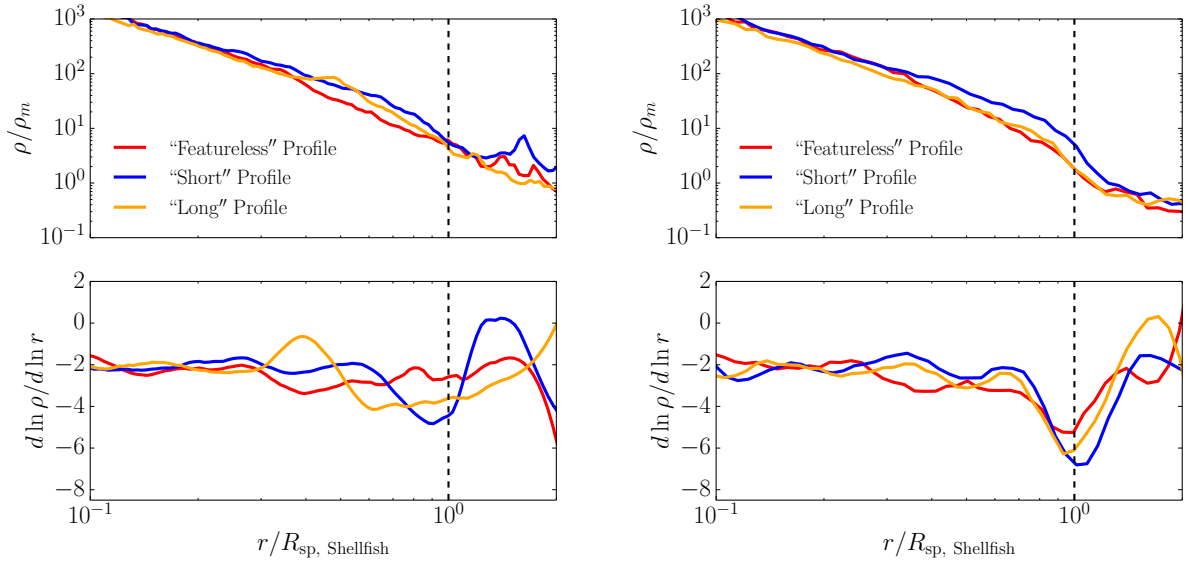

(a) (b)

Figure 4.7: Comparison between spherically averaged radial density profiles (Figure 4.7(a)) and the angular median density profiles described in 4.4.3 (Figure 4.7(b)). The top panels show density and the bottom panels show logarithmic slope after the density profiles have been smoothed with a fourth-order Savitzky-Golay filter with smoothing windows a third of a decade wide. Both density and slope profiles have had their radii normalized by $R_{\rm sp}$ as measured by SHELLFISH. The three halos are chosen to be representative of the three qualitative classes of halo profiles we identified in section 4.4.2. Because angular median profiles are designed to remove interfering substructure, they have deeper and more well-defined points of steepest slope. The level of agreement between the radius of steepest slope of the angular median profiles shown here and the $R_{\rm sp}$ values derived by SHELLFISH is typical.

2013].

Namely, we split each radial shell of the density profile into N solid angle segments, e.g., using a two-hemisphere variation on the algorithm described by Gringorten and Yepez [1992], or the HEALPix pixelation algorithm [Górski et al., 2005]. We then estimate density, $\rho_i(r)$, for each segment i and construct the halo density profile by taking the median of these densities in each radial shell, $\rho_{\rm med}(r) = {\rm med}\,[\rho_i(r)]$. This approach is based on the basic intuition that subhalos are generally much smaller in extent than the host and thus contribute to a fraction of the solid angle in a given radial shell, while most of the solid angle will be dominated by the diffuse matter of the host halo. The median density then will estimate the density of that diffuse component and will be largely insensitive to the outlier solid angle segments associated with massive subhalos.

Figure 4.7 shows comparisons between usual spherically averaged mean density profiles, $\rho(r)$, and angular median density profiles $\rho_{\rm med}(r)$ for three representative halos of the different classes described in section 4.4.2. The comparison of the profiles in the two panels of the figure shows that the angular median profiles of the halos are much more similar to each other than the mean profile. Unlike the mean density profiles, which have very different shapes, the angular median density profiles all behave similarly: there is a narrow, sharp steepening region in the logarithmic profile centered on the radius that SHELLFISH reports as $R_{\rm sp}$. Thus, the diversity of profile types noted in 4.4.2 is largely absent for profiles of this type. We also note that the point of steepest slope in angular median profiles is significantly sharper than it is in mean profiles. Thus the signature of the splashback shell is easier to detect when halos are analyzed in this way.

To compare $R_{\rm sp,shell}$ measured by SHELLFISH to $R_{\rm sp,med}$ derived from the individual angular median profiles, we follow the procedure described above for every halo in the sample described in section 4.4.1. We use 50 solid angle segments per halo with 30 logarithmically-distributed radial bins per decade. This relatively coarse spacing is needed to make up for the fifty-fold loss in number statistics and has a non-trivial impact on the maximum fidelity of our

angular median profiles: the width of every bin is 8% of the radius at which is occurs. Once the median profile is computed from these segments, we apply a Savitzky-Golay smoothing filter with a window size comparable to the characteristic radial width of the regions where profile slope steepens quickly. We set the window size to a 0.33 dex with the caveat that other reasonable choices, such as a sixth of half of dex, can induce systematic changes to the mean $R_{\rm sp,med}$ of a halo population of $\approx 5\%$. Thus, the population statistics on $R_{\rm sp,med}$ cannot be trusted to accuracies smaller than 5% regardless of any additional statistical error bars, and that individual $R_{\rm sp,med}$ values measured this way cannot be measured more accurately than 13%, regardless of additional profile noise. We leave more nuanced accuracy analysis on this method to a future work, but note that this level of accuracy is sufficient for our purposes, which is merely to test whether reducing effect of subhalos on the radial profiles results in $R_{\rm sp}$ estimates which are qualitatively consistent with the results of Shellfish.

We compare the $M_{\rm 200m}$ and $\Gamma_{\rm DK14}$ trends between $R_{\rm sp,shell}$ and $R_{\rm sp,med}$ for our $z = 0.5$ halo sample in Figure 4.8 and see fairly good agreement. The high $\Gamma_{\rm DK14}$ disagreement has dropped from $\gtrsim 30\%$ to $\approx 5\%$. This is consistent with the known systematic uncertainties in both methods and confirms that the high $\Gamma_{\rm DK14}$ disagreement with the estimates of the splashback radius from the stacked mean density profiles is due to the bias introduced into these profiles by massive subhalos.

At the same time, at $\Gamma_{\rm DK14} \lesssim 0.5$ there is $\approx 15\%$ disagreement between $R_{\rm sp}$ derived from the stacked angular median profiles and the median measurements of Shellfish. In principle, this difference could be caused by either the angular median profile method or Shellfish, but comparison against another splashback-measuring code, Sparta, which explicitly tracks particle orbits to find their apocenters, shows tight agreement with Shellfish at $\Gamma_{\rm DK14} > 0.5$ and a level of discrepancy comparable to that seen for angular median profiles at $\Gamma_{\rm DK14} < 0.5$. An extended discussion on how these two methods compare against one another can be found in Diemer et al. [2017].

It is not surprising that the splashback shell is difficult to measure at these accretion rates.

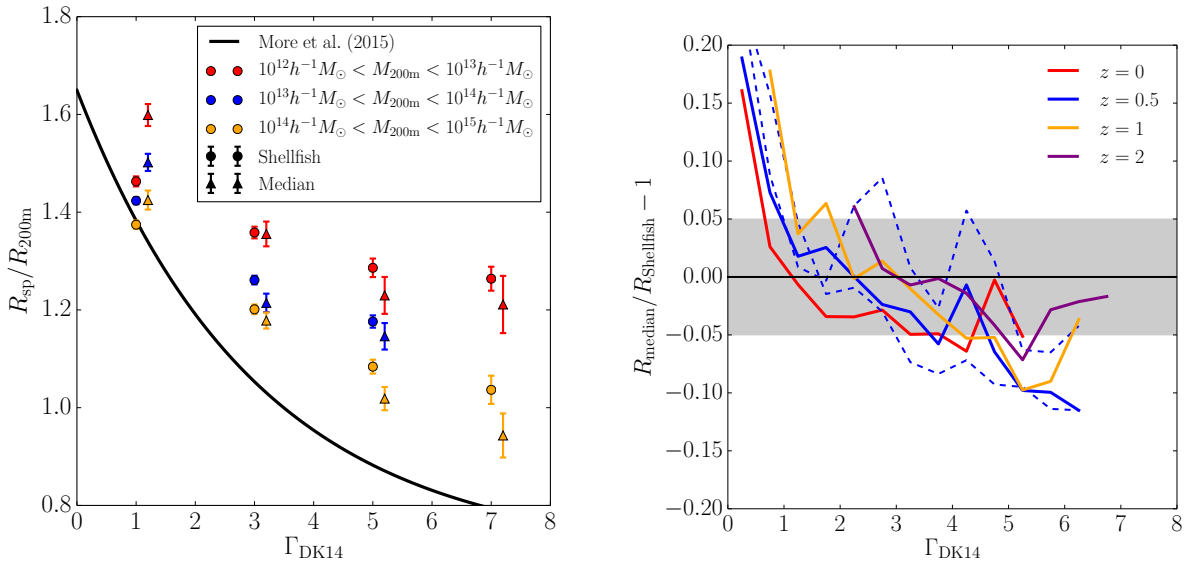

(a) (b)

Figure 4.8: Comparison between the mean R_{sp}/R_{200m} values measured by SHELLFISH and by the angular median profile method described in section 4.4.3. The left panel shows measurements made by the two methods for different Γ_{DK14} and M_{200m} bins at $z = 0.5$. Shellfish measurements are shown as circles on the left side of their respective Γ_{DK14} bins, and angular median profile measurements are shown as triangles on the right side of their respective Γ_{DK14} bins. Error bars represent only the bootstrapped error on the mean and do not account for known systematic uncertainty in the angular median profile method (see section 4.4.3). The right panel shows the median value of $R_{Shellfish}/R_{median} - 1$, for every halo in our sample at $z = 0$, 0.5, 1, and 2. The dashed blue lines show the shape of this curve when the angular median profile's Savitzky-Golay window width is varied to the edges of its physically reasonable value range to give a sense of the systematic variability in this method (see section 4.4.3). These two figures illustrate that when large subhalos are removed from the density profiles of halos, the location of the point of steepest slope becomes consistent with the value of R_{sp} measured by SHELLFISH. They also illustrate that there is a non-trivial disagreement between the two methods for very small Γ_{DK14}.

At $z = 0$, pseudo-evolution causes static NFW halos with $c_{\rm vir} \gtrsim 7$ to report $\Gamma_{\rm DK14} > 0.5$ purely due to the cosmological evolution of $\rho_{\rm m}$ [Diemer et al., 2013b]. This means that the majority of halos with accretion rates this low must be actively losing particles in order to offset their illusory accretion rates caused by pseudo-evolution. This particle loss is typically caused by dense environments, either because the halo is embedded in a massive filament feeding a cluster or because it is about to merge with a larger halo.

For this reason we believe that our algorithm should not be used to measure halos with $\Gamma_{\rm DK14} < 0.5$ unless $\gtrsim 15\%$-level systematic errors are acceptable. We exclude such halos from all subsequent analysis. This is an aggressive cut for Milky Way-sized halos at low redshifts, where 20% of halos have $\Gamma_{\rm DK14} < 0.5$. The cut is less severe for halos in all other mass bins and at all other redshifts, affecting less than 5% of halos in all such parameter slices. Clusters and high redshift halos in particular are almost completely unaffected by this cutoff.

4.4.4 The Relationship Between Mass, Accretion Rate, and Splashback Radius

One of the key results obtained by previous analyses of splashback shells using stacked radial density profiles [Diemer and Kravtsov, 2014, More et al., 2015, 2016, Adhikari et al., 2016] is the dependence of the splashback radius in units of the $R_{\rm 200m}$ on the mass accretion rate $\Gamma_{\rm DK14}$ (see Equation 3.14): halos with larger accretion rates have smaller values of $R_{\rm sp}/R_{\rm 200m} \equiv \tilde{R}_{\rm sp}$. In this section we present the result of fits to $\tilde{R}_{\rm sp}$ using the measurements from SHELLFISH.

Specifically, we fit the following log-normal distribution to $\tilde{R}_{\rm sp}$ as a function of $\nu_{\rm 200m}$,

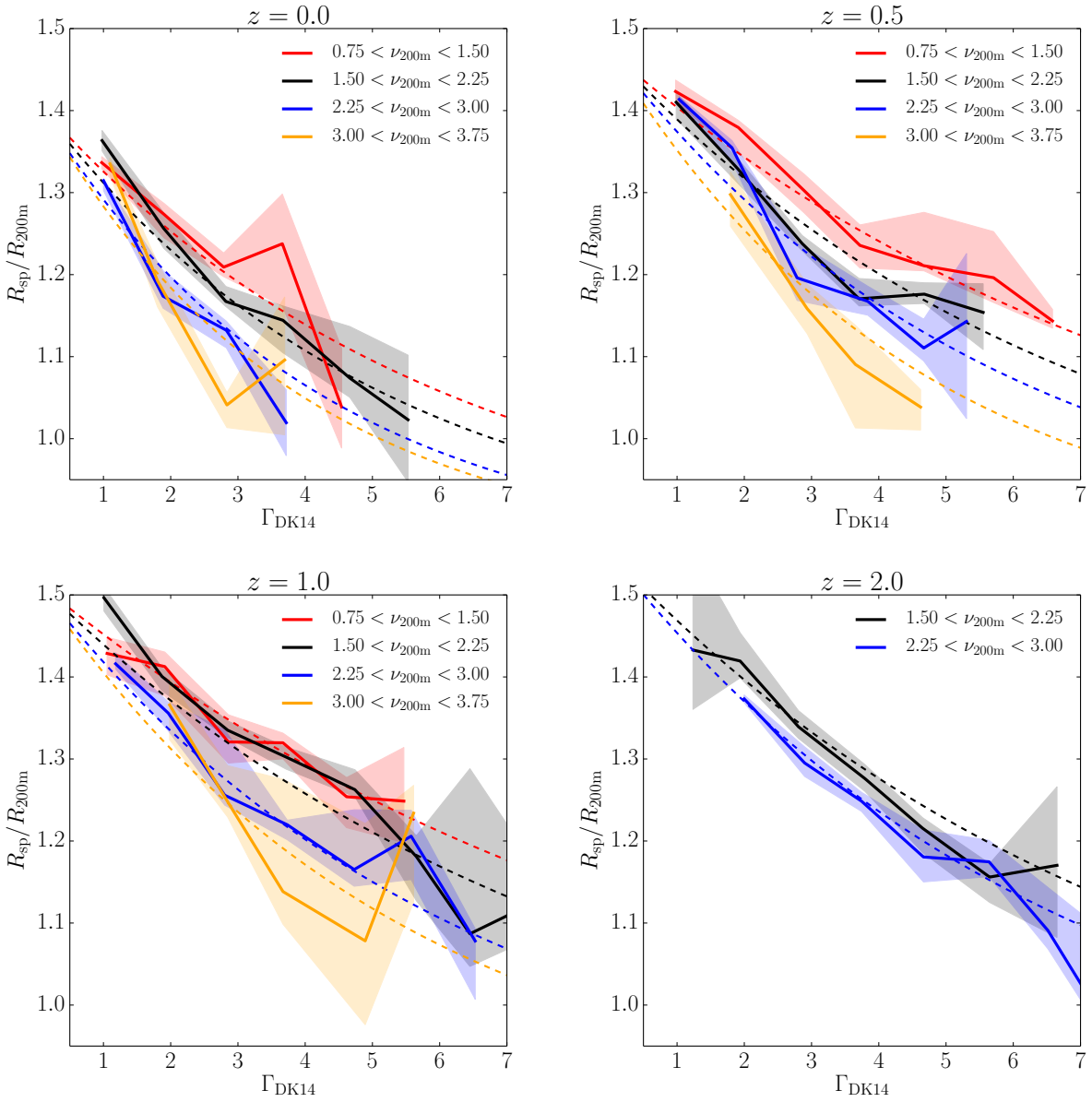

Figure 4.9: Comparison between our fit and SHELLFISH's measurements of $R_{\rm sp}/R_{\rm 200m} \equiv \tilde{R}_{\rm sp}(\Gamma_{\rm DK14}, \nu_{\rm 200m}, z)$. The thick lines represent the median value of $R_{\rm sp}/R_{\rm 200m}$ in each $\Gamma_{\rm DK14}$ bin and the shaded regions indicate the 68% errors on those medians, as determined by bootstrapping. The thin lines show the median of the distribution given by Equations 4.10 -4.12 evaluated at the median $\nu_{\rm 200m}$ value within the corresponding $\nu_{\rm 200m}$ bin.

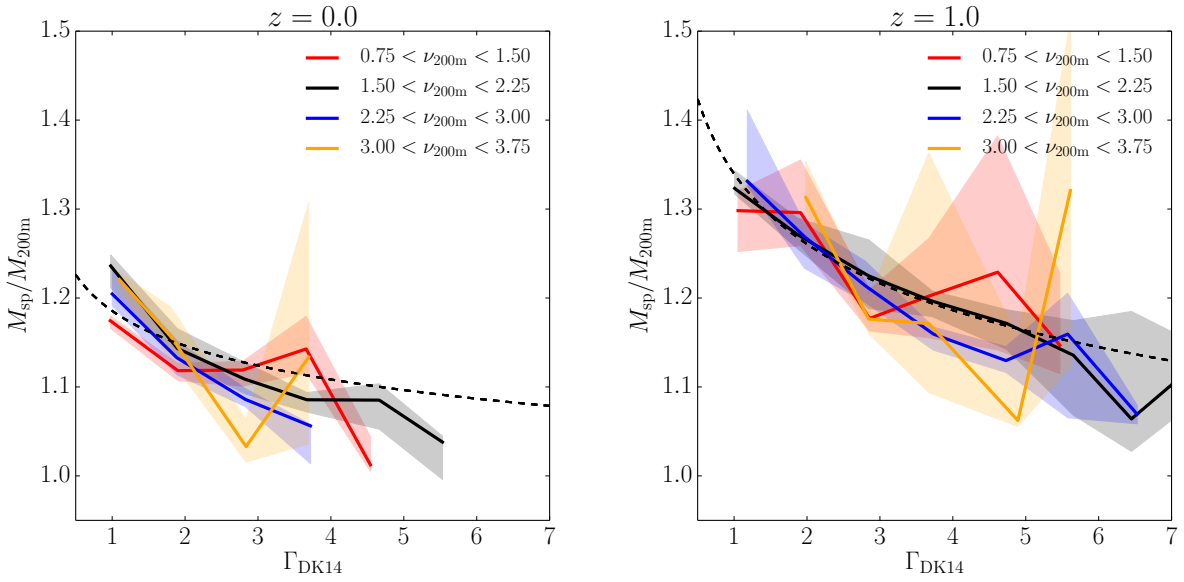

Figure 4.10: Comparison between our fit and SHELLFISH's measurements for $M_{\mathrm{sp}}/M_{200\mathrm{m}} \equiv \tilde{M}_{\mathrm{sp}}(\Gamma_{\mathrm{DK14}}, \nu_{200\mathrm{m}}, z)$. The visualization scheme is identical to the one used in Figure 4.10, with the thin line corresponding to the median of the distribution given by Equations 4.13 and 4.14. Note that unlike the fit displayed in Figure 4.9, our $\tilde{M}_{\mathrm{sp}}$ has no $\nu_{200\mathrm{m}}$ dependence, so only a single thin line is plotted. There are several important caveats to this fit, which we discuss in section 4.4.5.

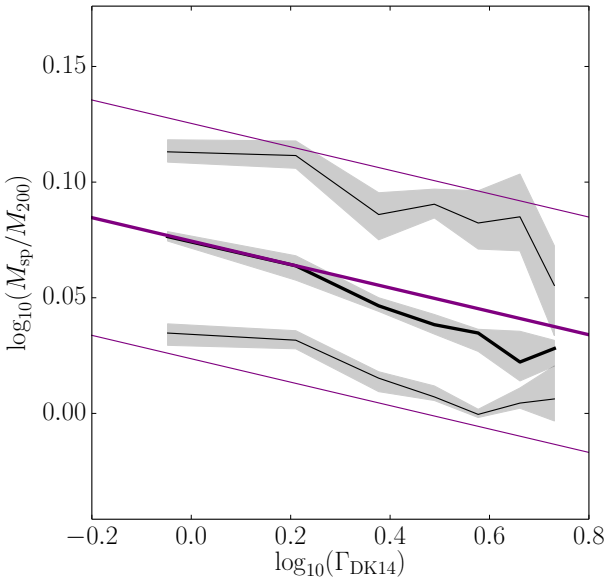

Figure 4.11: Comparison between the $\tilde{M}_{\mathrm{sp}}$ median and 68% contours for our data and our fit given by Equations 4.13 and 4.14 at $z = 0$. This Figure was made to emphasize the weaknesses in our $\tilde{M}_{\mathrm{sp}}$ fit and shows an $\approx 2\% - 4\%$ overestimation of the median at high Γ_{DK14} and a similar overestimation of the logarithmic scatter, σ_{dex}. An extended discussion of this Figure can be found in section 4.4.5.

$\Gamma_{\rm DK14}$, and Ω_m:

$$P(\tilde{R}_{\rm sp}) \propto \exp(-\log_{10}^2(\tilde{R}_{\rm sp}/R_{\rm med})/2\sigma_{\rm dex}^2), \tag{4.10}$$

$$R_{\rm med} = (R_0\Omega_m + R_1)\exp(\alpha\Gamma_{\rm DK14}) + A, \tag{4.11}$$

$$\alpha = \eta_0\Omega_m^2 + \eta_1\Omega_m + \eta_2 + \xi\nu_{\rm 200m}. \tag{4.12}$$

Here R_0, R_1, A, ξ, η_0, η_1, and η_2 are fit parameters.

As discussed above, our sample only includes halos with $\Gamma_{\rm DK14} > 0.5$. We fit the functional form given by Equations 4.10–4.12 using an implementation of the affine-invariant Markov Chain Monte Carlo sampling algorithm of Goodman and Weare [2010]. We also adopt a Heaviside prior on the logarithmic scatter, $\sigma_{\rm dex}$, to prevent it from becoming non-positive.

We find that the best fit parameters are

$$\begin{aligned} R_0 &= 0.2181, & \eta_0 &= -0.1742, \\ R_1 &= 0.4996, & \eta_1 &= 0.3386, \\ A &= 0.8533, & \eta_2 &= -0.1929, \\ \xi &= -0.04668, & \sigma_{\rm dex} &= 0.046. \end{aligned}$$

The resulting function is plotted against our data in Figure 4.9.

It is interesting that the radii estimated by SHELLFISH exhibit a strong dependence on *both* mass accretion rate and peak height. This trend can also be seen in other methods for measuring individual splashback shells around halos, such as the median angular profile method described in section 4.4.3 and the apocenter-based splashback-measuring code SPARTA [Diemer et al., 2017]. The trend cannot be attributed to convergence trends because all halos used in the sample have $N_{\rm 200m}$ above the convergence limit of 5×10^4 found in section 4.3 and because the mass bounds given in Table 4.2.1 restrict the halos in our sample

to a single decade in particle count.

Previous estimates from stacked density profiles only found a strong dependence on $\Gamma_{\rm DK14}$, while a $\nu_{\rm 200m}$ dependence was either not apparent or weak [e.g., More et al., 2015]. The $\nu_{\rm 200m}$ dependence is also not predicted in the collapse models of isolated peaks [e.g., Adhikari et al., 2014], even though they successfully predict a $\Gamma_{\rm DK14}$ dependence. The origin of the $\nu_{\rm 200m}$ dependence and the seeming discrepancy with the collapse model is not clear. Additionally, although we have made an empirical argument that stacked profiles are biased by massive subhalos, we do not yet propose a physical picture for why this bias should also erase or decrease trends with $\nu_{\rm 200m}$.

4.4.5 Splashback Shell Masses

In contrast to overdensity-based halo definitions, $M_{\rm sp}$ and $R_{\rm sp}$ are independent (albeit correlated) quantities. For this reason we do not fit the same functional form to both $R_{\rm sp}$ and $M_{\rm sp}$. We fit the following log-normal distribution to $\tilde{M}_{\rm sp} \equiv M_{\rm sp}/M_{\rm 200m}$ as a function of $\Gamma_{\rm DK14}$ and Ω_m:

$$P(\tilde{M}_{\rm sp}) \propto \exp(-\log_{10}^2(\tilde{M}_{\rm sp}/M_{\rm med})/2\sigma_{\rm dex}^2), \tag{4.13}$$

$$M_{\rm med} = (M_0\Omega_m + M_1)\left(\frac{\Gamma_{\rm DK14}}{\Gamma_{\rm pivot}}\right)^{\alpha_0\Omega_m+\alpha_1}. \tag{4.14}$$

Here $\Gamma_{\rm pivot} = 3$ is a characteristic pivot value, and M_0, M_1, α_0, and α_1 are fit parameters.

Using the same procedure described in section 4.4.4 we obtain the parameters

$$A_0 = 0.192 \qquad a_0 = -0.0781$$

$$A_1 = 1.072 \qquad a_1 = -0.0284$$

$$\sigma_{\rm dex} = 0.054$$

The median of this fit is shown in Figure 4.10. Note that unlike our fit to $\tilde{R}_{\rm sp}$, we do not model $\tilde{M}_{\rm sp}$ as having a $\nu_{\rm 200m}$ dependence because there is not strong evidence for such a trend in our data. This contrasts with the results of SPARTA, which did find a strong $\nu_{\rm 200m}$ trend [Diemer et al., 2017]. It is currently not clear whether higher quality data would reveal a small mass trend in the SHELLFISH data as well.

The left panel of Figure 4.10 shows a deviation between our fit and SHELLFISH's measurements at high $\Gamma_{\rm DK14}$ for $z = 0$. We investigate this further in Figure 4.11 which shows the median and 68% contours of the $\tilde{M}_{\rm sp}$ distribution at $z = 0$. This Figure shows that although the median of our data is well approximated by a power law, our Bayesian fit reports a shallower slope. This results in a $\approx 2\% - 4\%$ overestimation of $\tilde{M}_{\rm sp}$ at high accretion rates for this redshift.

This overestimation is caused by the fact that at high $\Gamma_{\rm DK14}$ $\tilde{M}_{\rm sp}$ follows an skewed log-normal distribution. Since our model assumes a log-normal distribution, our fit's median is pulled high relative to our data's median. The offset between the two medians also leads to an overestimation of the logarithmic scatter, $\sigma_{\rm dex}$ by a comparable amount.

Despite this, we deliberately choose not to model the skew for three reasons. The first reason is simplicity: our experiments with explicitly modeling the skew show that it has non-linear dependencies on $\Gamma_{\rm DK14}$ and z. The second reason is that this reduction in simplicity would result in an increase in accuracy for only a small number of halos: high accreting halos at $z = 0$ are rare. The third reason is that this effect is comparable to our stated systematic uncertainty in the radii and masses reported by SHELLFISH, so any subsequent analysis which would reach a qualitatively different conclusion from an improvement in fit modeling is not respecting the known uncertainty in SHELLFISH shells. Instead, we choose to use an extremely simple model - a power law with log-normal residuals and a linear dependence on Ω_m - and leave more precise modeling to future work.

The skew seen in the low redshift, high $\Gamma_{\rm DK14}$ has a simple explanation. The scatter in $\tilde{M}_{\rm sp}$ has two sources: the first is the variation in shell sizes which also causes the scatter in

$\tilde{R}_{\rm sp}$, the second is the presence or non-presence of high mass subhalos. Since halos with high accretion rates are more likely to have high mass subhalos than halos with low accretion rates, the second effect is particularly important for them. If a halo has a massive subhalo outside of $R_{\rm 200m}$ but inside its splashback shell, $\tilde{M}_{\rm sp}$ is scattered high. If a halo has a massive subhalo inside $R_{\rm 200m}$, both $M_{\rm 200m}$ and $M_{\rm sp}$ increase, so $\tilde{M}_{\rm sp}$ scatters towards 1. When the median of the of the $\tilde{M}_{\rm sp}$ distribution is close to 1, this means that the presence of massive subhalos has the effect of reducing down scatter and increasing upscatter relative to what we would expect from variation in shell sizes alone.

4.4.6 Splashback Shell Overdensities

We model the distribution of $\Delta_{\rm sp} \equiv 200\tilde{M}_{\rm sp}/\tilde{R}_{\rm 200m}$ by taking the ratios of our mass fit (Equations 4.13 and 4.14) and our radius fit (Equations 4.10 - 4.12). Because our $\Delta_{\rm sp}$ model is derived from our $\tilde{M}_{\rm sp}$ fit, it is subject to the same caveats discussed in section 4.4.5. However, because the dynamic range of $\Delta_{\rm sp}$ is larger than that of $\tilde{M}_{\rm sp}$, the affect of a few-percent disparity in masses is minimal.

This ratio is shown in Figure 4.12. Median overdensities range between ≈ 70 and ≈ 200 with strong dependencies on peak height, accretion rate, and redshift. The most important consequence of these relations is that *there is not a single classical overdensity boundary which corresponds to to the splashback shell.*

4.4.7 Splashback Shell Shapes

We also investigate the shapes of splashback shells using the asphericity, $A_{\rm sp}$, and ellipticity, $E_{\rm sp}$, parameters defined in Equations 4.9 and 4.8, respectively. A plot of these two quantities is shown in Figure 4.13. The shaded blue region shows the values of these parameters for ellipsoids with different axis ratios. The fact that $A_{\rm sp}$ and $E_{\rm sp}$ for all splashback shells lie above the shaded regions means that the shells are significantly more aspherical than ellipsoids.

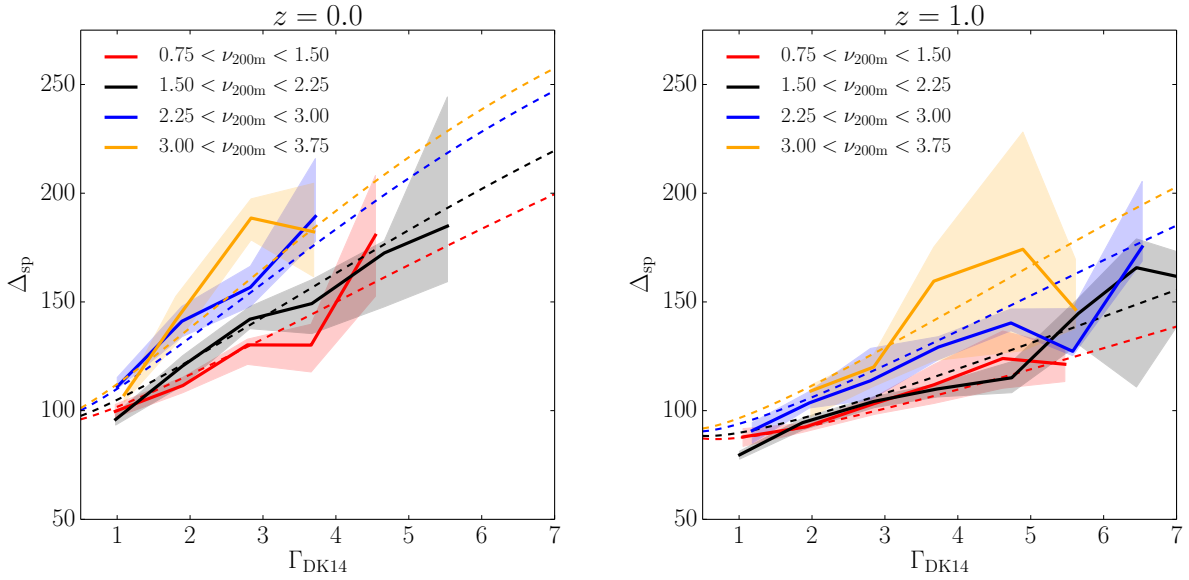

Figure 4.12: Comparison between our fits and SHELLFISH's measurements for $\Delta_{sp} \equiv 200\tilde{M}_{sp}/\tilde{R}_{200m}$ using the ratio of our mass and radius fits. The visualization scheme is identical to the one used in Figure 4.10, with the thin line corresponding to the median of the distribution given by Equations 4.13 and 4.14. There are several important caveats to this fit, which we discuss in section 4.4.5.

We perform checks for correlation between A_{sp}, E_{sp} and each of M_{200m}, Γ_{DK14}, R_{sp}, and redshift, but find no evidence of such correlations.

We also calculated the angle θ_Δ between the major axis of a halo's splashback shell and the major axis of the underlying dark matter distribution, as reported by the Rockstar halo finder [Behroozi et al., 2013a]. In Figure 4.14 we show the correlation function for the angle between these two axes, θ_Δ. We find anti-correlation at high values of θ_Δ and a high degree of correlation at low values of θ_Δ, indicating that splashback shells are preferentially aligned with major axis of the central dark matter distribution. This is consistent with earlier studies, which have shown that the axis ratios of the matter distribution near the centers of halos tend to be roughly aligned with the axis ratios near the outskirts of halos [Jing and Suto, 2002].

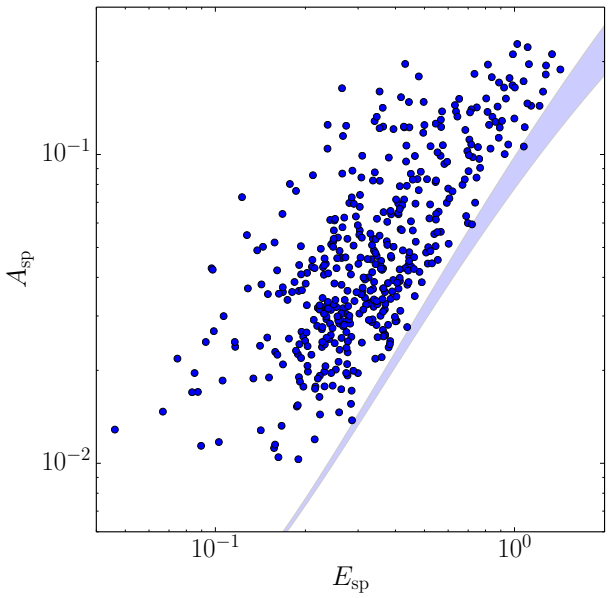

Figure 4.13: The asphericity parameter, $A_{\rm sp}$, versus the ellipticity parameter, $E_{\rm sp}$ (defined in Equations. 4.9 and Equation 4.8, respectively) for our $z = 0$ halo sample. The blue shaded region shows the range of values of these quantities for ellipsoids with different axis ratios. The fact that $A_{\rm sp}$ and $E_{\rm sp}$ of the splashback shells lie above the shaded regions means that the shells have significantly higher surface areas than ellipsoids of similar ellipticity and volume.

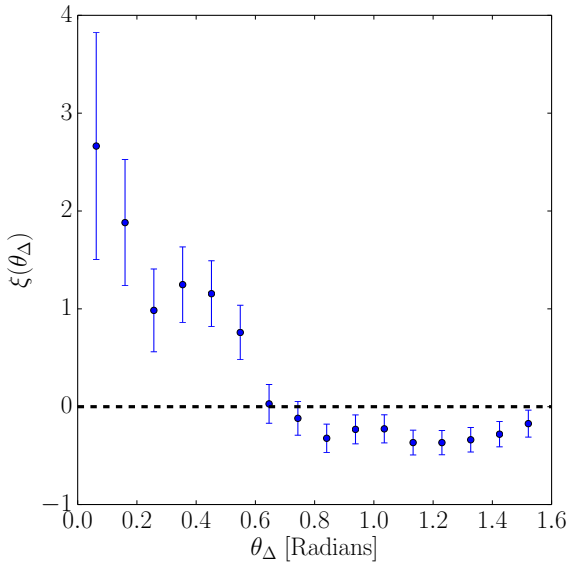

Figure 4.14: The correlation function, $\xi(\theta_\Delta)$, between the major axes of splashback shells and the major axes of total dark matter distribution. The dashed black line shows $\xi(\theta_\Delta) = 0$, and indicates the level of correlation expected for random alignment.

4.5 Summary and Conclusions

In this chapter we presented a new algorithm which identifies the splashback shells around individual halos in simulations. These shells are caused by the caustics formed by matter at the first apocenter of their orbits around the halo and correspond to rapid drops in the density field. Our algorithm relies only on the density distribution within a single simulation snapshot, and is capable of identifying shells with highly aspherical shapes.

We implemented our algorithm in the publicly available[1] code SHELLFISH and performed extensive tests on the correctness of this code. We performed convergence tests on the splashback shells found by our code and found that above a convergence limit of $N_{200\mathrm{m}} = 5 \times 10^4$, SHELLFISH can measure properties of splashback shells with $\lesssim 5\%$ systematic error (see Figure 4.3 and Figure 4.8(b)) and percent-level stochastic error (see Figure 4.16(b)). However, we identified a sub-population of halos with low mass accretion rates, $\Gamma_{\mathrm{DK14}} \lesssim 0.5$, for which the splashback shell radii estimated by SHELLFISH are biased low by $\gtrsim 10\%$. We therefore recommend that our code not be used for measurements of splashback shells for halos with $\Gamma_{\mathrm{DK14}} < 0.5$. This cutoff removes 20% of Milky Way-sized halos at $z = 0$ and has a negligible effect on all larger mass scales and all earlier redshift slices.

We presented the first measurements of several basic properties of splashback shells which are summarized below:

1. We confirmed that splashback radii generally decrease with increasing mass accretion rate, as previously found by analyses of stacked halo density profiles. However, we found that the splashback radii found by SHELLFISH are larger than these earlier estimates by 20%-30% for halos with high accretion rates, $\Gamma_{\mathrm{DK14}} \gtrsim 3$. We showed that the estimate of the splashback radius obtained from the stacked density profiles is biased low due to the existence of high-mass subhalos in many of these profiles.

2. We used a simple method, completely independent from SHELLFISH, for mitigating

1. `github.com/phil-mansfield/shellfish`

the effect of substructure on density profiles: the so-called "angular median profile" method. In this method, radial shells are split into solid angle segments with an estimate of density in each segment. The halo density at a given radius is then taken to be the median of all the segments in the corresponding shell. We showed that the effect of subhalos on these profiles is greatly reduced. Moreover, the angular median profiles are more self-similar in their outskirts and exhibit a sharper region of profile steepening (i.e., a much more distinct splashback feature). We showed that the splashback radii estimated from the stacked angular median profiles are in good agreement with the results of SHELLFISH for halos with $\Gamma_{\rm DK14} \gtrsim 0.5$.

3. We investigated the correlation between splashback radius and mass accretion rate, the scatter around it, and its evolution with redshift. We presented the first evidence that the splashback radius depends not only on accretion rate, but also has a strong dependence on the peak height, $\nu_{\rm 200m}$, with larger $\nu_{\rm 200m}$ halos having systematically smaller $R_{\rm sp}/R_{\rm 200m}$ at a fixed $\Gamma_{\rm DK14}$ and z. We found that the scatter of $R_{\rm sp}/R_{\rm 200m}$ around the median at a given accretion rate is significant, exceeding 10%. We provided an accurate fit for $R_{\rm sp}/R_{200m}$ and its scatter as a function of $\Gamma_{\rm DK14}$, $\nu_{\rm 200m}$, and $\Omega_{\rm m}$ (see Equations 4.10-4.12 and Figure 4.9). We provided a similar fit for $M_{\rm sp}/M_{\rm 200m}$ (see Equations 4.13 and 4.14 and Figure 4.10). Unlike our fit to $R_{\rm sp}$, there are several minor caveats to our $M_{\rm sp}$ fit, which we discuss in section 4.4.5.

4. We argued that a single classical overdensity density cannot be used as a model of the location of $R_{\rm sp}$ because the overdensity of splashback shells have a large dynamic range and have strong dependencies on mass, accretion rate, and redshift.

5. We studied the shapes of the splashback shells using an ellipticity parameter, $E_{\rm sp}$, and an asphericity parameter, $A_{\rm sp}$ (defined in Equations 4.8 and 4.9, respectively). We showed that splashback shells are generally highly aspherical, with non-ellipsoidal oval shapes being particularly common.

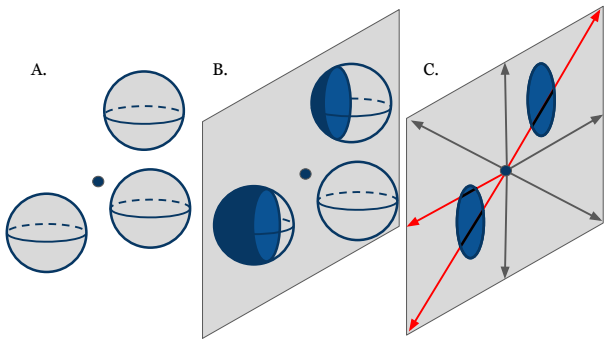

Figure 4.15: An illustration of the UpdateProfiles' algorithm described in Appendix 4.6.1. Panel A shows three, S_i, associated with three dark matter particles around the center of a halo, shown as a solid circle. Panel B shows one of the random planes, $P \in P_H$, passing through the halo center and intersections of P with each S_i. The top and left spheres intersect P while the remaining sphere does not. Panel C shows intersection checks being performed between the 2D intersection, C_i, of S_i and P along a set of lines of sight, $L_{P,i}$, in the plane. Inspection of the angular locations of the edges of the C_i shows that only the red lines of sight could intersect them, and thus these spheres contribute to density profiles only along the red lines. This last panel corresponds to the code inside the innermost conditional of the algorithm.

6. We investigated potential correlations between splashback shell properties and other halo properties, but found no significant correlations between $E_{\rm sp}$ and $A_{\rm sp}$ with either mass accretion rate, mass, splashback radius or redshift. However, we did find that the major axes of splashback shells were correlated with the major axis of mass distribution within the inner regions of halos.

This chapter is a pilot study of splashback shells of individual halos. Further applications of the algorithm presented here include investigation of alternative classifications of isolated halos and subhalos using the splashback shell instead of the virial radius, investigation of the systematic differences in halo masses and halo mass accretion histories when $M_{\rm sp}$ is compared to M_{Δ}, and a comparisons with other methods for measuring individual splashback shells.

4.6 Appendices

4.6.1 An Algorithm for Fast Line of Sight Density Estimates

In this Appendix we describe the method our algorithm uses to construct density profiles along a set of lines of sight via the evaluation of Equation 4.1. Generally, this can be broken up into two steps: first, the set of all spheres which intersect with a particular halo, H, is found, and second, for every sphere, S, which intersects with H a procedure UpdateProfiles(S, H) is run, which evaluates a term in Equation 4.1 corresponding to S for every line of sight in H.

In general, the first step is straightforward to perform efficiently. Even rudimentary spatial partitioning (such as breaking the simulation's particles into $\approx 10^2 - 10^3$ spatially coherent segments) results in this step being highly subdominant to the second, making UpdateProfiles the only performance bottleneck of this algorithm. A naive implementation of UpdateProfiles would look like the following:

procedure UpdateProfiles(S, H)
  for each L in L_H **do**
    if S intersects L **then**
      $R_{\rm enter}$, $R_{\rm exit} \leftarrow$ IntersectionRadii(L, S)
      InsertToProfile(L, $\rho_{\rm S}$, $R_{\rm enter}$, $R_{\rm exit}$)
    end if
  end for
end procedure

Here, L_H is the set of all line of sight profiles belonging to the halo H and ρ_S is the density of the sphere S. The existence of two simple functions has been assumed: IntersectionRadii(L, S) calculates the radii at which the line of sight L enters and exits the sphere S, respectively, and InsertToProfile(L, ρ, R, R') inserts a rectangular function with amplitude ρ between R and R' to the profile corresponding to the line of sight L.

Because UpdateProfiles performs an intersection check for every line of sight in L_H, the asymptotic cost of this approach is $O(|L_H|)$. Because $|L_H|$ is on the order of 10^4 for the parameter set used in this chapter, this leads to a large number of expensive intersection checks being performed for every particle, with the vast majority of these checks failing.

We take an alternative approach that allows us to avoid performing explicit calculations on any line of sight which does not intersect S. We require that lines of sight exist within a set of planes, P_H, that $|P_H| \ll |L_H|$, and that lines of sight are oriented in uniformly-spaced "rings" within their respective planes. This strong geometric restriction allows for two optimizations: first, intersection checks are performed on entire planes before any calculations are done on individual lines of sight, and second, we calculate the angle subtended by S in intersected planes, which allows us to find the exact set of lines of sight intersected by S in the plane. Concretely, our approach is:

procedure UpdateProfiles$'(S,\ H)$
  for each P in P_H **do**
    if S intersects P **then**
      $C \leftarrow$ SliceSphere$(S,\ P)$
      $\theta_{\text{low}},\ \theta_{\text{high}} \leftarrow$ AngularRange$(P,\ C,\ H)$
      $i_{\text{low}},\ i'_{\text{low}} \leftarrow$ ProfileIndices(θ_{low})
      $i_{\text{high}},\ i'_{\text{high}} \leftarrow$ ProfileIndices(θ_{high})
      for each i in $[i_{\text{low}},\ i'_{\text{high}}]$ **do**
        $R_{\text{enter}},\ R_{\text{exit}} \leftarrow$ IntersectionRadii$(L_{P,i},\ S)$
        InsertToProfile$(L_{P,i},\ \rho_{\text{S}},\ R_{\text{enter}},\ R_{\text{exit}})$
      end for
    end if
  end for
end procedure

Here, P_H is the set of all planes of profiles belonging to the halo H and $L_{P,i}$ is the i^{th}

profile within the profile ring corresponding to the plane P. Here, the existence of several simple functions has been assumed: SliceSphere(S, P) returns the circle created by slicing the sphere S by the plane P; AngularRange(P, C, H) returns two angles specifying the angular wedge within the plane P which the circle C subtends relative to the center of the halo H; and ProfileIndices(θ) returns the indices of the two nearest profiles to the angle θ, with the profile corresponding to the lower angle being returned first. For ease of reading, the pseudocode which would handle the periodicity of angles at $\theta = 0 \equiv 2\pi$ has been omitted.

This method is illustrated in Figure 4.15. Panel A shows a collection of spheres collected around a halo center, panel B shows the results of calling SliceSphere on each of these spheres for a particular plane, and panel C shows the profiles (in red) which would recieve intersection checks within the innermost loop of UpdateProfiles$'$.

The asymptotic cost of UpdateProfiles$'$ is $O(|P_H| + I_{H,S})$, where $I_{H,S}$ is the number of profiles in the halo H which intersect the sphere S. Since both $|P_H|$ and $I_{H,S}$ are multiple orders of magnitude smaller than $|L_H|$, this results in a significant increase in performance. In practice we find that the plane intersection checks are subdominant to the cost of the innermost loop.

The method described above is further optimized in several ways:

- If InsertToProfile is implemented naively - by representing profiles as arrays containing $\rho(r)$ and updating every element of the profile which is within the inserted rectangular function - it is the dominant cost of UpdateProfiles$'$. To prevent this, we represent our profiles as arrays containing $d\rho(r)/dr$. Since the derivative of a rectangular function is two delta functions, updating the derivative profile only requires updating array elements close to the edges of the rectangular function (note that in the discrete case this requires four element updates: two for each edge). Once UpdateProfiles$'$ has been called on every target sphere, each derivative profile is integrated to obtain $\rho(r)$.

- Instead of explicitly performing the 3D IntersectionRadii($L_{P,i}$, S), a faster 2D

analog is used to find the intersection radii of the projection of $L_{P,i}$ onto P with the circle C.

- A successful intersection check between P and S is performed in a way which immediately results in the value that would be returned by SLICESPHERE(S, P), as these two calculations share many geometric operations.

This algorithm is straightforward to generalize to non-constant density spheres and to density estimates constructed from other geometric solids (most notably tetrahedra), although the publicly released version of SHELLFISH does not allow access to either feature.

4.6.2 Splashback Candidate Filtering Algorithm

The Appendix will outline the filtering algorithm which we qualitatively introduced in section 4.2.2

The first step of constructing the filtering loop is dividing the point distribution into $2^{N_{\rm rec}}$ uniformly spaced angular wedges, for some user-defined $N_{\rm rec}$. We calculate an *anchor point* for each wedge, which is an estimate of the average location of the splashback shell within that wedge.

The location of the anchor point within the $i^{\rm th}$ wedge is given by

$$R_{{\rm anchor},i},\ \theta_{{\rm anchor},i} = \textsc{AnchorRadius}(0,\ i),\ 2\pi\frac{i+0.5}{2^{N_{\rm rec}}}. \tag{4.15}$$

Here, i is zero-indexed and ANCHORRADIUS is the following recursive algorithm:

function ANCHORRADIUS(k, i)

$\theta_{\rm low} \leftarrow 2\pi\lfloor i/2^k \rfloor 2^{k-N_{\rm rec}}$

$\theta_{\rm high} \leftarrow 2\pi(\lfloor i/2^k \rfloor + 1)2^{k-N_{\rm rec}}$

$f \leftarrow$ WEDGEKDE($\theta_{\rm low}$, $\theta_{\rm high}$)

if $k = N_{\rm rec}$ **then**

return GLOBALMAXIMUM(f)

else

$R_{\text{anchor}} \leftarrow \textsc{AnchorRadius}(k+1,\, i)$

maxes $\leftarrow \textsc{LocalMaxima}(f)$

$R'_{\text{anchor}} \leftarrow \min_R\{|R_{\text{anchor}} - R| \;\forall\; R \in \text{maxes}\}$

if $|R_{\text{anchor}} - R'_{\text{anchor}}| \;<\; R_{\text{refine}}$ **then**

return R'_{anchor}

else

return R_{anchor}

end if

end if

end function

We assume the existence of three simple functions: $\textsc{GlobalMaximum}(f)$, which returns the global maximum of the function f; $\textsc{LocalMaxima}(f)$, which returns all the local maxima of the function f; and $\textsc{WedgeKDE}(\theta_{\text{low}},\, \theta_{\text{high}})$, which returns a kernel density estimate (KDE) corresponding to the points contained within the wedge with boundaries θ_{low} and θ_{high}. A KDE is a method for converting a set of discrete points into a continuous density estimate by applying a smoothing kernel to every point. It performs much the same role as a histogram, except that an explicit choice of bin edges is replaced by an explicit choice of the smoothing kernel. For our purposes, the most useful property of a KDE is that it provides a simple way to estimate the point of maximum density. We define our KDE as the function

$$\text{KDE}(r) = \sum_j \exp\left(-\frac{(r - r_j)^2}{2R^2_{\text{KDE}}}\right) \tag{4.16}$$

where R_{KDE} is a user-defined smoothing scale, and r_j is a set of points.

The intuition behind this approach is that most candidate points in the plane correspond to lines of sight crossing the splashback shell, so the maximum of the $k = N_{\text{rec}}$ KDE is a good 0^{th} order estimate of of its location. Smaller wedges give more refined estimates.

But if their estimate deviates too far from the coarser estimates, it's likely that the region corresponds to a filament or a subhalo.

Once anchor points have been found for each wedge, we fit a cubic interpolating spline to them in the θ - R plane. This spline is the aforementioned filtering loop. To remove boundary effects, the range of the anchor points is extended to $[-2\pi,\ 4\pi)$ prior to fitting, but the spline is only ever evaluated in the $[0\ 2\pi)$ range. We then remove all points which are further than some distance, $R_{\rm filter}$ from this spline.

This procedure introduces three new free parameters, $R_{\rm KDE}$, $R_{\rm refine}$, and $R_{\rm filter}$. Tests indicate that the final shells are robust to changes in $R_{\rm KDE}$ and $R_{\rm filter}$, as long as they are of the same order of magnitude as $R_{\rm refine}$. For this reason we simplify parameters by requiring

$$R_{\rm KDE} = R_{\rm refine} = R_{\rm filter} = R_{\rm max}/\eta. \tag{4.17}$$

Here η is a tunable parameter which dictates how strict the filtering process is. Higher values of η are stricter than lower values of η.

4.6.3 Parameter-Specific Convergence Tests

Most of the fiducial values of parameters of our algorithm listed in Table 4.2.4 were set using one of the following three approaches, which start with constructing a representative sample of halos and identifying their splashback shells and estimating their properties for a range of values p_i for the selected parameter p.

A: Many parameters are known to be optimized when taken to either the low value or high value limit, but also decrease the performance of the algorithm as the parameter approaches this limit. In addition to the shells for the p_i values, we also fit a shell with p set to some very large value, $p_{\rm limit}$. For each halo we calculate a curve representing the fractional difference between the shells calculated with p_i and with $p_{\rm limit}$ for each of the properties defined in Equations 4.5 - 4.9. We then set the parameter to the

lowest p_i which leads to an average fractional error of $\lesssim 1\%$.

B: Some parameters are not optimized in either the low or high value limit. For each halo we construct curves for each of the properties defined in Equations 4.5 - 4.9. We manually inspect these curves: if they generally show an unchanging "plateau" for these properties over a wide range of p_i values, we set the parameter to an arbitrary p_i in the center of the plateau. The existence of a plateau over a wide range of p_i indicates that the shell shapes depend only weakly on this parameter.

C: For parameters where method B was attempted but a no wide plateau was found, we incorporate qualitative assessment of the shells into the selection procedure. For a pair of parameter values, p_i and p_j, we visually inspect every halo in the test set, compare the shells produced by both values to the underlying density field, and select one of the two as a qualitatively better fit. Once this has been completed for every halo, we label the parameter value with more successful fits as the better value. This allows us to construct an fitness ordering on all the values of p_i. We then select the maximally fit parameter. In principle, this methodology could lead to researcher-dependent results, but for the three parameters where we used this method, the optimal value was not ambiguous.

The specific methods we used to set each algorithm parameter are listed in Table 4.2.4. In all cases the halo sample is divided into $M_{200\mathrm{m}}$-selected and Γ_{DK14}-selected subsets to test for parameter dependence on halo properties. In all cases, we found no such dependence. Parameters which involved additional testing methodology are described below:

4.6.4 Setting R_{kernel}

In order for our algorithm to identify the splashback shell reliably, we need to sample the density distribution around the shell well. However, typical densities in this region are $(0.1-10)\times\rho_{\mathrm{m}}$ (see Figure 4.1(b)) and there are often relatively few particles. To compensate for

this, we need to make the radius of the spheres associated with particles, $R_{\rm kernel}$ sufficiently large.

To find the optimal value of $R_{\rm kernel}$, we use an approach similar to the approach A above. We generate a representative sample of halos and fit Penna-Dines shells to each halo in the sample for different values of $R_{\rm kernel}$. We then find the smallest converged value of $R_{\rm kernel}$ for each halo. An example of this comparison is shown in Figure 4.16(a). This figure also illustrates the second test described in section 4.3: in ¿99% of cases, $R_{\rm sp}$ falls within the visual fall-off region of the halo.

We find that for halos with $N_{\rm 200m} \geq 10^6$, properties of the splashback shells converge for $R_{\rm kernel} \gtrsim 0.1 R_{\rm 200m}$ and for halos with $N_{\rm 200m} \approx 5 \times 10^4$ for $R_{\rm kernel} \gtrsim 0.2 R_{\rm 200m}$. For simplicity, we set $R_{\rm kernel}$ to $0.2 R_{\rm 200m}$ for all halos.

4.6.5 Setting $N_{\rm planes}$

The parameter which has the largest effect on the stochastic error, as opposed to systematic error, in estimating shell shape is $N_{\rm planes}$. To determine a value for this parameter, we follow a procedure similar to method A. We identify the splashback shells for a representative sample of halos for five values of $N_{\rm planes}$, using randomly oriented normal vectors for each plane so that no lines of sight are shared between two different realizations. We then calculate the fractional standard deviation between shell properties determined for different random realizations of a given number of planes $N_{\rm planes}$, $\sqrt{\langle Q^2 \rangle - \langle Q \rangle^2} / \langle Q \rangle$ for each quantity Q defined in Equations 4.5 - 4.9. This standard deviation is plotted as a function of $N_{\rm planes}$ in Figure 4.16(b). For $N_{\rm planes} = 100$, SHELLFISH achieves sub-percent level per-halo scatter in $R_{\rm sp}$, $M_{\rm sp}$, and $1 + A_{\rm sp}$ and less than 2% scatter in $1 + E_{\rm sp}$. We do not find any evidence that the amplitudes of the curves shown in Figure 4.16(b) depend on halo mass or accretion rate.

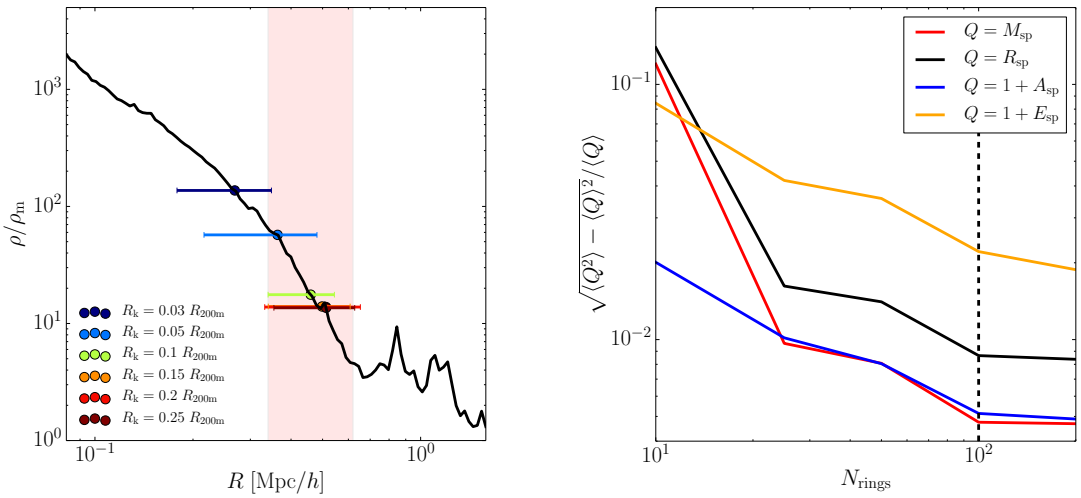

(a) (b)

Figure 4.16: *Left*: Convergence test of $R_{\rm sp}$ as a function of kernel radius for a representative halo. The black curve is the density profile of the halo obtained through conventional particle binning, the points are the $R_{\rm sp}$ values measured from density fields generated with different kernel radii, the horizontal lines show the range spanned by the minimum and maximum radii of these shells, and the shaded red region corresponds to the radial range which was visually identified as corresponding to the splashback range. This region was found by eye without knowledge of the measurements made by SHELLFISH in accordance with the procedure outlined in section 4.3. For this halo, $R_{\rm sp}$ is converged for kernel radii above $0.15R_{\rm k}$. *Right*:The mean fractional stochastic error in shell parameters (defined in Equations 4.5 - 4.9) as a function of $N_{\rm planes}$. The vertical dashed line corresponds to $N_{\rm planes} = 100$, the value given in Table 4.2.4.

4.6.6 Computing Moment of Inertia-Equivalent Ellipsoidal Shell Axes

It is non-trivial to analytically compute axis ratios from the moments of inertia for a constant-density ellipsoidal shell. Assuming that the shell is sampled by some collection of particles with weights m_k, the moments can be obtained by calculating the eigenvalues of the mass-distribution tensor,

$$M_{i,j} = \sum_k m_k (\vec{r}_k)_i (\vec{r}_k)_j. \tag{4.18}$$

The eigenvalues of the mass-distribution tensor are straightforward to calculate for a homoeoid: the volume enclosed by two ellipsoids with the same axes ratios and with aligned major axes a and a'. In the limit where $a' \to a$, the eigenvalues are given by

$$M_i = M_{\rm tot} \frac{a_i^2}{3}, \tag{4.19}$$

where M_i and a_i are the moment and ellipsoid axis aligned with the i$^{\rm th}$ Cartesian axis and $M_{\rm tot} = \sum_k m_k$. Note that this notation for ellipsoid axes is different that the convention used in Equation 4.7. Although an infinitely thin homoeoid is often equated with a uniform-density ellipsoid surface in the literature [see, for example Zemp et al., 2011], it actually corresponds to an ellipsoid surface with a non-uniform density. This non-uniformity means that major (minor) axes derived from Equation 4.19 are too small (large). This bias increases with increasing ellipticity: for ellipsoidal shells with axes ratio of $\approx 2:1$, this can bias measured axes ratios by tens of per cent.

A more accurate approximation would be to model a uniform density ellipsoidal shell by the volume enclosed by two ellipsoids with axes a, b, c and $a+\delta$, $b+\delta$, $c+\delta$ and to take $\delta \to 0$. This shape gives eigenvalues of

$$M_i = M_{\rm tot} \frac{a_i^2}{5} \left(\frac{a_i a_j + 3 a_j a_k + a_k a_i}{a_i a_j + a_j a_k + a_k a_i} \right), \tag{4.20}$$

which can then be numerically solved to obtain ellipsoid axes. Although for ellipsoids with

large axes ratios Equation 4.20 is a closer approximation than Equation 4.19, it still introduces errors close to our $N_{\rm ring} = 100$ stochastic noise limit. Thus for large axes-ratio ellipsoids we compute the mapping empirically.

We define the quantities $A_i \equiv \sqrt{M_i/M_{\rm tot}}$ and $R \equiv (M_i M_j M_k / M_{\rm tot}^3)^{1/6}$. Note that both A_i and R can be measured directly from the input point distribution. First, we generate a grid of ellipsoids in a_0/a_1 - a_0/a_2 space. Next we numerically compute A_0/A_1, A_0/A_2, and $a_0/R_{\rm V}$ for each ellipsoid. The resultant A_0/A_1 and A_0/A_2 values form a sheared grid, so we Delaunay triangulate [Delaunay, 1934] the A_0/A_1 - A_0/A_2 plane and perform linear interpolation on the resulting triangles. We construct three such interpolators which map from (A_0/A_1, A_0/A_2) pairs to a_0/a_1, a_0/a_2, and a_0/R, respectively. These interpolators can then be used to find a_0, a_1, and a_2 using only the eigenvalues of the mass-distribution tensor.

CHAPTER 5

HOW BIASED ARE COSMOLOGICAL SIMULATIONS?

This chapter is a modified version of my paper, Masfield & Avestruz [in prep].

5.1 Introduction

Understanding the non-linear predictions of the Λ Cold Dark Matter (ΛCDM) model requires the use of simulations. Simulations are required to understand the behavior of almost every system smaller than the Lagrangian footprint of a large dark matter halo, whether it be the structure of dark matter halos [e.g. de Blok, 2010], the abundances of galaxies [e.g. Klypin et al., 2015a] and satellites [e.g. Moore et al., 1999], or the properties of local dark matter streams [e.g. Vogelsberger et al., 2009].

The most common class of ΛCDM simulation is the N-body simulation that has been used to model both individual collapsed structures [see review in Griffen et al., 2016] and large cosmological volumes (see review in section 3.1). While the predictions of ΛCDM include the behavior of baryons, many simulators and analysts focus on "dark matter only" (DMO) simulations. Beyond the relative computational efficiency of DMO simulations, the fundamental reason for the popularity of DMO simulations lies in their parametrization. Baryonic simulations have a wide range of parameters, many of which have true physical meaning [e.g. table 2 in Hopkins et al., 2018]. On the other hand, once a cosmology is specified, a DMO simulation has much smaller set of parameters and all these parameters are purely numerical. This leads to the core fact that underpins all tests of DMO simulations: *any dependence on parametrization is evidence for numerical bias or error.*

In principle, the results of DMO simulations may depend on numerical parameters that determine initial condition generation, the starting redshift, box size, and "zoom-in" strategy. Simulations that follow conventional "best practices" usually avoid these effects at small scales [e.g. Power and Knebe, 2006, Crocce et al., 2006, Knebe et al., 2009, Hahn and Abel,

2011]. Beyond this, every N-body code has its own idiosyncratic parametrization, such as the node opening criteria for a force tree [e.g. Springel et al., 2001b], Adaptive Refinement Tree (ART) refinement criteria [e.g. Kravtsov et al., 1997], and light-bulb wattage [Holmberg, 1941]. These parametrizations are important, but generally ironed out during the early development and usage of a particular code.

Instead, our study – similar to most other DMO convergence studies – focuses on the three most important parameters of DMO simulations: particle mass, m_p (or interparticle spacing, $l = L/N$), timestepping, and the distribution of mass around each particle ("force softening"). Statements about the correctness and biases associated with these three parameters come from a combination of four classes of analyzes:

- **A priori models of numerical effects** [e.g. van Kampen, 2000, Dehnen, 2001, Power et al., 2003, Ludlow et al., 2019] In these studies, simulators create a model of how the numerical components of a simulation behave, often validating the predictions of this model with appropriate test simulations, and use that model to infer the correctness of other simulations.

- **Simulations of idealized systems** [e.g. Klypin et al., 2015b, van den Bosch and Ogiya, 2018, Joyce et al., 2020] In these studies, simulators either have a priori knowledge of the exact solution the simulation is expected to produce (such as the simulations of NFW halos in van den Bosch and Ogiya, 2018), or a priori knowledge of some invariant property of the system (such as the self-similar power spectra analyzed in Joyce et al., 2020). Measured deviations from a priori expectations are unambiguous numerical biases.

- **Resimulations of realistic systems** [e.g. Power et al., 2003, Navarro et al., 2010, Ludlow et al., 2019] In these studies, simulators resimulate a ΛCDM system with a variety of numerical parameters. Systems are typically either a single halo [e.g. Power et al., 2003, Navarro et al., 2010], or a small cosmological box [Ludlow et al., 2019].

Since there is no a priori expectation for these simulations, simulators will identify a region of numerical parameter space where results are locally independent of numerical parameters and measure deviations relative to this "converged" region.

- **Comparison of independent simulations** [e.g. Klypin et al., 2015b, Villarreal et al., 2017b, Child et al., 2018, Fig. 5.3] In these studies, simulators compare independently run simulations which inhomogogenously sample numerical parameter space, with the goal of identifying converged parameter ranges. While this type of test is particularly vulnerable to "false" convergence, it is substantially less labour-intensive than the previous classes of studies, and is often the only test available for assessing the correctness of expensive simulations which were not performed as part of a multi-resolution suite.

A simulator interested in assessing the biases of large cosmological DMO simulations – the class of simulations targeted by this chapter – must rely on tests of all four types of studies. Although the last class of tests mentioned above will always be a necessary component of such assessments, simply comparing the results of cosmological simulations cannot establish that the "converged" solutions which these tests identify are correct. Such an inference must come from detailed comparison with the other classes of tests.

Despite the vast literature on convergence testing in cosmological DMO simulations, there are still unknowns, disparities, and limitations to the tests performed. Tests of the first three types mentioned above focus almost exclusively on radial density profiles at fixed radii. However, dark matter halos are complex objects with a myriad of scientifically useful properties. To the best of our knowledge, there are *no* published reliability requirements for many commonly used halo properties, such as the offset between a halo"s center of mass and its most bound particle, $X_{\rm off}$. Even for the most well-tested halo properties, there is no clear consensus on what is required for reliability; examples including the peak of the rotation curve, $V_{\rm max}$, or the radius at which the logarithmic slope of the denisty profile is -2, r_{-2}. We surveyed twelve studies on the concentration mass-relation, all of which measure some form of r_{-2}. From this survey, we found that the minimum particle counts ($N_{\rm vir}$) which different

studies analyzed ranged from from 500 to 10,000 particles, with the 1σ scatter spanning more than a decade [Neto et al., 2007, Duffy et al., 2008, Gao et al., 2008, Zhao et al., 2009, Prada et al., 2012, Bhattacharya et al., 2013, Ludlow et al., 2013, Dutton and Macciò, 2014, Diemer and Kravtsov, 2015, Klypin et al., 2016, Poveda-Ruiz et al., 2016, Child et al., 2018]. Lastly, tests focused solely on how many particles halos are resolved with dominate much of the literature, despite demonstrations that force softening and timestepping have large effects on halo properties (see sections 5.5 and 5.6.1).

In this work, we aim to complete several components of the analysis needed to rectify these issues, incorporating components of all four classes of tests discussed above. We perform convergence tests using a large inhomogenous suite of publicly available cosmological simulations. These tests are performed over a wide range of halo properties, including halo properties which are traditionally overlooked by the testing literature. We also analyze the impact of timestepping and force softening parameters to extend beyond the standard particle count parameter. We organise the chapter as follows. In section 5.2 we outline our methods for comparing cosmological simulations and extracting empirical convergence limits. In section 5.3 we report these empirical limits and consider the variation in limits between simulations. In section 5.4, we study the dependence of various halo properties on the force softening scale. In section 5.5, we outline a model for estimating the impact of large force softening scales on halo profiles and apply this model to our simulation suites. Lastly, in section 5.6 we discuss our results (particularly the impact of timestepping), and in section 5.7 we summarise and conclude our analysis.

5.2 Methods

5.2.1 Simulations and Halo Finding

This chapter uses all the simulations listed in Table 3.1.

We use catalogs constructed by the ROCKSTAR halo finder [Behroozi et al., 2013d]. When

available, we also used merger trees constructed by CONSISTENT-TREES [Behroozi et al., 2013e] to determine growth history-dependent halo properties. The ν^2-gc and IllustrisTNG-Dark simulation suites do not currently have merger trees available.

The simulations we consider use a number of different versions of the ROCKSTAR halo finding software. ROCKSTAR has undergone a number of bug fixes since its original release, and halo catalogs generated with different versions can have significantly different property distributions. To understand the impact of different software versions, we obtained the approximate ROCKSTAR download times and configuration files for every suite considered in this chapter to identify the corresponding software version (Diemer; Klypin; Becker; Ishiyama; Behroozi, personal communication).

We then isolated the source of version-dependent results. First, we regenerated halo catalogs for the CBol_L125 simulation using the different versions – matching the exact commit hash if known – as well as the relevant parameters in each respective configuration file, and we cross-matched these catalogs against one another. Second, we performed an extensive review of the ROCKSTAR and consistent-trees version control commit histories[1]. By combining these two analyzes, we determined that there were two sets of variables which gave version-dependent results and that all other variables were consistent between versions. These variables are (1) the axis ratios calculated within R_{500c} and (2) properties that depend on internal energy calculations. The ROCKSTAR changelogs document both of these issues, meaning that, fortunately, our cross-matching of catalogs did not reveal any new significant inconsistencies.

Incorrect axis ratio measurements affect Erebos_CBol and Erebos_CPla, which used ROCKSTAR catalogs generated with code downloaded prior to October 22$^{\text{nd}}$, 2013. There is no method for correcting this issue, but as discussed below the convergence properties of these inner axis ratios are largely similar to the conventional larger axis ratios. We therefore

1. available at `https://bitbucket.org/gfcstanford/rockstar` and `https://bitbucket.org/pbehroozi/consistent-trees`

do not analyze this property. ROCKSTAR catalogs generated with code downloaded prior to May 15$^{\text{th}}$, 2014 have internal energies which are too large by a factor of two. This can be corrected by replacing variables, X, with updated versions, X'. In the cases of virial ratio and Peebles spin parameter, the replacement variables would appear as,

$$T/|U|' = 2\,T/|U| \tag{5.1}$$

$$\lambda'_{\text{Peebles}} = \lambda_{\text{Peebles}} \frac{\sqrt{1 - T/|U|'}}{\sqrt{2 - T/|U|'}} \tag{5.2}$$

We apply the corrections of Eq. 5.1 to catalogs for the Erebos_CBol, Erebos_CPla, Bolshoi, and BolshoiP suites. We also applied these corrections to Chinchilla_L250 and Chinchilla_L400, but Chinchilla_L125 did not require these corrections.

Another potential source of variation amongst ROCKSTAR catalogs is the choice of primary mass definition, which changes the values of other reported halo properties (see section 4 and appendix A of Mansfield and Kravtsov [2019] for a full discussion). However, we confirmed that all of the halo catalogs that we consider in our analyzes used M_{vir} as the primary mass definition. This particular source of variation does not impact our results.

We also generate ROCKSTAR catalogs for the $z = 0$ snapshots of the IllustrisTNG-Dark simulations listed in Table 3.1, made available through the IllustrisTNG public data release [Nelson et al., 2019]. We used the ROCKSTAR version corresponding to the git hash 99d56672092e88dbed446f87f6eed87c48ff0e77, downloaded on June 10$^{\text{th}}$ 2019. We use M_{vir} as our primary mass definition, consistent with other catalogs. As with the other catalogs in this chapter, we do not use strict spherical overdensity masses and removed "unbound" particles prior to analysis. We use a coarse-grained friends-of-friends linking length of $b = 0.28\,l$ for load-balancing. Note that this last setting leads to inaccurate $M_{200\text{m}}$ masses [section 4.3 and appendix A of Mansfield and Kravtsov, 2019], but we choose this setting for consistency with the other catalogs used in this study. Some analysis in this chapter also uses ROCKSTAR catalogs generated for the baryonic IllustisTNG simulations. In these cases, we use the same

ROCKSTAR parameters as we do with IllustrisTNG-Dark, but only consider dark matter particles when computing halo properties.

5.2.2 Halo Properties

The halo properties considered in this chapter are defined and discussed in section 3.2.

There are a number of quantities in ROCKSTAR and consistent-trees catalogs which we do not explicitly study in this chapter. In most cases this is because the convergence behavior of these properties is identical to that of another property: we find that the convergence limits for $\Gamma(t_{\rm dyn})$ are essentially the same as accretion rates defined over any other time scale tracked by any version of consistent-trees. We therefore only consider $\Gamma(t_{\rm dyn})$. Similarly, we find that the convergence properties of b/a, $(c/a)(< R_{\rm 500c})$, and $(b/a)(< R_{\rm 500c})$ are nearly identical to those of c/a and thus only consider c/a. Later versions of ROCKSTAR track the maximum single-halo tidal force on each halo, but we do not track convergence behavior for tidal force calculations. This is because too few of our catalogs contain this property to achieve meaningful statistics. We additionally note that computing the tidal force on halos has subtleties that indicate that the approximation used by ROCKSTAR may not be sufficiently physical (see section 2 of van den Bosch et al., 2018 and section 2.5 and appendix C of Mansfield and Kravtsov, 2019).

5.2.3 Finding Empirical "Convergence Limits"

In this section, we describe our procedure to establish particle count-based convergence limits for each halo property. We identify these limits for target accuracy levels. Finally, we note that this procedure does not rule out the possibility of false convergence.

To identify the corresponding convergence limits for a halo property, X, we:

1. group simulations by approximate cosmology and by subhalo status. We analyze each subgroup separately.

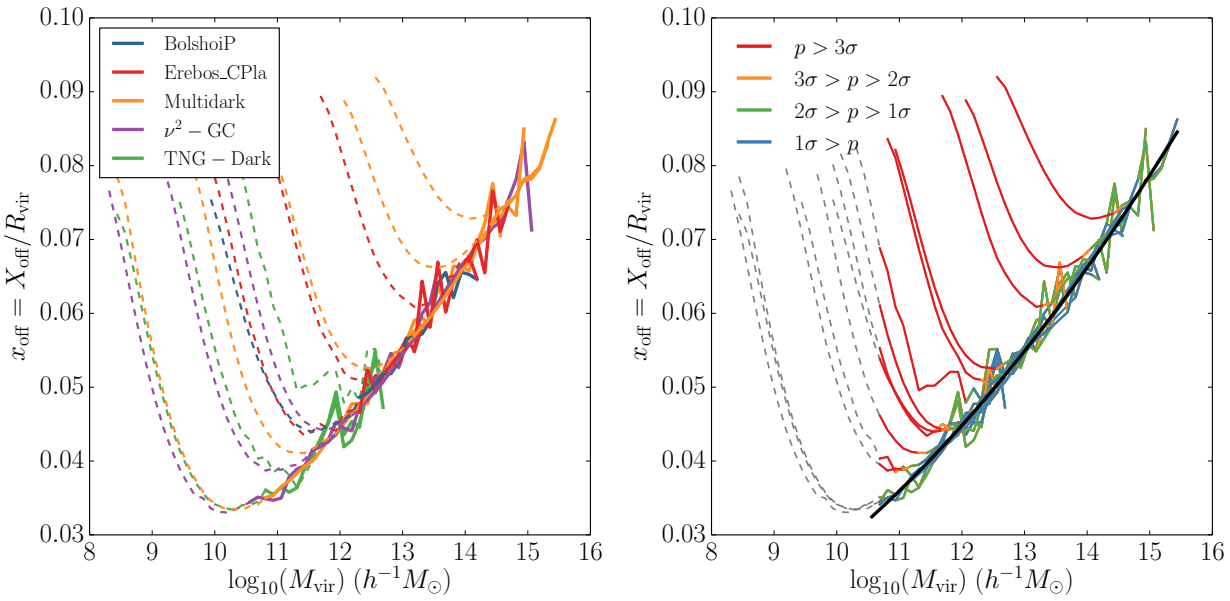

Figure 5.1: Illustration of the procedure used to determine the particle counts at which simulations diverge from the global, high-resolution mass trend. This is illustrated with $x_{\rm off}$. We collect all simulations with measured $x_{\rm off}$ values and visually identify a conservative $N_{\rm vir}$ cutoff such that all simulations fall along a single mass relation. This is shown for Planck-cosmology simulations in the left panel, with masses above this cutoff shown as solid curves and masses below this cutoff shown as dashed lines. Simulations are colored by the suite which they belong to (Table 3.1). We then fit a low-order polynomial to Planck- and WMAP-cosmology simulations separately, as shown by the black line in the right panel. After this, we estimate the significance of deviations from the fit using Eq. 5.3. We consider mass ranges which deviate from the fit by more than 2% with more than 2σ significance to be non-converged. This is shown in the right panel, where curves are colored by the significance of the deviation. This procedure is described with greater detail in section 5.2.3.

2. visually identify a conservative high-particle count cutoff above which all $M_{\rm vir} - X$ relations agree.

3. fit a polynomial-centered distribution to all high-resolution $M_{\rm vir} - X$ relations.

4. identify the highest particle count at which each simulation has a statistically significant deviation from the fitted distribution which is larger than a target accuracy level. This particle count, $N_{\rm cut}$ is the "convergence limit" for that simulation.

All the steps in this procedure are described in greater depth below and are illustrated in Fig. 5.1. Some aspects of this procedure are altered for properties which particularly poor convergence behavior. All such properties are described in depth in section 5.3.

Separation into Subgroups

Because many halo properties depend on cosmology (especially properties which depend on accretion histories), we separate simulations by cosmology to avoid misinterpreting these cosmological dependencies as non-convergence. We analyze the WMAP suites Bolshoi, Chinchilla, and Erebos_CBol as a group and the Planck suites ν^2-GC, BolshoiP, Multidark, and Erebos_CPla as a group. The exact parameters used still vary from suite-to-suite, mostly due to the year of each mission which these simulations attempt to match. This is most apparent when comparing the Chinchilla suite to other WMAP simulations like Bolshoi or Erebos_CBol (see Table 3.1).

We tested the impact of these small cosmology differences by repeating our analysis with groups based on the exact cosmological parameters and did not find a meaningful difference in our results. Because this split significantly reduces the number of simulations which have higher-resolution boxes available for comparison, we do not use this approach in the rest of this chapter.

We also separate halos by subhalo and isolated halo status (see section 5.2.2). This is important both because subhalos and isolated halos may have difference convergence

properties and because numerical parametrization can lead to changes in the artificial subhalo disruption rate [e.g. van den Bosch et al., 2018, van den Bosch and Ogiya, 2018, see also section 5.4.1]. Artificial disruption would lead to isolated halos being over-represented at a constant mass, and in cases where host halos and subhalos follow different mass relations this would propagate to a change in the global mass relation.

Using $R_{\rm vir}$ to define subhalo status (as we do here) is suboptimal. There is a large population of "splashback subhalos" which are qualitatively indistinguishable from other subhalos but whose orbits have apocenters outside the arbitrarily-defined virialy radius [Balogh et al., 2000, Mamon et al., 2004, Gill et al., 2005, Ludlow et al., 2009, Bahé et al., 2013, Wetzel et al., 2014, Xie and Gao, 2015]. Mansfield and Kravtsov [2019] showed that this population of misidentified subhalos is responsible for the entire high-concentration tail of the "isolated" halo population, thus opening the possibility that numerical subhalo disruption could affect our convergence limits. Although many schemes for identifying splashback subhalos exist [see Mansfield and Kravtsov, 2019, for review], we do not use them here: they rely on merger tree information and/or raw particles data, which are not available for all the simulations considered here, and these methods have not trivial convergence properties themselves [Mansfield et al., 2017] which would be a larger complicating issue than subhalo contamination.

Defining High-Resolution Particle Ranges

For each simulation, we measure the mean value of each property, X, as a function of $M_{\rm vir}$ within logarithmic 0.125 dex mass bins. We restrict analysis to mass bins containing at least 100 halos.

We identify non-convergence by identifying where simulations deviate from the mass-relation implied by the high-resolution regimes of other simulations. We identify a such a corresponding high-resolution cutoff, $N_{\rm HR}$, by eye such that no simulations in our sample deviate from others in their subgroup when mass relations are constructed for halos with

$N_{\rm vir} > N_{\rm HR}$.

This cutoff is chosen separately for each halo property and each analysis subgroup, although we use the same cutoffs for both Planck and WMAP cosmology. These cutoffs are shown in Appendix 5.8.2, Table 5.5. Our tests indicate that our results are not sensitive to the exact $N_{\rm HR}$ choices used.

The cutoff chosen for the $M_{\rm vir} - X_{\rm off}$ relation is shown as the transition of from solid to dashed lines in the left panel of Fig. 5.1.

As discussed in section 5.2.3 and 5.3.2, several simulations diverge significantly from other simulations at aberrant high particle counts for various halo properties. These simulations are not included in our determination of $N_{\rm HR}$ and are discussed extensively throughout section 5.3.

Fitting Mean Relations

For each halo property, X, we fit the $\log_{10}(M_{\rm vir}) - X$ relation with a Gaussian distribution with a centroid given by a mass-dependent d-degree polynomial and a 1σ dispersion given by σ_0. Since the posterior distributions for these fits are smooth and unimodal, we do this by maximising the likelihood function of this model across its parameter space. For each mass relation, we scale masses by the pivot mass $M_{\rm pivot} = 10^{12.5} h^{-1} M_\odot$ to increase numerical stability and scale X by $(M_{\rm vir}/M_{\rm pivot})^\alpha$ to decrease the polynomial degree needed to fit the relation. We show the values of d and α used for each halo property in Table 5.5. In the case of mass and velocity functions relative to the halo property X, we perform fits relative to $\log_{10}(\phi(X))$. We use a pivot value of $V_{\rm pivot} = 1$ km/s for velocity functions.

The best-fitting relation for the $M_{\rm vir} - X_{\rm off}$ relation is shown as the black curves in Fig. 5.1, and σ_0 is shown as the gray shaded contour around those curves.

For many halo properties, a subset of simulations diverge significantly from other simulations within the same suite. We manually remove these simulations prior to fitting. The number of outliers removed for each property is listed in Table 5.5. We remove all ν^2-gc

boxes, all TNG boxes, VSMDPL, HMDPL, and Chinchilla_L250 prior to fitting the $M_{\rm vir}-c/a$ relation, Chinchilla_L250 before fitting the $c_{\rm vir}$ relation, all ν^2-gc boxes, VSMDPL, SMDPL, and CHinchilla_L250 prior to fitting the $V_{\rm max}$ relation, and Chinchilla_L250 prior to fitting the $V_{\rm peak}$ relation.

Three sets of outlier removals require special comment. We found that the $M_{\rm vir} - c_{\rm vir}$ relation was well fit by a power law for each simulation suite individually, but that amplitude and power law index of these relations were noticeably different for each suite. As such, we fit each suite independently with the additional removal of Chinchilla_L250.

As is discussed in section 5.3.2, Illustris-TNG and the high resolution MDPL simulations appear to "converge" to different $M_{\rm vir} - V_{\rm max}$ relations. Because ν^2-gc-H2 and ν^2-gc-H1 give aberrant results, the only Planck-cosmology simulations in Table 3.1 which probe halo masses below $M_{\rm vir} \lesssim 10^{11}\,h^{-1}M_\odot$ fall into one of these two suites. To avoid a fit which "splits the difference" between the two, we perform two fits removing VSMDPL and SMDPL from one fit and all the TNG-Dark boxes from a second fit. We analyze both fits.

This removal of outlier simulations serves to emphasize that these fits cannot be interpreted as approximating the "correct" converged solutions for these mass relations, but as approximating the high-resolution solutions for a particular subset of simulations: we explicitly do not claim that any individual simulation considered in this chapter is converged or correct (or that the inverse is true). As such, we do not provide any of the fits produced from this part of this analysis to prevent their potential misuse.

Identifying Deviations

Traditional convergence tests are either performed by eye or by measuring the mass at which halo properties deviate from a reference relation by more than some fixed level of acceptable bias. We do not take these approaches for three reasons: first, even the mass relations of converged simulations can deviate from the high resolution relation due to Poissonian noise, cosmic variance, and uncertainties in the underlying fit. This makes percentage cuts

Property	Simulation	$N_{\mathrm{iso},0.00}$	$N_{\mathrm{sub},0.00}$	$N_{\mathrm{iso},0.01}$
x_{off}	Bolshoi	2.8×10^3	—	2.8×10^3
x_{off}	BolshoiP	4.2×10^3	1.8×10^3	4.2×10^3
x_{off}	Chinchilla_L125	—	—	—
x_{off}	Chinchilla_L250	1.4×10^4	6.0×10^3	1.4×10^4
		...		

Table 5.1: An excerpt of the measured particle count cutoffs, N_{vir}, associated with different halo properties, simulations, halo isolation classifications, and tolerance levels. $N_{\mathrm{iso},\delta}$ indicates the number of particles where fractional deviations larger than a tolerance level of δ can be reliably measured from the mean value of the given halo property for isolated halos. $N_{\mathrm{sub},\delta}$ indicates the corresponding value for subhalos. An empty value indicates that we cannot make a reliable measurement, often due to the high resolution of the simulation. The full table will be available in the online supplement to Mansfield & Avestruz [in prep] upon publication and ranges from $\delta = 0.00$ to $\delta = 0.10$.

sub-optimal. Second, visual identification is time-consuming, especially given the number of simulations, sub-groups, and halo properties considered in this chapter. Third, we noted unintentional researcher confirmation bias in our own tests of visually identified convergence limits. For these reasons, we have opted to use a different statistical test.

To do this, we measure the likelihood that that the sample of halos in each simulation is drawn from the same population as the high-resolution sample. This is performed separately for each mass bin. The field of statistics has no shortage of tests which can detect whether two samples are pulled from different populations, but we adopt the test which most closely resembles the conventional convergence testing procedure: the frequentist z-test. The z-test computes the probability that two samples, X_1 and X_2, could have the observed difference in means $\langle X_1 \rangle - \langle X_2 \rangle$ if the null hypothesis is true: that both samples are drawn from Gaussian populations with mean values that differ by exactly Δ_{12}. To do this the z-test constructs the z statistic:

$$z = \frac{\langle X_1 \rangle - \langle X_2 \rangle - \Delta_{12}}{\sqrt{\mathrm{err}(\langle X_1 \rangle)^2 + \mathrm{err}(\langle X_2 \rangle)^2}}. \tag{5.3}$$

Here, $\mathrm{err}(\langle X_1 \rangle)$ and $\mathrm{err}(\langle X_1 \rangle)$ are the 1σ uncertainties on the means of the two samples. Under the null hypothesis, z is distributed under normal distribution with mean zero and

Variable	$N_{\rm iso}$	$N_{\rm sub}$
$M_{\rm 2500c}/M_{\rm vir}$	$\star$	$\star$
$M_{\rm 500c}/M_{\rm vir}$	8.5×10^2	3.2×10^2
$M_{\rm 200c}/M_{\rm vir}$	1.3×10^2	1.4×10^2
$M_{\rm 200b}/M_{\rm vir}$	1.1×10^2	1.2×10^2
$V_{\rm max}$	$\star$	$\star$
$V_{\rm rms}$	$\star$	$\star$
$c_{\rm vir}$	$\star$	$\star$
$R_{1/2}$	3.5×10^3	4.6×10^3
c/a	$\star$	$\star$
$\lambda_{\rm Peebles}$	4.5×10^2	3.9×10^2
$\lambda_{\rm Bullock}$	1.1×10^2	4.9×10^2
$T/\lvert U\rvert$	$\star$	$\star$
$x_{\rm off}$	2.9×10^3	1.2×10^3
$V_{\rm off}$	4.8×10^3	1.7×10^3
$\Gamma(t_{\rm dyn})$	1.1×10^2	83
$a_{0.5}$	1.4×10^2	93
$a_{\rm MM}$	2.7×10^2	1.3×10^2
$M_{\rm peak}/M_{\rm vir}$	3.5×10^2	1.1×10^2
$V_{\rm peak}$	$\star$	$\star$
$\phi(M_{\rm 2500c})$	$\star$	$\star$
$\phi(M_{\rm 500c})$	1.6×10^2	$\star$
$\phi(M_{\rm 200c})$	1.6×10^2	$\star$
$\phi(M_{\rm vir})$	1.5×10^2	$\star$
$\phi(M_{\rm 200b})$	1.2×10^2	$\star$
$\phi(M_{\rm peak})$	1.4×10^2	$\star$
$\phi(V_{\rm max})$	$\star$	$\star$
$\phi(V_{\rm rms})$	$\star$	$\star$
$\phi(V_{\rm peak})$	$\star$	$\star$

Table 5.2: The particle count cutoffs at which 90% of the simulations in our sample show no measurable deviation in their mass relation, $\langle X \rangle (M_{\rm vir})$, relations with respect to fits against high-resolution halo samples. We show these cutoffs, $N_{\rm vir}$, for mean mass relations in the top block. The middle block shows the particle count cutoff, N_X, for each corresponding mass function $\phi(M_X)$. We provide cutoffs for both isolated and subhalo populations. Stars indicate limits that we cannot express with $N_{\rm vir}$ alone because of a strong dependence on ϵ. All numbers are accurate to 0.125 dex. The online supplement to Mansfield & Avestruz [in prep] will contain the corresponding cutoffs for individual simulations at varying degrees of accuracy. This will be available upon publication.

standard deviation 1. From this the probability, p, of the measurement under the null hypothesis can be calculated.

To apply the z-test to a single simulation and a single mass bin centered at the mass M, we take the amplitude and 1σ dispersion of best-fitting high resolution relation as $\langle X_1 \rangle$ and $\mathrm{err}(\langle X_1 \rangle)$, respectively, and the sample mean and the 1σ bootstrapping error of X for the simulation in that mass bin as $\langle X_2 \rangle$ and $\mathrm{err}(\langle X_2 \rangle)$, respectively. We adopt the convention that deviations with a probability of less than 5% under the null hypothesis indicate that a simulation is not converged to the high-resolution relation at that mass.

We show this test in the right panel of Fig. 5.1. Mass relations are color-coded by the value of p as a function of mass.

In some cases, the derivative of the difference between unconverged mass relations and the high resolution fit can change sign as a function of mass. This means that as a mass decreases, an unconverged simulation can briefly cross the high-resolution fit and can falsely appear to be converged for one or two mass bins. Additionally, since we adopted a 2σ significance cutoff for non-convergence, some poorly sampled very high resolution bins can appear to be unconverged. This latter effect can be seen in Fig. 5.1. To handle these edge cases, we consider only "strings" of consecutive mass bins which all falsify the null hypothesis with $p > 0.05$. We take the convergence limit of a simulation to correspond to the lower edge of the lowest mass bin which is a member of such a string containing at least three mass bins.

To confirm this procedure, we visually identified convergence limits for every simulation and halo property in each sub-group without knowledge of the bins that our statistical method selected. Visual identifications were generally within 0.125-0.25 dex of the statistical measurements with $\Delta_{12} = 0$. Qualitatively, no major results in this chapter change if these visual cutoffs are used. However, as noted above, the particle cutoffs for some halo properties showed somewhat smaller dispersions when visual cutoffs were used. Inspection of individual cases caused us to interpret this as confirmation bias.

There are some simulations which are converged across the entire mass range used to fit the high-resolution relation. This is the case for the highest resolution fits in Fig. 5.1. Rather than extrapolate our fits, the convergence limits of these simulations are left as upper limits. This is almost always the case for the highest resolution simulation in a sub-group. In rarer cases, there are simulations which are unconverged across the entire high-resolution mass range. The convergence limits for these boxes are left as lower limits.

Although all fiducial results reported in this chapter make use of the z-test as described above, we also extend it to account for the "practical significance" of deviations. Ultimately, the purpose of cosmological simulations is to facilitate a wide range of analyzes, and different types of analysis can tolerate different levels of non-convergence. To account for this, we introduce the parameter δ, which represents a minimum acceptable deviation as a percentage of the high resolution relation. We then add three additional conditions for a mass bin to be considered unconverged:

1. $|\langle X_1\rangle - \langle X_2\rangle| > \delta\langle X_1\rangle$,
2. $p_z(\Delta_{12} = \delta\langle X_1\rangle) < 0.05$,
3. $p_z(\Delta_{12} = -\delta\langle X_1\rangle) < 0.05$.

Here, $p_z(\Delta_{12})$ is the probability that the two samples have means that differ by as much as observed under the null hypothesis that they are drawn from populations which means that differ by Δ_{12}.

5.3 The Empirical $N_{\rm vir}$ Convergence Limits of Simulations

5.3.1 Typical Convergence Limits

We use the procedure described in section 5.2.3 to find the particle count, $N_{\rm vir}$, at which each simulation in Table 3.1 deviates from high resolution fits for a given mass relation, $\langle X\rangle(M_{\rm vir})$, of a halo property X. Table 5.2.3 shows example particle count cutoffs for $X = x_{\rm off}$, with

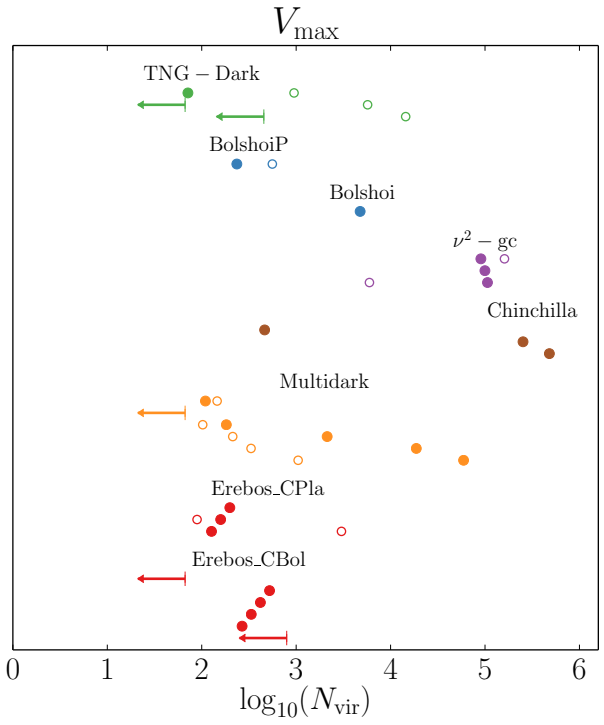

Figure 5.2: The $N_{\rm vir}$ values below which numerical effects measurably bias mean $V_{\rm max}$ value for each simulation in Table 3.1. These are conservative limits: all analysis can accept some level of numerical bias. There is significant variation in these limits from simulation to simulation. We first use color to group simulations by suite, then vertically order the simulations by particle mass; the bottom dot in each suite corresponds to the highest resolution box of that suite. We use points to indicate simulations where we measure diverging behavior and upper limits for simulations where we were not able to measure a divergence. As discussed in section 5.2.3 and shown in Fig. 5.3, the two highest resolution Planck suites, TNG-Dark and Multidark, appear to converge to two different $M_{\rm vir} - V_{\rm max}$ relations. The solid circles show cutoff values when the high-resolution fit does not include Multidark boxes and the open circles show cutoff values when the high-resolution fit does not include TNG-Dark.

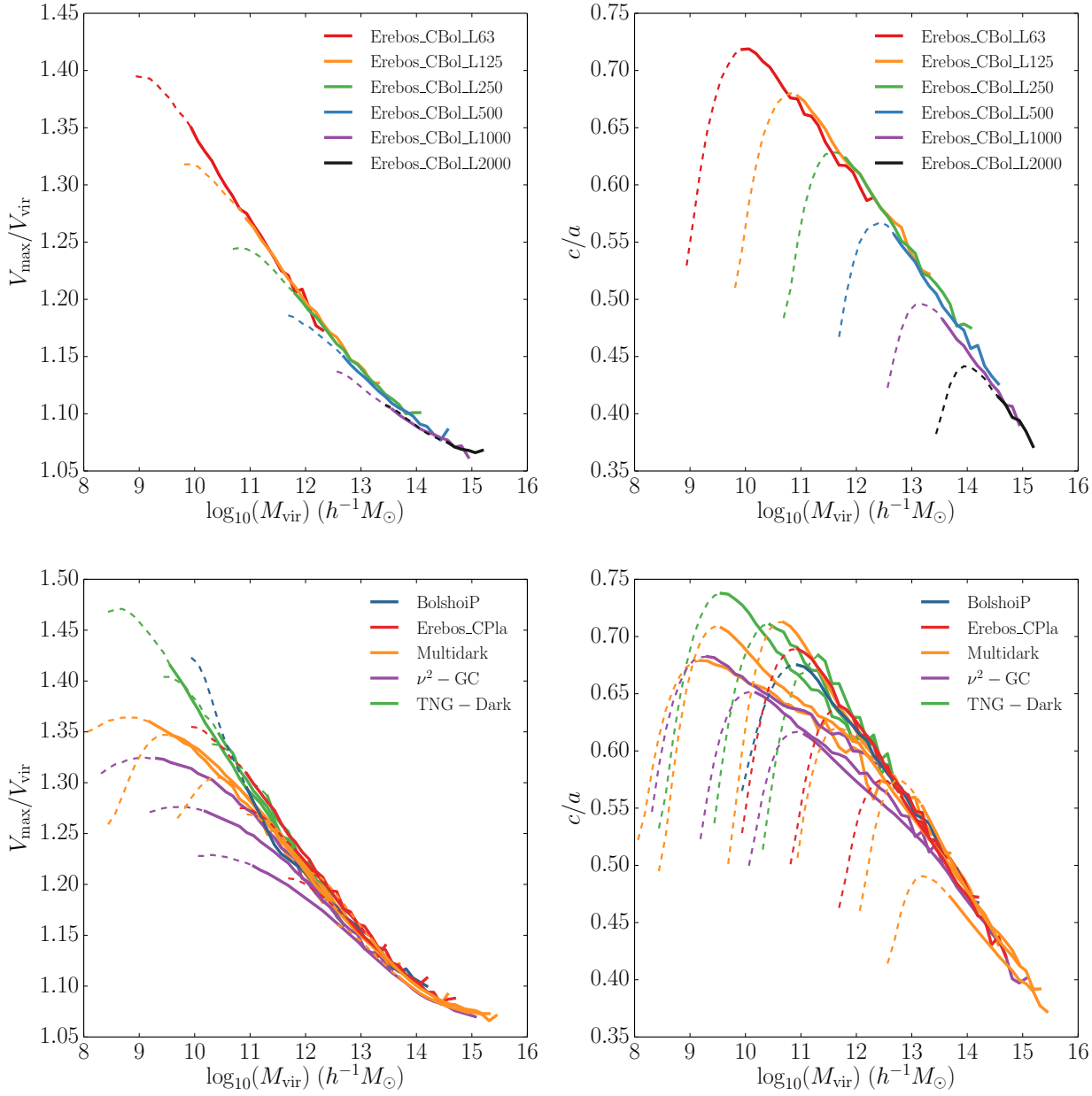

Figure 5.3: The convergence behavior of $\langle V_{\rm max}/V_{\rm vir}\rangle$ and $\langle c/a\rangle$ as functions of $M_{\rm vir}$. Top: "Classical" convergence tests using the six boxes from the Erebos_CBol suite. Each curve color corresponds to a different box, and the linestyle transitions from solid to dashed at $N_{\rm vir} \leq 500$. In isolation, these plots imply that rotation curve peaks and halo shapes measured for halos above 500 particles are converged. Bottom: The $M_{\rm vir} - V_{\rm max}/V_{\rm vir}$ and $M_{\rm vir} - c/a$ for every Planck-cosmology simulation suite in Table 3.1. Simulations are colored by suite and the solid-to-dashed transition still occurs at $N_{\rm vir} \leq 500$. There is disagreement between the mass relations above the convergence limit implied by the top plots. The bottom two panels contain a number of noteworthy features which we highlight in section 5.3.2.

particle count cutoffs provided for both isolated halos and subhalos and example accuracy tolerances of $\delta = 0.00$ and $\delta = 0.01$. The online supplement of Mansfield & Avestruz [in prep] will contain results for all properties listed in section 5.2.2 with accuracy tolerances ranging from $\delta = 0.00$ to $\delta = 0.10$, which will be available upon publication. Blank table entries indicate that we were not able to make a reliable measurement of a deviation from the mean mass relation for that property at that accuracy tolerance.

In Table 5.2.3, we show conservative "convergence limits" for many halo properties. These correspond to $N_{\rm vir}$ values at which 90% of the simulations in our sample show no measurable deviation from high resolution fits ($\delta = 0$; section 5.2.3). These limits should be viewed as a guideline in assessing the acceptable level of numerical bias in an analysis. We recommend that any analysis using halos with smaller $N_{\rm vir}$ either use accuracy-dependent limits in Table 5.2.3 or explicitly test for numerical biases and include the systematic uncertainty in the error estimates.

For each halo property in Table 5.2.3, we have performed detailed tests on how strongly this property depends on ϵ (see section 5.4). Properties which strongly depend on ϵ have been marked by a $\star$, as we cannot express convergence limits in terms of $N_{\rm vir}$ alone.

It is difficult to compare this table to previous tests in the literature. For most of the common properties with existing testing literature (e.g., $V_{\rm rms}$; Evrard et al., 2008 or $T/|U|$; Power et al., 2012), we conclude that there is such a strong dependence on ϵ that we cannot endorse a single $N_{\rm vir}$ limit. For many of the remaining properties, such as, $x_{\rm off}$ or a_{MM}, we are not aware of any previous convergence tests. That said, we note that our cutoff for $\lambda_{\rm Peebles}$ is consistent with the results of Villarreal et al. [2017b], and that our criteria for isolated halo abundances are consistent with existing literature on the topic [e.g. Angulo et al., 2012, Ishiyama et al., 2015, Ludlow et al., 2019], although different authors adopt different target accuracies. Finally, we note that our input catalogs did not have subhalos with fewer than 50 particles; we were not able to put competitive constraints on mass definitions with limits near or below this value.

5.3.2 Variation in Limits Between Simulations

Fig. 5.2 shows the $N_{\rm vir}$ values at which every simulation in our suite measurably deviates from from high resolution fits to $\langle V_{\rm max}\rangle(M_{\rm vir})$. These values correspond to $N_{\rm iso,0.00}$ in Table 5.2.3. These $N_{\rm vir}$ limits are conservative ($\delta = 0$; see section 5.2.3), and applications which can accommodate modest biases in $\langle V_{\rm max}\rangle$ may be able to use halos with smaller values of $N_{\rm vir}$. Nevertheless, the limits shown in Fig. 5.2 show the resolution scales at which numerical effects begin to measurably influence the behavior of the $V_{\rm max}$ distribution.

There is substantial variation in these convergence limits from simulation to simulation, with many simulations only reaching full statistical convergence at $10^5 - 10^6$ particles. Because TNG-Dark and Multidark appear to converge to different $V_{\rm max}$ relations (see section 5.3.3), we perform this analysis twice with separate fits to both suites. The filled in circles correspond to the fit to TNG-Dark and the unfilled circles correspond to the fit to Multidark. Noe that the limits for TNG-Dark become higher when Multidark is used to fit low-mass halos, and the opposite is true when TNG-Dark is used. However, the overall scatter in the convergence limits does not depend on this choice. Note that simulations with WMAP-like cosmologies (Chinchilla, Erebos_CBol, Bolshoi) are unaffected by this fitting choice because they were fit separately.

The simulations-to-simulation variation in convergence limits is not an artifact of our convergence procedure. In Fig. 5.3 we qualitatively demonstrate this effect for $V_{\rm max}$ and another commonly used halo property, c/a.

The top panels of Fig. 5.3 show the "classical" convergence test for $V_{\rm max}$ and c/a using the seven boxes in the Erebos_CBol suite. We show the mass relations, $V_{\rm max} - M_{\rm vir}$ and $c/a - M_{\rm vir}$, for isolated halos using different colors for each box in the suite. The curves are solid for halo masses corresponding to particle numbers above 500 and dashed for halo masses below this particle count. These simulations strongly agree with one another above this visually-identified convergence limit. There is some slight variation in the amplitude due to cosmic variance. The agreement *seems* to indicate that both quantities are converged

above 10^3 particles.

However, we do not find such agreement when comparing across simulation suites. The bottom two panels of Fig. 5.3 show the same mass relations for all of our Planck-cosmology simulations. Most of the simulations have many times more particles than the Erebos_CBol suite. As in the top panels, the curves are solid above 500 particles and dashed below. Unlike the top panels, there is disagreement between the simulations at halo masses corresponding to approximately 10^5 particles, *even for simulations in the same suite.*

We have ruled out many factors outside of numerical non-convergence that could potentially cause a difference in these mass relations. We address these factors in other sections of this chapter, but we collect them here for convenience.

- As discussed in section 5.2.1, we cross-matched catalogs to demonstrate that varying versions and parametrizations of the ROCKSTAR halo finder cannot cause this disagreement.

- The statistically estimated cutoffs shown in Fig. 5.2 are consistent in detail with the qualitative disagreement shown in Fig. 5.3. As described in section 5.2.3, our statistical cutoffs explicitly account for cosmic variance, estimated by jackknife resampling. Additionally, the disagreement extends to some very large boxes, such as ν^2-gc-L. This means that the disagreement is not caused by cosmic variance.

- Fig. 5.3 only contains isolated halos, so this disagreement cannot be due to the stricter convergence criteria on subhalo resolution. We have also inspected the distribution of halo properties at a constant mass to determine that a small population of outliers is not driving the differences.

- We also see disagreement between simulations in the same suite. Simulations within the same suite use identical codes, identical cosmologies, and nearly identical initial conditions setups. This means that differences of this type cannot be the sole cause of the disagreement.

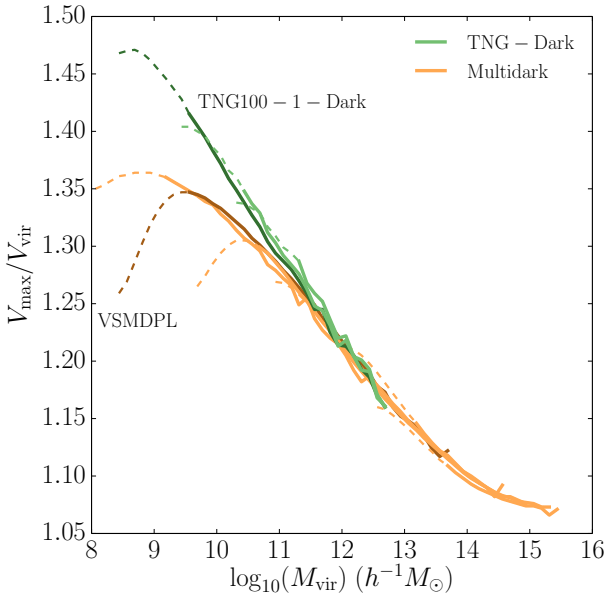

Figure 5.4: The same as the lower left panel of Fig. 5.3, except restricted to TNG-Dark and Multidark boxes. TNG100-1-Dark and VSMDPL, which have very similar parametrizations, are emphasized with darker colors. The two suites have converged to different solutions.

5.3.3 Differences Between Multidark and Illustris-TNG

As discussed above, the Multidark suite and the Illustris-TNG suite have converged to two different $\langle V_{\rm max}(M_{\rm vir})\rangle$ relations. We illustrate this in Fig. 5.4. This difference emphasizes that convergence alone is not sufficient to establish that a simulation is unbiased, a point which is discussed further in section 5.1. In the rest of this section we focus on isolating the cause of such a "false convergence" in detail. In particular, we focus on the TNG100-1-Dark and VSMDPL boxes, which have very similar parametrizations and are emphasized in Fig. 5.4.

Numerical differences between cosmological simulations come from a finite list of sources: cosmology, cosmic variance, halo finders, box size, m_p, timestepping, force softening scheme, ϵ, initial condition generation, code parameters, and code algorithms.

Cosmology cannot cause the difference between TNG100-1-Dark ($\Omega = 0.309$, $h_{100} = 0.677$, $\sigma_8 = 0.8159$) and VSMDPL ($\Omega_m = 0.307$, $h_{100} = 0.678$, $\sigma_8 = 0.832$), as the Planck-like parameters they adopt are almost identical. Cosmic variance can never lead

to false convergence because such fluctuations would be uncorrelated with simulation suite. Additionally, we find that the cosmic variance estimated through jackknife resampling for $\langle V_{\rm max}(M_{\rm vir})\rangle$ is small relative to the difference between the suites. As discussed at length in section 5.2.1, we have ruled out halo finder inconsistencies as a potential cause of non-convergence. Although TNG100-1 ($L = 75\,h^{-1}$Mpc) and VSMDPL ($L = 160\,h^{-1}$Mpc) have different box sizes, any small-box effects this large in an $L = 75\,h^{-1}$Mpc box would have been detected in the tests performed by Power and Knebe [2006]. TNG100-1-Dark ($m_p = 6.00 \times 10^6\,h^{-1}M_\odot$) and VSMDPL ($m_p = 6.16 \times 10^6\,h^{-1}M_\odot$) have virtually identical particle masses, meaning that the source of the false convergence cannot be related to mass resolution. Gadget-2 and Arepo use the same timestepping criteria, Eq. 3.1, and TNG100-1 ($\eta = 0.012$) and VSMDPL ($\eta = 0.01$) use nearly identical values of η, meaning that timestepping is very similar between the simulations.

Both simulations use the same softening scheme, Eq. 3.3, but TNG100-1-Dark ($\epsilon/l = 0.018$) and VSMDPL ($\epsilon/l = 0.024$) use softening lengths that differ by 25%. While small, this difference could, in principle contribute to the false convergence. However, in section 5.5 we construct an explicit model for the impact of ϵ/l in this regime. This model predicts that while both simulations should be biased to slightly low in $V_{\rm max}$ due to the adopted values of ϵ, this effect is too small to account for the false convergence.

After review of the configuration files for both simulations [Nelson et al., 2019, Yepes, personal communication], the only meaningful difference between parametrizations is α (also referred to as $f_{\rm acc}$, and `ErrTolForceAcc`), which sets the node opening criteria in Gadget's force tree. VSMDPL adopts $\alpha = 0.01$, while TNG100-1-Dark adopts a more conservative $\alpha = 0.0025$. The tests in Power et al. [2003] indicate that $\alpha = 0.01$ can lead to density biases in regions of halos with $N(< R) \approx 100$, but that this effect is also dependent on mass resolution, meaning that it's unlikely to contribute to biases which persist across multiple resolutions. However, the impact of α deserves further study.

Based on the process of elimination, we consider the most likely cause of the false con-

vergence seen in Fig. 5.4 to be updates in the Gadget force solver which were made during the development of Arepo. Gadget-2 dynamically updates force trees to avoid needing to reconstruct the entire tree for each step taken by particles in the finer time bins [Springel, 2005]. However, Weinberger et al. [2019] found that this process leads to force errors which are correlated with timestep size, leading to errors which occur predominantly in the central regions of halos where particles are on short orbits and scattering off one another on short timescales. This effect would depend chiefly on the acceleration felt by each particle, opening an avenue for a numerical effect which depends primarily on halo mass and not on resolution.

The cause of this false convergence must be established before high-accuracy measurements of rotation curves at low masses ($M_{\rm vir} \lesssim 10^{10} h^{-1} M_\odot$) can be performed. No statement can be made about which simulation suite(s) have and have not falsely converged until there is a positive identification of the source of the issue.

5.4 The Dependence of Halo Properties on Force Softening Scale

To investigate the dependence of halo properties on ϵ, we make use of four convergence boxes which were initially run as part of the Chinchilla simulation suite (as seen in, e.g., Mao et al., 2015, Desmond and Wechsler, 2015, Lehmann et al., 2017).[2] These boxes are resimulations of the same set of initial conditions but with different force softening scales (see Table 5.4). They were run with $L = 125\,h^{-1}$ Mpc, $N^3 = 1024^3$, $\Omega_{M,0} = 0.286$, $h_{100} = 0.7$, and $m_p = 1.44 \times 10^8\,h^{-1} M_\odot$. Aside from force softening scale, these boxes are very similar to the Erebos_CBol_L125 box (the orange curve in the upper panels of Fig. 5.3). We refer to this as the Chinchilla-ϵ suite.

The force softening scales in these boxes span a wide range. In units of the mean interparticle spacing, the smallest force softening scale, in Chinchilla_L125_e1, corresponds to $\epsilon/l = 0.0082$ a small but not uncommon length which is similar to simulations like Bolshoi or any of the Chinchilla boxes. The next smallest, Chinchilla_L125_e2, corresponds

2. Access to these catalogs was generously provided by Matthew Becker.

Simulations name	ϵ (h^{-1}kpc)	ϵ/l
Chinchilla_L125_e1	1	0.0082
Chinchilla_L125_e2	2	0.016
Chinchilla_L125_e5	5	0.041
Chinchilla_L125_e14	14	0.115

Table 5.3: Simulation parameters of the resimulated convergence boxes of the Chinchilla-ϵ resimulation suite. Shared parameters of these simulations are discussed in section 5.4.

to a fairly typical $\epsilon/l = 0.016$ which is similar to SMDPL or Erebos_CBol_L63. Next is Chinchilla_L125_e5, $\epsilon/l = 0.041$ which is close to the upper limit of ϵ typically found in cosmological simulations and is similar to Erebos_CBol_L1000 or the ν^2-gc boxes. The last box, Chinchilla_L125_e14, has a force softening scale much larger than any box in our simulation suite: $\epsilon/l = 0.115$, but which is comparable to the ϵ suggested by some convergence studies (see section 5.6.1). Timestepping in each simulation is performed via Eq. 3.1 with $\eta = 0.025$, meaning that timesteps are not constant between simulations.

We compare the mass-trends for every halo property described in section 5.2.2 across the boxes in the Chinchilla-ϵ resimulation suite. Most properties, such as $X_{\rm off}$ or $\lambda_{\rm Bullock}$ show either little to no dependence on ϵ or show agreement for typical values of ϵ and some mild non-convergence in Chinchilla_L125_e14. This is not true for all halo properties.

In Fig. 5.5 we show the $V_{\rm max} - M_{\rm vir}$, $c/a - M_{\rm vir}$, $V_{\rm rms} - M_{\rm vir}$, and $T/|U| - M_{\rm vir}$ relations for isolated halos in each of the Chinchilla resimulation boxes. The curves are solid above the cutoffs listed in Table 5.2.3 and dashed below it. If the traditional convergence tests in this chapter are correct, one would expect that these trends would not depend on numerical parametrization above these cutoffs. We find that all four properties vary meaningfully with ϵ. These mass relations vary continuously in amplitude and slope across the entire ϵ range.

To give a sense of the "practical significance" of these trends, we overplot the difference between the DMO TNG100-2-Dark and the baryonic TNG100-2 as a gray shaded region. For $V_{\rm max}$ and c/a, the shift in halo properties due to numerical effects is comparable to or greater than the impact of baryons.

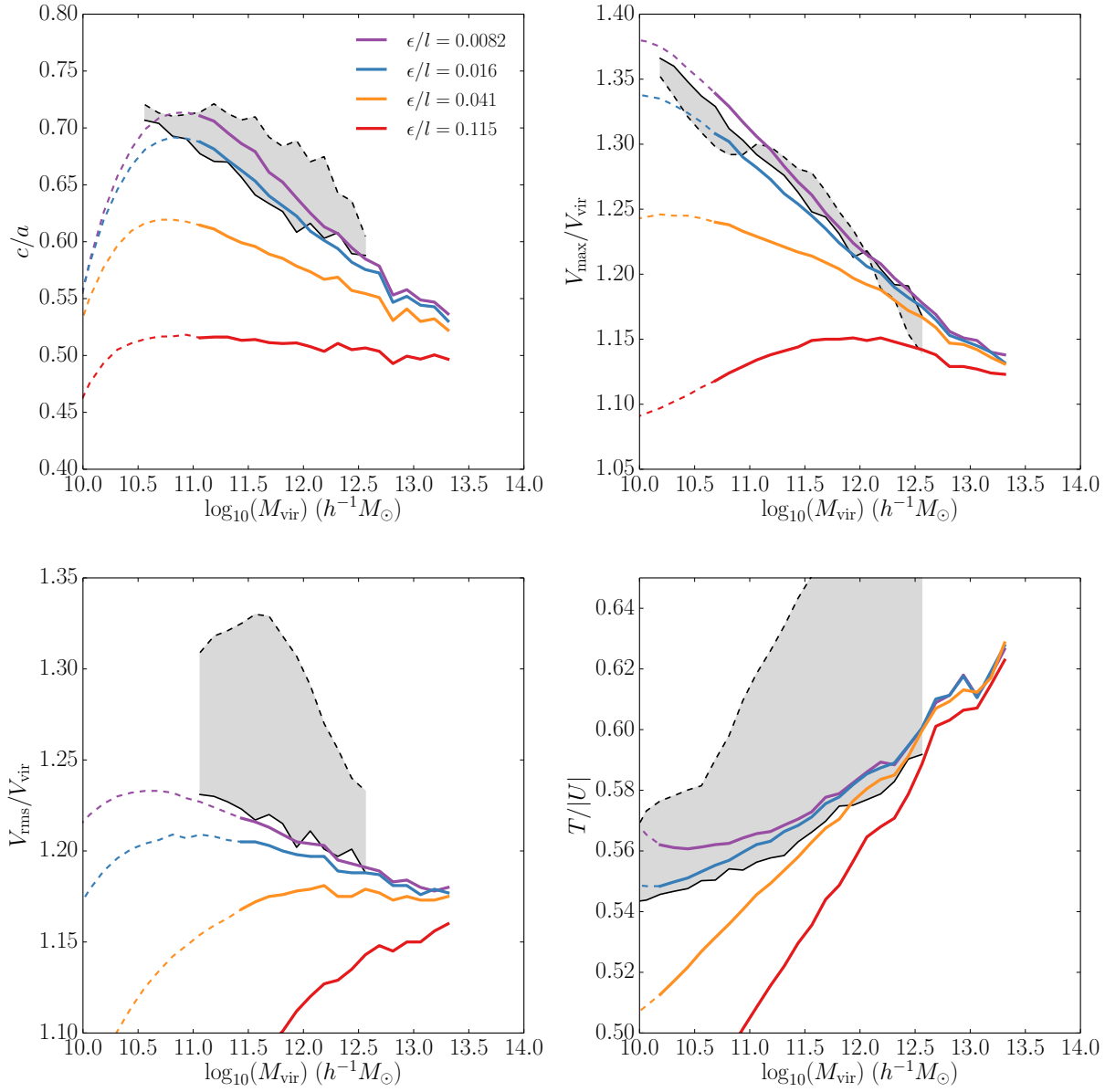

Figure 5.5: The dependence of various halo properties on force softening scale. Each panel shows the mean mass relation for various halo properties in isolated halos for four boxes which were resimulated from the same initial conditions The purple, blue, and yellow curves have ϵ in the range typically chosen by cosmological simulations. The red curves probes ϵ values suggested by some convergence studies (e.g., Power et al., 2003; see section 5.6.1). The curves transition from dashed to solid at the median $N_{\rm vir}$ cutoff from Table 5.2.3 and continue to $N_{\rm vir} \approx 2 \times 10^5$. c/a, $V_{\rm max}$, and $V_{\rm rms}$ are strongly dependent on ϵ, and $T/|U|$ is dependent on ϵ for softening scales smaller than $\epsilon/l \approx 0.016$. To give a sense of the "practical significance" of these dependencies, we show the impact of baryons in the Illustris-TNG simulations as gray shaded regions. The dashed edges of these regions correspond to mass relations from the baryonic TNG100-2 box and the solid edges correspond to mass relations from non-baryonic TNG100-2-Dark box.

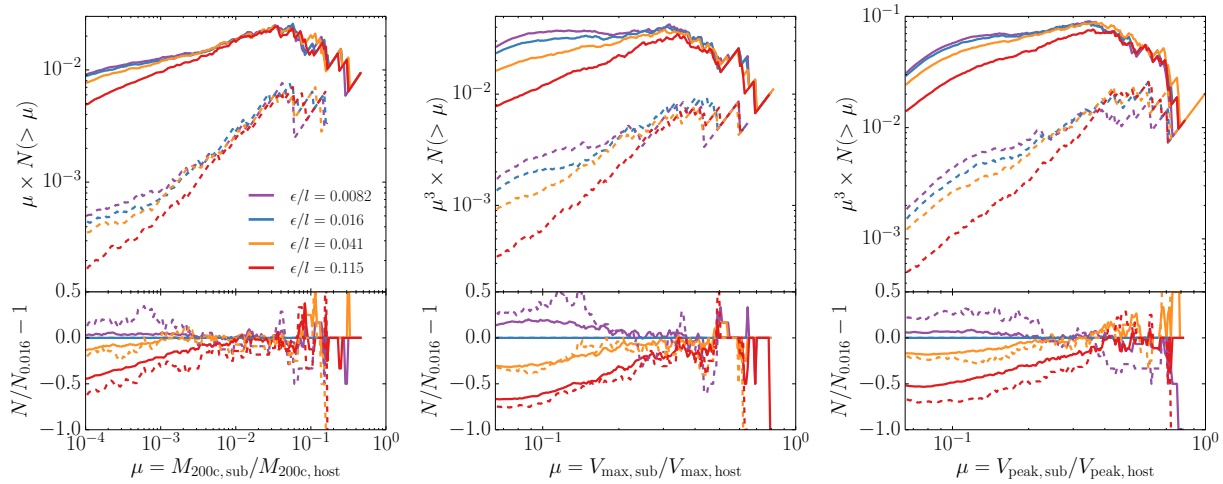

Figure 5.6: The impact of force softening on the subhalo abundance within 50 host halos from the Chinchilla-ϵ resimulation suite with masses $M_{200c} \approx 10^{14}$. Left: The dependence of the cumulative subhalo mass function on force softening scale. Plotted are the mean mean functions. The solid lines show all subhalos, and the dashed lines show all subhalos within $0.25\,R_{200c}$ of their hosts. The fractional deviation from the $\epsilon = 0.016$ simulation is shown in the bottom panel. center: the same for the mean V_{max} subhalo velocity function. Right: the same for the mean V_{peak} subhalo velocity function. The lowest mass subhalos shown in each plot have ≈ 70 particles. Note that the red curve corresponds to an atypically large value of ϵ. The subhalo mass function exhibits only a weak dependence on ϵ in the outer regimes of the halo. This dependence becomes stronger at small radii, confirming that artificial disruption is stronger in this regime. The subhalo velocity functions depend more strongly on ϵ, even at large radii. Although the impact of ϵ velocity functions becomes stronger at small radii, the strength of the dependence at large radii relative to the dependence seen in the subhalo mass function implies that most of this effect is from artificial suppression of V_{max} and not artificial subhalo disruption.

5.4.1 Dependence of the Subhalo Mass Function on ϵ

In Fig. 5.6 we show the dependence of the subhalo mass and velocity functions on ϵ. The left panel shows the mean subhalo mass functions functions of the 50 largest halos in the Chinchilla-ϵ resimulation suite, the middle panel shows the mean subhalo V_{max} functions for these halos, and the right panel shows the mean subhalo V_{peak} functions of these halos. The host halos have particle counts ranging across $5 \times 10^5 < N_{200c} < 1.4 \times 10^6$. We use the high-density M_{200c} mass definition to study subhalos over the lower density M_{vir} definition favored elsewhere in this chapter, as higher density regions survive longer prior to disruption.

Both types of subhalo velocity functions show a strong dependence on force softening scale

that becomes stronger when considering subhalos close to the center of the host. Subhalo mass functions have a weaker dependence on ϵ, although it also becomes stronger for central subhalos, implying that artificial subhalo disruption/stripping becomes stronger at small radii. The difference in ϵ-dependence between the mass and velocity functions implies that velocity functions are primarily impacted by artificial suppression of the velocity curve (which does not affect mass functions and which does not have a radial dependence) more than artificial subhalo disruption, but that artificial subhalo disruption likely leads to the radial dependence in ϵ-dependence.

Note that, as discussed in section 5.1, *convergence* between independent cosmological simulations cannot establish *correctness*. The lack of a strong ϵ dependence at larger radii or larger particle counts does not imply that artificial disruption of subhalos is a weak effect: such a statement requires comparison with idealized simulations. However, these measurements can be used to constrain disruption models which predict that disruption rates depend on ϵ.

The idealized tests in van den Bosch and Ogiya [2018] suggest that some aspects of artificial subhalo disruption have a strong dependence on force softening scale. They find that simulations of idealized subhalos experience substantial artificial disruption and that this disruption occurs even at high subhalo resolutions. The rate of tidal stripping is dependent on ϵ across the range of ϵ values adopted by the Chinchilla-ϵ test suite. Our results are not in conflict with these findings, despite the weak dependence of the subhalo mass function on ϵ.

van den Bosch and Ogiya [2018] found that numerical factors begin to artificially accelerate disruption once halos have already lost $\gtrsim 90-95$ per cent of their mass due to *physical* disruption. Due to the slope of infalling halo mass function, at any particular snapshot, the majority of subhalos at a given mass have not yet experienced this level of disruption. Additionally, the effect of artificial disruption due to force softening is strongest in subhalos on close orbits, with effect becoming particularly strong at $R \approx 0.1\,R_{\rm vir}$, a regime which

our simulations do not have sufficient resolution to probe. Subhalos on close-orbits are both located in the deepest part of the host halo's potential and are most likely to have already experienced many orbits. While close orbit subhalos make up a small fraction of the host's overall volume (and thus of our sample), the best constraints on the faint end of the satellite luminosity function come from the corresponding satellite population of the Milky Way [e.g. Drlica-Wagner et al., 2019]. Furthermore, the radial dependence of artificial disruption affects makes it more difficult to compare observed satellite number density profiles to the predictions of ΛCDM [e.g. Carlsten et al., 2020]. These effects are therefore still important for cosmological constraints.

The locations of even the most massive subhalos are altered substantially by changes in ϵ. It is possible that this is due to chaotic errors in halo phase while orbiting their hosts, but given that the tidal disruption rate in the host's central region is dependent on ϵ, it is also possible that this is caused by an ϵ dependence in the dynamical fiction experienced by each subhalo. This change in positions makes it impossible to directly measure subhalo disruption using only single-snapshot information. Such analysis would be possible by comparing the trajectories of subhalo progenitors prior to accretion. We defer such analysis of subhalo trajectories to future work.

Note that these tests only study the impact of ϵ on subhalo abundance. Particle count also substantially impacts the reliability of subhalo velocity functions [e.g. Guo and White, 2014, Klypin et al., 2015b] and must be accounted for accordingly.

5.5 Estimating the Impact of Large ϵ on $V_{\rm max}$

In sections 5.3.1 and 5.3.2 of this chapter, we showed that the distribution of halo properties measured in different simulations diverge from one another at unexpectedly high particle counts. In section 5.4, we showed that varying ϵ across the range typically used in cosmological simulations has a large impact on many commonly studied halo properties. In this section, we construct a model that predicts this behavior for the simplest property we have

considered: $V_{\rm max}$.

Previous convergence studies have established three channels that allow halo rotation curves to depend on ϵ. In the large ϵ limit, non-Newtonian forces suppress $V(R)$ with increasing ϵ. The suppression is primarily due to how softening reduces centripetal forces [e.g. Klypin et al., 2015b, van den Bosch and Ogiya, 2018, Ludlow et al., 2019]. As we show in Fig. 5.9, the suppression of $V(R)$ continues into regimes where the force kernel is Newtonian because the entire halo responds to the creation of a low-density core. As we discuss in section 5.6.1, some of this effect may be caused by poor timestep resolution under some timestepping schemes. In the limit where ϵ is small, two-body collisions begin to thermalize the dark matter particles over some local relaxation timescale [e.g. Power et al., 2003, Navarro et al., 2010, Ludlow et al., 2019]. This causes the otherwise adiabatic orbits of dark matter particles [e.g. Dalal et al., 2010] to become adiabatic and for the radial velocity dispersion profile to flatten [e.g. fig. 6 of van den Bosch and Ogiya, 2018]. The dominant effect of this transformation is that particles in the high velocity tails are transported to higher radii, leading to decreasing $V(r)$ as this timescale decreases. This timescale depends primarily on the size of r relative to l [Ludlow et al., 2019], although excessively small ϵ and $> t_{\rm Hubble}$ measurement timescales increase cause ϵ dependencies to become more important [van den Bosch and Ogiya, 2018]. Lastly, in the limit where ϵ is small and timestepping is coarse, integration errors (e.g. fig. 9 of Knebe et al., 2000). This last effect is discussed at length in section 5.6.1. The "art" of configuring a cosmological simulation is in selecting an ϵ and ϵ in a safe regime that avoids all three effects.

We illustrate the dominant trend in the top right panel of Fig. 5.5. Here, we see that $V_{\rm max}$ decreases with increasing ϵ, implying that large values of ϵ is the most likely driver of suppressed rotation curves.

When simulators account for large-ϵ effects, they typically restrict their analysis to halos where $R > X\epsilon$, where X is some constant. To give an idea of the typical values of X used, we surveyed several papers which studied the concentration-mass relation to identify

values for $X = \langle r_{-2} \rangle (M_{\rm vir,min})/\epsilon$. We found that the minimum values identified ranged from $2.5 \leq X \leq 6.4$ [Neto et al., 2007, Duffy et al., 2008, Gao et al., 2008, Zhao et al., 2009, Prada et al., 2012, Bhattacharya et al., 2013, Ludlow et al., 2013, Dutton and Macciò, 2014, Klypin et al., 2016, Poveda-Ruiz et al., 2016, Child et al., 2018]. This is broadly consistent with the behavior of ROCKSTAR, which downweights radii larger than 3ϵ. Diemer and Kravtsov [2015] performed a detailed review use the results of several zoom-in simulations to conclude that analysis is safe above $> 3\epsilon$ for individual halos, and that analysis of $\langle r_{-2} \rangle (M_{\rm vir})$ should be restricted to masses where $\langle r_{-2} \rangle (M_{\rm vir}) \gtrsim 8\epsilon$ to account for scatter in the $M_{\rm vir} - c_{\rm vir}$ relation. Below, we take a different approach and use out direct measurements of the impact of ϵ on rotation curves (Eq. 5.13) to estimate the impact of ϵ on the distribution of $V_{\rm max}$ in a halo population.

The left panel of Fig. 5.7 illustrates the rotation curve bias due to the Gadget force softening scale, as predicted by Eq. 5.13 for different halo profile shapes. We reference Klypin et al. [2015b] for a mathematical summary of NFW rotation curves and Garrison-Kimmel et al. [2014] for a similar summary of Einasto rotation curves. Einasto profiles require a second parameter beyond R_s, α, and provide a more accurate fit than NFW profiles [e.g. Gao et al., 2008, Springel et al., 2008]. The solid curves in Figure 5.7 show the unbiased rotation curves for an NFW profile in black and Einasto profiles with α=0.14, 0.18, and 0.22 in red, yellow, and blue, respectively. The selected α values roughly correspond to the range spanned by $z = 0$ halos [e.g. Child et al., 2018]. The dashed lines show the biased rotation curves predicted by Eq. 5.13 for $h_{\rm Gadget} = R_{\rm max}$ ($\epsilon = 0.278\, R_{\rm max}$). The biased maximum velocity, $V_{\rm max,bias}$, ranges from $0.943\, V_{\rm max}$ to $0.949\, V_{\rm max}$, exhibiting a small systematic uncertainty due to halo profile shape, which is $\approx$ 10 percent of $V_{\rm max} - V_{\rm max,bias}$. This uncertainty consistently stays at or below this level relative to $V_{\rm max} - V_{\rm max,bias}$ regardless of $R_{\rm max}/\epsilon$

By evaluating $\xi_{\rm bias} = V_{\rm max}/V_{\rm max,bias}$ for a range of $\epsilon/R_{\rm max}$, we can empirically construct the invertible function $\xi_{\rm bias}(\epsilon/R_{\rm max})$ for a given halo profile shape. For convenience, we note

that for both NFW and Einasto profiles this function is well-fit by,

$$\xi_{\rm bias} = 2 - \left(1 + (A\epsilon/R_{\rm max})^2\right)^{\beta}. \tag{5.4}$$

We fit this relation for Gadget-like kernels over the range of $0.01\ \epsilon/R_{\rm max} \lesssim h_{\rm Gadget} \lesssim 5\,\epsilon/R_{\rm max}$. Below this range, $V_{\rm max}/V_{\rm max,bias}$ is 1 for all practical purposes. Above this range, Eq. 5.13 is poorly constrained. By minimizing the least-squared error on $V_{\rm max}/V_{\rm max,bias}$, we find that the parameters $A = 6.049$ and $\beta = 0.05440$ lead to errors in $V_{\rm max,bias}$ which are $\lesssim 10^{-3}V_{\rm max}$ for NFW profiles and that the parameters $A = 5.884$ and $\beta(\alpha) = 0.02754\,\ln(\alpha) + 0.15566$ lead to errors which are $\lesssim 2 \times 10^{-3}\,V_{\rm max}$ for Einasto profiles with α ranging from 0.12 to 0.32. However, we use the raw empirical functions in all subsequent analyzes, derived from whichever force softening kernel is appropriate.

Note, no function describing $\xi_{\rm bias}(\epsilon/R_{\rm max})$ can be applied on its own to evaluate the bias in $V_{\rm max}$ because these functions depend on the unbiased value of $R_{\rm max}$, which is unknown. Therefore, such a function must be combined with a second, independent equation relating $\xi_{\rm bias}$ to $R_{\rm max}$.

For our application, the systematic errors in $\xi_{\rm bias}$ due to profile shape are small. We therefore restrict our analysis to NFW profiles because they depend on only a single parameter. With an NFW parametrization, we can directly compute an estimate for $\xi_{\rm bias}$ from the unbiased $c_{\rm vir}$ and $V_{\rm vir,bias}$ from the halo catalog. The estimate comes in the form of,

$$\xi_{\rm bias} = 0.469 \left(\frac{V_{\rm vir,bias}}{V_{\rm max,bias}}\right) \left(\frac{c_{\rm vir}}{f(c_{\rm vir})}\right)^{1/2} \left(\frac{V_{\rm vir}}{V_{\rm vir,bias}}\right) \tag{5.5}$$

where $V_{\rm vir}/V_{\rm vir,bias}$ is Eq. 5.13 evaluated at $R/\epsilon = 0.469\,c_{\rm vir}\frac{R_{\rm max}}{\epsilon}$ and $f(x) = \ln(1+x) - 1/(1+x)$. We compute the ratio $V_{\rm vir,bias}/V_{\rm max,bias}$ from halo catalogs, whose measurements are biased due to ϵ.

For NFW halos, $R_{\rm max} = 2.164R_s$. This and Eq. 5.5 provide two independent equations for $\xi_{\rm bias}(\epsilon/R_{\rm max})$. For halos with $R_{\rm max,bias} > R_{\rm vir,bias}$ (a criterion that holds for virtually

all halos in cosmological simulations), these two relations intersect at exactly one point: a unique solution for $\xi_{\rm bias} = V_{\rm max}/V_{\rm max,bias}$. This statement is only true for single parameter profile models, such as NFW profiles or Einasto profiles with fixed α.

With this de-biasing procedure, we can estimate the unbiased $V_{\rm max}/V_{\rm vir}$ for each halo in a given cosmological simulation from the biased measurements of $V_{\rm max,bias}/V_{\rm vir,bias}$. We can then estimate the mean unbiased $V_{\rm max}/V_{\rm vir}(M_{\rm vir})$ in that simulation. Note that the scatter in the $M_{\rm vir} - V_{\rm max}$ relation means that this estimate cannot only be applied to the mean of a particular mass bin, but must first be applied to individual halos before finding the mean relation as described.

The right panel of Fig. 5.7 shows the result of the "de-biased" estimate of $V_{\rm max}/V_{\rm vir}$ for the Chinchilla resimulation boxes. From this figure, we see that this procedure completely removes the ϵ dependence from this sample, *implying that the numerical bias of* $V_{\rm max}/V_{\rm vir}$ *is primarily due to large* ϵ.

There is a few-per cent dispersion between curves at moderate-to-high masses. While other numerical effects could cause this dispersion, the level of dispersion is consistent with the error level associated with the assumption of an NFW profile in our analysis. As discussed above, assuming a profile shape results in systematic errors in $V_{\rm max}$ on the order of $0.1\,(V_{\rm max} - V_{\rm max,bias})$. Given that some simulations are estimated to be biased at the 20% - 30% level, a 2%-3% error is to be expected. The dispersion increases at low particle counts (low halo masses) and small $R_{\rm max}/\epsilon$. While numerical effects could cause this as well, the dispersion occurs in a regime where corrections are large and Eq. 5.13 is poorly constrained.

In Fig. 5.8, we show the results of applying these bias estimates to various Planck cosmology simulations. In this Figure, dashed lines show the measured mean mass trends in each simulation. The solid lines show results from our de-biasing procedure, which are estimates of what these trends would have been if not for the large ϵ bias. We cut off the estimated trend when they disagree from the measured trend by more than one per cent. As with the Chinchilla boxes, we are able to account for all of the visibly-apparent deviations from the

mean measured trend using our de-biasing procedure for biases due to large ϵ.

We note that there is still a non-trivial amount of scatter between simulation suites along the mean trend. While is is possible that this dispersion is also due to numerical factors, another possible explanation is in variations due to exact cosmology. Despite the fact that all are "Planck" cosmology simulations, different suites are either associated with data releases from different years or round their cosmological parameters to a different number of decimal places.

Lastly, we note that the de-biasing procedure outlined in this section is appropriate for either qualitatively estimating the impact of ϵ on a simulation suite (such as the right panel of Fig. 5.7) or estimating mass ranges robust to biases due to large ϵ (such as Fig. 5.8). The procedure should *not* be used to "correct" the $V_{\rm max}$ distribution. The primary reason for this is that our model assumes an underlying halo profile. In applications where the true underlying profile is known, there is no need to measure its properties in a simulation.

5.6 Discussion

5.6.1 Timestepping as an Additional Source of Biases

Coarse timesteps have two well-discussed effects on halo profiles [e.g. Power et al., 2003]. First, particles orbiting a smooth potential can artificially gain or lose energy if their orbits are too poorly resolved in time (e.g. fig. 4 and fig. 6 of Springel, 2005). The exact effect on these orbits is dependent on a number of factors including the integration scheme, the local slope of the potential, the ellipticity of the orbits, and the adaptive timestepping scheme [Springel et al., 2001a, Springel, 2005]. The second effect occurs with particles orbiting potentials with noise due to small force softening scales. Here, particle-particle scattering can lead to integration errors (e.g. fig. 9 of Knebe et al., 2000). These collisions do not conserve energy and will add/remove energy from the affected regions of the halo at a rate which depends on the collision rate, the depth of each particle's potential, the length of the

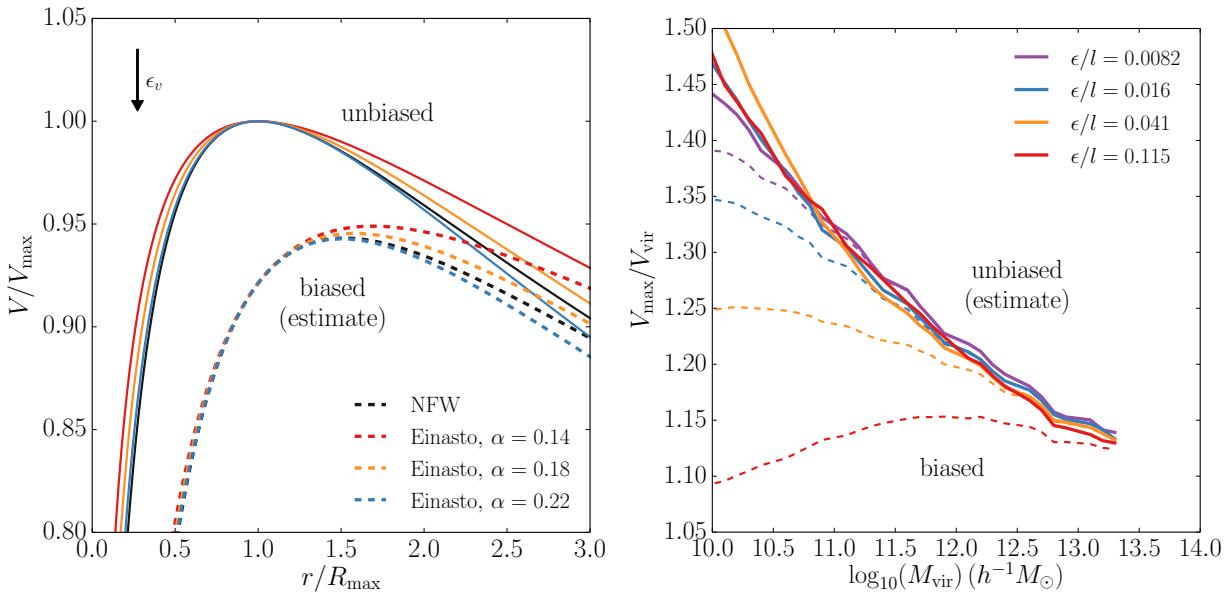

Figure 5.7: Left: An illustration of the bias estimate due to large softening scale on different halo profile shapes. Different colors correspond to the profile shape corresponding to the labeled parametrization. Dashed curves show rotation curves unbiased by force softening, and solid curves show predictions of the biased rotation curves from Eq. 5.13 for a Gadget simulation with $\epsilon = 0.357\,R_{\rm max}$ ($h_{\rm Gadget} = R_{\rm max}$). The systemic uncertainty in $V_{\rm max,bias}$ across the profile parameters shown here is $\approx 0.007 V_{\rm max}$ for the given value of $h_{\rm Gadget}$. Right: The result of applying the bias estimates described in section 5.5 to the top right panel of Fig. 5.5 (note, however, the change of axis range between these Figures). The dashed curves show the same mean $V_{\rm max}$ values measured in each mass bin and the solid curves the de-biased rotation curves, estimating what $V_{\rm max}$ would be if there were no bias due to force softening. The dependence on ϵ is almost entirely removed through the bias estimates, indicating that the majority of the ϵ dependence is due to large ϵ biases.

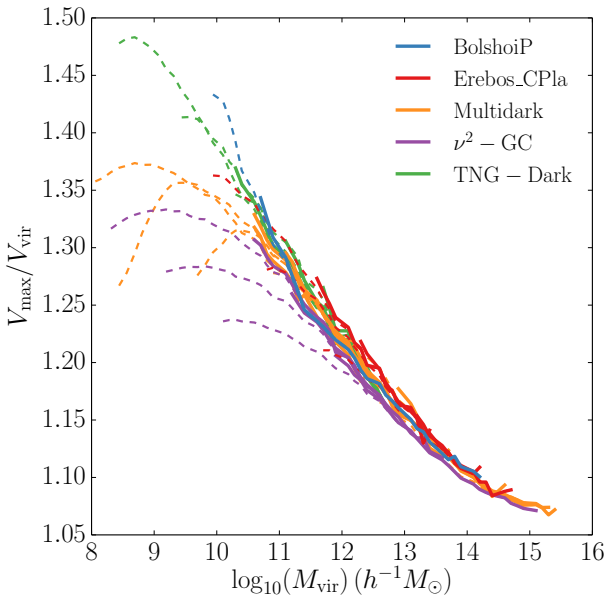

Figure 5.8: Fig. 5.3 recreated with the bias estimates from section 5.5. As in the right panel of Fig. 5.7, dashed curves show the mean mass trends measured in each simulation and the solid curves show estimates of what these mean trends would have been if not for large ϵ biases. To emphasize the mass ranges which are affected by these biases, we only plot solid curves down to mass bins at which they agree with the measured trend to 1 per cent or better. Although there is still some dispersion around a mean relation between simulation suites, all the strong, visually apparent divergences from the mean trend are consistent with being caused by large ϵ. Note that there are many science applications where a $V_{\rm max}$ bias of larger magnitudes is perfectly acceptable. This cutoff choice is only meant to mimic the divergences seen by the eye *and does not imply the "usable" mass ranges of these simulations for arbitrary analysis.* Such a mass range must be developed with the tolerances of a given analysis in mind.

timestep relative to the collisional timescale.

We will focus our analysis on the standard Gadget timestepping criteria, Eq. 3.1. Only two of the simulations in Table 3.1 use alternative schemes: Bolshoi and BolshoiP. For a spherically symmetric NFW potential, Bolshoi and BolshoiP will always have timesteps that are a factor of $\approx 10^2 - 10^3$ smaller than a Gadget simulation run with $\eta = 0.025$. Timestepping errors can be ignored for these two boxes.

For any spherically symmetric mass distribution, the Gadget timestepping criteria can be conveniently rewritten in terms of the number of timesteps per circular orbit:

$$\frac{t_{\rm circ}}{\Delta t} = 28.1 \left(\frac{R}{\epsilon}\right)^{1/2} \left(\frac{\eta}{0.025}\right)^{-1/2}. \tag{5.6}$$

We use this relationship to quantify integration errors in sections 5.6.1 and 5.6.1.

Integration Errors in Smooth Potentials

Integration errors in smooth potentials, are essentially irrelevant with the conventional Gadget integration settings. Tests of smooth integration errors in Power et al. [2003] show that simulations with constant timestepping converge to $\Delta V/V_{\rm ref} = 0.1$ above radii at which timesteps per circular orbit satisfy,

$$t_{\rm circ}(R)/t_{\rm 200c} > A(\Delta t/t_H)^{\alpha}, \tag{5.7}$$

with $A \approx 15$ and $\alpha \approx 5/6$. Empirical criteria determine if the underlying potential is smooth for halos in their study. The results from Power et al. [2003] agree with first-principles estimates of this class of integration errors. Combining the relation in Eq. 5.7 with Eq. 5.6 and the $t_{\rm circ}/t_{\rm 200c}$ profile of an NFW halo, we arrive at the requirement,

$$\frac{R}{\epsilon} \geq 4.96 \times 10^{-4} A^{2/\alpha} \left(\frac{\eta}{0.025}\right) \left(\frac{x^2\, f(c_{\rm 200c})}{c_{\rm 200c}^2\, f(x)}\right)^{2-2/\alpha}. \tag{5.8}$$

Here, $x = R/R_s$, $c_{200c} = R_{200c}/Rs$, and $f(x) = \ln(1+x) - x/(1+x)$. R/ϵ has only a weak dependence on c_{200c} and x. For example, concentrations in the range of $5 \leq c_{200c} \leq 15$, a 10 per cent error in $V_{\rm max}$ due to smooth integration errors requires a corresponding range of $0.6 \leq R_{\rm max}/\epsilon \leq 1.2$.

We note that smooth integration errors are typically subdominant or comparable to softening-induced errors in the centripetal force. As a comparison, Eq. 5.13 gives $\Delta V/V \approx 0.20 - 0.30$ at distances where Eq. 5.8 predicts a fractional error of 0.1. It is possible that even this is an overestimate: concentration- and radius-dependence at the level predicted by Eq. 5.8 – while small – would have been detectable in our tests described in Appendix 5.8.1. However, it is possible that the values in Table 5.8.1 have some dependence on Gadget timestepping parameter, η, and that high-precision estimates of $\Delta V/V_{\rm ref}$ require measurements at the same η as the target simulation. This is a question which deserves further study.

Integration Errors During Scattering

Excessively small force softening leads to noise in the halo potential. In sufficiently noisy potentials, integration errors from particle-particle scattering become more severe and require much smaller timesteps to suppress. The landmark study on these integration errors is Power et al. [2003]. Empirically, they find that integration errors during scattering occur for $\epsilon < \epsilon_{\rm opt,P03}$, where we can express the limit on ϵ with both,

$$\epsilon_{\rm opt,P03} = \frac{2.9\, R_{200c}}{\sqrt{N_{200c}}}, \tag{5.9}$$

and,

$$\epsilon_{\rm opt,P03}/l = 0.076 \left(\frac{\Omega_{\rm m}}{0.27}\right)^{1/3} \left(\frac{N_{200c}}{10^3}\right)^{-1/6}. \tag{5.10}$$

Here, l is the mean interparticle spacing. Eq. 5.10 is substantially larger than the ϵ/l values adopted by virtually all cosmological simulations. Fig. 5.5 shows that any cosmological simulations which abide by such a limit risk substantial biases in halo properties due to softened centripetal forces. Subsequent authors have suggested that Eq. 5.9 is too conservative by a factor of $\lesssim 2$ [Zhang et al., 2019, Ludlow et al., 2019]. However, part of the disagreement can be accounted for with a correction of the (now non-standard) Plummer equivalence scale which Power et al. [2003] used: $\epsilon = 0.5\, h_{\rm Gadget}$.

The most straightforward interpretation of the Power et al. [2003] tests is that particle-particle scattering in noisy halo potentials should lead to catastrophic non-convergence in cosmological simulations. Fig. 5 in Power et al. [2003] shows that for halos run at $\epsilon/\epsilon_{\rm opt,P03,}{}_v \approx 5$, fractional errors in $V(R)$ should be larger than 0.1 for radii at which timesteps per circular orbit satisfy Eq. 5.7, with $A = 11.2$ and $\alpha = 0.57$. These large fractional errors would be predicted for the Chinchilla-ϵ simulation, represented by the blue curves in Fig. 5.5 at $N_{\rm 200c} \approx 10^3$. The small α causes this level of bias to be reached at very large values of R/ϵ and to become strongly dependent on $c_{\rm 200c}$ and x. A $c_{\rm 200c} = 10$ halo would be predicted to have biases in $V_{\rm max}$ larger than $0.1V_{\rm max}$ for $\epsilon > 0.018\, R_{\rm max}$!

However, the massive biases predicted by the analysis in the previous paragraph (and comparable predicted biases used to argue for $\epsilon \lesssim \epsilon_{\rm opt,P03}$) are an artefact of the constant timesteps used in the Power et al. [2003]. Under constant timestepping schemes, the size of a timestep relative to the smallest possible collisional timescale, $t_{\rm circ}(m_p(<\epsilon),\epsilon)/\Delta t$, varies as $\epsilon^{3/2}$. This dependence on ϵ means that the resolution of close orbits worsens as ϵ decreases. However, Eq. 5.6 shows that with the standard Gadget timestepping criteria, $t_{\rm circ}(m_p(<\epsilon),\epsilon)/\Delta t$ is *independent of* ϵ. Timestepping errors are therefore far less catastrophic with the standard Gadget timestepping criteria.

Other recent convergence studies have investigated the impact of timestepping in the $\epsilon < \epsilon_{\rm opr,P03}$ regime. Ludlow et al. [2019] performed tests on halos across a wide range of ϵ values for $\eta = 0.025$ and $\eta = 0.0025$. These tests find catastrophic contraction of halos out

to large radii at $\eta = 0.025$ for $\epsilon/l \lesssim 0.003$, but find that halos in the range of the typical ϵ of cosmological simulations are relatively unaffected (see Ludlow et al., 2019 fig. 2).

The non-monotonic behavior in ϵ is surprising and deserves further study. The onset of profile contraction occurs at ϵ/l values that are close to what is needed to avoid large-ϵ biases in halo properties. A full characterisation of the profile contraction is therefore of practical relevance.

One potential explanation for the non-monotonicity is that Eq. 5.6 ensures that collisions occurring at distances with $\epsilon \ll r_{\rm peri}$ are well-resolved, and the fraction of particle collisions which occur at $\epsilon \approx r_{\rm peri}$ decreases as ϵ decreases. Although the Gadget timestepping scheme ensures that such collisions are never catastrophically unresolved, modest integration errors are sill possible. Springel [2005] shows that when using the adaptive timestepping of Gadget-2, small integration errors tend to decrease the energy of the system. Thus, as epsilon decreases, the average energy lost per collision increases as the potential of each particle decreases. In this case, however, the range of collision parameters that lead to $r_{\rm pericenter} \approx \epsilon$ also decreases until these collisions are so rare that they are not relevant to the internal dynamics of the halo.

5.6.2 What is the "Optimal" ϵ?

A number of studies aim to identify an optimal choice for ϵ. The [Power et al., 2003] suggestion for an optimal value, $\epsilon_{\rm opt,P03}$, is shown in Eq. 5.9 and discussed at length in section 5.6.1. However, cosmological simulations universally use scales smaller than $\epsilon_{\rm opt,P03}$. The use of smaller ϵ values is in part because – as Fig. 5.5 and Fig. 5.6 show – halos simulated at $\epsilon = \epsilon_{\rm opt}$ exhibit large biases at the particle counts that cosmological simulations typically consider. Klypin et al. [2015b] has also noted this effect in their analysis.

Recent convergence studies [van den Bosch and Ogiya, 2018, Ludlow et al., 2019] have

argued for an alternative optimal choice in ϵ:

$$\epsilon_{\rm opt,VO18}/l = 0.017. \tag{5.11}$$

The level of bias implied by Fig. 5.5 and Fig. 5.6 at $\epsilon_{\rm opt,VO18}$ would be acceptable for many applications, but is not zero. These Figures do not conclusively establish convergence in ϵ, but, the model presented in section 5.5 would predict that

$$\epsilon_{\rm opt,Vmax}/l \approx 0.008 \tag{5.12}$$

simulation would exhibit bias in $V_{\rm max}$ which is smaller than cosmic variance for simulations with comparable resolution and box sizes to the Chinchilla-ϵ.

However, we caution against uncritically accepting Eq. 5.12 as a blanket prescription for ϵ for three reasons. Most importantly, *the level of acceptable bias in a measurement is highly dependent on the science target.* While striving for zero numerical bias (a formally impossible goal) is the safest generic option, all analyzes can tolerate at least some deviation from the true predictions of ΛCDM. Second, this recommendation is based solely on reducing bias in $V_{\rm max}$. Halo properties which depend on the mass distribution at radii smaller than $R_{\rm max}$ will require smaller ϵ. Third, our simulation suites did not explicitly establish a range of converged ϵ and this recommendation is thus model-dependent. Fourth, poorly-explored timestepping effects can cause catastrophic halo contraction for ϵ values somewhat smaller than Eq. 5.12 for standard timestepping schemes. All four considerations must be accounted for before applying Eq. 5.12 or any other $\epsilon_{\rm opt}$ prescription.

5.7 Conclusion

In this chapter, we study the impact of DMO simulation parameters on halo properties. We provide several tools to help analysts avoid and quantify these numerical biases. We

do this by comparing a number of publicly available cosmological simulation suites against one another and by measuring the dependence of halo properties on both particle mass and several secondary simulation parameters. The most important of these is the "force softening scale", which controls the effective radius of dark matter particles. We also consider the impact of coarse timestep size.

- We report the $N_{\rm vir}$ cutoffs where our cosmological simulations have converged to shared mass relations (section 5.3.1). We do this for a wide range of halo properties and error tolerances.

- There are many halo properties (e.g. $x_{\rm off}$, $a_{1/2}$) where these cutoffs are consistent between simulations. For these properties, most analyzes can simply use a set of conservative "convergence limits" at modest values of $N_{\rm vir}$ (Table 5.2.3).

- For similarly high levels of agreement, other commonly used properties (e.g. $V_{\rm max}$, c/a) behave differently between simulations. Such levels of agreement can require $N_{\rm vir}$ as large as $\approx 10^5 - 10^6$ (section 5.3.2 and Fig. 5.3).

- This disagreement is partially because some simulation suites have internally converged to different solutions. We demonstrate this for Multidark and IllustrisTNG-Dark (section 5.3.3). The reasons for this disagreement between converged simulations are currently unknown.

- We show that many halo properties (e.g., $V_{\rm max}$, c/a, and subhalo abundances) exhibit a strong dependence on force softening (section 5.4). The biases associated with this dependence can be comparable to the impact of baryons on these properties.

- We develop a model which estimates the bias in $V_{\rm max}$ due to large force softening scales (section 5.5). This model predicts the dependence of $V_{\rm max}$ on force softening and most of the dispersion in simulation results for this property.

- We review previous studies on timestep size and conclude that commonly used timestepping schemes are unlikely to significantly bias halo properties (section 5.6.1). However, we outline several open questions in this topic.

We emphasize that *all analyzes can accommodate some level of numerical bias*. This chapter does not assert what those levels are. There is nothing incorrect about studying halos below the most conservative convergence limits, however such analyzes should incorporate some estimate of the associated systematic uncertainty. The results of this chapter will help analysts to identify the regimes where this is necessary and to estimate the resultant biases.

5.8 Appendices

5.8.1 Recalibrating the Plummer-Equivalence Scale

Rather than adopting a conversion based on the functional forms of kernels, in this work we use a novel Plummer equivalence scale, which has been calibrated from the empirical impact of varying h on halo velocity profiles. As is discussed at length in sections 5.5 and 5.6.1, large force softening scales can lower the inner densities of halos through a combination of lowering centripetal accelerations and (in some timestepping schemes) lowering the number of timesteps per orbit. These effects can impact the density of the halo at radii where forces are Newtonian as outer layers of the halo correctly respond to numerical density changes in the halo center.

We compare the results of Klypin et al. [2015b], van den Bosch and Ogiya [2018] and Ludlow et al. [2019], which measured circular velocity profiles for halos simulated with varying h for Plummer and Gadget kernels. Klypin et al. [2015b] and van den Bosch and Ogiya [2018] considered idealized isolated NFW halos, while Ludlow et al. [2019] studied stacked mass profiles from a series of small cosmological boxes.

We first consider the profiles in Ludlow et al. [2019]. These tests were performed with a "standard" Gadget timestepping parameter of $\eta = 0.025$ and with a higher resolution

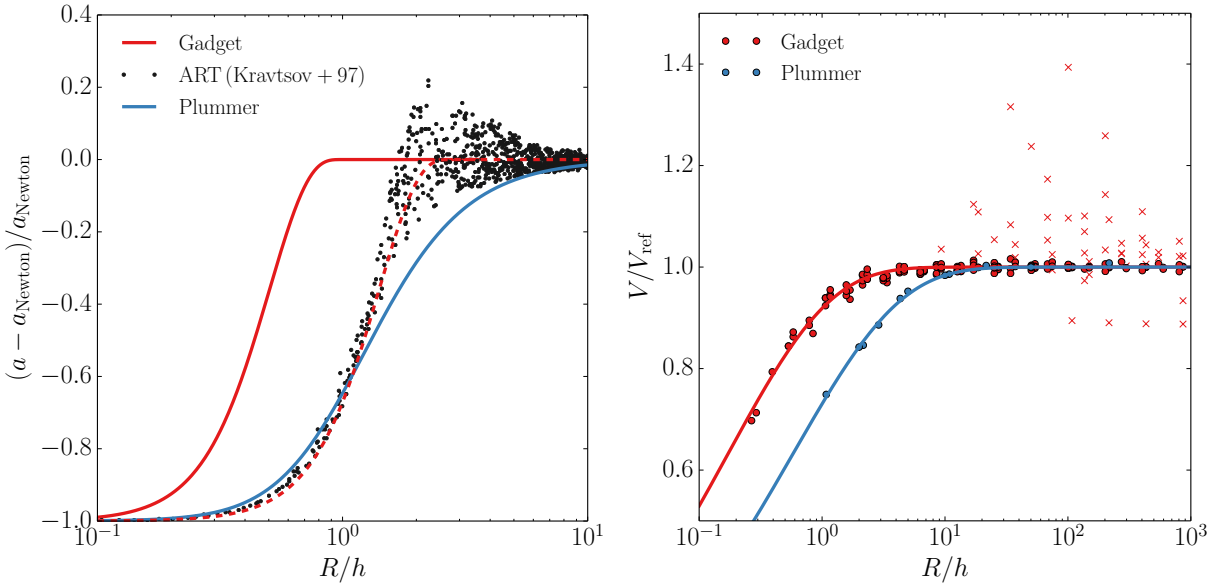

Figure 5.9: Left: The acceleration errors associated with different force softening schemes for a test point some distance r from a particle. Distances are noramalized by h, the scheme-specific formal resolution described in section 3.1.1. The points for ART are taken from Kravtsov et al. [1997]. The dashed red line shows the Gadget force error scaled by $h = 0.357\, h_{\rm Gadget}$. This plot illustrates the known fact that the traditional "Plummer-equivalent" conversion between formal resolution parameters leads to similar force errors for $r < \epsilon_\phi$, but highly discrepant force errors at larger radii. Right: The impact of different force softening schemes on halo circular velocity profiles. The points in this plot show the measured errors in circular velocity profiles as a function of the formal resolution, h, for different force softening schemes. Gadget measurements are from Ludlow et al. [2019], and Plummer measurements are from Klypin et al. [2015b] and van den Bosch and Ogiya [2018]. Points shown as red "x"s correspond to measurements from Ludlow et al. [2019] where deviations from the reference rotation curve were caused by timestepping errors. Curves show the results of fits against Eq. 5.13. These fits form the basis for our conversion of formal resolutions onto a shared scale. See Appendix 5.8.1 for discussion.

$\eta = 0.0025$. The $\eta = 0.025$ boxes were run with formal resolutions of $h_{\rm Gadget}(z = 0) = \{2^{-6}, 2^{-5}, ..., 2^{4}\} \times h_{\rm Gadget,fid}$ for $h_{\rm Gadget,fid}$ =0.6642 h^{-1} kpc and the $\eta = 0.0025$ boxes were run with $h_{\rm Gadget}(z = 0) = \{2^{-6}, 2^{-5}, ..., 2^{9}\} \times h_{\rm Gadget,fid}$. These profiles were stacked in mass bins centered on $M_{\rm 200c} = \{10^{9}, 10^{10}, 10^{11}, 10^{12}\} h^{-1} M_{\odot}$, and widths of 0.3 dex, corresponding to median $N_{\rm 200c}$ values of $\{6.4 \times 10^{5}, 6.5 \times 10^{4}, 6.3 \times 10^{3}, 6.7 \times 10^{2}\}$, respectively.

This range of parameters means that the Ludlow et al. [2019] measurements can probe the impact of $h_{\rm Gadget}$ across a wide range of halo radii, particle counts, and concentrations. The $\eta = 0.0025$ simulations allow the impact of numerical scattering due to coarse timesteps to be separated from timestep-independent effects like two-body relaxation effects and overly-large h.

The variation in profiles between $\eta = 0.0025$ boxes is at the per cent level and does not show strong dependence on h for the small h sclaes probed by these boxes, so we take the $h_{\rm Gadget} = h_{\rm Gadget,fid}$, $\eta = 0.0025$ box as our "reference" simulation. Our results are nearly identical if smaller values of h are used.

For each mass bin and $h_{\rm Gadget}$ value in the $\eta = 0.025$ boxes, we measure the value of $V_{\rm circ}(R)/V_{\rm circ,ref}(R)$ for $R = \{2^{-4}, 2^{-3}, ..., 2^{2}\} \times R_{\rm max,ref}$, where $V(R)$ is the circular velocity at radius R, $R_{\rm max}$ is the radius at which the circular velocity profile reaches its maximum value, and quantities subscripted with "ref" are measured in the reference simulation. We discard $V_{\rm circ}(R)/V_{\rm circ,ref}$ values at radii smaller than the convergence radii advocated for by Ludlow et al. [2019], although we find that our fits are strongly insensitive to this minimum radius. We also remove values which deviate by more than two per cent from values measured in $\eta = 0.0025$ simulations with identical $h_{\rm Gadget}$. While deviations in these regimes are relevant to convergence studies, they are caused by two-body scattering and time integration errors and not by errors due to large $h_{\rm Gadget}$.

We find that $V(R)/V_{\rm ref}$ has no meaningful dependence on particle count, radius, or halo concentration when scaled by $h_{\rm Gadget}/R$ [see also, the first three panels of fig. 5 in Ludlow

Fit type	Scheme	A	β
Free β	Gadget	0.172 ± 0.006	-0.522 ± 0.010
	Plummer	0.580 ± 0.026	-0.497 ± 0.016
Fixed $\beta = -0.522$	Plummer	0.616 ± 0.011	
Fixed $\beta = -0.497$	Gadget	0.160 ± 0.002	

Table 5.4: The best-fitting parameters for Eq. 5.13 for different force softening schemes. Gadget velocity deviations are measured at $\eta = 0.025$.

et al., 2019]. Because of this, we fit these measurements against a function of the form $V(R;h)/V_{\rm ref}(R)$, specifically:

$$\frac{V(R;h)}{V_{\rm ref}(R)} = 1 - \exp\left(-(Ah/R)^{\beta}\right). \tag{5.13}$$

Here, A and β are free parameters. We perform our fit using non-linear least squares minimization, because manual inspection of the likelihood posterior confirms that it is unimodal and approximately Gaussian near the minimum.

We show this fit in the right panel of Fig. 5.9 and give its best-fitting parameters in Table 5.8.1. $V/V_{\rm ref}$ measurements removed prior to fitting due to timestepping dependence are shown as "x"s. As an internal consistency check, we find that this fit predicts deviations equal to $0.1\,V(R;\,h)$ at $0.76\,h$, which is consistent with fig. 5 in Ludlow et al. [2019].

The lack of dependence on R, particle count, or concentration means that we can safely compare these fits against tests performed on narrower radius, particle count, and concentration ranges. We combine the $R = R_{\rm max}$ measurements from Klypin et al. [2015b] and the $R = R_s/2$ measurements from van den Bosch and Ogiya [2018] for our Plummer kernel data set. Our results are unchanged if we restrict ourselves to the results of either paper.Both studies analyze idealized NFW profiles instead of cosmological boxes, so we use NFW profiles as our reference $V_{\rm ref}(R)$ curves. The timestepping schemes used in both papers are substantially more aggressive than an $\eta = 0.025$ Gadget simulation, so we do not need to remove any simulations due to integration errors, as was done for the Ludlow et al. [2019] data set. However, we do remove the $h = 10^{-4}R_{\rm vir}$ simulation from van den Bosch and Ogiya [2018]

before fitting because that halo is undergoing thermalization at $R = R_s/2$.

We show this fit in the right panel of Fig. 5.9 and give its best-fitting parameters in Table 5.8.1.

Because A and β are slightly covariant, comparison between the A values of different fits can only be performed at a constant β. If β is fixed to -0.522 for the Plummer fit, $A_{\rm Plummer} = 0.616 \pm 0.011$, indicating that $\epsilon_{\rm Gadget} = A_{\rm Plummer}/A_{\rm Gadget} = 0.279 \pm 0.006$. Fixing $\beta = -0.497$ for the Gadget fit results in $\epsilon_{\rm Gadget} = 0.277 \pm 0.006$. Because Gadget-like softening kernels are more common in modern simulations than Plummer kernels, we choose to noramalize the relation to preserve the commonly-used conversion between $h_{\rm Gadget}$ and ϵ :

$$\epsilon = 1.284\, h_{\rm Plummer} = h_{\rm ART} = 0.357\, h_{\rm Gadget}. \tag{5.14}$$

Note that without comparable ART-based tests, we have arbitrarily chosen to take the convention from Klypin et al. [2016] that $h_{\rm ART} = 0.357\, h_{\rm Gadget}$. This leads to comparable mean force errors to Gadget at all radii. No analysis in this chapter relies on this portion of the convention.

We have performed this fit with several other functional forms in the place of Eq. 5.13 and found results which are similar. For example, when using $V(R;\, h)/V_{\rm ref}(R) = (1+(Ah/R)^2)^\beta$ – a form similar to the one used in Klypin et al. [2015b] – we find that ϵ ranges from $1.29, h_{\rm Plummer}$ to $1.28\, h_{\rm Gadget}$.

While Eq. 5.14 is most appropriate when estimating the effects of reduced centripetal forces on halo profiles, force softening also impacts halo profiles through two-body scattering and time integration errors. In regimes where these effects dominate, the depths and shapes of the kernel potentials may be more important than the long-distance deviations from Newtonian gravity. If so, these two body-scattering effects would be be best analyzed through ϵ_ϕ. To prevent readers from needing to frequently convert between ϵ conventions, we have

converted all values used in this chapter to ϵ, except in cases of specifying an algorithm which depends on ϵ_ϕ.

We note that Eq. 5.13 appears to "predict" that ϵ can be made arbitrarily small without error. This is only true over the R/ϵ range fitted here and only when timesteps are very fine. Coarse timesteps lead to very real errors at small ϵ (see section 5.6.1), the "convergence radius" which we use to select our fitting ranges has a weak dependence on ϵ [Ludlow et al., 2019], and fig. 6 of van den Bosch and Ogiya [2018] shows that aggresively small softening scales ($\epsilon \lesssim 10^{-4} R_{\rm vir}$) can accelerate the impact of two-body scattering. Similar effects can be seen in fig. 13 of Klypin et al. [2015b]. Large ϵ effects are only a portion of the story.

5.8.2 Fitting Parameters For Mean Halo Property Relations

In this Appendix we give the fitting parameters for each halo property considered in this chapter. These are listed in Table 5.5.

Variable	$\log_{10}(N_{\rm HR})$	d	α	$N_{\rm outlier}$
$M_{\rm 2500c}$	4	4	0	0
$M_{\rm 500c}$	3.25	4	0	0
$M_{\rm 200c}$	2	4	0	0
$M_{\rm 200m}$	2	4	0	0
$V_{\rm rms}$	4.5	4	0	0
$V_{\rm max}$	2.75	4	0	$4^\star$
$c_{\rm vir}$	3.5	4	0	$1^\star$
$R_{1/2}$	4	4	0	0
c/a	2.70	3	0	$9^\star$
$\lambda_{\rm Peebles}$	3	4	0	0
$\lambda_{\rm Bullock}$	3	4	0	0
$T/\|U\|$	3.5	4	0	0
$X_{\rm off}$	4	2	0	0
$V_{\rm off}$	4	2	0	0
$\Gamma(t_{\rm dyn})$	2	3	0	0
$a_{0.5}$	2.5	2	0	0
$a_{\rm MM}$	3	4	0	0
$M_{\rm peak}$	2.5	2	0	0
$V_{\rm peak}$	3.25	2	0	1
$\phi(M_{\rm 2500c})$	2.5	6	1	0
$\phi(M_{\rm 500c})$	2.5	6	1	0
$\phi(M_{\rm 200c})$	2.5	6	1	0
$\phi(M_{\rm vir})$	2.5	6	1	0
$\phi(M_{\rm 200m})$	2.5	6	1	0
$\phi(M_{\rm peak})$	2.5	6	1	0
$\phi(V_{\rm max})$	3.5	6	3	0
$\phi(V_{\rm rms})$	3.75	6	3	0
$\phi(V_{\rm peak})$	3.5	6	3	0

Table 5.5: The fitting parameters used for each halo property according to the procedure described in section 5.2.3. $N_{\rm HR}$ is the number of particles required for halos to be included in the fit, d is the degree of the fitted polynomial, α is the power law index of the mass scaling applied to data prior to fitting, and $N_{\rm outlier}$ indicates the number of simulations which were removed from the fit because they disagreed with other simulations within their own suite at high particle counts. Properties where outlier removal receives special discussion are marked with a *.

CHAPTER 6

THE THREE CAUSES OF LOW-MASS ASSEMBLY BIAS

This chapter is a modified version of my paper, Mansfield and Kravtsov [2019].

6.1 Introduction

The most visually striking feature of the large-scale structure of the universe is the clustered, web-like distribution of galaxies, with vast voids separated by walls and filaments [e.g., Bond et al., 1996]. Understanding the clustering of galaxies within the context of the Λ+Cold Dark Matter (ΛCDM) model relies on the generic model in which galaxies are formed by the dissipation of diffuse baryon plasma within growing dark matter halos [e.g., White and Rees, 1978]. Galaxy clustering is then interpreted in terms of the clustering of dark matter halos [e.g., see Desjacques et al., 2018, Wechsler and Tinker, 2018, for recent reviews], which is generally different from that of matter, i.e. the distribution of halos is "biased," relative to the mass distribution [Kaiser, 1984].

Halo bias depends primarily on halo mass [e.g., Mo and White, 1996, Sheth and Tormen, 1999] and this dependence is now both well-understood theoretically and well-calibrated numerically [Desjacques et al., 2018]. It is also now known that halo bias has secondary dependencies on other halo properties, such as formation time, concentration, spin, and ellipticity [Gao et al., 2005, Wechsler et al., 2006, Harker et al., 2006, Gao and White, 2007, Jing et al., 2007, Li et al., 2008, Faltenbacher and White, 2010, Villarreal et al., 2017a, Sato-Polito et al., 2018, Han et al., 2019]. The first such secondary dependence was found for halo formation time and its closely related proxy – halo concentration [Gao et al., 2005, Wechsler et al., 2006, Harker et al., 2006, Jing et al., 2007] and has become known as "assembly bias." Specifically, the bias of "old" halos (early formation time) is generally different than that of "young" (late formation time) halos, with the difference depending on halo mass and the definition of formation time[e.g., Li et al., 2008].

Assembly bias is important for the theoretical interpretation of galaxy clustering and its potential to provide useful cosmological constraints [e.g., Abazajian et al., 2005]. There have been significant observational efforts to detect halo assembly bias on galactic scales [see §5.4 and 6.2 of Wechsler and Tinker, 2018, for a review]. Nevertheless, unambiguous detection of halo assembly bias on galactic scales proved to be elusive due to the general difficulty of ensuring that host halo masses of galaxy subsamples with different clustering are similar [Campbell et al., 2015, Lin et al., 2016]. Lehmann et al. [2017] and Zentner et al. [2019] showed that simulation-based models with inherent assembly bias due to concentration dependence of halo clustering provide a better fit to clustering of Sloan Digital Sky Survey (SDSS) galaxies at some luminosities. However, it is not clear whether this is an unambiguous detection of assembly bias or improved fit is due to larger flexibility of the model compensating for a deficiency of the abundance matching assignment of galaxy luminosities. Hearin et al. [2015, 2016b] showed theoretically that the presence of galaxy conformity – the tendency of red galaxies to cluster around other red central galaxies – on large scales (i.e., in the "two-halo regime") would be a smoking gun of the halo assembly bias. However, this test also proved to be a non-trivial challenge due both to observational selection biases [Sin et al., 2017, Tinker et al., 2018] and due to the overall weakness of the two-halo conformity signal [Berti et al., 2017, Calderon et al., 2018, Tinker et al., 2018]. If low-mass halo assembly bias does have a signature in galaxy clustering, it would be important to understand its physical origin in order to construct robust and accurate models. Conversely, if halo assembly bias does not have observational signatures, it would be important to understand why tracers of halo age and tracers of galaxy age behave differently.

The focus of this chapter is to understand the physical origin of halo assembly bias, particularly in the regime of galaxy-scale halo masses. This is distinct from the origin of assembly bias at large masses, which is related to the properties of the peaks of the initial Gaussian density perturbations from which these massive halos collapse [Zentner, 2007, Dalal et al., 2008]. Peaks with the same mass but different curvature will cluster

differently because peaks with larger curvatures are located in lower-density environments, while peaks with smaller curvatures are in higher-density regions. This gives rise to assembly bias because peak curvature is directly related to a halo's mass accretion history, which is also affected by tidal torques from the surrounding anisotropic mass distribution [Desjacques, 2008]. Although this curvature-related bias can be reduced by compensating effects found in some proxies of halo age [Zentner, 2007, Sandvik et al., 2007, Mao et al., 2018], it is present for other age definitions and when more physical definitions of halo boundaries and masses are used [Chue et al., 2018].

At smaller halo masses, however, the physics of assembly bias is more complex because the mass evolution of halos is determined by a combination of the properties of their initial density peaks, and also by non-linear processes [e.g., Wang et al., 2007, Hahn et al., 2009]. The simple and striking manifestation of this is that the sign of assembly bias switches for small-mass halos when $c_{\rm vir}$ is used as a measure of halo age [Wechsler et al., 2006, Dalal et al., 2008].

A number of studies have explored the physical processes that can give rise to halo assembly bias in the small-mass regime. One readily apparent process is the non-linear effects that a massive host halo can exert on its smaller-mass neighbors. In particular, "splashback" (often also called "backsplash") subhalos pass within the inner regions of a larger halo but are located outside its virial radius at the epoch of analysis. Typically, analysis is done using only a single simulation snapshot, and the single-epoch isolation criteria used to distinguish subhalos from distinct halos will mix splashback subhalos into the distinct halo population. However, splashback subhalos will have had their mass accretion histories truncated due to their previous close encounters with their hosts and have thus been studied as a potential source of low-mass assembly bias [Wang et al., 2009, Li et al., 2008, Wetzel et al., 2014, Sunayama et al., 2016]

Although splashback subhalos are mostly found within three virial radii of their host halo, they can give rise to an assembly bias signal at much larger distances. This is because

at large scales the spatial distribution of splashback subhalos will track the distribution of their massive hosts and will therefore be more strongly clustered than that of distinct halos. A similar effect would occur if subhalos located within the virial radius of their host were included in the sample used to measure halo clustering and assembly bias. This is illustrated in Fig. 6.1, which compares the clustering of early- and late-forming halos with splashback subhalos included and removed, respectively. Removing splashback subhalos significantly reduces the difference in clustering between the two halo samples, even on scales much larger than the virial radius of the most massive halos within the volume. Nevertheless, multiple studies have demonstrated that splashback subhalos alone cannot be responsible for the entire assembly bias signal [Wang et al., 2009, Sunayama et al., 2016], a fact that can be seen visually in Fig. 6.1. A similar conclusion was reached by Hearin et al. [2015], albeit in the related but distinct context of galactic conformity.

Another process that could contribute to assembly bias is the truncation of a halo's mass growth by the tidal force generated its most gravitationally-dominant neighbor [Hahn et al., 2009, Behroozi et al., 2014, Hearin et al., 2016b, Salcedo et al., 2018, Johnson et al., 2019]. Even though single-halo tidal forces become small beyond $\approx 3 - 5 \times R_{\rm vir}$ of the host, the halos truncated by these forces can give rise to large-scale assembly bias in a way similar to splashback subhalos. A similar truncation of halo mass growth can be caused by the overall tidal force from all of the surrounding halos and structures in the matter distribution [Hahn et al., 2009, Wang et al., 2011, Paranjape et al., 2018, Musso et al., 2018], as the largest filaments and sheets generate strong tidal fields throughout their volumes. Since these structures can be several tens of Mpc in size, they can comfortably give rise to assembly bias on large scales. This effect has been characterized in terms of both the tidal force and the anisotropy of the tidal field, although, in practice, a high degree of anisotropy tends to correlate with the magnitude of the tidal force, so it is not clear that the two effects can be separated cleanly.

Finally, the gravitational heating of matter within large-scale structure structure has

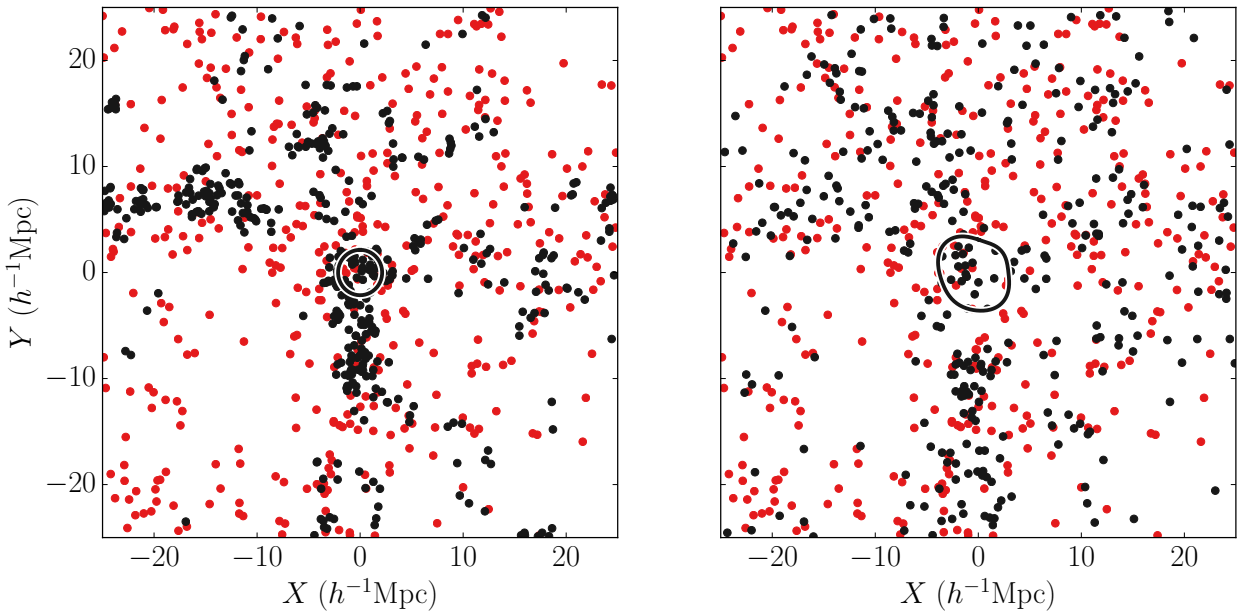

Figure 6.1: The effect of subhalo classification on the apparent distribution of "old" and "young" halos and their relative clustering. Both panels show the distribution of halos in a 25 h^{-1}Mpc cube centered on the largest cluster in the Bolshoi simulation. In the left panel, halos within the virial radii of larger hosts have been classified as subhalos and removed. The 15% of halos with the smallest $c_{\rm vir}$ ("young" halos) are plotted in red, while the 15% of halos with the largest $c_{\rm vir}$ ("old" halos) are plotted in black. For scale, the virial radius of the central cluster is shown as a black circle. While both young and old halo samples are distributed non-uniformly, old halos cluster more strongly and form prominent structures on scales exceeding $\approx 20\ h^{-1}$Mpc. Right panel: the same volume but all halos within the splashback shell of a larger host have been classified as subhalos and removed. For scale, the splashback shell of the central cluster is plotted in black. The age-dependent clustering of halos in the right panel, while still visually apparent, is significantly weaker. This is because splashback subhalos are preferentially old and trace the more clustered distribution of their massive hosts.

been proposed as a process that can contribute to assembly bias [Wang et al., 2007, Dalal et al., 2008]. For example, matter within the deep potentials of filaments can acquire large velocities during accretion, and thus cannot be accreted by small-mass halos located within the filament. The smaller accretion rates of such halos would thus give rise to assembly bias. Note that although gravitational heating and strong tidal forces generally happen in similar regions, they are physically distinct phenomena: tidal forces arise via large second derivatives in the gravitational potential, while gravitational heating is caused by the potential depth.

Although significant effort has been devoted to studying these effects [Wang et al., 2007, Dalal et al., 2008, Wang et al., 2009, Hahn et al., 2009, Wang et al., 2011, Li et al., 2013, Wetzel et al., 2014, Sunayama et al., 2016, Hearin et al., 2016b, Paranjape et al., 2018, Salcedo et al., 2018, Musso et al., 2018, Johnson et al., 2019], their relative importance and a coherent physical picture for the origin of low-mass halo assembly bias has not yet been established. The primary goal of this chapter is to rectify this. To this end, we define a set of quantitative proxies for each of the different processes outlined above and use them to investigate the relative contribution of these processes to the low-mass assembly bias signal. Specifically, we examine how efficiently sample cuts defined by each proxy can remove the signal.

The chapter is organized as follows. In section 6.2 we describe basic definitions and measurements and describe our cosmological simulations and halo sample, with sections 6.2.5-6.2.6 focusing on the proxies of the processes described above, and section 6.2.8 describing the core methodology of this chapter. In section 6.3 we present measurements and estimates of the relative contribution of different processes to low-mass assembly bias. We discuss topics related to the interpretation of this work in section 6.4 and summarize our results in 6.5. *The key results of this study are presented in Fig. 6.3.*

6.2 Methods

6.2.1 Simulations and codes

This chapter makes use of the Bolshoi and BolshoiP simulations described in Tables 3.1 and 3.1. We also use the simulations in the Erebos_CBol suite for some convergence testing.

Halos in the Bolshoi and BolshoiP simulations were identified using version 0.99RC2+ of the ROCKSTAR halo finder [Behroozi et al., 2013c], and version 1.0+ of the related consistent-trees method [Behroozi et al., 2013b] was used to construct halo merger trees. The catalogs and merger trees we use were downloaded from the CosmoSim database. We use the SHELLFISH algorithm to identify splashback shells – the 3D surfaces formed by the outermost apocenters of accreted matter [Mansfield et al., 2017][1]. We use the `Colossus` python package [Diemer, 2018][2] to calculate various relevant cosmological quantities and statistics and the halotools package [Hearin et al., 2016a][3] to calculate correlation functions efficiently.

6.2.2 Basic halo properties

As discussed in section 3.2, there are many ways to define halo mass. One can use M_Δ for a variety of overdensity contrasts, Δ, a non-parametric velocity-based tracer of potential depth, like $V_{\rm max}$, or a peak-based definition, like $M_{\rm peak}$ or $V_{\rm peak}$. It is non-trivial to compare assembly bias results across different mass definitions. This primarily manifests in the difference between peak and single-epoch definitions, which treat tidally stripped halos differently. The choice between $V_{\rm max}$- and M_Δ-based definitions also affects the strength of assembly bias because $V_{\rm max}/V_{\rm vir}$ is correlated with halo age. We explore these definitional choices at length in section 6.4.2, and urge readers to consider the discussion there before applying our results to alternative definitions.

1. https://github.com/phil-mansfield/shellfish

2. http://www.benediktdiemer.com/code/colossus/

3. https://halotools.readthedocs.io

As further discussed in section 3.2, there are a number of definitions of halo age used in the literature: single-epoch accretion rates [e.g., Lacey and Cole, 1993, Li et al., 2008], current halo properties - such as concentration - related to a halo's mass accretion history [e.g., Wechsler et al., 2006, Villarreal et al., 2017a, Sato-Polito et al., 2018], the epoch at which a halo first achieved half of its current mass [e.g., Gao et al., 2005], or a characteristic timescale of an analytic fit to halo mass accretion history [e.g., Wechsler et al., 2002, Zentner, 2007]. In this chapter, we primarily adopt $c_{\rm vir}$ as a tracer of halo age, with older halos having larger concentrations. We briefly explore the effect of using different definitions in section 6.4.2.

We focus on $c_{\rm vir}$ for several reasons. First, $c_{\rm vir}$ has been demonstrated to strongly correlate with a number of explicit indicators of halo age [Bullock et al., 2001, Wechsler et al., 2002, Zhao et al., 2003, Lu et al., 2006, Ludlow et al., 2013, 2014].) Although the correlation of two halo properties does not guarantee a similar effect on clustering [see Mao et al., 2018], this is not a concern for $c_{\rm vir}$ because it has been shown that low-mass halo assembly bias behaves similarly for $c_{\rm vir}$ and for the halo age proxy $a_{1/2}$ [Gao et al., 2005, Wechsler et al., 2006, Gao and White, 2007, see also our results in section 6.4.2]. Second, the connection between accretion history and $c_{\rm vir}$ has a solid theoretical underpinning [Zhao et al., 2003, Lu et al., 2006, Dalal et al., 2010], as demonstrated by the accuracy of the concentration models based on halo mass accretion history [e.g. Zhao et al., 2003, 2009, Dalal et al., 2010, Ludlow et al., 2014, Diemer and Joyce, 2019]. Third, the convergence criteria for halo density profiles [e.g. Power et al., 2003, Navarro et al., 2004, Springel et al., 2008], and for concentrations [see, e.g., section 3.2 in Diemer and Kravtsov, 2015] are well studied and it is thus relatively straightforward to identify regimes in which numerical concentrations can be trusted.

6.2.3 Definition of Halo Boundaries and Subhalos

Throughout this chapter, we define subhalos as the halos located within the boundary of a larger "host halo," and refer to all non-subhalos as "distinct halos." Of course, this classification depends on the definition of halo boundary and will have a clear meaning only if we use halo boundary definition that corresponds to an actual physical boundary.

Traditionally, spheres of radius $R_{\rm vir}$ (or some other overdensity radius) are used as halo boundaries, but this choice has a number of issues [see, e.g., Diemer et al., 2013b, More et al., 2015]. The first issue is that that there is no commonly-used overdensity radius that corresponds to any physical change or feature in the radial profiles of various halo properties [see, e.g., fig. 3 of Diemer et al., 2013a]. The second issue is that many studies have established that a substantial fraction of bound subhalos and matter have first orbits whose apocenters take objects out to as far as $\approx 2-3\times R_{\rm vir}$ of the host halo [Gill et al., 2005, Ludlow et al., 2012, Mansfield et al., 2017, Diemer, 2017a].

Fortunately, halos *do* have unambiguous edges manifested as sharp drops in density and caused by the pileup of particles at the apocenters of their first orbits. These edges in form 3D surfaces called "splashback shells," and enclose almost all matter and subhalos ever accreted by a halo. Halos outside $R_{\rm vir}$ of their host, but within its splashback shell are called "splashback subhalos."[4]

Splashback subhalos can be identified and removed in one of two ways. The first is a classification based on the past halo trajectories, where merger trees are used to determine whether a halo has ever been within a larger host [e.g., Ludlow et al., 2009, Wang et al., 2009, Diemer, 2017a, Diemer et al., 2017]. The second is to directly identify splashback shells of halos and flag all halos within them as subhalos. We adopt the second approach as our fiducial classification method, but employ both throughout the chapter to ensure that our

4. The terminology used to refer to these objects is varied: different authors refer to them as "backsplash suhalos" or "splashback subhalos," and often refer to them as "halos" instead of "subhalos." All these terms refer to the same concept. Some authors may use the term "flyby [sub]halos" interchangeably with "splashback [sub]halos," although the former term generally implies that merger tree analysis has been used.

results are robust and do not rely on the specifics of either approach.

For lexical clarity, we refer to subhalos identified through merger tree analysis as "flyby subhalos" and subhalos identified through the construction of splashback shells as "splashback subhalos."

Flyby Subhalos

To identify flyby subhalos, we use the following procedure for each halo in the $z = 0$ halo catalog. First, using consistent-trees [Behroozi et al., 2013b], we identify the main-line branch for the halo, labeling the $z = 0$ halo the "root halo" and all other halos on the branch its "progenitor halos." If any halos on the branch are within the virial radius of another halo at any redshift, the root is flagged as a flyby subhalo.

This process is complicated by the fact that during major mergers the virial radii of both merging halos fluctuate significantly and it is common for both host halos to be at least temporarily identified as subhalos of one another. This can lead to the final host halo being misidentified as a flyby subhalo of an object that no longer exists once the merger is complete. To rectify this, if the search of a root halo's progenitors reveals that some progenitor, P, is within $R_{\rm vir}$ of a host halo, H, we only classify the root halo of P as a flyby subhalo when the following three conditions are met:

1. H must have a root halo at $z = 0$.
2. The root halo of H must not be within $R_{\rm vir}$ of the root halo of P.
3. The root halo of H must have a strictly larger mass than the root halo of P.

Our tests indicate that just enforcing conditions 1 and 2 is sufficient to correct the overwhelming majority of false classifications. This procedure can be extended to root redshifts other than $z = 0$.

Although the identification of flyby subhalos is well-defined and only requires the use of a merger tree, it is not without drawbacks. First, the method uses $R_{\rm vir}$, which as we

discussed above does not correspond to a physical halo boundary. Second, this approach does not distinguish between ordinary subhalos with apocenters outside $R_{\rm vir}$, and subhalos that may have undergone dynamical three body interactions that resulted in their unbinding and ejection and are a qualitatively distinct population from splashback subhalos. Although a substantial fraction of subhalos may have undergone such interactions [Sales et al., 2007, Ludlow et al., 2009], we find that halos which have been ejected from the splashback shell are rare and do not have an impact on our analysis (see section 6.3.5). Third, this method does not count halos within the splashback shell on their first infall as subhalos, even though this population is similar to first-infall halos within $R_{\rm vir}$, which this method does classify as subhalos.

Splashback Shell Subhalos

The simplest way to estimate the size of a halo's splashback shell it to approximate it as a sphere and estimate its radius from the location of sharp steepening it causes in the halo's density and subhalo number density profiles [e.g. Fillmore and Goldreich, 1984, Bertschinger, 1985, Diemer and Kravtsov, 2014, Adhikari et al., 2014, More et al., 2015, Diemer, 2017a, Diemer et al., 2017]. This radius is then called the "splashback radius," $R_{\rm sp}$. However, the application of this method for individual halos is not straightforward [see Mansfield et al., 2017]. In addition, actual splashback shells are not spherical and spherical approximation may result in misclassification of a certain fraction of subhalos. For this reason, we use the Shellfish algorithm [Mansfield et al., 2017] to identify fully 3D splashback shells.

The Shellfish algorithm identifies splashback shells by measuring sharp density drops in many 1D density profiles along tens of thousands of lines of sight around a halo and fits a flexible smooth 3D surface to their location [Mansfield et al., 2017]. Once Shellfish has identified splashback shells, we use the efficient intersection-checking method described in Appendix 6.6.2 to flag all halos within the splashback shell of any larger halo as splashback subhalos.

There are three complications to using SHELLFISH which must be addressed before it can be used to construct subhalo catalogs: its $N_{200\mathrm{m}}$ convergence limit, the occurrence of rare but catastrophic fitting failures, and its behavior for low-accreting hosts. We perform extensive tests on all three issues and find that once accounted for in the ways described below, they do not have a significant effect on our results.

First, SHELLFISH has a rather stringent convergence limit and requires that halos have more than 5×10^4 particles within $R_{200\mathrm{m}}$, the overdensity radius corresponding to $\Delta = 200\,\rho_{\mathrm{m}}$, to achieve R_{sp} measurements with accuracy better than 5%. This corresponds to the $M_{200\mathrm{m}} \gtrsim 7 - 8 \times 10^{12}\ h^{-1} M_{\odot}$ or $V_{\mathrm{peak}} \gtrsim 280$ km s^{-1} in the Bolshoi and BolshoiP boxes. Below this mass, we use the fitting formula for the median R_{sp} provided in Mansfield et al. [2017], and flag halos within spheres of radius R_{sp} instead. Tests using the higher resolution L0063_CBol box from Diemer and Kravtsov [2014] indicate that this results in a negligible number of subhalo misclassifications compared to using real SHELLFISH-identified splashback shells because the majority of the splashback subhalos in our mass range have hosts larger than 280 km s^{-1}.

The second complication is that for a small number of host halos [$\approx$ 1%, Mansfield et al., 2017], irregularities in the local density field cause SHELLFISH to fail to identify the correct surface shape, adopting a barbell-shaped surface instead, which can cause subhalos well within R_{vir} to be misclassified as distinct halos. To mitigate this, we mark halos as splashback subhalos if they fall within either their host's splashback shell or within a sphere centered on that host of radius R_{vir}. We analyzed the distribution of the minimum radii of SHELLFISH shells in halos which were visually-identified to be unaffected by this surface fitting failure and found that the minimum radii are generally larger than R_{vir}. Thus, the procedure we adopt is unlikely to result in misclassification of distinct host halos as subhalos.

The third complication is that the SHELLFISH algorithm underestimates the size of splashback shells for halos that are accreting slower than the baseline pseudo-evolution accretion rate [Mansfield et al., 2017]. However, this only lowers the splashback radius by $\approx$ 10%

and few halos massive enough to host subhalos in our target mass range accrete this slowly, so it is not expected to be a significant issue. Empirically, we find that virtually all flyby splashback subhalos whose hosts are in this accretion regime are also within the splashback shells of their hosts (see section 6.3.5), so we do not explicitly account for this effect.

6.2.4 Halo Sample

Although we will examine the mass-dependence of assembly bias in section 6.3.4, the majority of our analysis focuses specifically on low-mass halos. Our primary concern when defining a halo sample is to prevent the inclusion of halos whose convergence radii are large enough that they introduce numerical effects into ROCKSTAR's measurements of $c_{\rm vir}$. As mentioned above, the numerical reliability of density profiles has been well studied, but for cosmological simulations with small softening scales the exact convergence properties are covariant with particle count, softening scale, halo mass, and time stepping scheme [Power et al., 2003, Ludlow et al., 2018], so determining convergence limits for an individual simulation should always be done through the comparison of carefully constructed multi-box suites.

Because there is only a single Bolshoi box, we place an upper bound on the convergence limit using the CBol simulation suite described in Diemer and Kravtsov [2015]. Of particular note is the box CBol_L0125, which has the same particle mass to Bolshoi, but which has much larger timesteps within halo centers, implying that the convergence radius of Bolshoi should be smaller than that of CBol_L0125.[5] We find that when using the same ROCKSTAR version and configuration variables as our Bolshoi catalog, the $V_{\rm peak} - c_{\rm vir}$ relation for the CBol_L0125 box agrees with the higher resolution CBol_L0063 box above $V_{\rm peak} = 120$ km s^{-1}, corresponding to a somewhat conservative cutoff particle count of $N_{\rm peak} \approx 1.3 \times 10^3$.

Our low-mass halo sample includes halos with 120 km s^{-1} $< V_{\rm peak} <$ 220 km s^{-1} (approximately 1.7×10^{11} h^{-1} $M_\odot < M_{\rm peak} < 1.2 \times 10^{12}$ h^{-1} $M_\odot$). Due to the slope of the halo

5. The difference in softening scale between these boxes makes an exact comparison difficult without a detailed analysis beyond the scope of this chapter. See Diemer and Joyce [2019] for some additional discussion on the subtleties of comparing Bolshoi to this simulation suite.

mass function, the majority of halos will be close to the lower mass limit, making the choice in upper mass limit less important. We chose the upper mass limit so our sample spans roughly a factor of eight in $M_{\rm peak}$ and find that our results are not particularly sensitive to this choice.

6.2.5 Measuring Tidal Force Strength

Tidal forces have been proposed as a potential cause of assembly bias [Hahn et al., 2009, Wang et al., 2009, Hearin et al., 2016b, Salcedo et al., 2018, Paranjape et al., 2018, Johnson et al., 2019] because they can slow down, stop, or reverse mass accretion. These fields are strongest in dense environments, such as within large-scale filaments or near the outskirts of massive halos, allowing distant halos in similar environments to have correlated accretion histories. Below, we describe methods for measuring the strength of both the single-halo tidal field, and the large-scale tidal field.

Tidal Force From a Single Halo

A typical simplifying assumption when calculating the tidal force felt by a halo is to assume that it is primarily caused by a single massive halo. If one also assumes that the point of interest is orbiting around that halo on a circular orbit, one can compute the tidal Hill radius, $R_{\rm Hill}$, corresponding to the distance to the nearest two Lagrangian points when the effective potential is approximated to second order. However, the assumptions that are made in calculating $R_{\rm Hill}$ are not correct for distinct halos in a ΛCDM cosmology. This is because these halos are almost never on circular orbits around each other and, as we discuss in section 6.2.5, the tidal force generally has a significant contribution from multiple halos and from the large-scale matter distribution. Thus, formally, the Hill radius is not a physically meaningful quantity for distinct halos. Nevertheless, the classical Hill radius can be used to estimate the tidal force of a halo's most gravitationally-dominant neighbor.

As a simple and definitionally robust proxy for $R_{\rm Hill}$ we use the virial radius-scaled

distance, $D_{\rm vir,i}$, for every distinct halo i:

$$D_{\rm vir,i} = \min_j \left\{ \frac{R_{ij}}{R_{{\rm vir},j}} \right\} \tag{6.1}$$

$$= 3^{1/3} \min_j \left\{ \frac{R_{ij}}{R_{\rm vir,i}} \left(\frac{M_{{\rm vir},i}}{3M_{{\rm vir},j}} \right)^{1/3} \right\} = 3^{1/3} \frac{R_{{\rm Hill},i}}{R_{{\rm vir},i}} \tag{6.2}$$

where j runs over all distinct halos within some search radius, R_0, which are more massive than the halo, and R_{ij} is the distance between halos i and j. halos with smaller $D_{\rm vir}$ experience larger tidal forces and halos with larger $D_{\rm vir}$ have smaller tidal forces. As Eq. 6.2 shows, $D_{\rm vir}$ is proportional to $R_{\rm Hill}$. This means that a rank-ordering by $D_{\rm vir}$ is equivalent to a rank-ordering by $R_{\rm hill}/R_{\rm vir}$, while formally $D_{\rm vir}$ is always a well-defined quantity and also allows for easy comparison with other assembly bias studies [e.g., Villarreal et al., 2017a, Salcedo et al., 2018, Johnson et al., 2019]

Our tests indicate that $D_{\rm vir}$ is well-converged for halos in the mass range 120 km s^{-1} < $V_{\rm peak}$ < 220 km s^{-1} for $R_0 \approx 100\, R_{\rm vir}$.

Large-Scale Tidal Radius and Mass

Although the single-source approximation is reasonably accurate for subhalos, our tests indicate that most distinct halos have multiple neighbors which contribute significantly to the tidal forces they feel. Moreover, we found that large-scale structures in mass distribution, such as filaments can contribute to the tidal force experienced by halos substantially. For example, by combining the assumption of cylindrical symmetry with the radial density profiles of filaments reported in Cautun et al. [2014], we construct a toy model for filament potentials. Applying this model, we find that even in moderate-sized filaments with $R_{\rm filament} \gtrsim 3\, h^{-1}$ Mpc, the tidal force generated by the filament is comparable to or stronger than the typical tidal force generated by a halo's single most gravitationally dominant neighbor.

For this reason, we compute the tidal radius of a halo calculated from the overall matter

distribution around a halo, $R_{\rm tidal}$, as a proxy for the combined tidal force from all neighbor halos and structures. To compute $R_{\rm tidal}$, we first construct the tidal tensor, $\mathbf{T}$, the Hessian of the external potential:

$$\mathbf{T} = \sum_k \frac{G\,m_k}{(x_k^2+y_k^2+z_k^2)^{5/2}} \times \begin{pmatrix} y_k^2+z_k^2-2x_k^2 & -3x_k y_k & -3x_k z_k \\ -3x_k y_k & x_k^2+z_k^2-2y_k^2 & -3y_k z_k \\ -3x_k z_k & -3y_k z_k & x_k^2+y_k^2-2z_k^2 \end{pmatrix}. \tag{6.3}$$

Here, k runs over all particles between two search radii, $R_{\rm min}$ and $R_{\rm max}$, m_k is the mass of particle k, and x_k, y_k, and z_k are the components of the displacement vector from the halo center to particle k. The tidal radius lies along the steepest repulsive axis of the tidal field, and since the tidal tensor, like all Hessians, equivalently describes the second derivatives at the origin of a paraboloid with eigenvectors pointing along the paraboloid's axes, the tidal field along the chief repulsive axis is given by

$$\Phi_{\rm steepest}(r_1) = \frac{1}{2}\alpha_1 r_1^2, \tag{6.4}$$

where α_1 is the most negative eigenvalue of $\mathbf{T}$, and r_1 is the radial distance along the corresponding eigenvector. We then assume that all non-tidal pseudo-forces (most notably the centrifugal force) are small and that at large distances the halo's mass is well-approximated by $M_{\rm vir}$, making the tidal radius and the corresponding tidal mass

$$R_{\rm tidal} = \left(-\frac{GM_{\rm vir}}{\alpha_1}\right)^{1/3}; \quad M_{\rm tidal} = M(< R_{\rm tidal}) \tag{6.5}$$

To increase computational efficiency, we make two further approximations. First, we do not add the tidal contribution from any particles further than $100\,R_{\rm vir}$, and second, we subsample particles by a factor of 64 and multiply m_k by 64 in Equation 6.3. Our tests

indicate that the combined effects of both these approximations on $R_{\rm tidal}$ are at the sub-percent level. We set the minimum cutoff radius, $R_{\rm min}$ to $10\,R_{\rm vir}$. This choice is discussed in detail in Appendix 6.6.3.

Some authors have suggested that the primary feature of interest in the tidal field is its anisotropy, which can be defined in a number of ways [Wang et al., 2011, Paranjape et al., 2018]. We chose to use $R_{\rm tidal}$ as a proxy for the total tidal force for two reasons. First, there are a number of different proxies for anisotropy and it is not clear a priori which definition is optimal. Second, we carried out analysis of assembly bias described in sections 6.2.7 and 6.2.8 using α_R and q_R from Paranjape et al. [2018] and t from Wang et al. [2011] as proxies for the tidal anisotropy and found that all of these proxies were not as efficient at removing assembly bias as $R_{\rm tidal}$.

6.2.6 Measuring Gravitational Heating

To gauge the contribution of gravitational heating to assembly bias, we use the mass of bound matter within the tidal radius, $R_{\rm tidal}$, defined in the previous section:

$$M_{\rm tidal,b} = \int_0^{R_{\rm tidal}} dR \int_0^{V_{\rm esc}(R)} dV \frac{dM}{dR\,dV} \tag{6.6}$$

Here, V is the absolute velocity of a particle relative to the halo center, while $V_{\rm esc}(R)$ is the escape velocity at a radius R from the halo center computed assuming that the halo is well-approximated by an NFW profile:

$$V_{\rm esc} = V_{\rm vir} \left\{ 2\,\frac{(1+c_{\rm vir})\,\ln(1+c_{\rm vir}x)}{x\,[(1+c_{\rm vir})\,\ln(1+c_{\rm vir}) - c_{\rm vir}]} \right\}^{1/2}. \tag{6.7}$$

Here, $x = r/R_{\rm vir}$, $V_{\rm vir} = \sqrt{GM_{\rm vir}/R_{\rm vir}}$, and $c_{\rm vir}$ is halo concentration. To speed up particle containment checks when computing mass profiles, we apply the algorithm described in Appendix 6.6.2.

We also construct the variable

$$M_{\beta,\mathrm{b}} = \int_0^{\beta\, R_{\mathrm{vir}}} dR \int_0^{V_{\mathrm{esc}}(R)} dV \frac{dM}{dR\, dV} \tag{6.8}$$

for some constant β. $M_{\beta,\mathrm{b}}$ allows us to isolate the effect of gravitational heating from the effect of external tidal fields because it does not include a dependence on R_{tidal}. Although a range of β were used in our analysis, our results are primarily reported in terms of $\beta = 3$, for reasons we describe in section 6.3.2.

While these approximations are standard practice for computing particle boundedness, it is likely that they break down significantly in the outskirts of halos. We discuss this in greater depth in Appendix 6.6.4 and argue that this should not have a significant effect on our results in section 6.4.1.

6.2.7 Assembly Bias Statistics

To study assembly bias, one must have a statistic that measures how clustering strength depends on a halo age proxy, c_{vir} in our case. The most direct approach is to split halos into high-c_{vir} and low-c_{vir} samples, measure the clustering strength of each sample independently using correlation functions, and compare them. There are multiple ways of doing this, ranging from measuring the two-point correlation function of halos, ξ_{hh}, in each c_{vir}-selected subsample to measuring the bias function, $b(r) = \xi_{\mathrm{hm}}/\xi_{\mathrm{mm}}$ [e.g, Gao et al., 2005, Gao and White, 2007, Faltenbacher and White, 2010]. While this family of approaches is a valid and commonly-used, there are a number of associated issues. First, the definition of subsamples is arbitrary, and the strength of the measured signal depends on this definition somewhat. Second, if small c_{vir} ranges are chosen to maximize signal strength, statistical errors increase due to the comparatively small number of halos used.

We use an alternative statistic – the marked correlation function [the MCF, Beisbart and Kerscher, 2000, Gottlöber et al., 2002] – which avoids this issue and which has been used in

a number of assembly bias studies [e.g., Wechsler et al., 2006, Villarreal et al., 2017a]. For a sample of objects with assigned mark, m, the MCF is computed as:

$$\mathcal{M}(r) = \frac{\langle m_i m_j \rangle_{i,j \in P(r)} - \langle m \rangle^2}{\langle m^2 \rangle - \langle m \rangle^2}. \tag{6.9}$$

Here, $P(r)$ is the set of all pairs which are separated by a distance within the same radial bin as r. Following Villarreal et al. [2017a], we define concentration marks for halos in narrow circular velocity bins as their percentile within the $c_{\rm vir}$ distribution of that bin. Specifically, we use ten logarithmic bins in $V_{\rm peak}$ from 120 km s^{-1} to 220 km s^{-1}. The narrow bin width is required because the $c_{\rm vir}$ distribution is mass-dependent. This, combined with the mass-dependence of clustering, would result in illusory assembly bias signals in any halo sample defined over a sufficiently large mass range.

6.2.8 Measuring the Connection Between Assembly Bias and Other Variables

To evaluate the relative contribution of different physical processes to assembly bias, we need a way to gauge how strongly proxies for these processes, such as $D_{\rm vir}$, $R_{\rm tidal}$, $M_{\beta,\rm b}$, $M_{\rm tidal}$, or $M_{\rm tidal,b}$, are related to assembly bias. One simple way to do this is to measure the correlation coefficient between $c_{\rm vir}$ and each variable. However, as discussed in section 6.2.8, any approach that relies on measuring the connection between a proxy and formation time has serious issues.

Instead, in this chapter, we follow an approach similar to that of Villarreal et al. [2017a]. We determine the strength of the connection between assembly bias and a proxy X by finding the percentage of halos ranked by X that need to be removed from the sample to eliminate the assembly bias signal. For example, if 30% of halos must be removed according to X before the assembly bias signal is eliminated, but only 5% of halos must be removed to achieve this for another proxy, Y, we conclude that the physical process traced by Y has

a more significant contribution to assembly bias than the process traced by X.

Specifically, we first sort distinct halos according to a proxy X, then remove a fraction of halos $f = N_{\rm removed}/N_{\rm tot}$ for a series of f values ranging from 0.01 to $N_{\rm distinct}/N_{\rm tot}$ in steps of 0.01. We then define $f_{\rm removed}$ as the minimum f for which the MCF is within $1-\sigma$ of zero. The sample variance of the MCF is estimated by dividing the simulation box into eight octants, and performing jackknife resampling these octants at a constant $f_{\rm removed}$. Note that our definition of $f_{\rm removed}$ is normalized by the total number of halos and not by the number of distinct halos to make it easier to combine with different subhalo classification schemes.

We use a similar method to estimate the sample variance of $f_{\rm removed}$ itself, computing $f_{\rm removed}$ with each octant removed and performing jackknife resampling. Note that these errors on $f_{\rm removed}$ account for contributions from sample variance computed using the same octants, which means that while the uncertainties accurately estimate the scatter on measurements in independent boxes, there is likely covariance between the $f_{\rm removed}$ errors measured for different proxies within the same simulation. This means that the uncertainty on the *relative ordering* of $f_{\rm removed}$ values for multiple proxies within a single simulation is likely to be smaller than these errors would estimate. We discuss this further in section 6.3.2.

When calculating $f_{\rm removed}$, we compute the MCF in the radial range $[6, 10]$ comoving $h^{-1}\,$Mpc. We have repeated all analysis in this chapter with several other choices of radial ranges and did not find any significant qualitative difference in results. The primary result of moving to larger radii is that the amplitude of the reference MCF becomes smaller relative to the error, meaning that smaller cutoffs are able to make the signal consistent with zero. Thus, to be conservative, we use a relatively small-radius cutoff. We illustrate this in Fig. 6.2, which shows the MCF after distinct halos below the $f_{\rm removed}$ cutoff for $M_{\rm tidal,b}/M_{\rm vir}$ have been removed from the sample: the MCF is consistent with zero out to 18 h^{-1} Mpc. We have repeated all analysis in this chapter using several different radial ranges and results remain qualitatively similar.

We note that this method is effective only for assembly bias models in which halos are initially unbiased or negatively biased but where a small subset of halos in extreme environments are pushed to older ages by some non-linear process. If, instead, assembly bias is strongly present in all environments, there will be no value of $f_{\rm removed}$ which can remove it. It is known that assembly bias is present across all halo ages [e.g., see fig. 3 in Wechsler et al., 2006], so a finding that there are variables with small values of $f_{\rm removed}$ would already put interesting constraints on the physics of assembly bias. We discuss this in more depth in section 6.3.

An important point to note about this approach is that the assembly bias signal may not remain zero at f values larger than $f_{\rm removed}$. In the model that we will outline in section 6.3, all halos experience "primordial" assembly bias due to the statistics of initial Gaussian peaks (following the arguments of Dalal et al. 2010), which corresponds to a negative MCF amplitude. halos below the non-linear mass scale experience various non-linear interactions which alter their ages in a way which correlates with density, thereby leading to the positive observed assembly bias. This evolution in the sign of assembly bias for low-mass halos can be seen in Appendix A of Hahn et al. [2009]. Since very aggressive cuts will eventually reduce the sample to halos which are within low-density void regions, and are thus in environments with lower effective non-linear mass scales, the samples of halos defined by larger f values can display this residual primordial assembly bias signal. Thus, in general we can expect assembly bias to either remain close to zero or become negative (the sign of the primordial bias) for larger values of f. Nevertheless, for the fiducial radial range of $6 - 10h^{-1}$ Mpc adopted in our analyses, the assembly bias does remain consistent with zero for larger values of f.

Note that these considerations do not invalidate our statement that cuts according to $f_{\rm removed}$ have "removed" assembly bias: these cuts result in a halo sample with assembly bias consistent with zero within uncertainties at all radii. Our arguments about what causes the observed positive assembly bias signal depend on how efficiently a given proxy allows

for the construction of such a sample. In principle these arguments could also be made by measuring how efficiently one recovers the primordial assembly bias signal, but it is not clear how this would be done in practice.

Difference Between $f_{\rm removed}$ and Age Correlation

A number of previous studies evaluated the contribution of a given physical process with an associated proxy, X, by measuring the correlation between X and a proxy of halo age, A [e.g., Hahn et al., 2009, Wang et al., 2011, Hearin et al., 2016b, Salcedo et al., 2018]. This can be done using the Spearman's rank coefficient, $\rho_S(A, X)$, or by measuring the slope of the average trend $X(A)$. While this approach provides indications of which proxies correlate well with halo age, by itself it cannot be used to gauge the relative contribution of different physical processes to assembly bias. This is because a correlation between age and proxy can only lead to assembly bias if clustering strength *also* varies strongly as a function of X. Comparison of the proxy–halo age correlation strength thus does not provide enough information to unambiguously gauge the contribution of the corresponding process to assembly bias. For example, $D_{\rm vir}$ and $R_{\rm tidal}/R_{\rm vir}$ have roughly the same level of correlation with $c_{\rm vir}$, but halos experience wildly different differential clustering with with respect to both variables. Consequently, assembly bias is not connected to these two variables with the same strength.

As an illustration, Table 6.3.2 lists values of $f_{\rm removed}$ and the Spearman's rank correlation coefficient, ρ_S, between $c_{\rm vir}$ and several different proxies and shows that these two quantities are almost completely unrelated. We therefore strongly recommend against drawing conclusions about assembly bias from measurements of correlation with halo age [see Mao et al., 2018, for additional discussion and caveats associated with using correlation coefficients in the context of assembly bias].

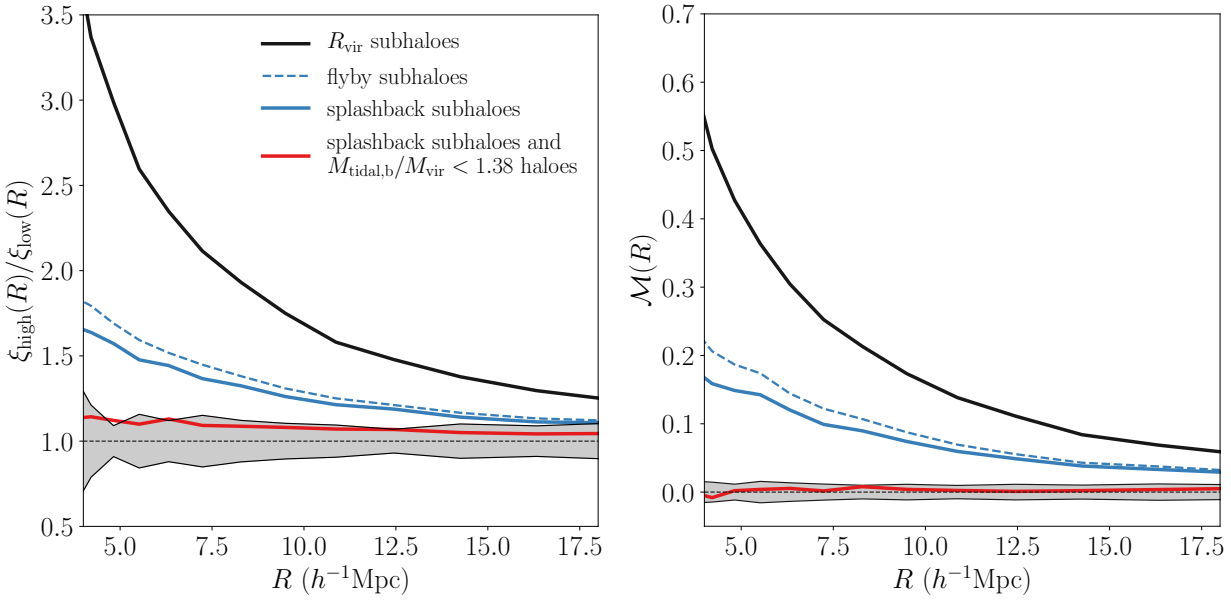

Figure 6.2: The effect of removing different halo populations on the low-mass (120 km s^{-1} < $V_{\rm peak}$ < 220 km s^{-1}) halo assembly bias signal. The left panel shows assembly bias measured as the ratio of the CF of the halos in the highest and lowest 15$^{\rm th}$ percentiles of $c_{\rm vir}$, while the right panel shows assembly bias measured as the $c_{\rm vir}$-based MCF. Lines are labeled by the groups of halos which were removed from the sample before measurement. The grey contours around zero show the 1-σ sample variance of the red curve. Uncertainties of the three other curves are comparable and not shown for visual clarity. Splashback subhalos have been removed in addition to the $M_{\rm tidal,b}$ cut for the red curve. Although high-$c_{\rm vir}$ halos cluster more strongly than low-$c_{\rm vir}$ halos when subhalos are excluded by $R_{\rm vir}$, most of this signal is due to splashback halos. When a small number of tidally truncated halos (10% of distinct halos, 6% of the total sample) are also removed, the difference becomes consistent with zero.

6.3 Analysis

6.3.1 Splashback Subhalos and Assembly Bias

We first test whether splashback subhalos misclassified as distinct halos by standard subhalo definitions (i.e., splashback subhalos outside $R_{\rm vir}$ of a larger host) are responsible for low-mass halo assembly bias. The number of halos removed by our different subhalo definitions is shown in Table 6.3.2. Our results are shown in Figure 6.2, using both methods discussed in section 6.2.7 for measuring assembly bias. The figure shows that splashback subhalos cannot account for the entirety of assembly bias, although they contribute about two thirds

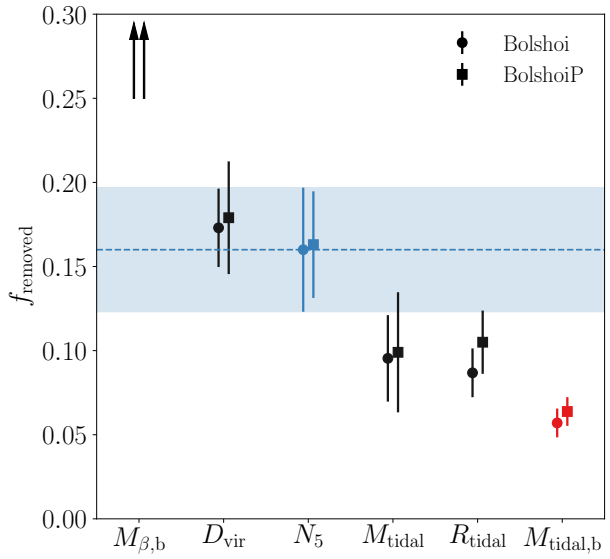

Figure 6.3: The fraction of *distinct* halos, $f_{\rm removed}$, rank-ordered by a given physical process proxy that need to be removed to eliminate $c_{\rm vir}$ assembly bias. Note that splashback subhalos have already been removed from the sample prior to computing $f_{\rm removed}$. The error bars indicate 1-σ sample variance. Each quantity listed on the x-axis is a proxy for a different physical process: $M_{\beta,b}$ is a proxy for gravitational heating with β adjusted to minimize $f_{\rm removed}$ (see §6.2.6), $D_{\rm vir}$ is a proxy for single-halo tidal fields (see §6.2.5), N_5 is an estimate of environmental density (see §6.3.2), $M_{\rm tidal}$ and $R_{\rm tidal}$ are proxies for large-scale tidal fields (see §6.2.5), and $M_{\rm tidal,b}$ is a proxy for a combination of large scale fields and tidal heating. The $f_{\rm removed}$ values for $M_{\beta,\rm b}$ are outside the vertical range of the plot, which is indicated by arrows (see Tables 6.3.2 and 6.3.2 for their actual values). Two proxies have been highlighted with colors: N_5 and $M_{\rm tidal,b}$. N_5 acts as our control: any variable which has a larger $f_{\rm removed}$ than N_5 is more weakly connected to assembly bias than a simple density proxy. A blue band has been added to the figure to make such comparisons easier. $M_{\rm tidal,b}$ is the most effective proxy at eliminating assembly bias, as it requires only $\approx 6\%$ of all halos (10% of distinct halos) to be removed.

of the signal. This is consistent with conclusions of the previous studies [Wang et al., 2009, Sunayama et al., 2016]. The novel feature of this analysis is that we find a similar effect for two independent definitions of the splashback halos: using evolutionary trajectories (§6.2.3) and using non-spherical 3D splashback shells identified using the Shellfish code (§6.2.3).

Note also that although results for the two definitions are similar, the two samples of halos are not identical. Flyby subhalos identified using merger trees are guaranteed to have passed their orbital pericenter and thus likely have experienced a strong tidal interaction with the host. On the other hand, when we use Shellfish all subhalos within the splashback shell are classified as splashback subhalos, including those halos that have entered the shell, but have not yet passed their pericenter. Given that both halo samples have exactly the same local environments, the fact that removal of infalling splashback subhalos results only in a small decrease of the assembly bias signal means that this portion of the assembly bias signal is due to the stripping subhalos experience during their pericenter passage. Conversely, any mass growth suppression subhalos experience on their way to pericenter is comparatively unimportant important.

We further compare the splashback subhalos and flyby subhalos in section 6.3.5.

6.3.2 Contribution of Tidal Truncation and Gravitational Heating to Assembly Bias

We now investigate how the truncation of halo mass growth by the tidal forces, both from a halo's most gravitationally-dominant neighbor and from the entire large-scale matter distribution, contributes to assembly bias. We also investigate the contribution of dynamical heating caused by the collapse of matter into sheets and filaments. To this end we use the five proxies of these processes defined in sections 6.2.5-6.2.6 – $D_{\rm vir}$, $R_{\rm tidal}$, $M_{\beta,{\rm b}}$, $M_{\rm tidal}$, and $M_{\rm tidal,b}$ – and evaluate what fraction of the distinct halo sample ranked by each of the proxies must be removed to eliminate the assembly bias signal.

$D_{\rm vir}$ is the $R_{\rm vir}$-normalized distance to the most tidally dominant halo. It is a proxy of

Subhalo definition	$f_{\rm subhalo}$		section
$R_{\rm vir}$ subhalos	0.27		§6.2.3
flyby subhalos	0.33		§6.2.3
splashback subhalos	0.37		§6.2.3
Removal criterion	$f_{\rm removed}$	ρ_S	section
$M_{\beta,\rm b}/M_{\rm vir} < 1.70 \pm 0.05$	0.448 ± 0.033	-0.47	§6.2.6
$D_{\rm vir} < 4.57 \pm 0.25$	0.183 ± 0.016	-0.16	§6.2.5
$N_5 > 18 \pm 1$	0.158 ± 0.018	0.09	§6.3.2
$M_{\rm tidal}/M_{\rm vir} < 1.67 \pm 0.07$	0.107 ± 0.025	-0.23	§6.2.5
$R_{\rm tidal}/R_{\rm vir} < 2.80 \pm 0.09$	0.089 ± 0.011	-0.19	§6.2.5
$M_{\rm tidal,b}/M_{\rm vir} < 1.38 \pm 0.02$	0.060 ± 0.005	-0.36	§6.2.6

Table 6.1: The fraction of halos in the Bolshoi simulation which are removed by the different cuts described in the text. The first three rows show the subhalo fraction, $f_{\rm subhalo}$, for the different subhalo cuts described in section 6.2.3. The last six rows correspond to the assembly-bias-removing cuts described in section 6.3.2 for different proxies and show $f_{\rm removed}$, the fraction of halos which must be removed after splashback subhalos have been cut from the sample, and ρ_S, the Spearman correlation coefficient between $c_{\rm vir}$ and a given proxy. Note that $f_{\rm removed}$ and $\rho_S(c_{\rm vir}, X)$ are completely uncorrelated, as discussed in section 6.2.8.

Subhalo definition	$f_{\rm subhalo}$		section
$R_{\rm vir}$ subhalos	0.28		§6.2.3
flyby subhalos	0.33		§6.2.3
splashback subhalos	0.38		§6.2.3
Removal criterion	$f_{\rm removed}$	ρ_S	section
$M_{\beta,\rm b}/M_{\rm vir} < 1.64 \pm 0.05$	0.401 ± 0.043	-0.47	§6.2.6
$D_{\rm vir} < 4.27 \pm 0.21$	0.167 ± 0.014	-0.18	§6.2.5
$N_5 > 21 \pm 2$	0.152 ± 0.025	0.09	§6.3.2
$M_{\rm tidal}/M_{\rm vir} < 1.58 \pm 0.04$	0.091 ± 0.016	-0.24	§6.2.5
$R_{\rm tidal}/R_{\rm vir} < 2.74 \pm 0.08$	0.093 ± 0.010	-0.20	§6.2.5
$M_{\rm tidal,b}/M_{\rm vir} < 1.35 \pm 0.02$	0.059 ± 0.005	-0.36	§6.2.6

Table 6.2: The same as Table 6.3.2, but for the BolshoiP simulation

the one-halo contribution to the tidal force proportional to the traditional Hill radius. $R_{\rm tidal}$ is the tidal radius calculated using only the distant matter distribution and $M_{\rm tidal}$ is the mass contained within the tidal radius. $M_{\beta,{\rm b}}$ is the bound mass within $\beta\, R_{\rm vir}$ for a specified constant β and serves as a proxy of dynamical heating. Finally, $M_{\rm tidal,b}$ is the bound mass contained within the tidal radius and serves as a proxy for the combined effects of the total tidal force and gravitational heating.

Some care needs to be taken in setting β for the proxy $M_{\beta,{\rm b}}$. The most straightforward option would be minimize the value of $f_{\rm removed}$ across all values of β, but this procedure selects $\beta \approx 1.5$, which will typically be within the halo's own splashback shell. $M_{\beta,{\rm b}}$ therefore correlates with $c_{\rm vir}$ simply because the latter determines the mass distribution within the halo. Indeed, we find the Spearman rank coefficient $\rho_S(M(< 1.5 \times R_{\rm vir}), c_{\rm vir}) = -0.26$, even before any unbinding procedure has been used. Instead, we choose to set $\beta = 3$. At this distance, correlations between the total enclosed mass and $c_{\rm vir}$ are negligible, and $\beta\, R_{\rm vir}$ will generally be larger than $R_{\rm sp}$. This choice has little effect on $f_{\rm removed}$, which remains approximately the same for $\beta \gtrsim 2$.

The proxies described above are strongly (anti-)correlated with local matter density. Thus, when we rank-order halos using these proxies and make cuts, we need to distinguish this procedure from simple density cuts, which do not differentiate between particular physical processes that operate in high-density regions. To this end, we use the number of distinct halos with $120\ \ {\rm km\,s^{-1}} < V_{\rm peak} < 220\,{\rm km\,s^{-1}}$ located within X comoving $h^{-1}\,{\rm Mpc}$ of the center of a halo, N_X, as a proxy of the density of the local environment. We tested radii ranging from $1 - 10\,h^{-1}\,{\rm Mpc}$ and found that the assembly bias signal can be eliminated by removing the smallest fraction of halos for $X = 5$. We thus use N_5 as our fiducial local environmental density proxy.

In Fig. 6.3 we show the fraction, $f_{\rm removed}$, of all halos rank-ordered by different proxies that must be removed to eliminate the assembly bias signal (see section 6.2.8). The corresponding $f_{\rm removed}$ thresholds for each proxy are presented in Table 6.3.2, and the red curves

in Fig. 6.2 show clustering strength as a function of distance after such a cut has been made to $M_{\rm tidal,b}$. Note that statistical errors on the MCF are smaller relative to its amplitude than errors on the $\xi_{\rm high}(r)/\xi_{\rm low}(r)$ curve, which is one of the chief reasons that we use the former in calculations of $f_{\rm removed}$.

The first feature apparent in Fig. 6.3 is that it is *possible* to remove assembly bias by making a cut on the local density, meaning that assembly bias is only present in high-density regions. This is consistent with models which predict that low-mass assembly bias is caused by non-linear processes, but is not necessarily a generic prediction of such models, as one could imagine assembly bias existing in all regions to different degrees of severity. Fig. 6.3 also shows that the portion of assembly bias which is not caused by misclassified splashback subhalos is due to a small number of halos in extreme environments: the cut $M_{\rm tidal,b}/M_{\rm vir} < 1.38$ removes only 6% of all halos but reduces assembly bias to statistically undetectable levels. For comparison, the cut to the density proxy N_5 removes assembly bias when 14% of halos are removed.

Further testing shows that there are two reasons why assembly bias can be eliminated by removing only a small fraction of halos. First, the mean value of $c_{\rm vir}$ ceases to be a strong function of these proxies once the halos below the $f_{\rm removed}$ cutoff have been removed from the sample. Second, halo clustering strength varies strongly as a function of proxy value within the cutoff range, but is almost constant throughout the remaining sample.

Finally, Fig. 6.3 shows that $f_{\rm removed}$ for both $D_{\rm vir}$, a proxy for the single-halo tidal force, and $M_{\beta,\rm b}$, a proxy for dynamical heating, are at least as large as $f_{\rm removed}$ for N_5. Even if $M_{\beta,\rm b}$ uses values of β small enough that it is primarily picking up features in the halo's own density profile, $f_{\rm removed}$ stays above 0.25. This means that the effect of single-halo tidal forces and dynamical heating on assembly bias cannot be distinguished from the trivial effect of environmental density on halo bias, which means that neither can account for the assembly bias on their own.

In contrast, $f_{\rm removed}$ for $R_{\rm tidal}$, $M_{\rm tidal}$, and $M_{\rm tidal,b}$ are smaller than for N_5, indicating

that these proxies are more closely connected to assembly bias than local density. The fact that $R_{\rm tidal}$ and $M_{\rm tidal}$, which are calculated using only the large-scale contribution to the tidal field, have lower $f_{\rm removed}$ than $D_{\rm vir}$ shows that it is the tidal force from large-scale structures, not from individual halos, that play the dominant role in the assembly bias. $M_{\rm tidal,b}$ has the lowest $f_{\rm removed}$ and is thus the most closely connected to assembly bias of all the proxies we consider.

To summarize, the results of this and previous subsections show that $\approx 70\%$ of the low-mass assembly bias signal in $c_{\rm vir}$ is due to splashback subhalos. The remaining $\approx 30\%$ of the signal is due to 10% of distinct halos (6% of all halos) that are affected by a combination of the truncation of their mass growth by large-scale tidal fields and dynamical heating caused by the collapse of sheets and filaments. There are thus three different physical processes that affect halo mass growth which all contribute significantly to the assembly bias signal.

6.3.3 The Spatial and Concentration Distributions of the Halos Responsible for Assembly Bias

In Fig. 6.4 we show the spatial distribution of splashback subhalos located outside $R_{\rm vir}$ of their hosts in a 25 h^{-1} Mpc thick slice of the Bolshoi simulation volume. In the same volume, we show the sets of distinct halos that are removed under the criteria $N_5 > 18$ and $M_{\rm tidal,b}/M_{\rm vir} < 1.38$, which each independently eliminate assembly bias. We also show the spatial distribution of a random $\times 5$ subsample of the set of distinct halos that were not removed by the $M_{\rm tidal,b}/M_{\rm vir} < 1.38$ cut.

Fig. 6.4 shows that both splashback subhalos and halos with low $M_{\rm tidal,b}/M_{\rm vir}$ values are strongly clustered in the fabric of the cosmic web: they lie within filaments, sheets, and nodes with characteristic scales of tens of h^{-1} Mpc. Splashback subhalos cluster strongly because they trace the spatial distribution of their massive host halos, which are predominantly found in these dense environments. halos with low $M_{\rm tidal,b}/M_{\rm vir}$, on the other hand, are strongly clustered because the two physical processes that reduce $M_{\rm tidal,b}/M_{\rm vir}$ – strong tidal forces

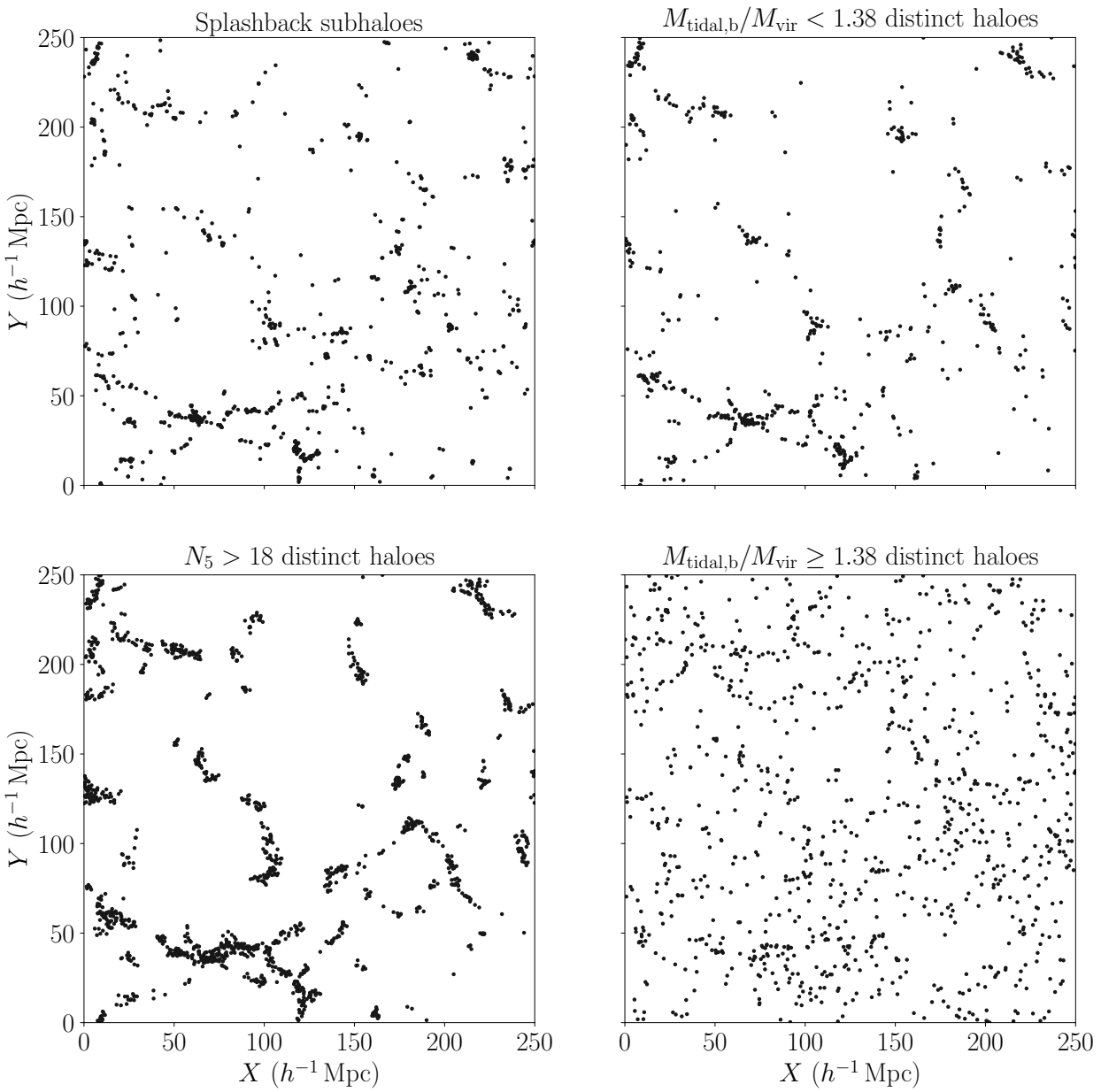

Figure 6.4: The spatial distribution of different classes of halos within a 25 h^{-1}Mpc-thick slice of the Bolshoi simulation. The top left panel shows the location of splashback subhalos outside $R_{\rm vir}$ of their hosts, the top right panel shows distinct halos with $M_{\rm tidal,b}/M_{\rm vir} < 1.38$, the bottom left panel shows distinct halos with $N_5 > 18$, and the bottom right panel shows the remaining halos after halos in the two top panels have been removed. The halos in the bottom right panel have been subsampled by a factor of five. Note that the assembly bias signal for the halos in the bottom right panel is consistent with zero.

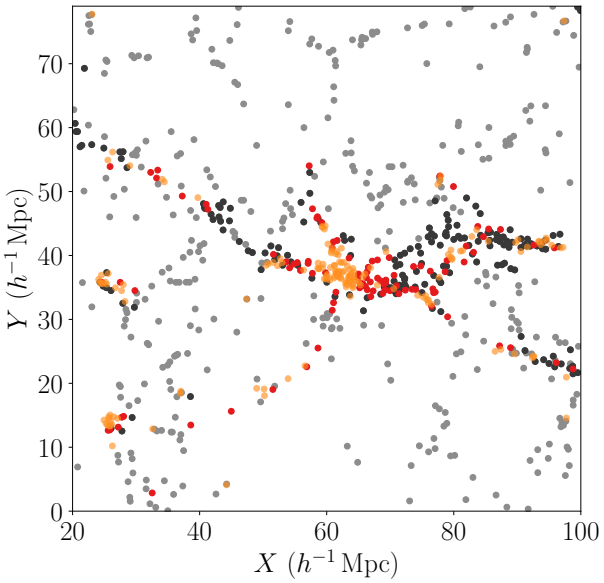

Figure 6.5: A zoomed-in view of the lower left corner of the panels in Fig. 6.4 with the halos that are removed by different criteria plotted with different colors. Splashback subhalos outside the virial radii of their hosts are shown as orange points, distinct halos cut using the $M_{\rm tidal,b}$ criterion are shown as red points, halos removed by the N_5 cut are shown as dark grey points, and halos surviving all of the cuts are shown by the light grey points. The assembly bias signal is consistent with zero when orange and red points are removed.

and gravitational heating – are strongest in similarly dense regions. The distributions of halos with larger values of $M_{\rm tidal,b}/M_{\rm vir}$ or smaller values of N_5 are less clustered. We also provide a zoomed-in view of the distribution of these different groups in Figure 6.5.

Fig. 6.6 shows concentration distributions for different groups of halos: all halos outside $R_{\rm vir}$ of any host, splashback subhalos outside $R_{\rm vir}$ that have not passed through pericenter of their orbit, splashback subhalos outside $R_{\rm vir}$ which have passed their first pericenter, and distinct halos outside the splashback shell of any host which have low $M_{\rm tidal,b}/M_{\rm vir}$. This figure shows that the $c_{\rm vir}$ distribution of post-pericenter splashback subhalos is biased to much larger values and are responsible for almost the entire high-$c_{\rm vir}$ tail of the overall concentration distribution. This indicates that the concentrations of such halos are affected substantially by the strong tidal interaction they experienced during their pericenter passage, which strips mass preferentially at the outskirts of halos, thereby increasing their concentration [e.g., Kazantzidis et al., 2004]. In contrast, splashback subhalos that are on their first

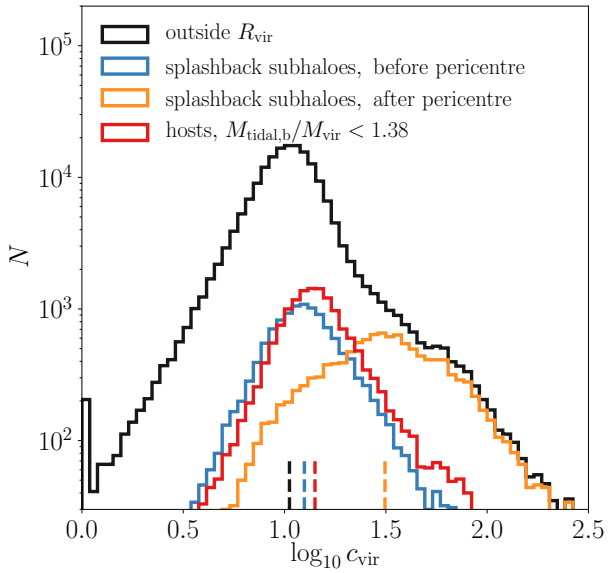

Figure 6.6: The distribution of concentrations for different low-mass halo populations. The black curve shows the concentration distribution for all halos outside $R_{\rm vir}$ of any host. The $c_{\rm vir}$ distributions of splashback subhalos on their first orbit are shown in blue and yellow. The blue curve corresponds to halos on first infall which have passed the splashback shell but not their first pericenter, and the yellow curve corresponds to splashback subhalos which have passed their first pericenter and have re-entered the region between $R_{\rm vir}$ and the splashback shell. The red curve shows the $c_{\rm vir}$ distribution for halos with $M_{\rm tidal,b}/M_{\rm vir} < 1.38$. Vertical dashed lines show the medians of each distribution. Note that when halos corresponding to the red, yellow, and blue curves have been removed from the general sample, the $c_{\rm vir}$ assembly bias signal is consistent with zero. Note also that post-pericenter splashback subhalos are responsible for almost all of the high-$c_{\rm vir}$ tail of the general population.

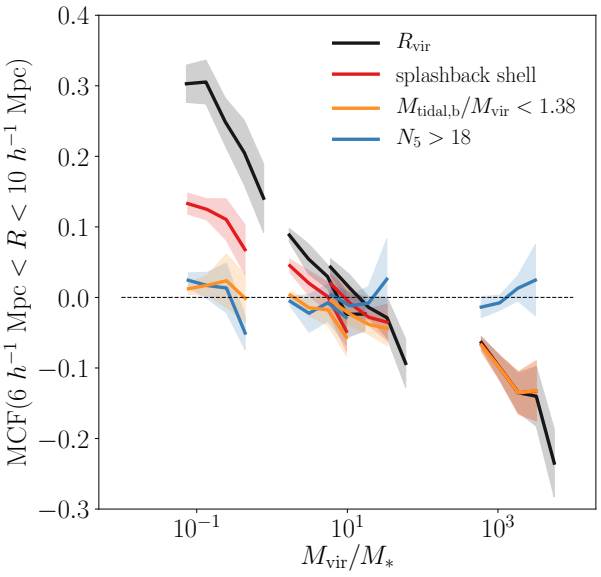

Figure 6.7: The dependence of assembly bias on $M_{\rm vir}$, scaled by the non-linear collapse mass scale, M_*. This plot was created from the $z = 0$, 1, 1.4, and 3 snapshots of Bolshoi and shows the median values of $M_{\rm vir}/M_*$ in thin $V_{\rm peak}$ bins versus the MCF between 6 h^{-1} Mpc and 10 h^{-1} Mpc for each bin. $1-\sigma$ sample variance of the MCFs are plotted as shaded regions. Lines of different color show MCFs for halo samples with different cuts indicated in the legend. $V_{\rm peak}$ bins below our convergence limit of 120 km s^{-1} and bins with errors on the MCF larger than 0.1 are not plotted (this typically occurs at $V_{\rm peak} \approx 300$ km s^{-1}). Non-linear effects strongly reduce assembly bias at low masses but have no impact on high-mass assembly bias because this effect has a different physical origin. However, a single cut to local density is effective at removing assembly bias at all masses.

infall and distinct halos with $M_{\rm tidal,b}/M_{\rm vir} < 1.38$ have comparable concentration distributions and are only slightly shifted relative to the overall distribution of concentrations. The modest shift in $c_{\rm vir}$ is consistent with an older age of these halos, rather than the large concentration boost in halos that have experienced tidal stripping. We note that the strength of the high $c_{\rm vir}$ tail becomes weaker if the halo sample is defined by $M_{\rm vir}$ or $V_{\rm max}$. This is because halos that lost mass after their first pericenter passage drop out of the $M_{\rm vir}$-defined sample, but stay within the $V_{\rm peak}$ defined sample.

6.3.4 Time and Mass Dependence of Assembly Bias

As discussed in section 6.1, $c_{\rm vir}$ halo assembly bias has opposite signs at masses above and below the non-linear collapse mass scale, M_*. Fig. 6.7 shows the dependence of assembly bias on $M_{\rm vir}/M_*$ in the Bolshoi simulation for the entire sample of distinct halos (black line and shading), and samples in which subsets of halos have been removed using different criteria discussed earlier in this section (colored lines). We first divide halos into logarithmic bins of $V_{\rm peak}$ with 0.08 dex width. We use bins of $V_{\rm peak}$ to be consistent with the rest of our analysis, although we show the assembly bias signal as a function of the median $M_{\rm vir}/M_*$ within each bin. For each bin above the convergence limit of $V_{\rm peak} = 120\,{\rm km\,s^{-1}}$ we measure the MCF in the separation range of $6-10$ comoving h^{-1} Mpc and split the simulation into eight equal-size sub-boxes to estimate the 1-σ error on the MCF amplitude. To probe a wide range of $M_{\rm vir}/M_*$ values, we use the $z = 0$, 1, 1.4, and 3 Bolshoi snapshots, with the $z = 0$ snapshot giving us access to the lowest values of $M_{\rm vir}/M_*$ and $z = 3$ giving us access to the highest.

The dependence of assembly bias on $M_{\rm vir}/M_*$ for distinct halos outside $R_{\rm vir}$ of any larger host is consistent with the results of Wechsler et al. [2006]. Removing splashback subhalos reduces the assembly bias substantially at $M_{\rm vir}/M_* \lesssim 10$, but does not eliminate it completely, and does not affect assembly bias at larger masses. Removing further distinct halos using $M_{\rm tidal,b}/M_{\rm vir} < 1.38$ cut eliminates assembly bias entirely at $M_{\rm vir}/M_* \lesssim 5$, but likewise does not affect the assembly bias at larger $M_{\rm vir}/M_*$. This illustrates that the physical origin of assembly bias in the high-mass regime is not related to tidal forces or dynamical heating.

Interestingly, Fig.6.7 also shows that removing halos using environmental density, N_5, *does* remove assembly bias at all $M_{\rm vir}/M_*$. Visual inspection reveals that this is because this cut removes the same spatial regions across time.

Given that halos and large-scale structure evolve with time, we also redid this analysis by removing a constant fraction of distinct halos ranked by $M_{\rm tidal,b}/M_{\rm vir}$ and by N_5 at different

redshifts rather than using a fixed cut as in Fig. 6.7. The results of such analysis are almost identical, albeit with slightly higher $f_{\rm removed}$.

6.3.5 Sensitivity to Splashback Subhalo Identification Method

As discussed above, we use two different methods to identify splashback subhalos: 1) halos that move within $R_{\rm vir}$ of a larger halo at some point during their evolution and ("flyby subhalos") 2) halos located within the splashback shell identified by the SHELLFISH algorithm ("splashback subhalos"). It is clear that the samples of subhalos identified using these methods cannot be identical: halos that are on their first approach to a host and are already within the splashback shell but are still outside $R_{\rm vir}$ will be classified as splashback subhalos by the second method, but not the first. Conversely, halos that previously passed within $R_{\rm vir}$ of the host, but are now outside of the splashback shell identified by SHELLFISH will be identified by the first method, but not the second.

We find that $\approx 40\%$ of splashback subhalos ($\approx 4\%$ of all halos) are not identified as flyby halos, but only $\approx 6-8\%$ of flyby subhalos ($0.4-0.5\%$ of all halos) are not identified as splashback subhalos. The latter subhalos are misidentified largely around host halos below convergence limit of the SHELLFISH algorithm: if we restrict this analysis to host halos that meet the convergence requirements of $N_{\rm 200m} > 5 \times 10^4$ and $\Gamma_{\rm DK14} > 0.5$ [see Mansfield et al., 2017, for details], we find that only $1-2\%$ of flyby halos ($\lesssim 0.1\%$ of all halos) are not identified by the second method. This small fraction indicates that the splashback shells identified by SHELLFISH for well-resolved halos capture the vast majority of the splashback subhalos identified by the traditional subhalo trajectory method. This also indicates that the fraction of subhalos ejected by three-body interactions via the slingshot process beyond the splashback shell [Kravtsov et al., 2004, Sales et al., 2007] is quite small and that most of the subhalos outside $R_{\rm vir}$ are on their natural dynamical orbit around their host halo. We note that this conclusion should not be extended to $V_{\rm peak} < 120$ without further testing: it is plausible that slingshot processes become more significant at lower masses.

This is consistent with earlier studies that analyzed the radial distribution of flyby subhalos [Ludlow et al., 2009, Wang et al., 2009, Li et al., 2013] and found that flyby subhalos are common at distances up to $2\,R_{200c}$, with numbers decreasing quickly at larger radii but with a small population present out to $\approx 4\,R_{200\mathrm{c}}$. We find that the radial distribution of flyby subhalos is due to large size of the splashback shell relative to $R_{200\mathrm{c}}$, its non-spherical shape, and the substantial scatter between $R_{200\mathrm{c}}$ and the maximum radius of the splashback shell. For our sample of distinct halos, the mean value of $R_{\mathrm{sp}}/R_{200\mathrm{c}}$ is 2.16 and the mean value of $R_{\mathrm{sp,max}}/R_{200c}$ is 2.80 with a $1-\sigma$ scatter of ≈ 0.6, where $R_{\mathrm{sp,max}}$ is the maximum radius of any point on the splashback shell.

Lastly, Figure 6.2 compares the MCF after both methods have been used to remove splashback subhalos. The difference is small relative to the overall amplitude of the signal. We also find that when the procedure described in sections 6.2.8 and 6.2.8 is used, both classification schemes find similar cutoff values. However, f_{removed} is necessarily $\approx 3\%$ larger when flyby flagging is used to remove splashback subhalos because these cuts must also remove infalling splashback subhalos. The exception to this is the M_{tidal} proxy, which is higher for almost all splashback subhalos than it is for almost all distinct halos. Thus, M_{tidal} cannot remove assembly bias without removing the entire sample. This leads us to conclude that our general results are robust to differences in the subhalo classification scheme.

6.3.6 Comparison of the Bolshoi and BolshoiP Simulations

All analysis presented above was done using the Bolshoi simulation with cosmological parameters consistent with the final WMAP mission constraints (see section 6.2.1). To test the dependence of our results on the assumed cosmology, we repeated all analysis using the BolshoiP simulation, which assumes cosmological parameters consistent with the Planck mission constraints and found that all of the results are qualitatively consistent. The difference in Ω_{m} in the Bolshoi and BolshoiP simulations leads to small changes in the cutoff values for $M_{\beta,\mathrm{b}}$, D_{vir}, M_{tidal}, R_{tidal}, and $M_{\mathrm{tidal,b}}$, but the values of f_{removed} are within 0.01 of the

values found for the Bolshoi simulation for all cuts, which the exception of the high-error $f_{\rm removed}$ value for our least efficient proxy, $M_{\beta,\rm b}$.

6.4 Discussion

6.4.1 Issues Associated with Proxy Definitions

In this study we define and use several proxies of physical processes that could conceivably contribute to assembly bias. Of these, $D_{\rm vir}$, $R_{\rm tidal}$, $M_{\rm tidal}$, $M_{\beta,\rm b}$, and $M_{\rm tidal,b}$ require estimating the local tidal force and/or determining whether a given particle is bound or unbound. However, it is not trivial to accurately determine whether a particle is bound in the outskirts of halos [see, e.g., Behroozi et al., 2013a, for an extended discussion of related issues], and strong assumptions and approximations must be employed in the estimates of tidal forces. Errors made in estimating a particular proxy should result in additional scatter in its correlation with $c_{\rm vir}$ and should increase the uncertainty in our estimate of its contribution to the assembly bias. As a corollary, *improvements in proxy definitions should only decrease the measured* $f_{\rm removed}$ *values.* In practice, only $M_{\rm tidal,b}$ is strongly affected both by uncertainties in the tidal force estimate and by issues of identifying bound particles, which means that improvements in proxy estimates would primarily reduce $f_{\rm removed}$ for $M_{\rm tidal,b}$, while having an equal or lesser effect on our other proxies. This means that such improvements would not change our conclusions.

A detailed analysis of the errors associated with the approximations necessary for tidal force calculation can be found in Appendix 6.6.3. A discussion of the issues related to identification of bound particles can be found in Appendix 6.6.4.

6.4.2 Sensitivity of Results to Definitional Choices

In this section we discuss the impact of the choices and assumptions made in our fiducial analysis on our results. We have already discussed how our choice of clustering statistic

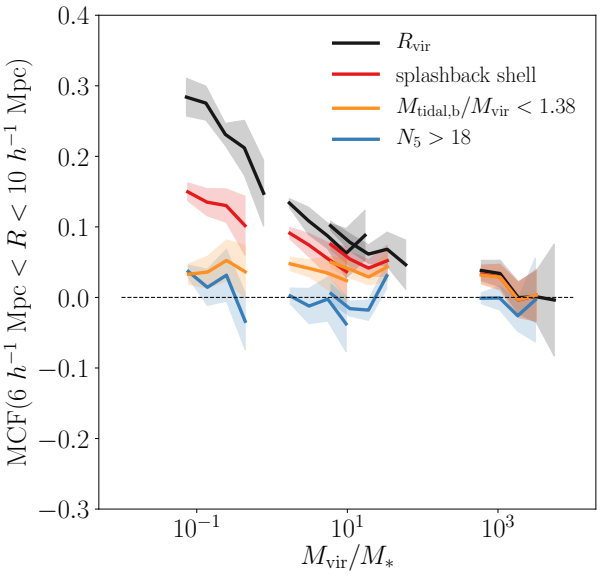

Figure 6.8: The same as Fig. 6.7, but for MCFs defined in terms of $-a_{1/2}$ instead of $c_{\rm vir}$. See section 6.4.2 for discussion.

used to estimate assembly bias affects out results in sections 6.2.7 and 6.3.2 (see Fig. 6.2), so here we focus on the effect of our choices of $V_{\rm peak}$ for defining halo samples, $R_{\rm vir}$ as our reference halo boundary, and halo concentration as our formation time proxy. Although we did present justifications for our choices in section 6.2, it is important to assess how sensitive our results and conclusions are to these choices.

As an alternative to $V_{\rm peak}$, we could define halo samples using $M_{\rm peak}$, $V_{\rm max}$, or $M_{\rm vir}$. We find that sample selection by $M_{\rm peak}$ leads to results similar to our fiducial case, but using $V_{\rm max}$ or $M_{\rm vir}$ leads to a somewhat different behaviour. The amplitude of the MCF with only $R_{\rm vir}$ subhalos removed is closer to the amplitude of the MCF with splashback subhalos removed for a $V_{\rm peak}$ or $M_{\rm peak}$ cut. However, further removing splashback subhalos with a $V_{\rm max}$ or $M_{\rm vir}$ cut results in only a small decrease in amplitude. This is because subhalos generally experience significant mass loss and therefore sample selection based on their peak mass or circular velocity results in larger subhalo fractions compared to selection on current mass [cf., also Nagai and Kravtsov, 2005]. The large-$c_{\rm vir}$ tail seen in Fig. 6.6 is weaker when $V_{\rm max}$ or $M_{\rm vir}$ is used to define the halo samples for the same reason. Our other results,

such as the values of $f_{\rm removed}$ or the spatial distribution of different halo subsets, are largely unaffected. This is because the halos removed by these cuts have merely had their accretion histories slowed: they have not experienced significant mass loss.

Although most analysis in this chapter uses splashback shells as halo boundaries, we use spheres of radius $R_{\rm vir}$ as halo boundaries when we compute fiducial $\mathcal{M}(r)$ curves and when we classify "flyby" subhalos. We have repeated these analyses using other commonly used values of $\Delta\bar{\rho}_{\rm m}$, and found that the main difference, unsurprisingly, is in the change of the amplitude of the reference MCF. Definitions with high values of density contrast, such as $\Delta\bar{\rho}_{\rm m} = 200\rho_{\rm c}$ or $\Delta\bar{\rho}_{\rm m} = 500\rho_{\rm c}$, result in a modest increase of the reference MCF amplitude, while definitions with low density contrasts, such as $\Delta\rho = 200\rho_{\rm m}$, result in a modest decrease of the MCF amplitude. To decrease the reference MCF amplitude to the level of the MCF after removal of splashback subhalos requires $\Delta\bar{\rho}_{\rm m} \approx 100\rho_{\rm m}$ – close to the typical density contrast enclosed by the splashback shell [see Fig. 12 in Mansfield et al., 2017]. Changes in Δ used for radius definition have little effect on the amplitude of the MCF when flyby subhalos have been removed because most subhalos have their first pericenters at radii well within all of the commonly-used definitions of halo radius.

We have chosen to use $c_{\rm vir}$ as a proxy of halo age, but assembly bias behaves differently for different proxies [e.g., Villarreal et al., 2017a, Mao et al., 2018, Salcedo et al., 2018], so one would reasonably wonder if halo removal criteria also depend on this choice. A full investigation of different definitions is beyond the scope of this work, but as a preliminary discussion, we repeat our analysis for the most commonly used alternative age proxy – the expansion factor at which the virial mass of the main progenitor of a halo was half of the halo's current mass, $a_{1/2}$:

$$M_{\rm vir}(a_{1/2}) = \frac{1}{2}\, M_{\rm vir}(a_{\rm current}). \tag{6.10}$$

Note that although large (small) $c_{\rm vir}$ values correspond to old (young) halos, the opposite is

true for $a_{1/2}$. To simplify comparison with $c_{\rm vir}$-based results, we use $-a_{1/2}$ as the formation time proxy, so the sign of the MCF retains the same qualitative meaning.

Results for the $-a_{1/2}$ proxy are shown in Fig. 6.8, where we use the same cuts that removed the assembly bias in the $c_{\rm vir}$-based analysis. The figure shows that stricter cuts are required to eliminate $-a_{1/2}$ assembly bias. When we follow the procedure described in section 6.2.8, the $M_{\rm tidal,b}$ cut that removes $-a_{1/2}$ assembly bias results in $f_{\rm removed} = 0.14$, compared to $f_{\rm removed} = 0.06$ for $c_{\rm vir}$ assembly bias. Other proxies experience similar increases in $f_{\rm removed}$, with the exception of N_5, which removes assembly bias for both definitions in almost all bins. The fact that Bolshoi and BolshoiP measurements of $f_{\rm removed}$ agree to within 0.01 for all variables (see §6.3.6) indicates that the differences in $f_{\rm removed}$ between the $c_{\rm vir}$ and $-a_{1/2}$ definitions are significant.

Another difference is that in contrast to the $c_{\rm vir}$ MCF, the amplitude of the $-a_{1/2}$ MCF does not reverse sign at large halo masses (see Fig. 6.8 and several previous studies: Gao et al. 2005, Gao and White 2007, Wetzel et al. 2007, Mao et al. 2018, Sato-Polito et al. 2018). This puzzling behaviour at first appears to be inconsistent with the physical origin of the high-mass assembly bias argued for by Dalal et al. [2008, see also section 9.4 of Zentner 2007]. However, Chue et al. [2018] showed that $a_{1/2}$ and similar measures of formation time can be problematic if measured relative to a standard overdensity mass. Because these definitions do not account for mass in the splashback shell, halos measured at a constant $M_{\rm vir}$ actually have a range of "true" splashback-enclosed masses, and the high-mass halos will preferentially have early $a_{1/2}$, which increases the level of bias measured for early $a_{1/2}$ halos. The intersection of this behaviour with Fig. 6.8 requires further study.

6.4.3 Comparison with Previous Work

The effect of splashback subhalos on assembly bias was investigated in a number of recent studies [Wang et al., 2009, Li et al., 2013, Sunayama et al., 2016], which concluded that splashback subhalos contribute significantly to low-mass halo assembly bias, but cannot ac-

count for the entire signal. These studies used the "flyby" approach to classify subhalos (similar to the method described in 6.2.3), which can include bona fide splashback subhalos, as well as subhalos ejected via slingshot effect after dynamical interactions with other subhalos. However, this classification cannot account for a large number of subhalos within splashback shells that are on their first infall. This left open the question of the contribution of such infalling subhalos on assembly bias. In this study we answer this question in section 6.3.5.

Additionally, these studies have not demonstrated the physical origin of the remaining assembly bias signal. Our results differ from those of Sunayama et al. [2016], which find that splashback subhalos have little effect on the MCF at large distances ($R \gtrsim 10\,h^{-1}\,\mathrm{Mpc}$). Sunayama et al. [2016] used the same simulation and underlying halo catalogs as this chapter, so this difference is likely due to the fact that their samples are defined by $M_{\rm vir}$ (see section 6.4.2) and their use of halo bias ratios to measure assembly bias. This statistic results in larger errors than the MCF, as we discussed in § 6.2.7 and 6.3.2. For example, comparison of the bin-to-bin scatter in Fig. 3 and Fig. 4 of Sunayama et al. [2016] to the 1-σ error contours in the right panel of our Fig. 6.2 indicates that their measurements may not have been sensitive enough to probe large-scale assembly bias.

The conjecture that non-linear tidal and dynamical heating effects can be responsible for low-mass halo assembly bias was discussed in a number of studies [e.g. Wang et al., 2007, Dalal et al., 2008, Hahn et al., 2009, Wang et al., 2011, Hearin et al., 2016b, Paranjape et al., 2018, Salcedo et al., 2018, Musso et al., 2018, Johnson et al., 2019]. Often, arguments for a particular process are based on establishing existence of a correlation between halo formation time or halo bias and a proxy for a particular process, such as $R_{\rm hill}$, bound mass fraction, the magnitude of tidal eigenvectors, or various measures of tidal anisotropy. While such correlations provide useful information, by themselves they are not sufficient to establish that a given physical process is responsible for assembly bias. This is because the proxies of all these processes are all strongly correlated: an explicit comparison, such as that shown in

Fig. 6.3, is more direct and compelling in identifying the responsible process.

Furthermore, looking at the global connection between halo formation time and a proxy is problematic for two reasons. First, we show that after splashback subhalos are removed low-mass halo assembly bias is due to only a small fraction of distinct halos. Thus, analysis relying on the global correlation strength is not optimal. Second, as discussed in section 6.2.8, the correlation between a proxy and halo formation time by itself contains no information about how closely that proxy is related to assembly bias: a strongly correlated proxy which experiences weak differential clustering, such as $M_{\beta,\mathrm{b}}$, will not contribute to assembly bias. We avoid both these issues with the procedure described in section 6.2.8.

We find a strong connection between tidal forces from the large-scale mass distribution and assembly bias in agreement with the conclusions of Hahn et al. [2009], Hearin et al. [2016b], Salcedo et al. [2018], and Johnson et al. [2019]. However, in contrast with these studies, we find that this this effect cannot be effectively approximated by assuming that halos only feel the tidal force of their most gravitationally dominant neighbor. In fact, we find that when such an approximation is made, the connection is sufficiently weak that it is likely caused simply because the Hill radius is a crude estimate of local density (see section 6.3.2). This discrepancy is due to two factors. First, some of these studies do not perform the type of multi-variate analysis that would be necessary to differentiate between different contributing physical processes. Second, while these studies effectively map out the connection between *formation time* and single-halo tidal proxies, this is unrelated to the connection between *assembly bias* and these proxies, an argument we make in section 6.2.8.

Also, contrary to the conclusion of Paranjape et al. [2018], we do not find a compelling evidence that large-scale tidal anisotropy contributes significantly to assembly bias beyond what is expected from its correlation with tidal field strength. Nevertheless, given the inaccuracies associated with all methods based on second-order approximations to the tidal field (see Appendix 6.6.3), a more detailed study of tidal field anisotropy could prove fruitful, especially in the context of explicitly studying the tidal environments within structures like

sheets and filaments.

Although our results are in qualitative agreement with the conjectures of Wang et al. [2007] and Dalal et al. [2008] that gravitational heating is a significant component of assembly bias, we also find that this connection only becomes strong when tracers simultaneously incorporate both gravitational heating and a halo's zone of influence over the local tidal field, such as $M_{\rm tidal,b}$.

Our work uses an approach similar to that of Villarreal et al. [2017a], so we have performed an in-depth comparison with their results. We find broad qualitative agreement between our $D_{\rm vir}$ results and the results of Villarreal et al. [2017a], but find that quantitatively the Δ values they report imply $D_{\rm vir}$ values smaller than our findings by $\approx 25\%$.

This difference is due to two factors. First, we find that the sample variance in the boxes used by Villarreal et al. [2017a] is larger than than they estimated. We estimate the sample variance using subvolumes of the BolshoiP simulation, which has nearly identical mass resolution and cosmology to the CPla_L0125 box used by Villarreal et al. [2017a] and find that the actual variance is larger than the uncertainty they estimated by repeatedly shuffling marks among halos. This means that MCFs in the CPla_L0125 box could be lower due to sample variance, which could thus result in less aggressive conditions for the removal of assembly bias. Second, while the ROCKSTAR halo finder used in Villarreal et al. [2017a] and in this chapter is a state-of-the-art tool for measuring the properties of halos with density contrasts of $\Delta \gtrsim \Delta_{\rm vir}$ [e.g., Knebe et al., 2013], it cannot effectively measure halo properties at lower density contrasts, such as the $\Delta = 20$ contrast used by Villarreal et al. [2017a]. This is because there is no FOF linking length which can fully percolate all matter out to such large overdensity radii, while also allowing for efficient load-balancing. This leads to underestimates of halo masses and artefacts in the density profile. Contrary to the findings of Villarreal et al. [2017a], we find that even with an unusually large linking length of $b = 0.5$, virtually all halos have underestimated $M_{\rm 20m}$ masses. The ratio $M_{\rm true}(< R_{\rm 20m,Rockstar})/M_{\rm 20m,all,Rockstar}$ has $1-\sigma$ contours of $1.04 - 1.13$, with 2σ fluctuations

reaching ≈ 2.5. The magnitude of underestimation is significantly worse at more commonly-used linking lengths. This and the fact that halos no longer follow NFW profiles at large radii [e.g., Becker and Kravtsov, 2011, Diemer and Kravtsov, 2014], adds biases and noise to the $R_{\rm s}$ and $R_{\rm sKlypin}$ values measured by ROCKSTAR. This, in turn, artificially reduces the amplitude of the MCF. We discuss this issue in greater depth in Appendix 6.6.1.

Our interpretation is consistent with the test presented in Figure 11 of Villarreal et al. [2017a], which shows that when $R_{\rm 20m}$ is used to exclude subhalos, but concentrations are measured from the halo catalogs constructed using larger Δ, the MCF is not consistent with zero. We find that when we replicate their analysis using manually-constructed overdensity profiles, excluding "subhalos" by spheres of radius $R_{\rm 20m}$ is no longer capable of mitigating assembly bias. Larger overdensity radii that are comparable with our reported $D_{\rm vir}$ cutoff values are required.

6.4.4 Directions for Future Work

In this chapter, we focus on the dependence of halo bias on $c_{\rm vir}$, but galaxy properties are likely related to a number of halo properties. This means that the effects of secondary biases on galaxy clustering may not be confined to the $c_{\rm vir}$ bias dependence and may remain even if $c_{\rm vir}$ dependence of bias is removed. As discussed in 6.4.2, this is true even for an alternative choice of halo formation time proxy, $-a_{1/2}$. Furthermore, Villarreal et al. [2017a] show that mitigating secondary biases in axis ratio and spin parameter is more difficult than removing bias in $c_{\rm vir}$, although the discussion in section 6.4.3 should be kept in mind when assessing these results. It would be useful to perform analysis comparable to the one presented here for a number of other key halo properties to build a more complete understanding of the physical origin of the corresponding dependencies of halo bias.

One of our key results is that despite the large contribution of tidal forces to $c_{\rm vir}$ assembly bias, this cannot be shown conclusively when using rough and inaccurate estimates of the tidal force, such as $D_{\rm vir}$ or the single-halo $R_{\rm hill}$. Although $R_{\rm tidal}$ defined in section 6.2.5

accounts for tidal forces from multiple halos, it still is rather inaccurate, as we show in Appendix 6.6.3 and discuss in 6.4.1. The accuracy of the tidal force estimate can be improved by using a higher order approximation of the tidal field, by iteratively recalculating $R_{\rm tidal}$ and removing nearby sources accordingly, or by explicitly evaluating the tidal field outside the halo and identifying the turnover associated with the tidal radius directly. More accurate estimate of the tidal radius could result in a better identification of halos responsible for assembly bias. This effort could also be aided by incorporating cosmic web classifiers [see review by Libeskind et al., 2018], which would allow higher accuracy analytic calculation of the tidal fields associated with nearby large-scale structure, rather than the low-order approximations that are required for generic point distributions.

Finally, all of the tidal field and dynamical heating proxy estimators discussed and used in this chapter are computed from simulated quantities and cannot be immediately be applied to observations. A follow-up exploration of possible observable proxies that can remove particular flavors of secondary halo bias using mock catalogs will be a useful future avenue of research.

6.5 Summary and Conclusions

In this study, we present analysis of the physical causes of assembly bias – the dependence of halo clustering on proxies of halo age. We present results for assembly bias across a broad range of masses, redshifts, and several definitions of halo age. Our main focus, however, is on the detailed analysis of nonlinear processes that modify the primordial assembly bias during the non-linear stages of structure formation using concentration as our primary age indicator.

Our results indicate a scenario in which halos of all masses initially exhibit primordial assembly bias arising from the properties of the initial Gaussian field of density perturbations. However, the assembly bias of halos with masses smaller than the current nonlinear mass scale is reduced to zero or to negative levels by three non-linear processes as mass decreases.

We first explore the contribution of "splashback subhalos" to assembly bias, where splashback subhalos are defined either as halos that have passed within the virial radius of a larger halo at some point in the past or as halos are located within the splashback shell of a larger halo, as determined by the method of Mansfield et al. [2017]. Assembly bias is measured both before and after the removal of these subhalos. We show that splashback subhalos are responsible for about two thirds of the assembly bias signal, but do not account for the entire effect. Moreover, it is the subhalos that have passed the pericenter of their orbit at least once that are responsible for the contribution of subhalos to assembly bias. In addition, we find that the high-$c_{\rm vir}$ tail of the distinct halo distribution is due almost entirely to these same post-pericenter subhalos.

At the mass ranges considered in this chapter, we find that the fraction of halos which have passed within the splashback shells of their hosts but are later located outside them is small, which indicates that the fraction of halos ejected beyond the splashback shell due to three-body interactions is small.

We then investigate which additional physical processes contribute to assembly bias. We do this by constructing proxies of these processes for each halo, ranking distinct halos according to each proxy, and measuring what fraction of the ranked halos need to be removed in order for the assembly bias signal to be statistically consistent with zero. We find that assembly bias is caused by a relatively small number of halos in dense regions. These halos have had their accretion histories truncated by a combination of large-scale tidal fields and the high velocities of ambient particles. We also demonstrate that neither process can cause assembly bias on its own and that these tidal fields are not well-modeled by assuming that the dominant tidal contribution comes from a single massive neighbor. We further argue that the commonly-used approach of measuring the correlation between a physical proxy and halo age cannot be used on its own to draw conclusions about the strength of the connection between that proxy and assembly bias.

A key finding of this study is that after splashback subhalos are removed, the residual

"negative" assembly bias is due to only 10% of distinct halos (5% of all halos). To summarize, 27% of halos are removed due to a traditional $R_{\rm vir}$-based subhalo cut, a further 10% are removed due to a splashback subhalo cut, and finally 6% of all halos are removed due to the cut based on $M_{\rm tidal,b}/M_{\rm vir}$. These low $M_{\rm tidal,b}/M_{\rm vir}$ halos are located within the largest filaments and are only slightly more concentrated than the general population. However, their strong spatial clustering results in an outsized effect on the global assembly bias signal.

We find that in the WMAP cosmology, the removal of halos above a certain local density, as measured by the number of halos within $5\,h^{-1}$ comoving Mpc, $N_5 > 18$, removes assembly bias for both $c_{\rm vir}$ and $a_{1/2}$ at all distances across all mass scales and redshifts and that a similar cut exists in a Planck cosmology. Such a cut removes a much larger fraction of halos from the sample than the cut in $M_{\rm tidal,b}/M_{\rm vir}$, and thus does not correspond to a real physical process contributing to assembly bias. Nevertheless, this result indicates that it may be fruitful to explore whether density-based cuts on mock galaxy catalogs can be used to remove assembly bias from galaxy samples and motivates further studies in this direction.

6.6 Appendices

6.6.1 Effects of Halo Definition on Concentration in the Rockstar Halo Finder

The ROCKSTAR halo finder works by dividing the simulation into 3D friends-of-friends (FOF) groups, adaptively creating smaller 6D FOF groups in phase space, placing halo centers at the most refined 6D FOF groups, and finally calculating halo properties relative to those centers [Behroozi et al., 2013c]. The size of the initial 3D FOF groups is set by the input linking length in units of the mean interparticle separation, b. The accuracy of the halo properties computed by ROCKSTAR depends on the original 3D FOF groups percolating out to the baseline overdensity radius of the corresponding halos [More et al., 2011, Behroozi et al., 2013c]. This is particularly important when fitting halo density profiles: if halo bound-

aries extend into the unpercolated regions of the FOF group, the density in the outermost radial bins will be systematically underestimated, shifting the location of profile features. In this Appendix, we examine the effect of using different halo definitions on the measured concentrations.

Behroozi et al. [2013c] perform convergence tests that show that using linking length of $b = 0.28$ leads to full percolation within $R_{\rm vir}$. They note that when one defines halo boundary larger than $R_{\rm vir}$, a larger linking length should be used and additional tests should be performed to ensure full percolation within such boundary. We test the effect of the halo boundary choice by running ROCKSTAR repeatedly on the CBol_L0125 simulation from Diemer and Kravtsov [2015] for a variety of overdensity radii, R_Δ, with overdensity ranging from $\Delta = 20\rho_{\rm m}$ to $\Delta = 1600\,\rho_{\rm m}$ for $b = 0.28, 0.5$ and for a reference catalog with $\Delta = \Delta_{\rm vir}$ and $b = 0.28$. We then matched halos across the catalogs to our reference $R_{\rm vir}$ catalog. Our tests indicate that results are not sensitive to the way this matching is done, so we use a simple procedure where a halo is considered a "match" if its center lies within 0.25 kpc of the center of a counterpart in the $R_{\rm vir}$ catalog. This criterion is sufficient to unambiguously match most halos, but in the event that multiple halos meet it, we match to the halo in that group with the closest $M_{\rm vir}$ to the reference halo. Subhalo and distinct halo status are not factored in to this matching. We restrict our sample to halos classified as hosts by the $\Delta_{\rm vir}$ catalog with $10^{11.5}\,h^{-1}\,M_\odot < M_{\rm vir} < 10^{12}\,h^{-1}\,M_\odot$, as measured by the same catalog. The choice of mass range has only a slight effect on results.

Fig. 6.9 shows the ratio of $R_{\rm s}$ measured in catalogs constructed for different values of Δ, denoted $R_{\rm s,\,\Delta}$, to $R_{\rm s}$ measured in the reference catalog, denoted $R_{\rm s,\,vir}$. We show this ratio as a function of Δ for two values of b. We find that creating catalogs with larger linking lengths takes an inordinate amount of time, presumably because a large fraction of the simulation is placed into the same FOF group. The figure shows that $.R_{\rm s}$ measurements for $\Delta \lesssim 200$ are biased low relative to the values found for $\Delta = \Delta_{\rm vir}$ and there is a significant scatter between the two. The bias is about twice larger for $b = 0.28$ compared to $b = 0.5$.

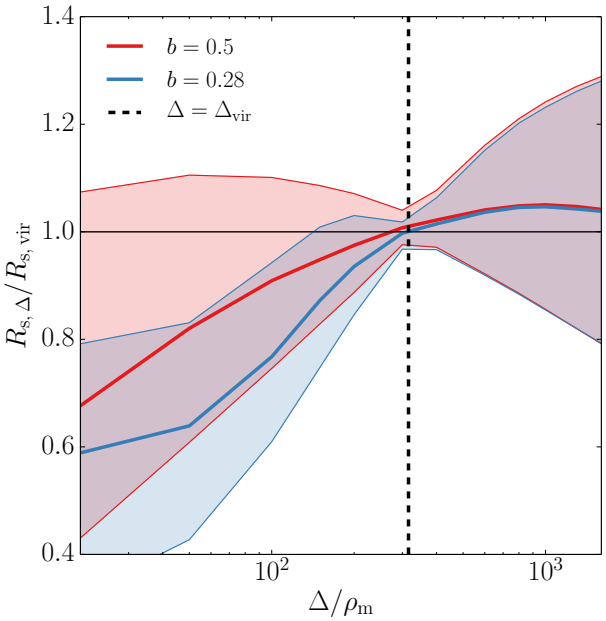

Figure 6.9: The value of $R_{\rm s}$ measured by ROCKSTAR using different overdensities, Δ, to define halo radius, R_{Δ}. The scale radii are normalized by the value of $R_{\rm s}$ measured for the same halos in a catalog with a primary definition of $\Delta_{\rm vir}$ for two different values of the ROCKSTAR's 3D FOF linking length, b. The median values of this ratio are shown as solid lines and the contours enclosing 68% of ratios are shown as shaded regions. Note that $R_{\rm s}$ measurements for $\Delta \lesssim 200$ are biased low relative to the values found for $\Delta = \Delta_{\rm vir}$ and there is a significant scatter between the two. The bias is larger for smaller b.

The primary implication of this result is that concentrations measured for halos identified and analyzed by ROCKSTAR using low Δ, such as $\Delta = 20\,\rho_{\rm m}$, should not be trusted due to large systematic bias and scatter. This is due to lack of FOF percolation in the outskirts of halos, which biases densities in the outskirts low and this, in turn, biases the best-fit $R_{\rm s}$ values low. This is also true for other ways of estimating concentration, such as deriving it from $V_{\rm max}/V_{\rm vir}$. The context of this fact in relation to our work on assembly bias is discussed in section 4.3.

Behaviour at commonly used choices, such as $\Delta = 200\,\rho_{\rm m}$, $200\,\rho_{\rm c}$, $500\,\rho_{\rm c}$ is also noteworthy. For $b = 0.28$, the systematic biases on $R_{\rm s}$ for these three definitions relative to our reference $\Delta = \Delta_{\rm vir}$ catalog are +6%, -5%, and -5%, respectively. While the difference for $\Delta = 200\rho_{\rm m}$ has contributions from lack of percolation, the difference between $\Delta_{\rm vir}$ and higher density definitions must be due to a different effect, such as deviations of halo profiles from the fitted NFW form. Any attempt to compare, for example, mass-concentration relations to the $\approx 5\%$ level measured with different primary definitions should account for this effect.

Lastly, as discussed in section 2.3, overdensity radii are fundamentally unphysical choices for halo boundaries, and $\Delta_{\rm vir}$ cannot be thought of as a more "correct" choice than other nearby overdensities. Consequently, Fig. 6.9 should not be interpreted as showing deviations from the true value of $R_{\rm s}$, but merely deviations from a particular reference value where the FOF groups are known to be percolated.

6.6.2 Fast Halo Containment Checks

Numerous components of the analysis presented in this chapter rely on containment checks, particularly when computing subhalo status, computing $R_{\rm tidal}$, or computing $M_{\rm tidal}$. Out sample contains $\approx 300,000$ halos and the Bolshoi simulations contain 2048^3 particles each, so a naive N^2 check of every pair of objects would be prohibitively expensive. This is particularly true when identifying splashback subhalos through the surfaces found by SHELLFISH be-

cause SHELLFISH represents splashback shells using third-order Penna-Dines surfaces, which take roughly fifty math library function calls to evaluate. In this Appendix, we describe our approach for computing containment checks.

First, suppose we are given a set of points P, which we must check for containment within a set of halos, H. First, we construct a uniform 3D grid spanning the simulation volume and place all elements of P within lists associated with each cell in the grid. Then, for each halo in H we construct a bounding box fully enclosing its boundary and compute containment checks for only the particles which reside in grid cells that intersect with it. Because the lists associated with each grid cell are created once and potentially iterated over many times, we represent lists as dynamically allocated arrays instead of as linked lists to increase cache locality. We find that for a grid with 250^3 cells containment checks are no longer a significant component of the runtime cost of any analysis in this chapter.

In the case where a halo boundary is determined by an expensive function $f(\phi, \theta)$, such as the Penna-Dines functions used by the SHELLFISH code to approximate splashback shells, we use the following procedure to accelerate containment checks. First, for every halo in H, we compute the minimum and maximum values of $f(\phi, \theta)$, $f_{\rm max}$ and $f_{\rm min}$. Since a point at a distance r is automatically contained if $r < f_{\rm min}$ and automatically not contained if $r > f_{\rm max}$, we only evaluate $f(\phi, \theta)$ if the points is at a distance, r, that satisfies $f_{\rm min} < r < f_{\rm max}$.

6.6.3 Tidal Force Errors

In this Appendix, we investigate some of the error properties of the tidal radius and discuss an important approximation made in our calculation of $R_{\rm tidal}$, the inclusion of a minimum cutoff radius when adding contributions to a halo's local tidal tensor. For the purpose of clarity, we will refer to the tidal radius calculated after a second-order approximation of the external gravitational potential has been made as $R^{(2)}_{\rm tidal}$ and the tidal radius when the exact tidal field is used as $R^{(\rm ex)}_{\rm tidal}$. Other quantities will use an analogous referencing scheme. Elsewhere in this chapter, $R^{(2)}_{\rm tidal}$ is referred to as $R_{\rm tidal}$. We also take the convention that

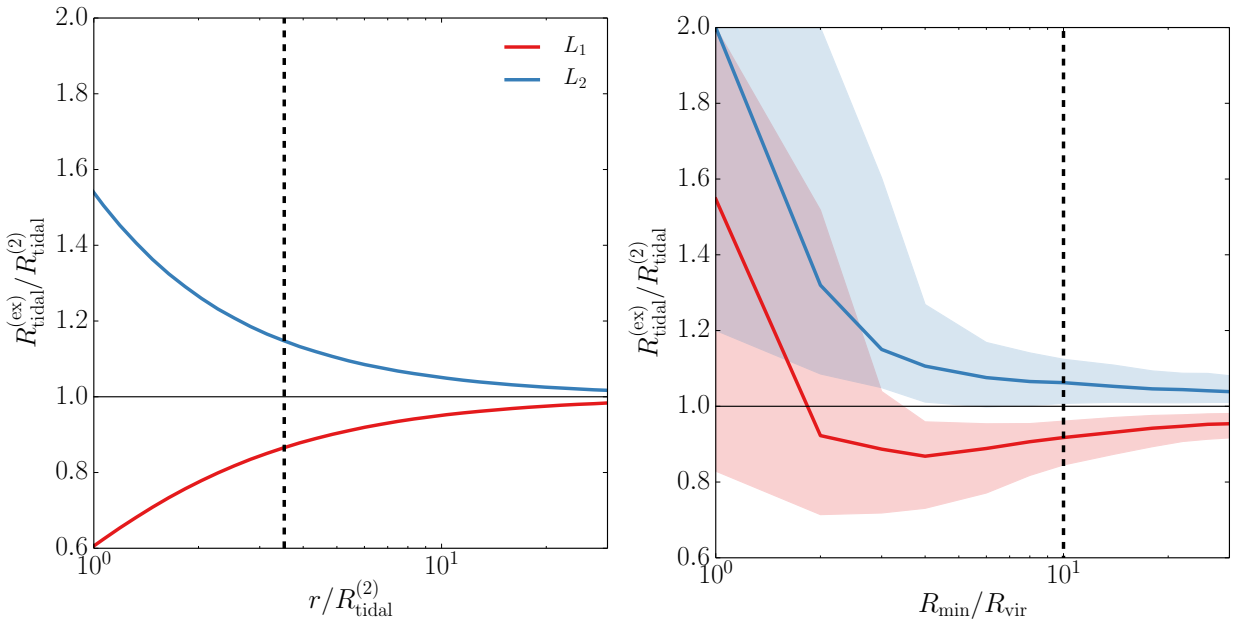

Figure 6.10: Two methods for estimating the error associated with different choices of the minimum cutoff radius, $R_{\rm min}$. Left: Analytic calculation of the error on $R^2_{\rm tidal}$ for a model system where the entire external potential is generated by a point source separated from the halo by a distance r. The dashed black line shows the median value of $R_{\rm min}/R^{(2)}_{\rm tidal}$ for our sample. Right: The approximate error on $R^{(2)}_{\rm tidal}$ as a function of $R_{\rm min}/R_{\rm vir}$ for the halos in our sample. Solid lines show the median values of $R^{\rm (ex)}_{\rm tidal}/R^{(2)}_{\rm tidal}$ and the shaded bands give the 68% contours. $R^{\rm (ex)}_{\rm tidal}$ was estimated by evaluating $F^{\rm (ex)}_{\rm tidal}$ at $L^{(2)}_1$ and $L^{(2)}_2$ and applying the methods described in Appendix 6.6.3. The black dashed line shows the value of $R_{\rm min}$ used in our analysis. Note that the x-axes of these two plots are scaled by different characteristic radii.

the Lagrangian point between a halo and an external source is L_1 and that the point on the opposite side of the halo is L_2. In cases where analysis is performed on halos without a single external source, L_1 is the Lagrangian point with the lowest external potential.

Like the classical $R_{\rm Hill}$ derivation, our calculation of $R^{(2)}_{\rm tidal}$ (see Equation 6.5) assumes that the external tidal field felt by the halo is well-approximated by a second-order hyperparaboloid. This is necessary because the tidal tensor which is used to determine the principle components of the tidal field only contains second derivatives of the gravitational potential. Note that in the special case where there is only a single external point source,

$$R^{(2)}_{\rm tidal} = \left(\frac{3}{2}\right)^{1/3} R^{(2)}_{\rm Hill}, \tag{6.11}$$

so the discussion below can be extended to error analysis on the classical Hill radius. Note that the factor of $(3/2)^{1/3}$ is because the derivation of $R^{(2)}_{\rm Hill}$ assumes that the halo is on a circular orbit around the external point source and thus experiences a centrifugal force in addition to a tidal force, while the derivation of $R^{(2)}_{\rm tidal}$ assumes that all non-tidal pseudo-forces are zero. Given the scale of errors discussed below, and the fact that this factor decreases as halos deviate from circular orbits – a configuration which is very rare for distinct halos – we do not consider this difference to be significant.

We perform two complementary tests on the accuracy of $R^{(2)}_{\rm tidal}$. First, we analytically compute $R^{(2)}_{\rm tidal}/R^{(\rm ex)}_{\rm tidal}$ for a single source at a distance r from a halo, and second, we measure exact the error on $F^{(2)}_{\rm tidal}$ for our halo sample and combine this with reasonable assumptions about the shape of the tidal field to estimate upper limits on $R^{(2)}_{\rm tidal}/R^{(\rm ex)}_{\rm tidal}$.

We show the results of this first calculation in the left panel of Fig. 6.10. Although there is no closed-form expression for $R^{(\rm ex)}_{\rm tidal}$, it can be found numerically by maximizing the effective potential. We parameterize the error as a function of $r/R^{(2)}_{\rm tidal}$ which also absorbs the dependence on the mass ratio. We recover the well-known fact that as the mass ratio between the halo and the external source decreases and the tidal radius increases, the two

Lagrangian points become asymmetric and that errors become increasingly significant. This can also be interpreted as an estimate of the error associated with a particular value inner cutoff radius for $r = R_{\rm min}$ when following the procedure described in section 6.2.5. This can be considered a worst-case estimate of the error at a given $R^{(2)}_{\rm tidal}$ because the true matter distribution will generally contain many points at distances larger than $R_{\rm min}$ which contribute significantly to the tidal field.

We perform our second test by first computing $L^{(2)}_1$, $L^{(2)}_2$, $R^{(2)}_{\rm tidal}$, and $F^{(2)}_{\rm tidal}$ for every halo in our sample for a particular choice of $R_{\rm min}$. Then, we use the raw particle data to compute the radial and tangential components of $F^{(\rm ex)}_{\rm tidal}(L^{(2)}_1)$ and $F^{(\rm ex)}_{\rm tidal}(L^{(2)}_2)$ for these halos. Particles within $R_{\rm min}$ are not included in this calculation. To obtain an estimate of $R^{(\rm ex)}_{\rm tidal}$ from this, we make two simplifying assumptions about the shape of the tidal field. First, we assume that the exact Lagrangian points lie along the same axis as a halo's second-order Lagrangian points. We find that the tangential components of $F^{(\rm ex)}_{\rm tidal}(L^{(2)}_1)$ and $F^{(\rm ex)}_{\rm tidal}(L^{(2)}_2)$ are small compared to the radial components, implying that this is a reasonable assumption. Second, we assume that along the lines connecting $L^{(2)}_1$ to $L^{(\rm ex)}_1$ and $L^{(2)}_2$ to $L^{(\rm ex)}_2$, the tidal force varies slowly enough that it can be well approximated by

$$F^{(\rm ex)}_{\rm tidal}(r) \propto \left(\frac{r}{R^{(2)}_{\rm tidal}}\right)^{1+\alpha}, \tag{6.12}$$

Here, α is an arbitrary constant which varies from halo to halo and may be different for different Lagrangian points within the same halo. It represents the deviation from the scaling seen when the tidal potential is approximated to second order. In this case,

$$\frac{R^{(\rm ex)}_{\rm tidal}}{R^{(2)}_{\rm tidal}} = \left(\frac{F^{(\rm ex)}_{\rm tidal}(L^{(2)}_i)}{F^{(2)}_{\rm tidal}(L^{(2)}_i)}\right)^{-\frac{1}{3+\alpha}}, \tag{6.13}$$

where i indexes over Lagrangian points. This assumption is informed by tests on single-source effective potentials, which find that for all but the smallest external point sources,

$-1 < \alpha < 0$. For halos where $R_{\rm min} > R^{(2)}_{\rm tidal}$, we would expect that at a constant $R^{(2)}_{\rm tidal}$ the tidal field would be varying more quickly at $L^{(2)}_i$ when the field is generated by a single point source than when it is generated by a more diffuse matter distribution, so it's likely that this range of α values holds for our simulated halos as well. For this reason we can place the following upper bound on the error in tidal radius:

$$|R^{\rm (ex)}_{\rm tidal}/R^{(2)}_{\rm tidal} - 1| < |F^{\rm (ex)}_{\rm tidal}/F^{(2)}_{\rm tidal} - 1|^{-1/2}. \tag{6.14}$$

We show the fractional error in $R_{\rm tidal}$ using this limit in the right panel of Fig. 6.10 as a function of the adopted $R_{\rm min}$. Errors balloon uncontrollably for $R_{\rm min} \lesssim 4\,R_{\rm vir}$ but are more well-behaved at larger radii, with errors dropping to the $\approx 10\%$ level at $\approx 10\,R_{\rm vir}$.

One interesting feature of this Figure is that for $R_{\rm min} \lesssim 2\,R_{\rm vir}$, the error on the location L_1 becomes positive. This is likely because this is the characteristic size of the splashback radius, meaning that the halo's own particles will be incorporated into the calculation of $F^{\rm (ex)}_{\rm tidal}$. Since the tidal force is repulsive, this inclusion of halo particles will reduce the apparent strength of the field and increase $R_{\rm tidal}$.

These tests indicate that for $R_{\rm min} = 10\,R_{\rm vir}$, the errors in $R^{(2)}_{\rm tidal}$ which are specifically due to the second order approximation of the tidal field are small. However, this analysis is performed at a constant $R_{\rm min}$, so it doesn't account for errors due to the removal of significant sources close to the halo. This is not an issue for our analysis because $R_{\rm tidal}$ is explicitly a proxy for the *large-scale* tidal field, and our proxy $D_{\rm vir}$ is better suited for close sources. This would, however, become a significant issue for studies which need $R_{\rm tidal}$ for purposes other than rank-ordering halos. Further discussion on the impact that improvements in the accuracy of $R_{\rm tidal}$ would have on our results can be found in section 6.4.1.

More generally, while the issue of measuring tidal radii around halos with only a single significant source is well-explored [see §2 in van den Bosch et al., 2018, for a review], and the tidal radius due to the large scale field can be measured effectively with the tidal tensor,

there currently does not exist an effective method for combining these two regimes. We outline a number of potential approaches which could be used to address this issue in 6.4.4, but consider the testing and calibration of such methods to be beyond the scope of this chapter.

6.6.4 Identifying Bound Particles in Halo Outskirts

While the concept of gravitational binding is straightforward to define for particles near the center of a non-accelerating halo, the same is not true for particles in the outskirts of halos, especially those experiencing a strong tidal force. These difficulties arise from two key areas: first, it is difficult to disentangle the potential caused by a halo from the potential of its surroundings. Although halos have a non-trivial amount of mass stored outside $R_{\rm vir}$, the so-called "two-halo" term starts to dominate the density distribution at $r \gtrsim 1 - 2R_{\rm vir}$ [e.g. Diemer and Kravtsov, 2014], meaning that any calculation of the potential which is done directly from the density profile or from the particle distribution must be done with care. Second, for particles near the tidal radius, the effective potential due to the external tidal field becomes significant. While this issue could in principle be solved by defining escape velocities relative to the minimum potential at either Lagrangian point, it also means that boundedness calculations will suffer from the same accuracy issues as the tidal radius calculations (see Appendix 6.6.3).

The effect of tidal forces on particle escape velocities presents another issue for the analysis in this chapter, specifically. If this effect is taken into account, it means that *gravitational heating and tidal forces can no longer be disentangled*. Even a "control" variable like $M_{\beta,\rm b}$ would depend on the tidal field, and could potentially make gravitational heating appear to be more a more significant contributor to assembly bias than it actually is. Primarily because of this reason, and to a lesser extent because of the issues described in the previous paragraph, we take on the simple and standard boundedness condition given in Eq. 6.7, but note that the $f_{\rm removed}$ value for $M_{\rm tidal,b}$ could become even lower if more sophisticated

approaches were used.

REFERENCES

S. J. Aarseth. Dynamical evolution of clusters of galaxies, I. *MNRAS*, 126:223, January 1963. doi: 10.1093/mnras/126.3.223.

K. Abazajian, Z. Zheng, I. Zehavi, D. H. Weinberg, J. A. Frieman, A. A. Berlind, M. R. Blanton, N. A. Bahcall, J. Brinkmann, D. P. Schneider, and M. Tegmark. Cosmology and the Halo Occupation Distribution from Small-Scale Galaxy Clustering in the Sloan Digital Sky Survey. *ApJ*, 625:613–620, June 2005. doi: 10.1086/429685.

T. Abel, O. Hahn, and R. Kaehler. Tracing the dark matter sheet in phase space. *MNRAS*, 427:61–76, November 2012a. doi: 10.1111/j.1365-2966.2012.21754.x.

Tom Abel, Oliver Hahn, and Ralf Kaehler. Tracing the dark matter sheet in phase space. *MNRAS*, 427(1):61–76, November 2012b. doi: 10.1111/j.1365-2966.2012.21754.x.

Tamra Adams. *Dictionary of Nature Myths: Legends of Earth, Sea, and Sky.* ABC-CLIO Inc., 1998.

S. Adhikari, N. Dalal, and R. T. Chamberlain. Splashback in accreting dark matter halos. *JCAP*, 11:019, November 2014. doi: 10.1088/1475-7516/2014/11/019.

S. Adhikari, N. Dalal, and J. Clampitt. Observing dynamical friction in galaxy clusters. *ArXiv e-prints*, May 2016.

Brandon Allgood, Ricardo A. Flores, Joel R. Primack, Andrey V. Kravtsov, Risa H. Wechsler, Andreas Faltenbacher, and James S. Bullock. The shape of dark matter haloes: dependence on mass, redshift, radius and formation. *MNRAS*, 367(4):1781–1796, April 2006. doi: 10.1111/j.1365-2966.2006.10094.x.

R. E. Angulo, V. Springel, S. D. M. White, A. Jenkins, C. M. Baugh, and C. S. Frenk. Scaling relations for galaxy clusters in the Millennium-XXL simulation. *MNRAS*, 426(3): 2046–2062, November 2012. doi: 10.1111/j.1365-2966.2012.21830.x.

Horace W. Babcock. The rotation of the Andromeda Nebula. *Lick Observatory Bulletin*, 498:41–51, January 1939. doi: 10.5479/ADS/bib/1939LicOB.19.41B.

N. A. Bahcall and R. M. Soneira. The spatial correlation function of rich clusters of galaxies. *ApJ*, 270:20–38, July 1983. doi: 10.1086/161094.

Yannick M. Bahé, Ian G. McCarthy, Michael L. Balogh, and Andreea S. Font. Why does the environmental influence on group and cluster galaxies extend beyond the virial radius? *MNRAS*, 430(4):3017–3031, April 2013. doi: 10.1093/mnras/stt109.

Michael L. Balogh, Julio F. Navarro, and Simon L. Morris. The Origin of Star Formation Gradients in Rich Galaxy Clusters. *ApJ*, 540(1):113–121, September 2000. doi: 10.1086/309323.

M. R. Becker and A. V. Kravtsov. On the Accuracy of Weak-lensing Cluster Mass Reconstructions. *ApJ*, 740:25, October 2011. doi: 10.1088/0004-637X/740/1/25.

Steven V. W. Beckwith, Massimo Stiavelli, Anton M. Koekemoer, John A. R. Caldwell, Henry C. Ferguson, Richard Hook, Ray A. Lucas, Louis E. Bergeron, Michael Corbin, Shardha Jogee, Nino Panagia, Massimo Robberto, Patricia Royle, Rachel S. Somerville, and Megan Sosey. The Hubble Ultra Deep Field. *AJ*, 132(5):1729–1755, November 2006. doi: 10.1086/507302.

P. Behroozi, R. Wechsler, A. Hearin, and C. Conroy. UniverseMachine: The Correlation between Galaxy Growth and Dark Matter Halo Assembly from z=0-10. *ArXiv e-prints*, June 2018.

P. S. Behroozi, A. Loeb, and R. H. Wechsler. Unbound particles in dark matter halos. *JCAP*, 6:019, June 2013a. doi: 10.1088/1475-7516/2013/06/019.

P. S. Behroozi, R. H. Wechsler, and C. Conroy. The Average Star Formation Histories of

Galaxies in Dark Matter Halos from z = 0-8. *ApJ*, 770:57, June 2013b. doi: 10.1088/0004-637X/770/1/57.

P. S. Behroozi, R. H. Wechsler, and H.-Y. Wu. The ROCKSTAR Phase-space Temporal Halo Finder and the Velocity Offsets of Cluster Cores. *ApJ*, 762:109, January 2013c. doi: 10.1088/0004-637X/762/2/109.

P. S. Behroozi, R. H. Wechsler, and H.-Y. Wu. The ROCKSTAR Phase-space Temporal Halo Finder and the Velocity Offsets of Cluster Cores. *ApJ*, 762:109, January 2013d. doi: 10.1088/0004-637X/762/2/109.

P. S. Behroozi, R. H. Wechsler, H.-Y. Wu, M. T. Busha, A. A. Klypin, and J. R. Primack. Gravitationally Consistent Halo Catalogs and Merger Trees for Precision Cosmology. *ApJ*, 763:18, January 2013e. doi: 10.1088/0004-637X/763/1/18.

P. S. Behroozi, R. H. Wechsler, Y. Lu, O. Hahn, M. T. Busha, A. Klypin, and J. R. Primack. Mergers and Mass Accretion for Infalling Halos Both End Well Outside Cluster Virial Radii. *ApJ*, 787:156, June 2014. doi: 10.1088/0004-637X/787/2/156.

Peter S. Behroozi, Guangtun Zhu, Henry C. Ferguson, Andrew P. Hearin, Jennifer Lotz, Joseph Silk, Susan Kassin, Yu Lu, Darren Croton, Rachel S. Somerville, and Douglas F. Watson. Using galaxy pairs to probe star formation during major halo mergers. *MNRAS*, 450(2):1546–1564, June 2015. doi: 10.1093/mnras/stv728.

C. Beisbart and M. Kerscher. Luminosity- and Morphology-dependent Clustering of Galaxies. *ApJ*, 545:6–25, December 2000. doi: 10.1086/317788.

V. Belokurov, D. Erkal, N. W. Evans, S. E. Koposov, and A. J. Deason. Co-formation of the disc and the stellar halo. *MNRAS*, 478(1):611–619, July 2018. doi: 10.1093/mnras/sty982.

Andreas A. Berlind and David H. Weinberg. The Halo Occupation Distribution: Toward

an Empirical Determination of the Relation between Galaxies and Mass. *ApJ*, 575(2): 587–616, August 2002. doi: 10.1086/341469.

A. M. Berti, A. L. Coil, P. S. Behroozi, D. J. Eisenstein, A. D. Bray, R. J. Cool, and J. Moustakas. PRIMUS: One- and Two-halo Galactic Conformity at 0.2 ¡ z ¡ 1. *ApJ*, 834: 87, January 2017. doi: 10.3847/1538-4357/834/1/87.

E. Bertschinger. Self-similar secondary infall and accretion in an Einstein-de Sitter universe. *ApJs*, 58:39–65, May 1985. doi: 10.1086/191028.

Suman Bhattacharya, Salman Habib, Katrin Heitmann, and Alexey Vikhlinin. Dark Matter Halo Profiles of Massive Clusters: Theory versus Observations. *ApJ*, 766(1):32, Mar 2013. doi: 10.1088/0004-637X/766/1/32.

Michael R. Blanton, David W. Hogg, Neta A. Bahcall, J. Brinkmann, Malcolm Britton, Andrew J. Connolly, István Csabai, Masataka Fukugita, Jon Loveday, Avery Meiksin, Jeffrey A. Munn, R. C. Nichol, Sadanori Okamura, Thomas Quinn, Donald P. Schneider, Kazuhiro Shimasaku, Michael A. Strauss, Max Tegmark, Michael S. Vogeley, and David H. Weinberg. The Galaxy Luminosity Function and Luminosity Density at Redshift z = 0.1. *ApJ*, 592(2):819–838, August 2003. doi: 10.1086/375776.

Siegfried Bodenmann. The 18th-century battle over lunar motion. *Physics Today*, 63(1):27, January 2010. doi: 10.1063/1.3293410.

J. R. Bond, L. Kofman, and D. Pogosyan. How filaments of galaxies are woven into the cosmic web. *Nature*, 380:603–606, April 1996. doi: 10.1038/380603a0.

G. L. Bryan and M. L. Norman. Statistical Properties of X-Ray Clusters: Analytic and Numerical Comparisons. *ApJ*, 495:80–99, March 1998. doi: 10.1086/305262.

J. S. Bullock, T. S. Kolatt, Y. Sigad, R. S. Somerville, A. V. Kravtsov, A. A. Klypin,

J. R. Primack, and A. Dekel. Profiles of dark haloes: evolution, scatter and environment. *MNRAS*, 321:559–575, March 2001. doi: 10.1046/j.1365-8711.2001.04068.x.

V. F. Calderon, A. A. Berlind, and M. Sinha. Small- and large-scale galactic conformity in SDSS DR7. *MNRAS*, 480:2031–2045, October 2018. doi: 10.1093/mnras/sty2000.

D. Campbell, F. C. van den Bosch, A. Hearin, N. Padmanabhan, A. Berlind, H. J. Mo, J. Tinker, and X. Yang. Assessing colour-dependent occupation statistics inferred from galaxy group catalogues. *MNRAS*, 452:444–469, September 2015. doi: 10.1093/mnras/stv1091.

Duncan Campbell, Frank C. van den Bosch, Nikhil Padmanabhan, Yao-Yuan Mao, Andrew R. Zentner, Johannes U. Lange, Fangzhou Jiang, and Antonio Villarreal. The galaxy clustering crisis in abundance matching. *MNRAS*, 477(1):359–383, June 2018. doi: 10.1093/mnras/sty495.

Claude Carignan, Laurent Chemin, Walter K. Huchtmeier, and Felix J. Lockman. The Extended H I Rotation Curve and Mass Distribution of M31. *ApJL*, 641(2):L109–L112, April 2006. doi: 10.1086/503869.

Scott G. Carlsten, Jenny E. Greene, Annika H. G. Peter, Johnny P. Greco, and Rachael L. Beaton. Radial Distributions of Dwarf Satellite Systems in the Local Volume. *arXiv e-prints*, art. arXiv:2006.02444, June 2020.

M. Cautun, R. van de Weygaert, B. J. T. Jones, and C. S. Frenk. Evolution of the cosmic web. *MNRAS*, 441:2923–2973, July 2014. doi: 10.1093/mnras/stu768.

C. Chang, E. Baxter, B. Jain, C. Sánchez, S. Adhikari, T. N. Varga, Y. Fang, E. Rozo, E. S. Rykoff, A. Kravtsov, D. Gruen, W. Hartley, E. M. Huff, M. Jarvis, A. G. Kim, J. Prat, N. MacCrann, T. McClintock, A. Palmese, D. Rapetti, R. P. Rollins, S. Samuroff, E. Sheldon, M. A. Troxel, R. H. Wechsler, Y. Zhang, J. Zuntz, T. M. C. Abbott, F. B. Abdalla, S. Allam, J. Annis, K. Bechtol, A. Benoit-Lévy, G. M. Bernstein, D. Brooks, E. Buckley-Geer, A. Carnero Rosell, M. Carrasco Kind, J. Carretero, C. B. D'Andrea, L. N. da Costa,

C. Davis, S. Desai, H. T. Diehl, J. P. Dietrich, A. Drlica-Wagner, T. F. Eifler, B. Flaugher, P. Fosalba, J. Frieman, J. García-Bellido, E. Gaztanaga, D. W. Gerdes, R. A. Gruendl, J. Gschwend, G. Gutierrez, K. Honscheid, D. J. James, T. Jeltema, E. Krause, K. Kuehn, O. Lahav, M. Lima, M. March, J. L. Marshall, P. Martini, P. Melchior, F. Menanteau, R. Miquel, J. J. Mohr, B. Nord, R. L. C. Ogando, A. A. Plazas, E. Sanchez, V. Scarpine, R. Schindler, M. Schubnell, I. Sevilla-Noarbe, M. Smith, R. C. Smith, M. Soares-Santos, F. Sobreira, E. Suchyta, M. E. C. Swanson, G. Tarle, J. Weller, and DES Collaboration. The Splashback Feature around DES Galaxy Clusters: Galaxy Density and Weak Lensing Profiles. *ApJ*, 864(1):83, September 2018. doi: 10.3847/1538-4357/aad5e7.

William Chapman. *Workshop Technology Part 1.* Routledge, 2019.

Hillary L. Child, Salman Habib, Katrin Heitmann, Nicholas Frontiere, Hal Finkel, Adrian Pope, and Vitali Morozov. Halo Profiles and the Concentration-Mass Relation for a ΛCDM Universe. *ApJ*, 859(1):55, May 2018. doi: 10.3847/1538-4357/aabf95.

C. Y. R. Chue, N. Dalal, and M. White. Some assembly required: assembly bias in massive dark matter halos. *JCAP*, 10:012, October 2018. doi: 10.1088/1475-7516/2018/10/012.

A. R. Conn, G. F. Lewis, R. A. Ibata, Q. A. Parker, D. B. Zucker, A. W. McConnachie, N. F. Martin, D. Valls-Gabaud, N. Tanvir, M. J. Irwin, A. M. N. Ferguson, and S. C. Chapman. The Three-dimensional Structure of the M31 Satellite System; Strong Evidence for an Inhomogeneous Distribution of Satellites. *ApJ*, 766(2):120, April 2013. doi: 10.1088/0004-637X/766/2/120.

Alan Cook. *Edmond Halley. Charting the heavens and the seas.* 1998.

Martín Crocce, Sebastián Pueblas, and Román Scoccimarro. Transients from initial conditions in cosmological simulations. *MNRAS*, 373(1):369–381, November 2006. doi: 10.1111/j.1365-2966.2006.11040.x.

N. Dalal, M. White, J. R. Bond, and A. Shirokov. Halo Assembly Bias in Hierarchical Structure Formation. *ApJ*, 687:12–21, November 2008. doi: 10.1086/591512.

N. Dalal, Y. Lithwick, and M. Kuhlen. The Origin of Dark Matter Halo Profiles. *ArXiv e-prints*, October 2010.

W. J. G. de Blok. The Core-Cusp Problem. *Advances in Astronomy*, 2010:789293, January 2010. doi: 10.1155/2010/789293.

W. J. G. de Blok, F. Walter, E. Brinks, C. Trachternach, S. H. Oh, and Jr. Kennicutt, R. C. High-Resolution Rotation Curves and Galaxy Mass Models from THINGS. *AJ*, 136(6): 2648–2719, December 2008. doi: 10.1088/0004-6256/136/6/2648.

Gerard de Vaucouleurs. Classification and Morphology of External Galaxies. *Handbuch der Physik*, 53:275, January 1959. doi: 10.1007/978-3-642-45932-07.

Walter Dehnen. Towards optimal softening in three-dimensional N-body codes - I. Minimizing the force error. *MNRAS*, 324(2):273–291, June 2001. doi: 10.1046/j.1365-8711.2001.04237.x.

B. Delaunay. Sur la sphère vide. *Bulletin de l'Académie des Sciences de l'URSS, Classe des sciences mathématiques et naturelles*, 6:793–800, 1934.

V. Desjacques. Environmental dependence in the ellipsoidal collapse model. *MNRAS*, 388: 638–658, August 2008. doi: 10.1111/j.1365-2966.2008.13420.x.

V. Desjacques, D. Jeong, and F. Schmidt. Large-scale galaxy bias. *Physics Reports*, 733: 1–193, February 2018. doi: 10.1016/j.physrep.2017.12.002.

Harry Desmond and Risa H. Wechsler. The Tully-Fisher and mass-size relations from halo abundance matching. *MNRAS*, 454(1):322–343, November 2015. doi: 10.1093/mnras/stv1978.

B. Diemer. The Splashback Radius of Halos from Particle Dynamics. I. The SPARTA Algorithm. *ApJs*, 231:5, July 2017a. doi: 10.3847/1538-4365/aa799c.

B. Diemer. The splashback radius of halos from particle dynamics: I. The SPARTA algorithm. *ArXiv e-prints*, March 2017b.

B. Diemer. COLOSSUS: A Python Toolkit for Cosmology, Large-scale Structure, and Dark Matter Halos. *ApJs*, 239:35, December 2018. doi: 10.3847/1538-4365/aaee8c.

B. Diemer and M. Joyce. An Accurate Physical Model for Halo Concentrations. *ApJ*, 871: 168, February 2019. doi: 10.3847/1538-4357/aafad6.

B. Diemer and A. V. Kravtsov. Dependence of the Outer Density Profiles of Halos on Their Mass Accretion Rate. *ApJ*, 789:1, July 2014. doi: 10.1088/0004-637X/789/1/1.

B. Diemer and A. V. Kravtsov. A Universal Model for Halo Concentrations. *ApJ*, 799:108, January 2015. doi: 10.1088/0004-637X/799/1/108.

B. Diemer, A. V. Kravtsov, and S. More. On the Evolution of Cluster Scaling Relations. *ApJ*, 779:159, December 2013a. doi: 10.1088/0004-637X/779/2/159.

B. Diemer, S. More, and A. V. Kravtsov. The Pseudo-evolution of Halo Mass. *ApJ*, 766:25, March 2013b. doi: 10.1088/0004-637X/766/1/25.

B. Diemer, P. Mansfield, A. V. Kravtsov, and S. More. The Splashback Radius of Halos from Particle Dynamics. II. Dependence on Mass, Accretion Rate, Redshift, and Cosmology. *ApJ*, 843:140, July 2017. doi: 10.3847/1538-4357/aa79ab.

Scott Dodelson. *Modern cosmology*. 2003.

A. Drlica-Wagner, K. Bechtol, S. Mau, M. McNanna, E. O. Nadler, A. B. Pace, T. S. Li, A. Pieres, E. Rozo, J. D. Simon, A. R. Walker, R. H. Wechsler, T. M. C. Abbott, S. Allam,

J. Annis, E. Bertin, D. Brooks, D. L. Burke, A. Carnero Rosell, M. Carrasco Kind, J. Carretero, M. Costanzi, L. N. da Costa, J. De Vicente, S. Desai, H. T. Diehl, P. Doel, T. F. Eifler, S. Everett, B. Flaugher, J. Frieman, J. Garcia-Bellido, E. Gaztanaga, D. Gruen, R. A. Gruendl, J. Gschwend, G. Gutierrez, K. Honscheid, D. J. James, E. Krause, K. Kuehn, N. Kuropatkin, O. Lahav, M. A. G. Maia, J. L. Marshall, P. Melchior, F. Menanteau, R. Miquel, A. Palmese, A. A. Plazas, E. Sanchez, V. Scarpine, M. Schubnell, S. Serrano, I. Sevilla-Noarbe, M. Smith, E. Suchyta, and G. Tarle. Milky Way Satellite Census – I. The Observational Selection Function for Milky Way Satellites in DES Y3 and Pan-STARRS DR1. *arXiv e-prints*, art. arXiv:1912.03302, December 2019.

Alan R. Duffy, Joop Schaye, Scott T. Kay, and Claudio Dalla Vecchia. Dark matter halo concentrations in the Wilkinson Microwave Anisotropy Probe year 5 cosmology. *MNRAS*, 390(1):L64–L68, Oct 2008. doi: 10.1111/j.1745-3933.2008.00537.x.

Aaron A. Dutton and Andrea V. Macciò. Cold dark matter haloes in the Planck era: evolution of structural parameters for Einasto and NFW profiles. *MNRAS*, 441(4):3359–3374, Jul 2014. doi: 10.1093/mnras/stu742.

Jaan Einasto, Ants Kaasik, and Enn Saar. Dynamic evidence on massive coronas of galaxies. *Nature*, 250(5464):309–310, July 1974. doi: 10.1038/250309a0.

A. Einstein and W. de Sitter. On the Relation between the Expansion and the Mean Density of the Universe. *Proceedings of the National Academy of Science*, 18(3):213–214, March 1932. doi: 10.1073/pnas.18.3.213.

The HIPPARCOS and TYCHO catalogues. Astrometric and photometric star catalogues derived from the ESA HIPPARCOS Space Astrometry Mission, volume 1200 of *ESA Special Publication*, January 1997. ESA.

Leonhard Euler. *De motu rectilineo trium corporum se mutuo attrahentium.* 1765. URL `http://eulerarchive.maa.org//docs/originals/E327.pdf`.

A. E. Evrard, J. Bialek, M. Busha, M. White, S. Habib, K. Heitmann, M. Warren, E. Rasia, G. Tormen, L. Moscardini, C. Power, A. R. Jenkins, L. Gao, C. S. Frenk, V. Springel, S. D. M. White, and J. Diemand. Virial Scaling of Massive Dark Matter Halos: Why Clusters Prefer a High Normalization Cosmology. *ApJ*, 672(1):122–137, January 2008. doi: 10.1086/521616.

S. M. Faber and J. S. Gallagher. Masses and mass-to-light ratios of galaxies. *ARA&A*, 17: 135–187, January 1979. doi: 10.1146/annurev.aa.17.090179.001031.

A. Faltenbacher and S. D. M. White. Assembly Bias and the Dynamical Structure of Dark Matter Halos. *ApJ*, 708:469–473, January 2010. doi: 10.1088/0004-637X/708/1/469.

J. A. Fillmore and P. Goldreich. Self-similar gravitational collapse in an expanding universe. *ApJ*, 281:1–8, June 1984. doi: 10.1086/162070.

Robert A Freitas. *Nanomedicine, volume I: basic capabilities*, volume 1. Landes Bioscience Georgetown, TX, 1999.

A. Friedmann. Über die Krümmung des Raumes. *Zeitschrift fur Physik*, 10:377–386, January 1922. doi: 10.1007/BF01332580.

L. Gao and S. D. M. White. Assembly bias in the clustering of dark matter haloes. *MNRAS*, 377:L5–L9, April 2007. doi: 10.1111/j.1745-3933.2007.00292.x.

L. Gao, S. D. M. White, A. Jenkins, F. Stoehr, and V. Springel. The subhalo populations of ΛCDM dark haloes. *MNRAS*, 355(3):819–834, December 2004. doi: 10.1111/j.1365-2966.2004.08360.x.

L. Gao, V. Springel, and S. D. M. White. The age dependence of halo clustering. *MNRAS*, 363:L66–L70, October 2005. doi: 10.1111/j.1745-3933.2005.00084.x.

Liang Gao, Julio F. Navarro, Shaun Cole, Carlos S. Frenk, Simon D. M. White, Volker Springel, Adrian Jenkins, and Angelo F. Neto. The redshift dependence of the struc-

ture of massive Λ cold dark matter haloes. *MNRAS*, 387(2):536–544, Jun 2008. doi: 10.1111/j.1365-2966.2008.13277.x.

Shea Garrison-Kimmel, Michael Boylan-Kolchin, James S. Bullock, and Evan N. Kirby. Too big to fail in the Local Group. *MNRAS*, 444(1):222–236, October 2014. doi: 10.1093/mnras/stu1477.

Shea Garrison-Kimmel, Andrew Wetzel, James S. Bullock, Philip F. Hopkins, Michael Boylan-Kolchin, Claude-André Faucher-Giguère, Dušan Kereš, Eliot Quataert, Robyn E. Sanderson, Andrew S. Graus, and Tyler Kelley. Not so lumpy after all: modelling the depletion of dark matter subhaloes by Milky Way-like galaxies. *MNRAS*, 471(2):1709–1727, October 2017. doi: 10.1093/mnras/stx1710.

Chong Ge, Ming Sun, Eduardo Rozo, Neelima Sehgal, Alexey Vikhlinin, William Forman, Christine Jones, and Daisuke Nagai. X-ray scaling relations from a complete sample of the richest maxBCG clusters. *MNRAS*, 484(2):1946–1971, April 2019. doi: 10.1093/mnras/stz088.

S. P. D. Gill, A. Knebe, and B. K. Gibson. The evolution of substructure - III. The outskirts of clusters. *MNRAS*, 356:1327–1332, February 2005. doi: 10.1111/j.1365-2966.2004.08562.x.

J. Goodman and J. Weare. Ensemble samplers with affine invariance. *Communications in Applied Mathematics and Computational Science*, 5:65–80, January 2010. doi: 10.2140/camcos.2010.5.65.

K. M. Górski, E. Hivon, A. J. Banday, B. D. Wandelt, F. K. Hansen, M. Reinecke, and M. Bartelmann. HEALPix: A Framework for High-Resolution Discretization and Fast Analysis of Data Distributed on the Sphere. *ApJ*, 622:759–771, April 2005. doi: 10.1086/427976.

S. Gottlöber, M. Kerscher, A. V. Kravtsov, A. Faltenbacher, A. Klypin, and V. Müller.

Spatial distribution of galactic halos and their merger histories. *A&Ap*, 387:778–787, June 2002. doi: 10.1051/0004-6361:20020339.

Stefan Gottloeber and Anatoly Klypin. The ART of Cosmological Simulations. *arXiv e-prints*, art. arXiv:0803.4343, Mar 2008.

Gravity Collaboration, R. Abuter, A. Amorim, M. Bauböck, J. P. Berger, H. Bonnet, W. Brand ner, Y. Clénet, V. Coudé Du Foresto, P. T. de Zeeuw, J. Dexter, G. Duvert, A. Eckart, F. Eisenhauer, N. M. Förster Schreiber, P. Garcia, F. Gao, E. Gendron, R. Genzel, O. Gerhard, S. Gillessen, M. Habibi, X. Haubois, T. Henning, S. Hippler, M. Horrobin, A. Jiménez-Rosales, L. Jocou, P. Kervella, S. Lacour, V. Lapeyrère, J. B. Le Bouquin, P. Léna, T. Ott, T. Paumard, K. Perraut, G. Perrin, O. Pfuhl, S. Rabien, G. Rodriguez Coira, G. Rousset, S. Scheithauer, A. Sternberg, O. Straub, C. Straubmeier, E. Sturm, L. J. Tacconi, F. Vincent, S. von Fellenberg, I. Waisberg, F. Widmann, E. Wieprecht, E. Wiezorrek, J. Woillez, and S. Yazici. A geometric distance measurement to the Galactic center black hole with 0.3% uncertainty. *AAp*, 625:L10, May 2019. doi: 10.1051/0004-6361/201935656.

Alan Grier. *When Computers Were Human*. Princeton University Press, 2013.

Brendan F. Griffen, Alexander P. Ji, Gregory A. Dooley, Facundo A. Gómez, Mark Vogelsberger, Brian W. O'Shea, and Anna Frebel. The Caterpillar Project: A Large Suite of Milky Way Sized Halos. *ApJ*, 818(1):10, Feb 2016. doi: 10.3847/0004-637X/818/1/10.

I. I. Gringorten and P. J. Yepez. The Division of a Circular or Spherical Surface Into Equal-Area Cells or Pixels. *Instrumentation Papers*, 343:1–7, June 1992.

J. E. Gunn and J. R. Gott, III. On the Infall of Matter Into Clusters of Galaxies and Some Effects on Their Evolution. *ApJ*, 176:1, August 1972a. doi: 10.1086/151605.

J. E. Gunn and J. R. Gott, III. On the Infall of Matter Into Clusters of Galaxies and Some Effects on Their Evolution. *ApJ*, 176:1, August 1972b. doi: 10.1086/151605.

Qi Guo and Simon White. Numerical resolution limits on subhalo abundance matching. *MNRAS*, 437(4):3228–3235, February 2014. doi: 10.1093/mnras/stt2116.

H. Gursky, E. Kellogg, S. Murray, C. Leong, H. Tananbaum, and R. Giacconi. A Strong X-Ray Source in the Coma Cluster Observed by UHURU. *ApJL*, 167:L81, August 1971. doi: 10.1086/180765.

O. Hahn and R. E. Angulo. An adaptively refined phase-space element method for cosmological simulations and collisionless dynamics. *MNRAS*, 455:1115–1133, January 2016. doi: 10.1093/mnras/stv2304.

O. Hahn, C. Porciani, A. Dekel, and C. M. Carollo. Tidal effects and the environment dependence of halo assembly. *MNRAS*, 398:1742–1756, October 2009. doi: 10.1111/j.1365-2966.2009.15271.x.

Oliver Hahn and Tom Abel. Multi-scale initial conditions for cosmological simulations. *MNRAS*, 415(3):2101–2121, August 2011. doi: 10.1111/j.1365-2966.2011.18820.x.

Zoltan Haiman, Anne A. Thoul, and Abraham Loeb. Cosmological Formation of Low-Mass Objects. *ApJ*, 464:523, June 1996. doi: 10.1086/177343.

J. Han, Y. Li, Y. Jing, T. Nishimichi, W. Wang, and C. Jiang. The multidimensional dependence of halo bias in the eye of a machine: a tale of halo structure, assembly, and environment. *MNRAS*, 482:1900–1919, January 2019. doi: 10.1093/mnras/sty2822.

G. Harker, S. Cole, J. Helly, C. Frenk, and A. Jenkins. A marked correlation function analysis of halo formation times in the Millennium Simulation. *MNRAS*, 367:1039–1049, April 2006. doi: 10.1111/j.1365-2966.2006.10022.x.

Roslynn D Haynes. *Astronomy and the Dreaming: The Astronomy of the Aboriginal Australians*. Springer Science Business Media, B. V., 1998.

A. Hearin, E. Tollerud, T. Robitaille, M. Droettboom, A. Zentner, E. Bray, M. Craig, L. Bradley, K. Barbary, C. Deil, K. Tan, M. R. Becker, S. More, H. M. Günther, and B. Sipocz. Halotools: Galaxy-Halo connection models. Astrophysics Source Code Library, April 2016a.

A. P. Hearin, D. F. Watson, and F. C. van den Bosch. Beyond halo mass: galactic conformity as a smoking gun of central galaxy assembly bias. *MNRAS*, 452:1958–1969, September 2015. doi: 10.1093/mnras/stv1358.

A. P. Hearin, P. S. Behroozi, and F. C. van den Bosch. On the physical origin of galactic conformity. *MNRAS*, 461:2135–2145, September 2016b. doi: 10.1093/mnras/stw1462.

D. J. Heath. The growth of density perturbations in zero pressure Friedmann-Lemaitre universes. *MNRAS*, 179:351–358, May 1977. doi: 10.1093/mnras/179.3.351.

Amina Helmi, Carine Babusiaux, Helmer H. Koppelman, Davide Massari, Jovan Veljanoski, and Anthony G. A. Brown. The merger that led to the formation of the Milky Way's inner stellar halo and thick disk. *Nature*, 563(7729):85–88, October 2018. doi: 10.1038/s41586-018-0625-x.

Y. Hoffman and J. Shaham. Local density maxima: progenitors of structure. *ApJ*, 297: 16–22, October 1985. doi: 10.1086/163498.

Erik Holmberg. On the Clustering Tendencies among the Nebulae. II. a Study of Encounters Between Laboratory Models of Stellar Systems by a New Integration Procedure. *ApJ*, 94: 385, November 1941. doi: 10.1086/144344.

Philip F. Hopkins, Andrew Wetzel, Dušan Kereš, Claude-André Faucher-Giguère, Eliot Quataert, Michael Boylan-Kolchin, Norman Murray, Christopher C. Hayward, Shea Garrison-Kimmel, Cameron Hummels, Robert Feldmann, Paul Torrey, Xiangcheng Ma, Daniel Anglés-Alcázar, Kung-Yi Su, Matthew Orr, Denise Schmitz, Ivanna Escala, Robyn

Sanderson, Michael Y. Grudić, Zachary Hafen, Ji-Hoon Kim, Alex Fitts, James S. Bullock, Coral Wheeler, T. K. Chan, Oliver D. Elbert, and Desika Narayanan. FIRE-2 simulations: physics versus numerics in galaxy formation. *MNRAS*, 480(1):800–863, Oct 2018. doi: 10.1093/mnras/sty1690.

Song Huang, Alexie Leauthaud, Andrew Hearin, Peter Behroozi, Christopher Bradshaw, Felipe Ardila, Joshua Speagle, Ananth Tenneti, Kevin Bundy, Jenny Greene, Cristóbal Sifón, and Neta Bahcall. Weak lensing reveals a tight connection between dark matter halo mass and the distribution of stellar mass in massive galaxies. *MNRAS*, 492(3):3685–3707, March 2020. doi: 10.1093/mnras/stz3314.

Edwin Hubble. A Relation between Distance and Radial Velocity among Extra-Galactic Nebulae. *Proceedings of the National Academy of Science*, 15(3):168–173, March 1929. doi: 10.1073/pnas.15.3.168.

Tomoaki Ishiyama, Toshiyuki Fukushige, and Junichiro Makino. GreeM: Massively Parallel TreePM Code for Large Cosmological N -body Simulations. *PASJ*, 61:1319, Dec 2009. doi: 10.1093/pasj/61.6.1319.

Tomoaki Ishiyama, Keigo Nitadori, and Junichiro Makino. 4.45 Pflops Astrophysical N-Body Simulation on K computer – The Gravitational Trillion-Body Problem. *arXiv e-prints*, art. arXiv:1211.4406, Nov 2012.

Tomoaki Ishiyama, Motohiro Enoki, Masakazu A. R. Kobayashi, Ryu Makiya, Masahiro Nagashima, and Taira Oogi. The ν^2GC simulations: Quantifying the dark side of the universe in the Planck cosmology. *PASJ*, 67(4):61, Aug 2015. doi: 10.1093/pasj/psv021.

Tomoaki Ishiyama, Francisco Prada, Anatoly A. Klypin, Manodeep Sinha, R. Benton Metcalf, Eric Jullo, Bruno Altieri, Sofía A. Cora, Darren Croton, Sylvain de la Torre, David E. Millán-Calero, Taira Oogi, José Ruedas, and Cristian A. Vega-Martínez. The Uchuu Sim-

ulations: Data Release 1 and Dark Matter Halo Concentrations. *arXiv e-prints*, art. arXiv:2007.14720, July 2020.

M. James Jee, John P. Hughes, Felipe Menanteau, Cristóbal Sifón, Rachel Mandelbaum, L. Felipe Barrientos, Leopoldo Infante, and Karen Y. Ng. Weighing "El Gordo" with a Precision Scale: Hubble Space Telescope Weak-lensing Analysis of the Merging Galaxy Cluster ACT-CL J0102-4915 at z = 0.87. *ApJ*, 785(1):20, April 2014. doi: 10.1088/0004-637X/785/1/20.

Y. P. Jing and Y. Suto. Triaxial Modeling of Halo Density Profiles with High-Resolution N-Body Simulations. *ApJ*, 574:538–553, August 2002. doi: 10.1086/341065.

Y. P. Jing, Y. Suto, and H. J. Mo. The Dependence of Dark Halo Clustering on Formation Epoch and Concentration Parameter. *ApJ*, 657:664–668, March 2007. doi: 10.1086/511130.

Diane Johnson. *Night Skies of Aboriginal Australia: a Noctuary*. Sydney University Press, 1998.

J. W. Johnson, A. H. Maller, A. A. Berlind, M. Sinha, and J. K. Holley-Bockelmann. The secondary spin bias of dark matter haloes. *MNRAS*, 486:1156–1166, June 2019. doi: 10.1093/mnras/stz942.

Michael Joyce, Lehman Garrison, and Daniel Eisenstein. Quantifying resolution in cosmological N-body simulations using self-similarity. *arXiv e-prints*, art. arXiv:2004.07256, April 2020.

F. D. Kahn and L. Woltjer. Intergalactic Matter and the Galaxy. *ApJ*, 130:705, November 1959. doi: 10.1086/146762.

N. Kaiser. On the spatial correlations of Abell clusters. *ApJl*, 284:L9–L12, September 1984. doi: 10.1086/184341.

S. Kazantzidis, L. Mayer, C. Mastropietro, J. Diemand, J. Stadel, and B. Moore. Density Profiles of Cold Dark Matter Substructure: Implications for the Missing-Satellites Problem. *ApJ*, 608:663–679, June 2004. doi: 10.1086/420840.

S. Kazantzidis, A. R. Zentner, and A. V. Kravtsov. The Robustness of Dark Matter Density Profiles in Dissipationless Mergers. *ApJ*, 641:647–664, April 2006. doi: 10.1086/500579.

A. Klypin, G. Yepes, S. Gottlöber, F. Prada, and S. Heß. MultiDark simulations: the story of dark matter halo concentrations and density profiles. *MNRAS*, 457:4340–4359, April 2016. doi: 10.1093/mnras/stw248.

A. A. Klypin and A. I. Kopylov. The Spatial Covariance Function for Rich Clusters of Galaxies. *Soviet Astronomy Letters*, 9:41–44, February 1983.

A. A. Klypin, S. Trujillo-Gomez, and J. Primack. Dark Matter Halos in the Standard Cosmological Model: Results from the Bolshoi Simulation. *ApJ*, 740:102, October 2011. doi: 10.1088/0004-637X/740/2/102.

Anatoly Klypin, Stefan Gottlöber, Andrey V. Kravtsov, and Alexei M. Khokhlov. Galaxies in N-Body Simulations: Overcoming the Overmerging Problem. *ApJ*, 516(2):530–551, May 1999. doi: 10.1086/307122.

Anatoly Klypin, Igor Karachentsev, Dmitry Makarov, and Olga Nasonova. Abundance of field galaxies. *MNRAS*, 454(2):1798–1810, December 2015a. doi: 10.1093/mnras/stv2040.

Anatoly Klypin, Francisco Prada, Gustavo Yepes, Steffen Heß, and Stefan Gottlöber. Halo abundance matching: accuracy and conditions for numerical convergence. *MNRAS*, 447 (4):3693–3707, Mar 2015b. doi: 10.1093/mnras/stu2685.

A. Knebe, F. R. Pearce, H. Lux, Y. Ascasibar, P. Behroozi, J. Casado, C. C. Moran, J. Diemand, K. Dolag, R. Dominguez-Tenreiro, P. Elahi, B. Falck, S. Gottlöber, J. Han, A. Klypin, Z. Lukić, M. Maciejewski, C. K. McBride, M. E. Merchán, S. I. Muldrew,

M. Neyrinck, J. Onions, S. Planelles, D. Potter, V. Quilis, Y. Rasera, P. M. Ricker, F. Roy, A. N. Ruiz, M. A. Sgró, V. Springel, J. Stadel, P. M. Sutter, D. Tweed, and M. Zemp. Structure finding in cosmological simulations: the state of affairs. *MNRAS*, 435:1618–1658, October 2013. doi: 10.1093/mnras/stt1403.

Alexander Knebe, Andrey V. Kravtsov, Stefan Gottlöber, and Anatoly A. Klypin. On the effects of resolution in dissipationless cosmological simulations. *MNRAS*, 317(3):630–648, Sep 2000. doi: 10.1046/j.1365-8711.2000.03673.x.

Alexander Knebe, Christian Wagner, Steffen Knollmann, Tobias Diekershoff, and Fabian Krause. On the Starting Redshift Cosmological Simulations: Focusing on Halo Properties. *ApJ*, 698(1):266–274, June 2009. doi: 10.1088/0004-637X/698/1/266.

Alexander Knebe, Steffen R. Knollmann, Stuart I. Muldrew, Frazer R. Pearce, Miguel Angel Aragon-Calvo, Yago Ascasibar, Peter S. Behroozi, Daniel Ceverino, Stephane Colombi, Juerg Diemand, Klaus Dolag, Bridget L. Falck, Patricia Fasel, Jeff Gardner, Stefan Gottlöber, Chung-Hsing Hsu, Francesca Iannuzzi, Anatoly Klypin, Zarija Lukić, Michal Maciejewski, Cameron McBride, Mark C. Neyrinck, Susana Planelles, Doug Potter, Vicent Quilis, Yann Rasera, Justin I. Read, Paul M. Ricker, Fabrice Roy, Volker Springel, Joachim Stadel, Greg Stinson, P. M. Sutter, Victor Turchaninov, Dylan Tweed, Gustavo Yepes, and Marcel Zemp. Haloes gone MAD: The Halo-Finder Comparison Project. *MNRAS*, 415(3):2293–2318, August 2011. doi: 10.1111/j.1365-2966.2011.18858.x.

A. V. Kravtsov and S. Borgani. Formation of Galaxy Clusters. *Annual Reviews of Astronomy & Astrophysics*, 50:353–409, September 2012. doi: 10.1146/annurev-astro-081811-125502.

A. V. Kravtsov, A. A. Berlind, R. H. Wechsler, A. A. Klypin, S. Gottlöber, B. Allgood, and J. R. Primack. The Dark Side of the Halo Occupation Distribution. *ApJ*, 609:35–49, July 2004. doi: 10.1086/420959.

A. V. Kravtsov, A. A. Vikhlinin, and A. V. Meshcheryakov. Stellar Mass—Halo Mass

Relation and Star Formation Efficiency in High-Mass Halos. *Astronomy Letters*, 44(1): 8–34, January 2018. doi: 10.1134/S1063773717120015.

Andrey V. Kravtsov. *High-resolution simulations of structure formation in the universe*. PhD thesis, NEW MEXICO STATE UNIVERSITY, Jan 1999.

Andrey V. Kravtsov, Anatoly A. Klypin, and Alexei M. Khokhlov. Adaptive Refinement Tree: A New High-Resolution N-Body Code for Cosmological Simulations. *ApJs*, 111(1): 73–94, Jul 1997. doi: 10.1086/313015.

Gary Kronk. *Cometography: A Catalog of Comets*, volume 1. Cambridge University Press, 1999.

C. Lacey and S. Cole. Merger rates in hierarchical models of galaxy formation. *MNRAS*, 262:627–649, June 1993. doi: 10.1093/mnras/262.3.627.

O. Lahav, P. B. Lilje, J. R. Primack, and M. J. Rees. Dynamical effects of the cosmological constant. *MNRAS*, 251:128–136, July 1991. doi: 10.1093/mnras/251.1.128.

Jérôme Lalande. *Astronomie*. 1792.

Henrietta S. Leavitt. 1777 variables in the Magellanic Clouds. *Annals of Harvard College Observatory*, 60:87–108.3, January 1908.

Henrietta S. Leavitt and Edward C. Pickering. Periods of 25 Variable Stars in the Small Magellanic Cloud. *Harvard College Observatory Circular*, 173:1–3, March 1912.

B. V. Lehmann, Y.-Y. Mao, M. R. Becker, S. W. Skillman, and R. H. Wechsler. The Concentration Dependence of the Galaxy-Halo Connection: Modeling Assembly Bias with Abundance Matching. *ApJ*, 834:37, January 2017. doi: 10.3847/1538-4357/834/1/37.

G. Lemaître. Un Univers homogène de masse constante et de rayon croissant rendant compte de la vitesse radiale des nébuleuses extra-galactiques. *Annales de la Société Scientifique de Bruxelles*, 47:49–59, January 1927.

R. Li, L. Gao, L. Xie, and Q. Guo. Assembly bias of dwarf-sized dark matter haloes. *MNRAS*, 435:3592–3599, November 2013. doi: 10.1093/mnras/stt1551.

Y. Li, H. J. Mo, and L. Gao. On halo formation times and assembly bias. *MNRAS*, 389: 1419–1426, September 2008. doi: 10.1111/j.1365-2966.2008.13667.x.

N. I. Libeskind, R. van de Weygaert, M. Cautun, B. Falck, E. Tempel, T. Abel, M. Alpaslan, M. A. Aragón-Calvo, J. E. Forero-Romero, R. Gonzalez, S. Gottlöber, O. Hahn, W. A. Hellwing, Y. Hoffman, B. J. T. Jones, F. Kitaura, A. Knebe, S. Manti, M. Neyrinck, S. E. Nuza, N. Padilla, E. Platen, N. Ramachandra, A. Robotham, E. Saar, S. Shandarin, M. Steinmetz, R. S. Stoica, T. Sousbie, and G. Yepes. Tracing the cosmic web. *MNRAS*, 473:1195–1217, January 2018. doi: 10.1093/mnras/stx1976.

Noam I. Libeskind, Yehuda Hoffman, R. Brent Tully, Helene M. Courtois, Daniel Pomarède, Stefan Gottlöber, and Matthias Steinmetz. Planes of satellite galaxies and the cosmic web. *MNRAS*, 452(1):1052–1059, September 2015. doi: 10.1093/mnras/stv1302.

Y.-T. Lin, R. Mandelbaum, Y.-H. Huang, H.-J. Huang, N. Dalal, B. Diemer, H.-Y. Jian, and A. Kravtsov. On Detecting Halo Assembly Bias with Galaxy Populations. *ApJ*, 819: 119, March 2016. doi: 10.3847/0004-637X/819/2/119.

Y. Lu, H. J. Mo, N. Katz, and M. D. Weinberg. On the origin of cold dark matter halo density profiles. *MNRAS*, 368:1931–1940, June 2006. doi: 10.1111/j.1365-2966.2006.10270.x.

A. D. Ludlow, J. F. Navarro, V. Springel, A. Jenkins, C. S. Frenk, and A. Helmi. The Unorthodox Orbits of Substructure Halos. *ApJ*, 692:931–941, February 2009. doi: 10.1088/0004-637X/692/1/931.

A. D. Ludlow, J. F. Navarro, M. Li, R. E. Angulo, M. Boylan-Kolchin, and P. E. Bett. The dynamical state and mass-concentration relation of galaxy clusters. *MNRAS*, 427: 1322–1328, December 2012. doi: 10.1111/j.1365-2966.2012.21892.x.

A. D. Ludlow, J. F. Navarro, M. Boylan-Kolchin, P. E. Bett, R. E. Angulo, M. Li, S. D. M. White, C. Frenk, and V. Springel. The mass profile and accretion history of cold dark matter haloes. *MNRAS*, 432:1103–1113, June 2013. doi: 10.1093/mnras/stt526.

A. D. Ludlow, J. F. Navarro, R. E. Angulo, M. Boylan-Kolchin, V. Springel, C. Frenk, and S. D. M. White. The mass-concentration-redshift relation of cold dark matter haloes. *MNRAS*, 441:378–388, June 2014. doi: 10.1093/mnras/stu483.

A. D. Ludlow, J. Schaye, and R. Bower. Numerical convergence of simulations of galaxy formation: the abundance and internal structure of cold dark matter haloes. *arXiv e-prints*, page 1, December 2018.

Aaron D. Ludlow, Joop Schaye, and Richard Bower. Numerical convergence of simulations of galaxy formation: the abundance and internal structure of cold dark matter haloes. *MNRAS*, 488(3):3663–3684, Sep 2019. doi: 10.1093/mnras/stz1821.

Andrea V. Macciò, Aaron A. Dutton, Frank C. van den Bosch, Ben Moore, Doug Potter, and Joachim Stadel. Concentration, spin and shape of dark matter haloes: scatter and the dependence on mass and environment. *MNRAS*, 378(1):55–71, June 2007. doi: 10.1111/j.1365-2966.2007.11720.x.

G. A. Mamon, T. Sanchis, E. Salvador-Solé, and J. M. Solanes. The origin of H I-deficiency in galaxies on the outskirts of the Virgo cluster. I. How far can galaxies bounce out of clusters? *AAp*, 414:445–451, February 2004. doi: 10.1051/0004-6361:20034155.

P. Mansfield, A. V. Kravtsov, and B. Diemer. Splashback Shells of Cold Dark Matter Halos. *ApJ*, 841:34, May 2017. doi: 10.3847/1538-4357/aa7047.

Phil Mansfield. phil-mansfield/shellfish: Version 1.0.0, April 2017. URL `https://doi.org/10.5281/zenodo.569034`.

Philip Mansfield and Andrey V. Kravtsov. The Three Causes of Low-Mass Assembly Bias. *arXiv e-prints*, art. arXiv:1902.00030, Jan 2019.

Y.-Y. Mao, A. R. Zentner, and R. H. Wechsler. Beyond assembly bias: exploring secondary halo biases for cluster-size haloes. *MNRAS*, 474:5143–5157, March 2018. doi: 10.1093/mnras/stx3111.

Yao-Yuan Mao, Marc Williamson, and Risa H. Wechsler. The Dependence of Subhalo Abundance on Halo Concentration. *ApJ*, 810(1):21, September 2015. doi: 10.1088/0004-637X/810/1/21.

Federico Marinacci, Mark Vogelsberger, Rüdiger Pakmor, Paul Torrey, Volker Springel, Lars Hernquist, Dylan Nelson, Rainer Weinberger, Annalisa Pillepich, Jill Naiman, and Shy Genel. First results from the IllustrisTNG simulations: radio haloes and magnetic fields. *MNRAS*, 480(4):5113–5139, Nov 2018. doi: 10.1093/mnras/sty2206.

Jorryt Matthee, Joop Schaye, Robert A. Crain, Matthieu Schaller, Richard Bower, and Tom Theuns. The origin of scatter in the stellar mass-halo mass relation of central galaxies in the EAGLE simulation. *MNRAS*, 465(2):2381–2396, February 2017. doi: 10.1093/mnras/stw2884.

Alan W. McConnachie, Michael J. Irwin, Rodrigo A. Ibata, John Dubinski, Lawrence M. Widrow, Nicolas F. Martin, Patrick Côté, Aaron L. Dotter, Julio F. Navarro, Annette M. N. Ferguson, Thomas H. Puzia, Geraint F. Lewis, Arif Babul, Pauline Barmby, Olivier Bienaymé, Scott C. Chapman, Robert Cockcroft, Michelle L. M. Collins, Mark A. Fardal, William E. Harris, Avon Huxor, A. Dougal Mackey, Jorge Peñarrubia, R. Michael Rich, Harvey B. Richer, Arnaud Siebert, Nial Tanvir, David Valls-Gabaud, and Kimberly A. Venn. The remnants of galaxy formation from a panoramic survey of the region around M31. *Nature*, 461(7260):66–69, September 2009. doi: 10.1038/nature08327.

R. Minkowski. Internal Dispersion of Velocities in Other Galaxies. In George Cunliffe

McVittie, editor, *Problems of Extra-Galactic Research*, volume 15 of *IAU Symposium*, page 112, January 1962.

H. J. Mo and S. D. M. White. An analytic model for the spatial clustering of dark matter haloes. *MNRAS*, 282:347–361, September 1996. doi: 10.1093/mnras/282.2.347.

J. J. Monaghan and J. C. Lattanzio. A refined particle method for astrophysical problems. *AAp*, 149(1):135–143, Aug 1985.

Ben Moore, Sebastiano Ghigna, Fabio Governato, George Lake, Thomas Quinn, Joachim Stadel, and Paolo Tozzi. Dark Matter Substructure within Galactic Halos. *ApJl*, 524(1): L19–L22, October 1999. doi: 10.1086/312287.

S. More, A. V. Kravtsov, N. Dalal, and S. Gottlöber. The Overdensity and Masses of the Friends-of-friends Halos and Universality of Halo Mass Function. *ApJs*, 195:4, July 2011. doi: 10.1088/0067-0049/195/1/4.

S. More, B. Diemer, and A. V. Kravtsov. The Splashback Radius as a Physical Halo Boundary and the Growth of Halo Mass. *ApJ*, 810:36, September 2015. doi: 10.1088/0004-637X/810/1/36.

S. More, H. Miyatake, M. Takada, B. Diemer, A. V. Kravtsov, N. K. Dalal, A. More, R. Murata, R. Mandelbaum, E. Rozo, E. S. Rykoff, M. Oguri, and D. N. Spergel. Detection of the Splashback Radius and Halo Assembly bias of Massive Galaxy Clusters. *ArXiv e-prints*, January 2016.

RD Mosteller. Simplified calculation of body-surface area. *The New England journal of medicine*, 317(17):1098–1098, 1987.

M. Musso, C. Cadiou, C. Pichon, S. Codis, K. Kraljic, and Y. Dubois. How does the cosmic web impact assembly bias? *MNRAS*, 476:4877–4906, June 2018. doi: 10.1093/mnras/sty191.

D. Nagai and A. V. Kravtsov. The Radial Distribution of Galaxies in Λ Cold Dark Matter Clusters. *ApJ*, 618:557–568, January 2005. doi: 10.1086/426016.

Jill P. Naiman, Annalisa Pillepich, Volker Springel, Enrico Ramirez-Ruiz, Paul Torrey, Mark Vogelsberger, Rüdiger Pakmor, Dylan Nelson, Federico Marinacci, Lars Hernquist, Rainer Weinberger, and Shy Genel. First results from the IllustrisTNG simulations: a tale of two elements - chemical evolution of magnesium and europium. *MNRAS*, 477(1):1206–1224, Jun 2018. doi: 10.1093/mnras/sty618.

J. F. Navarro, C. S. Frenk, and S. D. M. White. A Universal Density Profile from Hierarchical Clustering. *ApJ*, 490:493–508, December 1997. doi: 10.1086/304888.

J. F. Navarro, E. Hayashi, C. Power, A. R. Jenkins, C. S. Frenk, S. D. M. White, V. Springel, J. Stadel, and T. R. Quinn. The inner structure of ΛCDM haloes - III. Universality and asymptotic slopes. *MNRAS*, 349:1039–1051, April 2004. doi: 10.1111/j.1365-2966.2004.07586.x.

J. F. Navarro, A. Ludlow, V. Springel, J. Wang, M. Vogelsberger, S. D. M. White, A. Jenkins, C. S. Frenk, and A. Helmi. The diversity and similarity of simulated cold dark matter haloes. *MNRAS*, 402:21–34, February 2010. doi: 10.1111/j.1365-2966.2009.15878.x.

Dylan Nelson, Annalisa Pillepich, Volker Springel, Rainer Weinberger, Lars Hernquist, Rüdiger Pakmor, Shy Genel, Paul Torrey, Mark Vogelsberger, Guinevere Kauffmann, Federico Marinacci, and Jill Naiman. First results from the IllustrisTNG simulations: the galaxy colour bimodality. *MNRAS*, 475(1):624–647, Mar 2018. doi: 10.1093/mnras/stx3040.

Dylan Nelson, Volker Springel, Annalisa Pillepich, Vicente Rodriguez-Gomez, Paul Torrey, Shy Genel, Mark Vogelsberger, Ruediger Pakmor, Federico Marinacci, Rainer Weinberger, Luke Kelley, Mark Lovell, Benedikt Diemer, and Lars Hernquist. The IllustrisTNG sim-

ulations: public data release. *Computational Astrophysics and Cosmology*, 6(1):2, May 2019. doi: 10.1186/s40668-019-0028-x.

Angelo F. Neto, Liang Gao, Philip Bett, Shaun Cole, Julio F. Navarro, Carlos S. Frenk, Simon D. M. White, Volker Springel, and Adrian Jenkins. The statistics of Λ CDM halo concentrations. *MNRAS*, 381(4):1450–1462, Nov 2007. doi: 10.1111/j.1365-2966.2007.12381.x.

Maria K. Neuzil, Philip Mansfield, and Andrey V. Kravtsov. The Sheet of Giants: Unusual properties of the Milky Way's immediate neighbourhood. *MNRAS*, 494(2):2600–2617, April 2020. doi: 10.1093/mnras/staa898.

Isaac Newton. Newton, isaac (sir), 1642-1727 to halley, edmond, 1656-1742, Oct 1695.

Christine O'Donnell, Peter Behroozi, and Surhud More. Observing Correlations Between Dark Matter Accretion and Galaxy Growth: I. Recent Star Formation Activity in Isolated Milky Way-Mass Galaxies. *arXiv e-prints*, art. arXiv:2005.08995, May 2020.

Marilyn Bailey Ogilvie and Joy Dorothy Harvey. *The biographical dictionary of women in science : pioneering lives from ancient times to the mid-20th century.* New York: Routledge, 2000.

J. H. Oort. Some Problems Concerning the Structure and Dynamics of the Galactic System and the Elliptical Nebulae NGC 3115 and 4494. *ApJ*, 91:273, April 1940. doi: 10.1086/144167.

Wayne Orchiston. *A Polynesian Astronomical Perspective: the Maori of New Zealand.* Springer Science Business Media, B. V., 1998.

J. P. Ostriker and P. J. E. Peebles. A Numerical Study of the Stability of Flattened Galaxies: or, can Cold Galaxies Survive? *ApJ*, 186:467–480, December 1973. doi: 10.1086/152513.

J. P. Ostriker, P. J. E. Peebles, and A. Yahil. The Size and Mass of Galaxies, and the Mass of the Universe. *ApJL*, 193:L1, October 1974. doi: 10.1086/181617.

Thornton Page. Masses of the double galaxies. *AJ*, 64:53, March 1959. doi: 10.1086/107865.

A. Paranjape, O. Hahn, and R. K. Sheth. Halo assembly bias and the tidal anisotropy of the local halo environment. *MNRAS*, 476:3631–3647, May 2018. doi: 10.1093/mnras/sty496.

A. Patej and A. Loeb. Density Jumps Near the Virial Radius of Galaxy Clusters. *ApJ*, 824: 69, June 2016. doi: 10.3847/0004-637X/824/2/69.

Marcel S. Pawlowski. The planes of satellite galaxies problem, suggested solutions, and open questions. *Modern Physics Letters A*, 33(6):1830004, February 2018. doi: 10.1142/S0217732318300045.

P. J. E. Peebles. Origin of the Angular Momentum of Galaxies. *ApJ*, 155:393, Feb 1969. doi: 10.1086/149876.

P. J. E. Peebles. Structure of the Coma Cluster of Galaxies. *AJ*, 75:13, February 1970. doi: 10.1086/110933.

Michael A. Penna and Kris A. Dines. A simple method for fitting sphere-like surfaces. *IEEE Transactions on Pattern Analysis and Machine Intelligence*, 29(9):1673, 2007.

Antonio Pigafetta. *First Voyage Round the World by Magellan: Translated from the Accounts of Pigafetta and Other Contemporary Writers*. Number 52. Cambridge University Press, 1522.

Annalisa Pillepich, Dylan Nelson, Lars Hernquist, Volker Springel, Rüdiger Pakmor, Paul Torrey, Rainer Weinberger, Shy Genel, Jill P. Naiman, Federico Marinacci, and Mark Vogelsberger. First results from the IllustrisTNG simulations: the stellar mass content of groups and clusters of galaxies. *MNRAS*, 475(1):648–675, Mar 2018. doi: 10.1093/mnras/stx3112.

C. N. Poveda-Ruiz, J. E. Forero-Romero, and J. C. Muñoz-Cuartas. Quantifying and Controlling Biases in Estimates of Dark Matter Halo Concentration. *ApJ*, 832(2):169, Dec 2016. doi: 10.3847/0004-637X/832/2/169.

D. Powell and T. Abel. An exact general remeshing scheme applied to physically conservative voxelization. *ArXiv e-prints*, December 2014.

C. Power, J. F. Navarro, A. Jenkins, C. S. Frenk, S. D. M. White, V. Springel, J. Stadel, and T. Quinn. The inner structure of ΛCDM haloes - I. A numerical convergence study. *MNRAS*, 338:14–34, January 2003. doi: 10.1046/j.1365-8711.2003.05925.x.

Chris Power and Alexander Knebe. The impact of box size on the properties of dark matter haloes in cosmological simulations. *MNRAS*, 370(2):691–701, August 2006. doi: 10.1111/j.1365-2966.2006.10562.x.

Chris Power, Alexander Knebe, and Steffen R. Knollmann. The dynamical state of dark matter haloes in cosmological simulations - I. Correlations with mass assembly history. *MNRAS*, 419(2):1576–1587, January 2012. doi: 10.1111/j.1365-2966.2011.19820.x.

Francisco Prada, Anatoly A. Klypin, Antonio J. Cuesta, Juan E. Betancort-Rijo, and Joel Primack. Halo concentrations in the standard Λ cold dark matter cosmology. *MNRAS*, 423(4):3018–3030, Jul 2012. doi: 10.1111/j.1365-2966.2012.21007.x.

W. H. Press and P. Schechter. Formation of Galaxies and Clusters of Galaxies by Self-Similar Gravitational Condensation. *ApJ*, 187:425–438, February 1974. doi: 10.1086/152650.

Rachel M. Reddick, Risa H. Wechsler, Jeremy L. Tinker, and Peter S. Behroozi. The Connection between Galaxies and Dark Matter Structures in the Local Universe. *ApJ*, 771 (1):30, Jul 2013. doi: 10.1088/0004-637X/771/1/30.

Ignasi Ribas, Carme Jordi, Francesc Vilardell, Edward L. Fitzpatrick, Ron W. Hilditch, and Edward F. Guinan. First Determination of the Distance and Fundamental Properties of

an Eclipsing Binary in the Andromeda Galaxy. *ApJL*, 635(1):L37–L40, December 2005. doi: 10.1086/499161.

K. Rines, M. J. Geller, A. Diaferio, and M. J. Kurtz. Measuring the Ultimate Halo Mass of Galaxy Clusters: Redshifts and Mass Profiles from the Hectospec Cluster Survey (HeCS). *ApJ*, 767:15, April 2013. doi: 10.1088/0004-637X/767/1/15.

M. S. Roberts and R. N. Whitehurst. The rotation curve and geometry of M31 at large galactocentric distances. *ApJ*, 201:327–346, October 1975. doi: 10.1086/153889.

Vera Rubin. Seeing Dark Matter in the Andromeda Galaxy. *Physics Today*, 59(12):8, January 2006. doi: 10.1063/1.2435662.

Vera C. Rubin and Jr. Ford, W. Kent. Rotation of the Andromeda Nebula from a Spectroscopic Survey of Emission Regions. *ApJ*, 159:379, February 1970. doi: 10.1086/150317.

A. N. Salcedo, A. H. Maller, A. A. Berlind, M. Sinha, C. K. McBride, P. S. Behroozi, R. H. Wechsler, and D. H. Weinberg. Spatial clustering of dark matter haloes: secondary bias, neighbour bias, and the influence of massive neighbours on halo properties. *MNRAS*, 475: 4411–4423, April 2018. doi: 10.1093/mnras/sty109.

L. V. Sales, J. F. Navarro, M. G. Abadi, and M. Steinmetz. Cosmic ménage à trois: the origin of satellite galaxies on extreme orbits. *MNRAS*, 379:1475–1483, August 2007. doi: 10.1111/j.1365-2966.2007.12026.x.

H. B. Sandvik, O. Möller, J. Lee, and S. D. M. White. Why does the clustering of haloes depend on their formation history? *MNRAS*, 377:234–244, May 2007. doi: 10.1111/j.1365-2966.2007.11595.x.

G. Sato-Polito, A. D. Montero-Dorta, L. R. Abramo, F. Prada, and A. Klypin. The dependence of halo bias on age, concentration and spin. *ArXiv e-prints*, October 2018.

A. Savitzky and M. J. E. Golay. Smoothing and differentiation of data by simplified least squares procedures. *Analytical Chemistry*, 36(8):1627, 1964.

M. Schwarzschild. Mass distribution and mass-luminosity ratio in galaxies. *AJ*, 59:273, September 1954. doi: 10.1086/107013.

R. K. Sheth and G. Tormen. Large-scale bias and the peak background split. *MNRAS*, 308: 119–126, September 1999. doi: 10.1046/j.1365-8711.1999.02692.x.

Ravi K. Sheth and Giuseppe Tormen. On the environmental dependence of halo formation. *MNRAS*, 350(4):1385–1390, June 2004. doi: 10.1111/j.1365-2966.2004.07733.x.

X. Shi. The outer profile of dark matter haloes: an analytical approach. *MNRAS*, 459: 3711–3720, July 2016. doi: 10.1093/mnras/stw925.

Jonathan Sick, Stephane Courteau, Jean-Charles Cuilland re, Julianne Dalcanton, Roelof de Jong, Michael McDonald, Dana Simard, and R. Brent Tully. The Stellar Mass of M31 as inferred by the Andromeda Optical & Infrared Disk Survey. In Michele Cappellari and Stéphane Courteau, editors, *Galaxy Masses as Constraints of Formation Models*, volume 311 of *IAU Symposium*, pages 82–85, April 2015. doi: 10.1017/S1743921315003440.

L. P. T. Sin, S. J. Lilly, and B. M. B. Henriques. On The Evidence For Large-Scale Galactic Conformity In The Local Universe. *MNRAS*, 471:1192–1207, October 2017. doi: 10.1093/mnras/stx1674.

Sinclair Smith. The Mass of the Virgo Cluster. *ApJ*, 83:23, January 1936. doi: 10.1086/143697.

Keith Snedegar. *Astronomical Practices in Africa South of the Sahara*. Springer Science Business Media, B. V., 1998.

Yoshiaki Sofue and Vera Rubin. Rotation Curves of Spiral Galaxies. *ARA&A*, 39:137–174, January 2001. doi: 10.1146/annurev.astro.39.1.137.

V. Springel, J. Wang, M. Vogelsberger, A. Ludlow, A. Jenkins, A. Helmi, J. F. Navarro, C. S. Frenk, and S. D. M. White. The Aquarius Project: the subhaloes of galactic haloes. *MNRAS*, 391:1685–1711, December 2008. doi: 10.1111/j.1365-2966.2008.14066.x.

Volker Springel. The cosmological simulation code GADGET-2. *MNRAS*, 364(4):1105–1134, December 2005. doi: 10.1111/j.1365-2966.2005.09655.x.

Volker Springel. E pur si muove: Galilean-invariant cosmological hydrodynamical simulations on a moving mesh. *MNRAS*, 401(2):791–851, Jan 2010. doi: 10.1111/j.1365-2966.2009.15715.x.

Volker Springel, Naoki Yoshida, and Simon D. M. White. GADGET: a code for collisionless and gasdynamical cosmological simulations. *New Astron.*, 6(2):79–117, April 2001a. doi: 10.1016/S1384-1076(01)00042-2.

Volker Springel, Naoki Yoshida, and Simon D. M. White. GADGET: a code for collisionless and gasdynamical cosmological simulations. *New Astron.*, 6(2):79–117, Apr 2001b. doi: 10.1016/S1384-1076(01)00042-2.

Volker Springel, Rüdiger Pakmor, Annalisa Pillepich, Rainer Weinberger, Dylan Nelson, Lars Hernquist, Mark Vogelsberger, Shy Genel, Paul Torrey, Federico Marinacci, and Jill Naiman. First results from the IllustrisTNG simulations: matter and galaxy clustering. *MNRAS*, 475(1):676–698, Mar 2018. doi: 10.1093/mnras/stx3304.

T. Sunayama, A. P. Hearin, N. Padmanabhan, and A. Leauthaud. The scale-dependence of halo assembly bias. *MNRAS*, 458:1510–1516, May 2016. doi: 10.1093/mnras/stw332.

Johnathan Swift. *Gulliver's Travels*. 1726.

G. Andreas Tammann. Karl Schwarzschild Lecture: The Ups and Downs of the Hubble Constant (With 12 Figures). *Reviews in Modern Astronomy*, 19:1, January 2006. doi: 10.1002/9783527619030.ch1.

Max Tegmark, Joseph Silk, Martin J. Rees, Alain Blanchard, Tom Abel, and Francesco Palla. How Small Were the First Cosmological Objects? *ApJ*, 474:1, January 1997. doi: 10.1086/303434.

J. L. Tinker, C. Hahn, Y.-Y. Mao, A. R. Wetzel, and C. Conroy. Halo histories versus galaxy properties at z = 0 II: large-scale galactic conformity. *MNRAS*, 477:935–945, June 2018. doi: 10.1093/mnras/sty666.

Jeremy L. Tinker, Andrew R. Wetzel, Charlie Conroy, and Yao-Yuan Mao. Halo histories versus Galaxy properties at z = 0 - I. The quenching of star formation. *MNRAS*, 472(2): 2504–2516, December 2017. doi: 10.1093/mnras/stx2066.

R. C. Tolman. Effect of Inhomogeneity on Cosmological Models. *Proceedings of the National Academy of Science*, 20:169–176, March 1934. doi: 10.1073/pnas.20.3.169.

R. B. Tully. Galaxy Groups. *The Astronomical Journal*, 149:54, February 2015. doi: 10.1088/0004-6256/149/2/54.

K. Umetsu and B. Diemer. Lensing Constraints on the Mass Profile Shape and the Splashback Radius of Galaxy Clusters. *ApJ*, 836:231, February 2017. doi: 10.3847/1538-4357/aa5c90.

F. C. van den Bosch, G. Ogiya, O. Hahn, and A. Burkert. Disruption of dark matter substructure: fact or fiction? *MNRAS*, 474:3043–3066, March 2018. doi: 10.1093/mnras/stx2956.

Frank C. van den Bosch. Dissecting the evolution of dark matter subhaloes in the Bolshoi simulation. *MNRAS*, 468(1):885–909, June 2017. doi: 10.1093/mnras/stx520.

Frank C. van den Bosch and Go Ogiya. Dark matter substructure in numerical simulations: a tale of discreteness noise, runaway instabilities, and artificial disruption. *MNRAS*, 475 (3):4066–4087, Apr 2018. doi: 10.1093/mnras/sty084.

Roeland P. van der Marel and Johannes Sahlmann. First Gaia Local Group Dynamics:

Magellanic Clouds Proper Motion and Rotation. *ApJL*, 832(2):L23, December 2016. doi: 10.3847/2041-8205/832/2/L23.

Roeland P. van der Marel, Gurtina Besla, T. J. Cox, Sangmo Tony Sohn, and Jay Anderson. The M31 Velocity Vector. III. Future Milky Way M31-M33 Orbital Evolution, Merging, and Fate of the Sun. *ApJ*, 753(1):9, July 2012. doi: 10.1088/0004-637X/753/1/9.

Roeland P. van der Marel, Mark A. Fardal, Sangmo Tony Sohn, Ekta Patel, Gurtina Besla, Andrés del Pino, Johannes Sahlmann, and Laura L. Watkins. First Gaia Dynamics of the Andromeda System: DR2 Proper Motions, Orbits, and Rotation of M31 and M33. *ApJ*, 872(1):24, February 2019. doi: 10.3847/1538-4357/ab001b.

Eelco van Kampen. Overmerging in N-body simulations. *arXiv e-prints*, art. astro-ph/0002027, February 2000.

A. Vikhlinin, A. Kravtsov, W. Forman, C. Jones, M. Markevitch, S. S. Murray, and L. Van Speybroeck. Chandra Sample of Nearby Relaxed Galaxy Clusters: Mass, Gas Fraction, and Mass-Temperature Relation. *ApJ*, 640(2):691–709, April 2006. doi: 10.1086/500288.

F. Vilardell, I. Ribas, C. Jordi, E. L. Fitzpatrick, and E. F. Guinan. The distance to the Andromeda galaxy from eclipsing binaries. *A&Ap*, 509:A70, January 2010. doi: 10.1051/0004-6361/200913299.

A. S. Villarreal, A. R. Zentner, Y.-Y. Mao, C. W. Purcell, F. C. van den Bosch, B. Diemer, J. U. Lange, K. Wang, and D. Campbell. The immitigable nature of assembly bias: the impact of halo definition on assembly bias. *MNRAS*, 472:1088–1105, November 2017a. doi: 10.1093/mnras/stx2045.

Antonio S. Villarreal, Andrew R. Zentner, Yao-Yuan Mao, Chris W. Purcell, Frank C. van den Bosch, Benedikt Diemer, Johannes U. Lange, Kuan Wang, and Duncan Campbell. The immitigable nature of assembly bias: the impact of halo definition on assembly bias. *MNRAS*, 472(1):1088–1105, Nov 2017b. doi: 10.1093/mnras/stx2045.

Maya Vitvitska, Anatoly A. Klypin, Andrey V. Kravtsov, Risa H. Wechsler, Joel R. Primack, and James S. Bullock. The Origin of Angular Momentum in Dark Matter Halos. *ApJ*, 581(2):799–809, December 2002. doi: 10.1086/344361.

Mark Vogelsberger and Simon D. M. White. Streams and caustics: the fine-grained structure of Λ cold dark matter haloes. *MNRAS*, 413(2):1419–1438, May 2011. doi: 10.1111/j.1365-2966.2011.18224.x.

Mark Vogelsberger, Amina Helmi, Volker Springel, Simon D. M. White, Jie Wang, Carlos S. Frenk, Adrian Jenkins, Aaron Ludlow, and Julio F. Navarro. Phase-space structure in the local dark matter distribution and its signature in direct detection experiments. *MNRAS*, 395(2):797–811, May 2009. doi: 10.1111/j.1365-2966.2009.14630.x.

S. von Hoerner. Die numerische Integration des n-Körper-Problemes für Sternhaufen. I. *ZAp*, 50:184–214, January 1960.

H. Wang, H. J. Mo, and Y. P. Jing. The distribution of ejected subhaloes and its implication for halo assembly bias. *MNRAS*, 396:2249–2256, July 2009. doi: 10.1111/j.1365-2966.2009.14884.x.

H. Wang, H. J. Mo, Y. P. Jing, X. Yang, and Y. Wang. Internal properties and environments of dark matter haloes. *MNRAS*, 413:1973–1990, May 2011. doi: 10.1111/j.1365-2966.2011.18301.x.

H. Y. Wang, H. J. Mo, and Y. P. Jing. Environmental dependence of cold dark matter halo formation. *MNRAS*, 375:633–639, February 2007. doi: 10.1111/j.1365-2966.2006.11316.x.

R. H. Wechsler and J. L. Tinker. The Connection Between Galaxies and Their Dark Matter Halos. *Annual Review of Astronomy and Astrophysics*, 56:435–487, September 2018. doi: 10.1146/annurev-astro-081817-051756.

R. H. Wechsler, J. S. Bullock, J. R. Primack, A. V. Kravtsov, and A. Dekel. Concentrations of Dark Halos from Their Assembly Histories. *ApJ*, 568:52–70, March 2002. doi: 10.1086/338765.

R. H. Wechsler, A. R. Zentner, J. S. Bullock, A. V. Kravtsov, and B. Allgood. The Dependence of Halo Clustering on Halo Formation History, Concentration, and Occupation. *ApJ*, 652:71–84, November 2006. doi: 10.1086/507120.

Rainer Weinberger, Volker Springel, and Rüdiger Pakmor. The Arepo public code release. *arXiv e-prints*, art. arXiv:1909.04667, September 2019.

A. R. Wetzel, J. D. Cohn, M. White, D. E. Holz, and M. S. Warren. The Clustering of Massive Halos. *ApJ*, 656:139–147, February 2007. doi: 10.1086/510444.

A. R. Wetzel, J. L. Tinker, C. Conroy, and F. C. van den Bosch. Galaxy evolution near groups and clusters: ejected satellites and the spatial extent of environmental quenching. *MNRAS*, 439:2687–2700, April 2014. doi: 10.1093/mnras/stu122.

S. D. M. White. The dynamics of rich clusters of galaxies. *MNRAS*, 177:717–733, December 1976. doi: 10.1093/mnras/177.3.717.

S. D. M. White and M. J. Rees. Core condensation in heavy halos - A two-stage theory for galaxy formation and clustering. *MNRAS*, 183:341–358, May 1978. doi: 10.1093/mnras/183.3.341.

Curtis Wilson. Clairut's Calculation of the Eighteenth-century Return of Halley's Comet. *Journal for the History of Astronomy*, 24:1, May 1993. doi: 10.1177/002182869302400101.

Lizhi Xie and Liang Gao. Assembly history of subhalo populations in galactic and cluster sized dark haloes. *MNRAS*, 454(2):1697–1703, December 2015. doi: 10.1093/mnras/stv2077.

Xiaohu Yang, H. J. Mo, and Frank C. van den Bosch. Constraining galaxy formation and cosmology with the conditional luminosity function of galaxies. *MNRAS*, 339(4):1057–1080, March 2003. doi: 10.1046/j.1365-8711.2003.06254.x.

M. Zemp, O. Y. Gnedin, N. Y. Gnedin, and A. V. Kravtsov. On Determining the Shape of Matter Distributions. *ApJs*, 197:30, December 2011. doi: 10.1088/0067-0049/197/2/30.

A. R. Zentner. The Excursion Set Theory of Halo Mass Functions, Halo Clustering, and Halo Growth. *International Journal of Modern Physics D*, 16:763–815, 2007. doi: 10.1142/S0218271807010511.

A. R. Zentner, A. P. Hearin, and F. C. van den Bosch. Galaxy assembly bias: a significant source of systematic error in the galaxy-halo relationship. *MNRAS*, 443:3044–3067, October 2014. doi: 10.1093/mnras/stu1383.

A. R. Zentner, A. Hearin, F. C. van den Bosch, J. U. Lange, and A. Villarreal. Constraints on Assembly Bias from Galaxy Clustering. *ArXiv e-prints*, June 2016.

A. R. Zentner, A. Hearin, F. C. van den Bosch, J. U. Lange, and A. Villarreal. Constraints on assembly bias from galaxy clustering. *MNRAS*, 485:1196–1209, May 2019. doi: 10.1093/mnras/stz470.

Tianchi Zhang, Shihong Liao, Ming Li, and Liang Gao. The optimal gravitational softening length for cosmological N-body simulations. *Monthly Notices of the Royal Astronomical Society*, 487(1):1227–1232, Jul 2019. doi: 10.1093/mnras/stz1370.

D. H. Zhao, H. J. Mo, Y. P. Jing, and G. Börner. The growth and structure of dark matter haloes. *MNRAS*, 339:12–24, February 2003. doi: 10.1046/j.1365-8711.2003.06135.x.

D. H. Zhao, Y. P. Jing, H. J. Mo, and G. Börner. Accurate Universal Models for the Mass Accretion Histories and Concentrations of Dark Matter Halos. *ApJ*, 707:354–369, December 2009. doi: 10.1088/0004-637X/707/1/354.

I. Zhuravleva, E. Churazov, A. Kravtsov, E. T. Lau, D. Nagai, and R. Sunyaev. Quantifying properties of ICM inhomogeneities. *MNRAS*, 428:3274–3287, February 2013. doi: 10.1093/mnras/sts275.

Judith Zinsser. *Emile du Chatelet: Daring Genius of the Enlilghtenment*. The Penguin Group, 2006.

F. Zwicky. Die Rotverschiebung von extragalaktischen Nebeln. *Helvetica Physica Acta*, 6: 110–127, January 1933.